Towards the observation of the radiation pressure noise in a suspended interferometer : the QuRaG experiment

Sibilla Di Pace

UNIVERSITÉ DE NICE - SOPHIA ANTIPOLIS - UFR Sciences
École Doctorale SFA : Science Fondamentales et Appliquées
UNIVERSITÀ DI ROMA - LA SAPIENZA - Dipartimento di Fisica
Scuola Dottorale "VITO VOLTERRA": Dottorato in Fisica XXVII Ciclo

T H È S E

pour obtenir le titre de

Docteur en Sciences

de l'Université de Nice - Sophia Antipolis
dell'Università di Roma - La Sapienza
Spécialité : Physique

Présentée par

Sibilla Di Pace

Vers l'Observation du Bruit Quantique de la Pression de Radiation dans un Interféromètre Suspendu: l'expérience QuRaG

Thèse dirigée par Alain Brillet et Fulvio Ricci

préparée à l'Observatoire de la Côte d'Azur

sera présentée le 15 décembre 2014

Jury :

Rapporteurs :	A.Porzio	Pr.	Università di Napoli, Federico II
	P.-F.Cohadon	Pr.	Université Pierre et Marie Curie, Paris
Examinateurs :	N.Dimarcq	DR	CNRS, Laboratoire SYRTE, Paris
	H.Vocca	Pr.	Università di Perugia
	G.Cagnoli	Pr.	LMA, Université Claude Bernard, Lyon
Directeurs :	A.Brillet	DR	CNRS, Laboratoire Artemis, Nice
	F.Ricci	Pr.	Università di Roma, La Sapienza
Membre invité :	W.Chaibi	Dr.	CNRS, Laboratoire Artemis, Nice

UNIVERSITÉ DE NICE - SOPHIA ANTIPOLIS - UFR Sciences
École Doctorale SFA : Science Fondamentales et Appliquées
UNIVERSITÀ DI ROMA - LA SAPIENZA - Dipartimento di Fisica
Scuola Dottorale "VITO VOLTERRA": Dottorato in Fisica XXVII Ciclo

T H E S I S

for the achievement of the qualification of

Doctor of Philosophy in Sciences

of the University of Nice - Sophia Antipolis
of the University of Roma - La Sapienza
Specialization : Physics

Presented by

Sibilla Di Pace

Towards the Observation of the Quantum Radiation Pressure Noise in a Suspended Interferometer: the QuRaG experiment

Thesis directed by Alain Brillet and Fulvio Ricci

prepared at the Observatoire de la Côte d'Azur

will be defended the 15^{th} December 2014

Jury :

Referees :	A.Porzio	Pr.	Università di Napoli, Federico II
	P.-F.Cohadon	Pr.	Université Pierre et Marie Curie, Paris
Examiners :	N.Dimarcq	DR	CNRS, Laboratoire SYRTE, Paris
	H.Vocca	Pr.	Università di Perugia
	G.Cagnoli	Pr.	LMA, Université Claude Bernard, Lyon
Supervisors :	A.Brillet	DR	CNRS, Laboratoire Artemis, Nice
	F.Ricci	Pr.	Università di Roma, La Sapienza
Invited Member :	W.Chaibi	Dr.	CNRS, Laboratoire Artemis, Nice

Alla mia famiglia e al mio amore,
per avermi sostenuta in questo lungo cammino

Contents

Résumé

L'existence des ondes gravitationnelles (OG) est l'une des prédictions les plus intéressantes de la théorie de la relativité générale (RG) d'Einstein [57]. La découverte expérimentale des OG serait donc un test important de la théorie elle-même. En outre, puisque les OG interagissent faiblement avec la matière, elles peuvent voyager à travers des régions très denses sans subir de changements importants, contrairement à ce qui se passe avec les ondes électromagnétiques [108]. La détection des ondes gravitationnelles permettra donc d'ouvrir une nouvelle fenêtre d'observation en particulier dans les régions de l'Univers inaccessible à l'observation électromagnétique. Les détecteurs interférométriques, comme Virgo [55, 38], sont actuellement les dispositifs les plus prometteurs pour la détection d'ondes gravitationnelles issues de sources astrophysiques. Actuellement, la sensibilité des détecteurs des OG n'est pas encore suffisante pour avoir un taux d'observation de quelques événements par an. Un intense programme expérimental visant à améliorer la sensibilité est actuellement en cours [38, 39]. Particulièrement, les prochaines générations de détecteurs d'OG, aux basses fréquences (10 Hz - 50 Hz), seront limitées par l'effet de la pression de radiation quantique sur les miroirs suspendus [38, 122, 34]. Ce phénomène, pas encore observé expérimentalement, est l'objet d'un des champs de recherche le plus actif en ce moment. Riche de l'expérience acquise avec Virgo, le travail ici présenté vise à la construction d'un détecteur pour l'étude des effets quantiques de la pression de radiation dans les détecteurs d'ondes gravitationnelles: l'expérience QuRaG. QuRaG sera constitué d'un interféromètre de Michelson suspendu, dans lequel la géométrie est optimisée afin de détecter le bruit quantique de la pression de radiation. Chaque bras de l'interféromètre sera composé d'une cavité Fabry-Pérot (FP) de très haute *finesse*, dans laquelle seulement le miroir de fond sera suspendu et donc sensible au bruit quantique de la pression de radiation. Par conséquent, durant ma thèse, un grand effort de R&D a été réalisé afin d'être capable de construire l'interféromètre final. Au cours de mes trois années de thèse, j'ai eu une participation active dans la conception et le développement de tous les sous-systèmes de QuRaG. Donc le travail que j'ai fait durant ma thèse porte sur divers aspects du projet QuRaG dont les problématiques appartiennent à différents domaines de la physique. Ce manuscrit présente en détail les différentes études réalisées. Par conséquent, j'ai analysé de nombreux systèmes de suspension pour les miroirs de fond de QuRaG en estimant et en comparant leur bruit thermique avec le bruit de la pression de radiation. Mes calculs ont permis de valider la meilleure configuration comme étant celle avec un niveau de bruit thermique inférieur au niveau de bruit de la pression de radiation, mais

qui soit aussi réalisable pour QuRaG.

Le dernier niveau de suspension des miroirs de fond devra être donc un **Double Pendule monolithique en silice fondue** avec deux fils de suspension de $40\mu m$ de diamètre et $2cm$ de longueur, et le miroir suspendu devra avoir une masse $\leq 0.1g$ et comme dimensions $5mm \times 3mm \times 3mm$. De plus, l'analyse modale sur la totalité des optiques de l'interféromètre suspendu QuRaG montre également que le disque qui maintient directement les optiques de l'interféromètre doit être plus épais que prévu dans le dessin préliminaire, et avoir une épaisseur de $40mm$ à la place de $10mm$ afin d'empêcher les résonances internes du disque de tomber dans la bande de détection de QuRaG.

Cette analyse a permis de conclure que QuRaG ne sera pas limité par le bruit thermique, et que donc sera capable de détecter le bruit de la pression de radiation dans la même bande d'observation des détecteurs terrestres d'OG, en particulier de Virgo.

La problématique de réaliser les fils des suspensions requis par l'analyse de bruit thermique, a demandé la collaboration du groupe Virgo de Perugia. Par conséquent, j'ai travaillé à Perugia presque un mois pour apprendre la technique de tirage de fibres de silice fondue à partir d'une 'graine' de silice de $3mm$ de diamètre, par une machine à flamme oxhydrique. En outre, j'ai appris la technique de mesure des pertes dans les fibres tirées. J'ai après pu transférer toute l'expertise acquise à Nice, où nous avons mis en place une procédure similaire pour tirer des fibres de silice. En faisant des tests de soudure des fibres, j'ai découvert que la machine à souder pouvait être utilisée pour tirer des fibres. Donc elle a été adapté avec deux moteurs commandés sur le PC pour contrôler très précisément la position du point de fusion et le temps de chauffage. Elle a permis de tirer des fibres d'un ordre de grandeur plus fines que les fibres de départ ayant $400\mu m$ de diamètre . Actuellement, les meilleurs échantillons tirés qui se rapprochent le plus des spécifications ont une partie centrale de $1.5cm$ pour $40\mu m$ de diamètre.

Mon travail couvre également la problématique du contrôle électrostatique des miroirs suspendus, car le système de contrôle de QuRaG prévoit un dernier niveau de contrôle directement appliqué sur les miroirs suspendus. Par conséquent, j'ai étudié le problème sur un miroir prototype de $1g$ en suspension dans un interféromètre de Michelson simple. Le contrôle électrostatique a été réalisé en plaçant un condensateur sur un support mobile derrière le miroir suspendu avec l'autre miroir du Michelson collé sur une barre piézoélectrique. Quand une tension est appliquée sur le condensateur, une force agit sur le miroir suspendu. Ce déplacement du miroir est compensé grâce au signal de correction renvoyé à la barre piézoélectrique qui déplace l'autre miroir pour compenser le déplacement du miroir suspendu. Le problème du contrôle électrostatique se trouve être directement connecté au problème de suspendre le miroir. Ainsi, plusieurs techniques et types de fils de suspension ont été testés. Néanmoins, la configuration qui a donné un meilleur résultat est constituée par deux oreilles en PVC collées sur le miroir, et un unique fil de suspension noué autour des oreilles qui se trouve être un de mes cheveux ayant $(58 \pm 3)\mu m$ de diamètre. Avec cette suspension, j'ai obtenu un déplacement maximal de $\sim 800nm$ pour une tension appliquée de $\sim 100V$ sur le condensateur. Un test préliminaire a montré que l'augmentation d'un facteur 10 sur

le déplacement maximal sera possible avec un amplificateur qui permet d'atteindre la tension de $300V$.

Un autre sujet important couvert par mon travail est la génération et l'optimisation des modes d'Hermite Gauss d'ordre supérieur. Ces modes ont une plus large répartition de l'intensité par rapport au faisceau Gaussien fondamental, ils peuvent donc mieux moyenner les distorsions de surface de miroir causées par les mouvements thermiques. Bien que mes estimations de bruit thermique ont montré que la sensibilité de QuRaG ne sera pas limitée par ce bruit, nous pourrions néanmoins utiliser ultérieurement ces modes pour réduire le niveau de bruit thermique des miroirs de QuRaG, si durant la phase opérationnelle cela sera nécessaire. En outre, ces modes peuvent être également appliquées pour améliorer la sensibilité des expériences d'horloges optiques, qui ont approché la limite de bruit thermique du miroir, et des d'interféromètres d'OG de prochaines générations. Le travail effectué sur ces modes démontre que le système qui a été mis en place est capable de générer des modes d'Hermite Gauss propres jusqu'à l'ordre $HG_{25,25}$. Des pourcentages de couplage en cavité *mode-cleaner* de $\simeq 90\%$ pour les modes $HG_{1,1}$ et $HG_{2,2}$, $\simeq 80\%$ pour le $HG_{5,5}$ et $\simeq 70\%$ pour le $HG_{10,10}$ ont été obtenus.

L'ensemble du travail ici présenté démontre qu'il est possible de construire un interféromètre suspendu de petite échelle qui soit capable d'observer le bruit de la pression de radiation dans la même bande de détection de détecteurs d'ondes gravitationnelles terrestres.

Introduction

The existence of gravitational waves (GWs) is one of the most interesting predictions of Einstein's theory of General Relativity (GR) [57]. The experimental discovery of GWs would therefore be an important test of the theory itself. Moreover, since GWs interact weakly with matter, they can travel through very dense regions without undergoing significant changes, contrary to what happens to electromagnetic waves [108]. The detection of GWs would therefore open a new window of investigation especially in regions of the Universe inaccessible to electromagnetic observation. Interferometric detectors, such as Virgo [55, 38], are currently the most promising devices for the detection of gravitational waves originated from astrophysical sources. Currently, the sensitivity of GW detectors (GWd) is not yet sufficient to observe signals with the rate of few events per year, so there is underway an experimental program to improve it [38, 39]. In particular the next generations of GWd, at low frequencies (10Hz - 50Hz), will be limited by the quantum radiation pressure effect on the suspended mirrors [38, 122, 34]. This phenomenon, not yet experimentally observed, is the subject of one of the most active research field at the time. Rich of the experience acquired with Virgo, the present work aims at building a detector for the observation of the effects of the Quantum Radiation Pressure Noise in GWd: the QuRaG experiment. It will consist of a suspended Michelson interferometer in which the geometry is optimized in order to detect the quantum radiation pressure noise. Each arm of the interferometer will be a high *finesse* Fabry-Pérot (FP) cavity in which only the end mirrors will be suspended and then sensitive to the quantum radiation pressure noise. Hence, it has been done a great effort of R&D in order to be able to build the final interferometer. During my three years of thesis I took active part in the conception and development of all the subsystems involved, as the generation and optimization of HG modes, the thermal noise reduction through the choice of the best suspension system, the electrostatic control of the suspended mirrors, the pulling of thin silica fiber, the technique of welding it to a light silica test mass and the direct measure of their losses.

Therefore, in the **First Chapter** I introduce the scientific background in which the QuRaG experiment is framed and the leading motivations to this experiment. Hence, I will discuss about the gravitational wave detections, and all the noise sources that limit the actual sensitivity of the ground based gravitational wave interferometers.

A specific chapter is then dedicated to radiation pressure noise, since it is the subject of the observation that our QuRaG interferometer is aimed to attain. Therefore, in the **Second Chapter** I introduce the project QuRaG and I explain why and how this

noise will limit the sensitivity of next generations of Earth based gravitational wave interferometers. I also make a brief excursus on the current other experiments for the observation of this effect, and then I explain how QuRaG will be sensitive to this effect and what is the signal that we do expect to observe.

The **Third Chapter** is devoted to discuss on the thermal noise in a suspended interferometer. This noise is currently one of the most important limit in the ground based gravitational wave detectors. In particular, the thermal fluctuations of the suspensions is dominant in the low frequencies and the thermal fluctuations of the mirror surface in the middle frequencies. Therefore, I make an historical overview on the problem and I explain in detail all the different thermal dissipation mechanisms that are encountered in a suspended interferometer like QuRaG and Virgo.

The goal of the chapter on thermal noise is to introduce the theory elements necessary to then explain, in the **Fourth Chapter**, the thermal noise analysis on QuRaG. All these analyses that I have done allowed us to constrain the design of the QuRaG last stage suspensions. In fact, thermal noise is likely to be one of the most important limit on the sensitivity of QuRaG. The validated configuration requires two suspension wires of length $2cm$ and very thin diameter of only $40\mu m$.

This requirement on the suspension wires characteristics obtained from my thermal noise estimations, lead to the realization of such thin wires. Thus, in the **Fifth Chapter** I describe the evolution of the procedure for pulling thin silica fibers and the system to measure their intrinsic losses, and I show how the best pulled samples at the present time are getting closer to the thermal noise analysis requirements.

The **Sixth Chapter** describes the part of my work that has been devoted to the study of the electrostatic control of a prototype 1g mirror suspended in a Michelson interferometer, with a capacitor placed on a movable support behind the suspended mirror. This work has been necessary since the overall control system of the QuRaG interferometer foresees a last control stage directly applied on the suspended mirror. The problematic of electrostatically control a suspended prototype mirror turned out to be directly connected to the problematic of suspending the prototype mirror. Thus, several techniques and kinds of wires have been tested.

In the **Seventh Chapter** I present the work done to generate and optimize the Hermite Gauss modes of Higher Order. These modes have a wider intensity distribution with respect to the fundamental Gaussian beam, thus they can average better over the mirror surface distortions caused by the thermal motions. However, my estimations of QuRaG thermal noise showed that its sensitivity will not be limited by this noise source, we could employ these modes to further reduce the thermal noise level of the QuRaG mirrors, if during operation it will result necessary. Moreover, these modes could be also applied for improving the sensitivity of the optical clock experiments, which approached the mirror thermal noise limit, and of the next generation of ground based gravitational interferometer.

In the conclusive **Eight Chapter**, I make an overall discussion on the obtained results.

Chapter 1

Scientific Motivations and Background

In this first chapter I will describe the scientific context in which this thesis and the QuRaG experiment are involved and the scientific motivations that lead this work. Both the scientific motivations and the scientific background are related with the detection of the Gravitational Waves and in particular with the future generation of ground based detectors. Ground based gravitational wave detectors are Michelson interferometers with Fabry-Pérot cavities, having a detection band within $10Hz$ and $10kHz$. The current sensitivity of these instruments has not been able to make the first detection, since it is limited by several noises, such as the thermal noise in the low frequency range, and the shot noise it the high frequency range. Therefore, the scientific community is currently making a great effort to upgrade these instruments in order to increase the sensitivity of a factor 10, hence the detection rate of a factor 1000 (i.e. for Virgo from 0.01 events/year or few events/ 100years, to few events/years). Nevertheless, this improvement requires a higher power circulating within the Fabry-Pérot cavities, which will lead these instruments to face the limits due to the quantum nature of the light. The shot noise will still dominate in the high frequencies, while the radiation pressure noise will dominate in the low frequencies. The radiation pressure effect has neither been observed yet by gravitational wave detectors nor by other small scale experiments operating in the same frequency range and in similar conditions. Therefore, it is crucial to develop table top experiments to study this effect, to verify the theory and to test and develop methods that circumvent this limit. This is the primary aim of our experiment, called QuRaG: a suspended interferometer which will be able to observe the Quantum Radiation Pressure in the same detection band as the Virgo gravitational wave interferometer.

1.1 Scientific Motivations

Interferometric detectors, such as Virgo [55, 38], are currently the most promising devices for the detection of gravitational waves (GWs) originated from astrophysical

sources. Virgo is a Michelson interferometer (ITF) for the detection of gravitational waves that works in the range of frequencies (10Hz-10kHz), trying to detect signals from massive astrophysical sources, such as supernovae and coalescing binaries [38] present in clusters of galaxies, like the Virgo Cluster, from which the interferometer was named after. Currently, the sensitivity of GW detectors (GWd) is not yet sufficient to observe signals with the rate of a few events per year, so there is underway an experimental program to improve it [38, 39]. In particular the next generations of GWd, at low frequencies (10Hz - 50Hz), will be limited by the quantum radiation pressure effect on the suspended mirrors [38, 122, 34]. This phenomenon, not yet experimentally observed, is the subject of one of the most active research field at the time. Rich of the experience acquired with Virgo, this work aims at building a detector for Quantum Radiation Pressure Noise: the QuRaG experiment. It will consist of a suspended Michelson interferometer in which the geometry is optimized in order to detect the quantum radiation pressure noise. Each arm of the interferometer will be a high $finesse$ Fabry-Pérot cavity in which only the end mirrors will be suspended and then sensitive to the quantum radiation pressure noise. This phenomenon is due to the quantum fluctuations of the electromagnetic field of the laser within the cavity which generates a pressure effect responsible for movements of the suspended mirrors. For a free test mass in a Fabry-Pérot cavity, this effect can be modeled as [122]

$$X_{RP}(\omega) = 2\frac{\mathcal{F}}{m\omega^2}\sqrt{\frac{8h}{(2\pi)^2}\frac{P_{las}}{\lambda c}} \tag{1.1}$$

where $\mathcal{F}$ is the $finesse$ of the cavity, h is the Planck's constant, c the speed of light, λ the laser's wavelength and P_{las} the power of the laser.

For QuRaG, we will use the same laser as Virgo, a Nd:YAG of wavelength $\lambda = 1.064\mu m$. The values for the cavity $finesse$ and the laser's input power that will be used are probably $\mathcal{F} = few10^4$ and $P_{las} = (few\ mW\text{-}few \times 10mW)$. The requirement of having a high $finesse$ assures that the mirrors will be more sensitive to what happens inside the cavity with respect to what comes from the outer part.

Not only the finesse and the laser's power, but the whole design of the interferometer, as well as all the important parameters should be optimized in order that the displacement of the suspended mirror induced by the radiation pressure noise, eq.(1.1), will be at least ~ 10 times greater than the displacements due to all the other effects in the frequency range of interest $\sim (10Hz - 1kHz)$. Therefore, it is necessary to reduce all the other noises that could limit the sensitivity of QuRaG. Hence, the whole interferometer will be under vacuum, to reduce the residual gas viscous damping effect and unwanted effects due to diffused light, it will be suspended through mechanical filters (superattenuators) to reduce the seismic noise and the elements of the suspended interferometer will be made of silica to reduce thermal noise losses [125]. Moreover, we took into account the possibility, if required, to further reduce the internal thermal noise of the mirrors using Hermite-Gauss (HG) modes [138] of higher order [66, 103, 110].

I delay the discussion on the radiation pressure noise to the second chapter, where I will explain the theory, some of the experiments done to study this phenomenon and

I will explain our experiment starting from the preliminary design and the spectrum of radiation pressure noise that we expect QuRaG will detect. In the present chapter I will explain the scientific background of this thesis and of QuRaG experiment: the detection of gravitational waves.

1.2 Scientific Background: The Detection of Gravitational Waves

The Theory of General Relativity (GR), developed by Albert Einstein from 1907 and enunciated definitively in 1916 [57], is still the most robust theory of gravitation after the Isaac Newton's one [112] in 1687.
However Newton's theory is still very powerful, some predictions, such as the precession of the perihelion of inner planets of the Solar System and in particular of Mercury, are not in agreement with the experimental results. In fact, the subtraction of all the Newtonian effects from the observational data gives an excess in the advance of Mercury's perihelion equal to 43 *arcsec/century* (with respect to the ICRF international celestial reference frame [5]). Nevertheless, GR explains well this phenomena and this was just one of its first successes. Although not fully exact, Newton's theory is still in excellent agreement with the observations in the limit of low speed motions (much lower than the speed of light) and in the presence of weak gravitational fields. Therefore, in this limit, any relativistic theory of gravity must be traced back to the Newtonian one, condition that is satisfied by Einstein's theory.
GR is a theory of extreme complexity which is based on mathematical structures particularly sophisticated and it introduces a totally new vision on the physicals concepts through the idea of their geometrization. Gravity is no more described as a force, but as a geometric property of space-time no longer Euclidean, but with the structure of a Riemannian manifold. Its metric tensor $g_{\mu\nu}$, is different from the Minkowski's one $\eta_{\mu\nu}$ proper of a flat space-time metric.
The basic idea of the Einstein's relativistic theory of gravitation is that the presence of a massive object curves space-time around it. Any changes over time in the distribution of mass induce perturbations in the metric that propagate at the speed of light as ripples of the metric which defines the space-time.
The parameter used to distinguish between strong fields and weak fields is $GM/(Rc^2)$, where G is the universal gravitational constant of Newton, M the characteristic mass scale, R the characteristic scale of the dimension of the system and c the speed of light in vacuum [108]. This parameter tells us that the intensity of this kind of emission of radiation strongly depends on the mass and length scale of the source (see eqs. (B.3), (B.4) and (B.6)). Therefore, detectable sources should have mass of typically more than $few \times 10 M_{Sun}$ or being a system of compact stars, like for example two solar mass neutron stars orbiting at a distance from each other of $R = 1.89 \cdot 10^8 m$. Hence, the detectable gravitational sources are very massive, compact and energetic astrophysical objects.
Only with the birth of the Relativistic Astrophysics in the 60s, new experimental

activities were carried out and many relativistic effects were discovered and observed [116]. Moreover, the explication of these new discovered astrophysical processes could only be done within a theory based on GR. General Relativity concerns the study of very energetic phenomena and very massive object, as already said. Therefore, the search for gravitational waves (GWs) aims at investigating regimes of strong gravity associated with the formation and dynamics of very massive and energetic objects such as blacks holes and neutron stars.

GWs interact weakly with matter, so they can travel through very dense regions without undergoing significant changes. On the contrary the electromagnetic waves change from their original state because they are absorbed and diffused while traveling through dense media. Therefore, when they arrive at the observer they have lost important information about their source. The detection of GWs will then open a new window of observation and investigation, particularly in those regions of the universe inaccessible to the electromagnetic observation.

One of the most interesting phenomenon which produces emission of gravitational waves is the stochastic background of cosmological origin, which will allow us to directly look into the firsts seconds of the Universe. Other important sources are very massive astrophysics objects which involve very energetic phenomena as the coalescence of compact binaries (neutron stars and black holes), supernovae, and gamma ray bursts. The observation of the GWs from these phenomena will give deeper information about the physical processes that govern the formation and evolution of these objects, and the states of matter in the regime of strong gravitational field.

Although gravitational radiation has not been yet directly detected, there are indirect evidences for its existence. For example, the 1993 Nobel Prize in Physics was awarded by Hulse and Taylor for the discovery and the measurements of the orbital decay of the binary pulsar PSR B1913+16 by GWs emission, as predicted by Einstein's theory of GR. The pulsar's orbit gradually contracts, due to the emission of energy in the form of GWs, causing the pulsar to reach periastron slightly earlier [151]. This confirmed that GWs are more than mathematical anomalies.

Recently, on 17^{th} March 2014, astronomers at the Harvard-Smithsonian Center for Astrophysics announced that they had detected and produced *the first direct image of gravitational waves across the primordial sky* within the Cosmic Microwave Background, providing strong evidence for inflation and the Big Bang [37]. This polarization map, which is reminiscent of the way iron filings arrange themselves on a surface under the effects of a magnetic field, was found to have particular vortex-like, or curly, patterns known as B modes. The presence of B modes is a tell-tale sign of the passage of GWs generated during inflation, as the interviewed John Kovac said to NATURE [49]. With BICEP it has not yet been obtained a direct measurements of GWs, but only indirect evidence: the measurement made by BICEP indicates an interaction between gravity waves and the cosmic background radiation. Although peer review will be needed, this discovery is an important media-spotlight to encourage interest in the search for gravitational waves.

The Detection of Gravitational Waves

Interferometry is currently the most promising technique for the detection of gravitational waves (GWs). However, the history of gravitational wave (GW) detectors traces back to the Sixties, with the resonant bars of the pioneer Joseph Weber [149]. A resonant bar is essentially a suspended cylinder whose main internal mode of oscillation is excited by a passing gravitational wave. A transducer converts the small vibrations of the bar into electrical signals. This type of detector is efficient only in a narrow frequency band around the main resonant frequency. Typically with a sensitivity of the order of $h \sim few\ 10^{-21} 1/\sqrt{Hz}$ at 1 kHz, as shown in fig. 1.1. The exemplification of a detector of this type is represented by two test masses at the opposite ends of a spring. The footprint left by the passage of a gravitational wave is the elastic response to a variation of the metric [149]. The pioneer idea of a detector based on an electromagnetic signal transmitted between two free test masses showing the effect of the space-time curvature of in the nearby region dates back to 1956, in a work by Pirani [121]. Different classes of detectors belong to this fundamental scheme. Nevertheless, the present discussion is limited to laser interferometers [130]. Precursor of this detection technique was already Weber himself, that together with Forward, took into account the possibility of using a laser beam, instead of the spring, to measure the variation of distance between the two test masses. Afterward, at the Hughes laboratories, Forward carried out en experiment of this type [62]. However, it is in 1972 that the idea of interferometric detection of GWs is successfully tested by R. Weiss. At M.I.T. Weiss carried out a detailed study on the viability of this experimental configuration, laying the foundations of modern GW detectors [152].
Important progress (see fig. 1.1), both in sensitivity and in bandwidth, are achieved thanks to the concept of interferometric antenna. Virgo is one of these detectors. In fig. 1.1 are compared the great improvement in sensitivity obtained with the starting Virgo with respect to the resonant bars. The modern Michelson interferometric detectors have reached such an impressive sensitivity (much better than in fig. 1.1) in measuring small displacements of test masses (of the order of the attometer $10^{-18}m$) that next generation detectors will have to face the quantum nature of light (the Standard Quantum Limit, SQL). Beating those limits will be one of the challenges of the third generation detectors. Thus, a further improvement of the detector sensitivity will require to circumvent the standard quantum limit of the detector. Few ideas have been proposed for the quantum enhancement of gravitational wave interferometers, and one of the most promising is Cave's [34, 35] (see chapt.2). In 1981 he first proposed the possibility to circumvent the SQL on GW interferometers by injecting squeezed vacuum, a non classical state of light, into the output port of the interferometer [35] (see sec.2.3.1). Then, several experiments have been carried on to produce squeezed light, first in the few MHz band, and in the audio frequency band ($10Hz - 10kHz$) interesting for GW ground based detectors, by means of optical parametric processes (see chapt.2) [143]. The squeezing produced in this way is frequency independent (see sec.2.3.1) [89]. If the squeezing angle of the injected vacuum state is constant all over the detection band the squeezing is called frequency independent and the SQL is beaten only at a

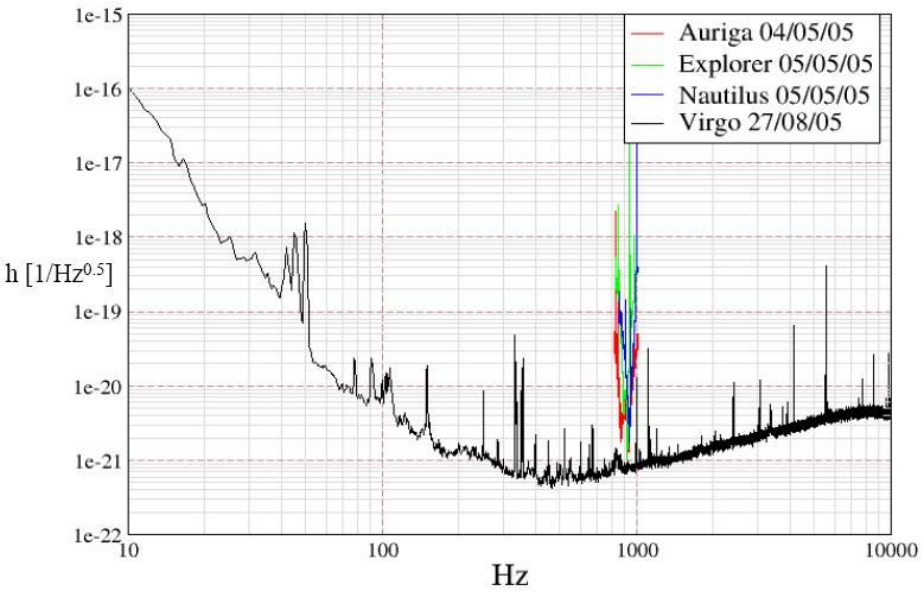

Figure 1.1: Comparison of the sensitivity curves of Virgo and bar detectors. The gain in sensitivity and bandwidth obtained by the Virgo interferometer is straitforward noticed.

given detection frequency. For the frequency dependent squeezing, the squeezing angle is suitably adjusted for each detection frequency so that the SQL is beaten all over the detection frequency band. In order to implement the frequency dependent squeezing, some methods have been studied, such as the use of detuned filter cavity that allows to rotate the squeezing angle. Another powerful method seems to be the ponderomotive squeezing, which uses the radiation pressure to produce squeezing as a result of the coupling between the radiation inside an interferometer and the mechanical motion of a suspended mirror [45, 89, 23]. This method, which will provide frequency dependent squeezing, still needs to be studied in small scale experiments, as well as the radiation pressure noise. This phenomenon, not yet observed in GW interferometers, will limit the sensitivity of these instruments at low frequencies. Hence, it is necessary to observe and study it on table top experiments in order to verify the theory and have a deeper knowledge of this back action effect due to the quantum nature of light. Squeezing apparatus are currently under study to be implemented in the next future on the next generation of advanced GW interferometers [70, 43, 64]. The QuRaG experiment and my doctoral research work are framed within this scientific background.

The Interferometric Detection of Gravitational Waves

The principle of operation of a detector based on a Michelson interferometer is the following. The equation of geodesic deviation (eq.(B.9)), enunciated in the appendix B, shows the effect of the passage of a GW on the distance between two free particles and states the theoretical foundation of the detection of GWs. Since the intensity

of the gravitational signal from astrophysical sources arriving on Earth is small (of the order of $h \sim 10^{-21} 1/\sqrt{Hz}$) [108, 91, 48, 61, 132, 54], it is expected that the effect of the passage of the GW occurs with a similarly weak variation of the distance between the free test masses (displacements of the order of the attometer). Therefore, the choice of measuring these variations with a laser interferometer is reasonable and appropriate for two main reasons. First, because the Michelson interferometer is an instrument whose response is directly proportional to the differential variations of the arm-lengths, then because the use of an L-arms configuration maximizes the coupling with the quadrupolar deformation imposed by the GW on a system of free test masses (see fig. 1.13 and fig.B.1). Moreover, since the noise sources related to amplitude and frequency fluctuations in the light source of the interferometer are common in the two arms, in this way are canceled.

1.2.1 The Michelson Interferometer

The Michelson interferometer is born as a Fourier Transform Spectrometer (FTS), but it is largely used as a displacement sensor, as in the case of the GW detection. The phenomenon of the interference is the most used one to measure a spectrum (first results by [41, 42, 52]). The Michelson interferometer is based on the interference between two beams, the simplest possible. The coherent source, generally a laser, is divided

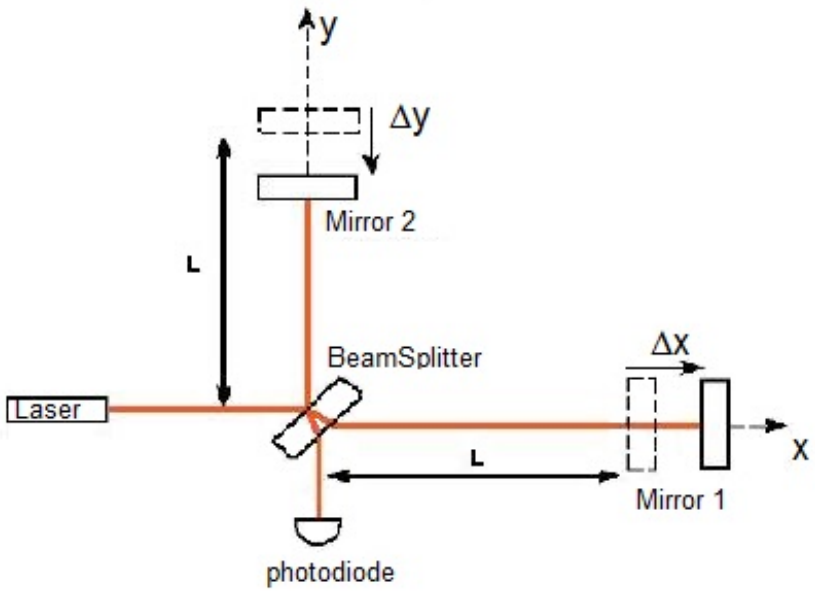

Figure 1.2: Scheme of a Michelson Interferometer. In the figure is shown the effect of the passage of a gravitational wave through the displacement of the mirrors (Δx and Δy).

through a beam splitter (BS) into two beams perpendicular to each other. At the ends of each beam is placed a mirror that reflects back the beam recombining it on the BS. The coherence of the source is needed to ensure the interference. It is also required the condition that the length of the coherence should be higher than the arm-difference of

the interferometer. The recombined beams then arrive on the detector. The distance between the end mirror and the BS is called arm of the interferometer. Any difference in the optical path between the two arms produces a phase shift between the recombined beams. Then, the output signal, which is the intensity of the recombined beam, is a function of the delay (called interferogram), and it is detected and analysed. The interferogram is uniquely related to the spectrum of the radiation as they are a pair of Fourier transforms. Hence the name FTS [52, 106]. The invention of the FTS is due to Albert Abraham Michelson (1880) which, together with Edward Morley, used this tool for the famous Michelson-Morley experiment that proved the non-existence of the luminiferous ether [107]. In his interferometer the two arms were of the same length. Therefore the non-constructive interference would have occurred only if the speed of light in the two arms had been different. At the time it was believed that the electromagnetic waves propagate through a medium called ether. According to this theory, the Earth would have to be in relative motion to the ether. Then, by aligning one arm of the interferometer with the direction of motion of the Earth, the speed of light would have to vector sum with that of the Earth, causing a phase shift with respect to that of the arm perpendicular to the motion. The Earth was considered just moving with a velocity of $v = 30km/s$ with respect to the Sun, and no motion of the Solar System with respect to the center of our Galaxy ($220km/s$) and of the Galaxy with respect to the Great Attractor of the Local Group of Galaxy Clusters was known at the time. The light traveling the interferometer along the arm orthogonal to the direction of motion of the Earth will not sum with the velocity c, then after a full round trip it will have a phase $\omega_L \frac{2L}{c}$, where L is the arm length and ω_L is the angular frequency of the laser source. On the other hand, the light traveling in the arm aligned with the direction of motion of the Earth, will accumulate a phase of $\omega_L\big(\frac{L}{c+v} + \frac{L}{c-v}\big)$. Hence, the light which recombines at the beam splitter will have accumulated a phase difference

$$\Delta\varphi = \omega_L\big(\frac{2L}{c} - \frac{L}{c+v} + \frac{L}{c-v}\big) = \omega_L\big(\frac{2L}{c} - \frac{2L}{c(1-\frac{v^2}{c^2})}\big) \approx \omega_L\big(\frac{v^2}{c^2}\big). \tag{1.2}$$

Therefore, Michelson and Morley where looking for a quadratic effect in $\frac{v}{c}$. The absence of this effect marked the death of the ether theory and the beginning of Einstein's Special Relativity. Michelson was aware of the capabilities of its spectroscopic interferometer [105, 106], but at that time it lacked detectors that were capable of accurately measuring the light intensity. The eye was the only detector that Michelson used. In 1911 a huge step head was done by Rubens and Wood, when they published the first interferogram using a micro-radiometer as detector [131]. However, the FTS was not very useful until efficient techniques for calculating the Fourier transforms have been developed. In the '50s and '60s, with the first computers, there were the first astronomical use of FTS (P & J.Connes, spectra of the planets [41]). In 1965, Cooley and Tukey published the algorithm of the fast Fourier transform [42], that speeded up the calculations of several orders of magnitude, thus allowing the practical use of the Michelson interferometers as spectrometers [52]. In the following the operation of the interferometer is briefly summarized in order to then calculate the power incident on the detector [101].

Let the ψ_{in} be the electric field of the monochromatic light emitted by the laser (of frequency ν_L) of the Michelson interferometer

$$\psi_{in} = Ke^{i\omega_L t}, \tag{1.3}$$

where K is the amplitude of the incoming beam and $\omega_L t$ the phase, being $\omega_L = 2\pi\nu_L$.

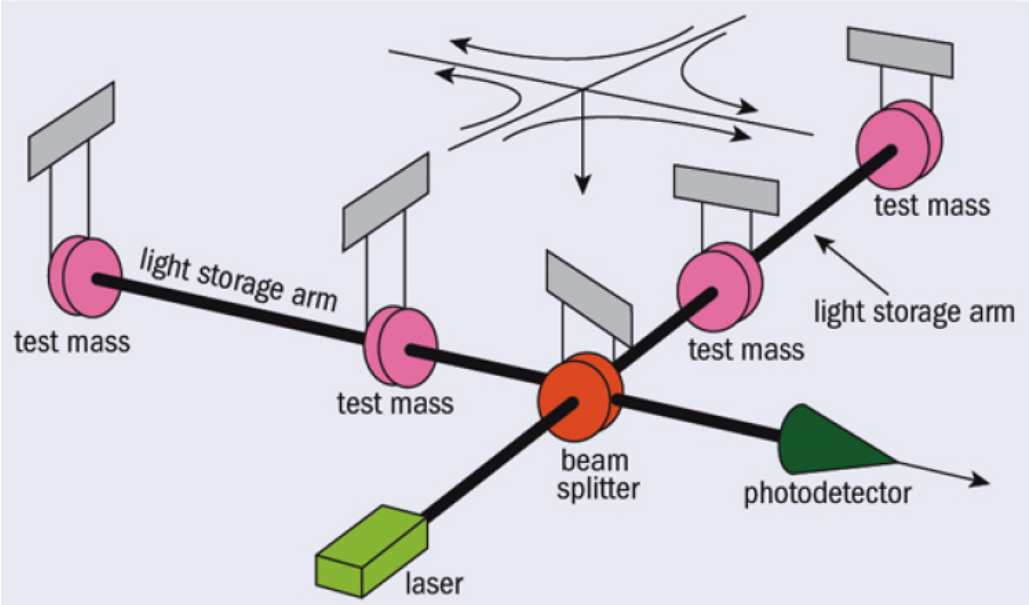

Figure 1.3: Michelson interferometer for the detection of GWs.

The beam is then separated in two equal beams by the BS. One beam is transmitted towards the mirror 1, $\psi_1 = t_{BS}\psi_{in}$, and the other is reflected and rotated by $\pi/2$ with respect to the incoming beam, $\psi_5 = ir_{BS}\psi_{in}$, where t_{BS} and r_{BS} are respectively the coefficients of transmission and reflection of the BS. Later, the two beams ψ_1 and ψ_5 accomplish respectively the paths l_1 and l_2 and become $\psi_2 = e^{-ik_L l_1}\psi_1$ and $\psi_6 = e^{-ik_L l_2}\psi_5$. The end mirrors reflect the beams ψ_2 and ψ_6 and rotate them of π. Then, we have the beams $\psi_3 = -r_1\psi_2$ and $\psi_7 = -r_2\psi_6$, where r_1 and r_2 are the coefficient of reflection respectively of the mirror 1 and of the mirror 2. After having done again the paths l_1 and l_2, the beams are $\psi_4 = e^{-ik_L l_1}\psi_3$ and $\psi_8 = e^{-ik_L l_2}\psi_7$ and they are located in the vicinity of the BS, where they are recombined in the output beam $\psi_{out} = ir_{BS}\psi_4 + t_{BS}\psi_8$. The power of the output signal is then

$$P_{out} = P_{in} r_{BS}^2 t_{BS}^2 (r_1^2 + r_2^2)\left(1 + \frac{2r_1 r_2}{r_1^2 + r_2^2} cos(2k_L \cdot \Delta l)\right), \tag{1.4}$$

where $P_{out} = |\psi_{out}|^2$, $P_{in} = |\psi_{in}|^2$ and

$$\Delta l = l_1 - l_2. \tag{1.5}$$

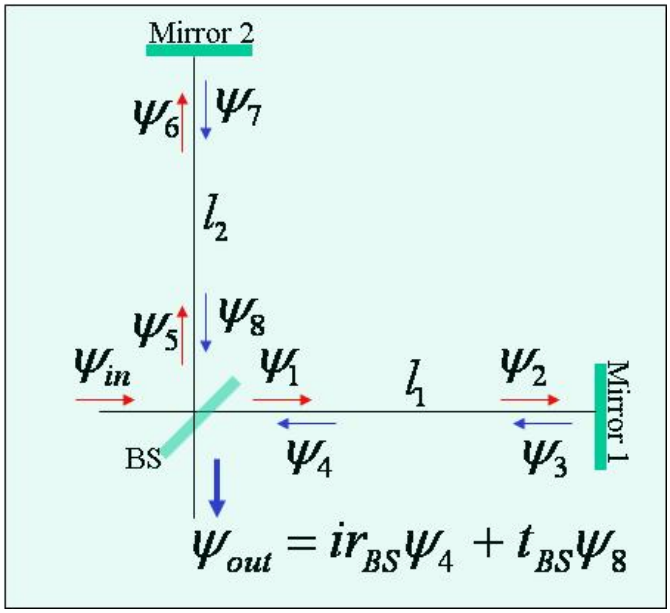

Figure 1.4: Scheme of the reflection-transmission and recombination of the two beams in the Michelson interferometer.

It follows that if the Δl varies, as a consequence of the passage of a GW, or due to the mechanical spurious displacement of a mirror, also the intensity of the output beam varies. The optical path difference in the two arms Δl causes a phase shift between the two beams recombined on the BS of an amount

$$\Delta\phi_L = 2\frac{2\pi}{\lambda_L}\Delta l \tag{1.6}$$

where λ_L is the wavelength of the laser.
The light beam is focused on a photodiode placed at the exit of the interferometer. In this way it is measured the variation of light power which is a function of the phase shift $\Delta\phi_L$.
Moreover, the contrast C of the interference pattern at the exit of the interferometer is defined as

$$C = \frac{P_{out}^{max} - P_{out}^{min}}{P_{out}^{max} + P_{out}^{min}} = \frac{2r_1 r_2}{r_1^2 + r_2^2}, \tag{1.7}$$

where the second equality is true because $P_{out}^{max} = P_{in} r_{BS}^2 t_{BS}^2 (r_1 + r_2)^2$ and $P_{out}^{min} = P_{in} r_{BS}^2 t_{BS}^2 (r_1 - r_2)^2$. Then

$$P_{out} = P_{in} r_{BS}^2 t_{BS}^2 (r_1^2 + r_2^2)\Big(1 + Ccos(\Delta\phi_L)\Big). \tag{1.8}$$

The contrast, which depends on the reflection coefficients, indicates whether there are defects on the optical surfaces. Moreover, remember that the reflection coefficient r is related to the coefficients of transmission t and absorption a by the relation $r^2 +$

$t^2 + a^2 = 1$, which corresponds to the conservation of energy. If we consider an ideal interferometer, it would have lossless mirrors with equal reflectivity $r_1 = r_2 = r$ and totally reflective $r = 1$, and the BS which transmits and reflects the same amount of light and perfectly equal to $t_{BS} = r_{BS} = \sqrt{1/2}$. Furthermore, in this case, the contrast would be maximum, $C = 1$, and the power output measured by the photodiode would be equal to

$$P_{out} = \frac{P_{in}}{2}\Big(1 + cos(\Delta\phi_L)\Big). \tag{1.9}$$

When the interference observed at the output is destructive, i.e. $P_{out}^{min} = 0$, it is called the dark fringe. The dark fringe is the working condition for GW interferometers, since around a null signal it is easier to detect the tiny signal coming from GW sources. In this case we have that

$$2k_L\Delta l = (2n+1)\pi \qquad \text{with } n \in \mathbb{N} \tag{1.10}$$

and, if we do not substitute $C = 1$ as in eq. (1.9) the output power becomes

$$P_{out} = \frac{P_{in}}{2}\Big(1 - C\Big). \tag{1.11}$$

1.2.2 The Effect of an Incident Gravitational Wave

The purpose here is to describe how an incoming GW affects the phase shift between the two beams of light that pass through the arms of the interferometer. A schematic

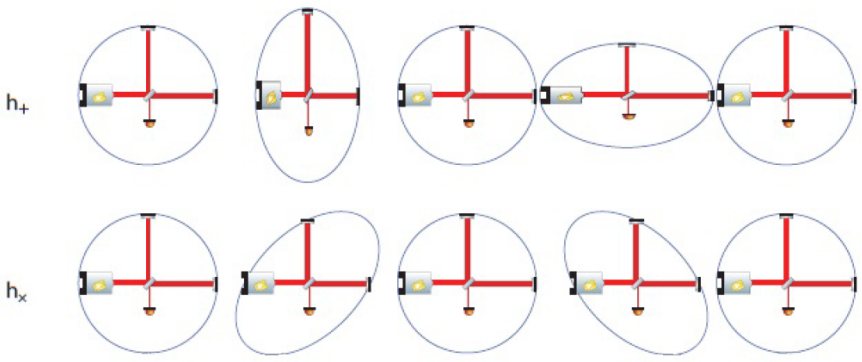

Figure 1.5: Effect of an incoming GW of polarization + (upper figure) and x (lower figure) on the arms of a Michelson interferometer.

representation is shown in fig.1.5.
A key feature of the interferometer concerns the mirrors which, in order to be considered as free falling test masses, they are suspended by a sophisticated apparatus of pendulums in cascade, the so called suspension system. This condition has its theoretical foundation in the equation of geodesic deviation (eq.(B.8)), which states that

the variation of the distance between two free test masses, i.e. electrically neutral and subjected only to the gravity force, is proportional to the intensity of the impinging gravitational wave. The system of pendulums makes the interferometer behave as a low-pass filter for all disturbances at frequencies lower than those of the suspension system. The free falling condition of the test masses is therefore limited only to the band in which the noises are small compared to the gravitational signal to detect, namely the detection-band of the interferometer. Given a characteristic frequency of the pendulum system, ω_p, the mechanical quality factor characteristic of the energy lost in one cycle of oscillation is $Q = \omega_p \tau_p$ [60], where τ_p is half of the amplitude time decay of the oscillation τ_A, i.e. $\tau_p = \tau_A/2$. Assume to be valid the weak field approximation explained in appendix A, and to have a gravitational signal due to the progressive wave $h_{\mu\nu}(z,t)$ propagating along z and given by the equation (A.59). Consider, also, the wave $h_{\mu\nu}(z,t)$ to be plane, monochromatic of frequency ν and with polarization h_+ [129]. In order to simplify the notation, the chosen polarization (+) is implicit in the expression of the wave $h_+(z,t) = h(z,t)$. The metric element is then

$$ds^2 = -c^2dt^2 + [1 + h(z,t)]dx^2 + [1 - h(z,t)]dy^2 + dz^2. \tag{1.12}$$

Suppose that the wave $h(z,t)$ is oriented like the axes of the interferometer and passes through it along the perpendicular direction. In this way the maximal deformations are along the axis of the arms x and y. Let the origin of the reference system coincide with the BS of the Michelson interferometer and let l_1 and l_2 being the distances of the mirrors from the origin.
Consider the optical path of the beam along the arm x. From the Special Relativity [95], for the light it is $ds^2 = 0$, therefore

$$c^2dt^2 = \big[1 + h(z,t)\big]dx^2. \tag{1.13}$$

Then the time interval necessary for the photon to travel along the path l_1 of the arm x is

$$\tau_A = \int_0^{\tau_A} dt = \frac{1}{c}\int_0^{l_1} \sqrt{1 + h(z,t)}dx, \tag{1.14}$$

and since $h(z,t) \ll 1$

$$\tau_A \approx \frac{1}{c}\int_0^{l_1} \left(1 + \frac{1}{2}h(z,t)\right)dx. \tag{1.15}$$

In addition, the considered wave can be written in the complex form

$$h(z,t) = h(t) = h_0 e^{i\omega t}, \tag{1.16}$$

and assuming that the GW can be considered almost constant during the time taken by photons to make a full round-trip in the arms ($\nu t \ll 1$), then

$$\tau_A \approx \frac{1}{c}\left(l_1 + \frac{1}{2}h_0 l_1\right). \tag{1.17}$$

Similarly, for the way back it is

$$\tau_B - \tau_A = \int_{\tau_A}^{\tau_B} dt = -\frac{1}{c}\int_{l_1}^{0} \sqrt{1+h(z,t)}dx \approx \frac{1}{c}\left(l_1 + \frac{1}{2}h_0 l_1\right), \tag{1.18}$$

where the - sign in the second integral is because in the return path the dx is negative. The total time taken to travel back and forth in the x arm is then

$$\Delta\tau_x = \tau_B - \tau_A + \tau_A = \frac{2l_1}{c} + \frac{1}{c}\int_0^{l_1} h(z,t)dx \approx \frac{2l_1}{c} + \frac{l_1}{c}h_0. \tag{1.19}$$

Hence for the y arm, the round trip time of the photons is

$$\Delta\tau_y = \frac{2l_2}{c} - \frac{1}{c}\int_0^{l_2} h(z,t)dy \approx \frac{2l_2}{c} - \frac{l_2}{c}h_0. \tag{1.20}$$

Then the time shift, $\Delta\tau$, of the light recombined at the BS after a full round trip in the two arms x and y, is

$$\Delta\tau = \Delta\tau_x - \Delta\tau_y = \frac{2}{c}(l_1 - l_2) + \frac{1}{c}(l_1 + l_2)h_0. \tag{1.21}$$

The overall optical path difference between the mirrors is the equal to

$$\Delta L' = \Delta l + \Delta l_{GW}, \tag{1.22}$$

where, while Δl is given by the initial length variation between the two arms, previously defined by the eq.(1.5), Δl_{GW} is the additional difference caused by the passing GW

$$\Delta l_{GW} = \frac{1}{2}(l_1 + l_2)h_0. \tag{1.23}$$

So $\Delta L'$ corresponds to a phase shift of

$$\Delta\varphi'_L = 2\frac{2\pi}{\lambda_L}\Delta L' = \frac{4\pi}{\lambda_L}\left(\Delta l + \frac{1}{2}(l_1 + l_2)h_0\right), \tag{1.24}$$

where λ_L is the wavelength of the laser. The above equation shows directly that the longer are the arms of the interferometer, i.e. the largest is L ($L = \frac{l_1+l_2}{2}$), then the largest is the phase shift associated to the GW.

Furthermore, assuming that the approximation according to which the GW is constant in the time taken by the photons to make a full round trip in the arms is not valid, the time shifts in the two arms are given by

$$\Delta\tau_x = \frac{1}{c}\int_0^{l_1}\left(1 + \frac{1}{2}h_0 e^{i\omega t(x)}\right)dx - \frac{1}{c}\int_{l_1}^{0}\left(1 + \frac{1}{2}h_0 e^{i\omega t(x)}\right)dx, \tag{1.25}$$

$$\Delta\tau_y = \frac{1}{c}\int_0^{l_2}\left(1 - \frac{1}{2}h_0 e^{i\omega t(y)}\right)dy - \frac{1}{c}\int_{l_2}^{0}\left(1 - \frac{1}{2}h_0 e^{i\omega t(y)}\right)dy. \tag{1.26}$$

Note also that the travel times, $t(x)$ and $t(y)$, depend on the displacements x and y. Before the reflection they are equal to

$$t(x) = \frac{x}{c} + t_0, \tag{1.27}$$

$$t(y) = \frac{y}{c} + t_0 \tag{1.28}$$

with t_0 initial time. And after reflection they are

$$t(x) = \frac{2l_1 - x}{c} + t_0, \tag{1.29}$$

$$t(y) = \frac{2l_2 - y}{c} + t_0. \tag{1.30}$$

Therefore the equations (1.25) and (1.26) become

$$\Delta\tau_x = \frac{1}{c}\int_0^{l_1}\left(1 + \frac{1}{2}h_0 e^{i\omega\left(\frac{x}{c}+t_0\right)}\right)dx - \frac{1}{c}\int_{l_1}^{0}\left(1 + \frac{1}{2}h_0 e^{i\omega\left(\frac{2l_1-x}{c}+t_0\right)}\right)dx \tag{1.31}$$

$$\Delta\tau_y = \frac{1}{c}\int_0^{l_2}\left(1 - \frac{1}{2}h_0 e^{i\omega\left(\frac{y}{c}+t_0\right)}\right)dy - \frac{1}{c}\int_{l_2}^{0}\left(1 - \frac{1}{2}h_0 e^{i\omega\left(\frac{2l_2-y}{c}+t_0\right)}\right)dy. \tag{1.32}$$

Solving the integrals they give

$$\Delta\tau_x = \frac{2l_1}{c} + \frac{1}{2}\frac{h_0}{i\omega}e^{i\omega t_0}\left(e^{i\omega\frac{2l_1}{c}} - 1\right) \tag{1.33}$$

$$\Delta\tau_y = \frac{2l_2}{c} - \frac{1}{2}\frac{h_0}{i\omega}e^{i\omega t_0}\left(e^{i\omega\frac{2l_2}{c}} - 1\right). \tag{1.34}$$

The optical path difference between the two arms is then

$$\Delta l' = \Delta l + \frac{1}{4}\frac{h_0 c}{i\omega}e^{i\omega t_0}\left(e^{i\omega\frac{2l_1}{c}} + e^{i\omega\frac{2l_2}{c}} - 2\right). \tag{1.35}$$

Without loss of generality, it can be assumed that initially, before the passage of a GW, the arms are of equal length $l_1 = l_2 = L$. Then the previous equation becomes

$$\Delta l' = \frac{1}{2}\frac{h_0 c}{i\omega}e^{i\omega t_0}\left(e^{i\omega\frac{2L}{c}} - 1\right). \tag{1.36}$$

Then by multiplying and dividing by $e^{-i\omega\frac{L}{c}}$ it is

$$\Delta l' = \frac{h_0 c}{\omega}e^{i\omega\left(t_0+\frac{L}{c}\right)}sin\left(\frac{\omega L}{c}\right). \tag{1.37}$$

In more compact form it then becomes

$$\Delta l' = h_0 L e^{i\omega\left(t_0+\frac{L}{c}\right)}\frac{sin\left(\frac{\omega L}{c}\right)}{\frac{\omega L}{c}}. \tag{1.38}$$

Finally it follows that the complex phase shift associated with $\Delta l'$ is

$$\Delta\varphi'_L = 2\frac{2\pi}{\lambda_L}\Delta l' = \frac{4\pi}{\lambda_L}h_0 L e^{i\omega\left(t_0+\frac{L}{c}\right)}\frac{sin\left(\frac{\omega L}{c}\right)}{\frac{\omega L}{c}}. \tag{1.39}$$

This is the relationship that directly links the response of the interferometer to the gravitational signal [40]. Notice that the phase shift is proportional to the amplitude h_0, and not to the power, as for the electromagnetic detectors.

This is important because the phase shift measured at the output is a direct measure of the gravitational signal. Nevertheless, it is important also to notice that the phase shift is also directly proportional to the arm length L. Consider the case of a GW of amplitude $h_0 \sim 10^{-21}1/\sqrt{Hz}$ impinging on a Michelson interferometer of arm-length $L = 1km$. In order to detect this signal with an IR laser of $\lambda = 1\mu m$, it is necessary an angular resolution on the output phase signal of about $\sim 10^{-11}rad$, which corresponds to an arm-length variation of $\sim 10^{-18}m$.

Therefore, Fabry-Pérot cavities of length L are placed along the arms to increase the phase of the light reflected by the arms at the point of optical recombination (BS) and thus amplifying the phase difference of the output signal. The effective cavity length is then the real length multiplied by the Fabry-Pérot gain G.

1.2.3 The Fabry-Pérot Cavity

The Fabry-Pérot instrument has been invented by C. Fabry and A. Pérot in 1899. It takes advantage of the multiple reflections between two parallel and partially reflecting surfaces. The following treatise explains the principle of operation of a Fabry-Pérot. Consider two mirrors (see figure 1.6) [63]:

- parallel and separated by a distance d,
- identical, thin and semi-reflecting,
- with coefficient of reflection r, coefficient of transmission t and with negligible coefficient of absorption ($a \simeq 0$).

From the figure 1.7 notice that the optical path difference between two following transmitted beams is:

$$\delta = \frac{2d}{\cos\theta} - 2d\tan\theta\sin\theta = \frac{2d}{\cos\theta}(1-\sin^2\theta) = 2d\cos\theta. \tag{1.40}$$

The optical path difference δ (eq. 1.40) corresponds to a phase difference φ

$$\varphi = k\delta = 2kd\cos\theta = \frac{4\pi}{\lambda}d\cos\theta = \frac{4\pi}{\lambda_0}nd\cos\theta, \tag{1.41}$$

where λ is the wavelength in the medium of refractive index n and λ_0 is the wavelength in vacuum. The two are related by the relationship:

$$\lambda = \frac{\lambda_0}{n}. \tag{1.42}$$

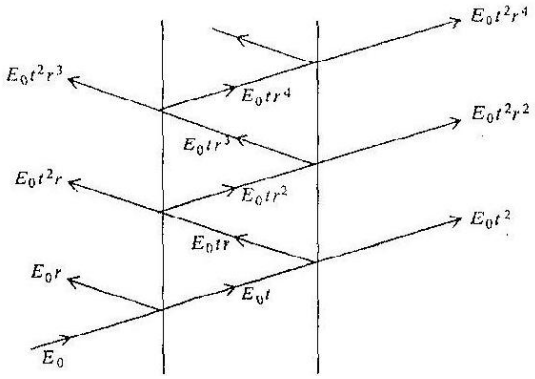

Figure 1.6: Representative basic scheme of the Fabry-Pérot: 2 thin parallel and semireflecting plane mirrors.

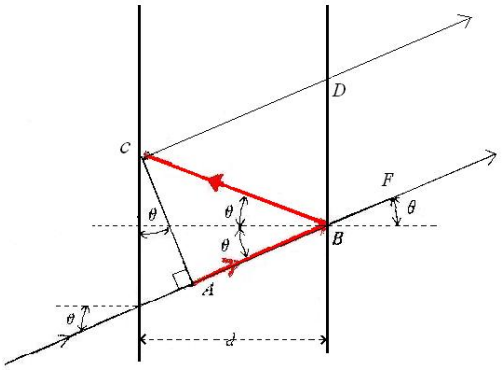

Figure 1.7: The optical path difference between to following transmitted beams is highlighted in red.

A lens at the output of the second mirror, focuses all the parallel beams outcoming from the Fabry-Pérot onto the focus plane of the lens. The electric field transmitted is then:

$$E_T = E_0t^2 + E_0t^2r^2e^{i\varphi} + E_0t^2r^4e^{i2\varphi} + ... = E_0t^2\sum_{n=0}^{+\infty}(r^2e^{i\varphi})^n \tag{1.43}$$

and since $r^2 < 1$, the previous geometric series is converging:

$$E_T = E_0t^2\sum_{n=0}^{+\infty}(r^2e^{i\varphi})^n = \frac{E_0t^2}{1-r^2e^{i\varphi}}. \tag{1.44}$$

Therefore, the transmitted intensity of the field is

$$I_T = |E_T|^2 = I_0\frac{t^4}{|1-r^2e^{i\varphi}|^2} \tag{1.45}$$

where $I_0 = |E_0|^2$ is the input intensity. It is then useful to introduce:

$$R = r^2 \quad \text{reflectivity,} \tag{1.46}$$

$$T = t^2 \quad \text{transmissivity.} \tag{1.47}$$

Hence, the transmitted intensity becomes:

$$I_T = I_0 \frac{T^2}{|1 - Re^{i\varphi}|^2}, \tag{1.48}$$

where the quantity in the denominator can be rewritten as [63]:

$$|1 - Re^{i\varphi}|^2 = (1-R)^2 \left[1 + \frac{4R}{(1-R)^2} \sin^2 \frac{\varphi}{2}\right]. \tag{1.49}$$

Therefore:

$$I_T = I_0 \frac{T^2}{(1-R)^2} \left[1 + \frac{4R}{(1-R)^2} \sin^2 \frac{\varphi}{2}\right]^{-1}. \tag{1.50}$$

In the previous equation appears the **coefficient of Finesse** F, which measures how narrow are the interference fringes (see fig. 1.8) and can be defined as:

$$F = \frac{4R}{(1-R)^2}. \tag{1.51}$$

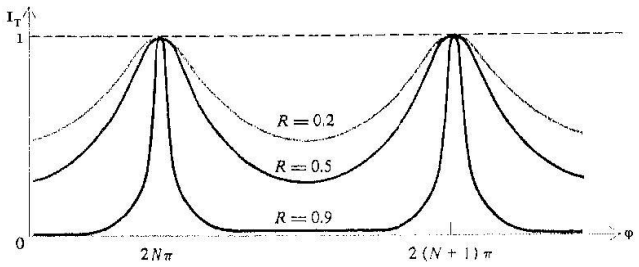

Figure 1.8: Diagram of the transmitted intensity I_T in function of the phase φ, by varing the reflectivity R, hence the coefficient of Finesse F. As R increases, the interference fringes become thinner.

Hence, the intensity is:

$$I_T = I_0 \frac{T^2}{(1-R)^2} \left[\frac{1}{1 + F \sin^2 \frac{\varphi}{2}}\right], \tag{1.52}$$

where

$$\mathcal{A} = \frac{1}{1 + F \sin^2 \frac{\varphi}{2}} \tag{1.53}$$

is called the **Airy function**. The maximum of intensity recurs for the phase values $\frac{\varphi}{2} = N\pi$, where N is the order of the interference. Hence, recalling the eq. (1.41), the maximum are obtained for

$$\varphi = 2N\pi = \frac{4\pi}{\lambda_0} nd \cos\theta. \tag{1.54}$$

Then, the *free spectral range* (FSR) is defined as the separation between two adjacent orders of interference. In terms of phase this corresponds to

$$\varphi_{N+1} - \varphi_N = 2\pi. \tag{1.55}$$

From the equation (1.41), it can be rewritten as

$$\varphi_{N+1} - \varphi_N = 2(k_{N+1} - k_N)nd\cos\theta = 2\frac{(\omega_{N+1} - \omega_N)}{c}nd\cos\theta \tag{1.56}$$

then in terms of angular frequency ω it corresponds to

$$\omega_{N+1} - \omega_N = \frac{2\pi c}{2nd\cos\theta}. \tag{1.57}$$

The FSR in terms of frequency, for small θ, is then:

$$\nu_{N+1} - \nu_N = \frac{c}{2nd\cos\theta} \simeq \frac{c}{2nd}. \tag{1.58}$$

Lets analyse a spectrum consisting of two neighbour components ω and ω', which for simplicity are assumed to have equal maximum intensity I_0. The interference pattern will be the sum of two Airy functions as follows

$$I_T = I(\varphi) + I(\varphi') = \frac{I_0}{\left(1 + F\sin^2\frac{\varphi}{2}\right)} + \frac{I_0}{\left(1 + F\sin^2\frac{\varphi'}{2}\right)} \tag{1.59}$$

where for small θ, $\cos\theta \approx 1$, and the phase of the two components in the two maximums of intensity are equal to $\varphi = \frac{2\omega d}{c}$ and $\varphi' = \frac{2\omega' d}{c}$.

The two components are said to be resolved (see fig.1.9) if the single curves intersect

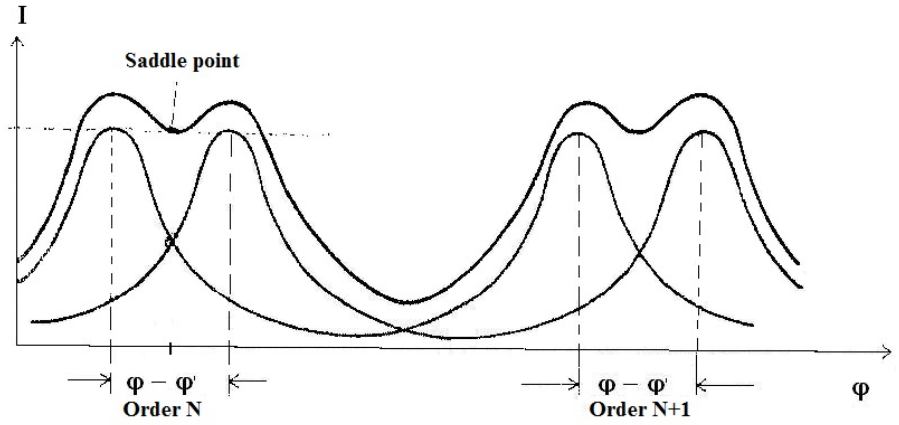

Figure 1.9: Two neighbour spectral components. They are said to be resolved if the individual curves intersect at half of the maximum intensity I_0 (*Taylor's criterion*).

at half of the maximum intensity I_0 (*Taylor's criterion*).
Therefore, at the saddle point it is $\varphi_s = \frac{\varphi - \varphi'}{2}$ (fig. 1.9)

$$I_s = I(\varphi_s) = \frac{2I_0}{\left[1 + F\sin^2\left(\frac{\varphi-\varphi'}{4}\right)\right]} \equiv I_0. \tag{1.60}$$

From which it follows

$$F\sin^2\left(\frac{\varphi - \varphi'}{4}\right) = 1. \tag{1.61}$$

If the two components are close to each other, then the quantity $\varphi - \varphi'$ is small and such that

$$\sin\left(\frac{\varphi - \varphi'}{4}\right) \approx \left(\frac{\varphi - \varphi'}{4}\right), \tag{1.62}$$

hence

$$|\varphi - \varphi'| = \frac{4}{\sqrt{F}} = 2\left(\frac{1-R}{\sqrt{R}}\right). \tag{1.63}$$

From the equation (1.56), for small angles of incidence θ, the amplitude resolution of the Fabry-Pérot can be obtained:

$$\delta\omega = |\omega - \omega'| = \frac{c}{2d}|\varphi - \varphi'| = \frac{c}{d}\left(\frac{1-R}{\sqrt{R}}\right). \tag{1.64}$$

An important parameter of the Fabry-Pérot used in interferometry is the ***finesse*** ($\mathcal{F}$), which, in spectroscopy is defined as the ratio between the FSR and the full-width half-maximum (FWHM):

$$\mathcal{F} = \frac{\varphi_{N+1} - \varphi_N}{|\varphi - \varphi'|}, \tag{1.65}$$

while in metrology the finesse is defined

$$\mathcal{F} = \frac{\pi}{2}\sqrt{F} = \pi\left(\frac{\sqrt{R}}{1-R}\right), \tag{1.66}$$

in fact the two are equivalent if we consider that $R > 0.5$, as it is for the highly reflective mirror of the Fabry-Pérot cavity of an interferometer like Virgo (see eq.(1.75)), where a high number of multiple reflections inside the cavity is needed. The **resolving power (RP)**, or quality factor of the cavity, is defined as [63]:

$$RP = \frac{\omega}{\delta\omega} = \frac{c2\pi}{\lambda}\frac{d}{c}\frac{\sqrt{R}}{(1-R)} = \frac{2d}{\lambda}\pi\frac{\sqrt{R}}{(1-R)}. \tag{1.67}$$

The order of the interference N can be expressed by the equation (1.54) and for the approximation of small angles of incidence it is

$$N = \frac{2d\cos\theta}{\lambda} \approx \frac{2d}{\lambda}. \tag{1.68}$$

The RP is therefore

$$RP = \frac{2d}{\lambda}\pi\frac{\sqrt{R}}{(1-R)} = N\mathcal{F}. \tag{1.69}$$

In the Fabry-Pérot of a Virgo-like interferometer, the stored intensity is

$$|\psi_1(\varphi)|^2 = G\frac{1}{1+F\sin^2(\frac{\varphi}{2})} \tag{1.70}$$

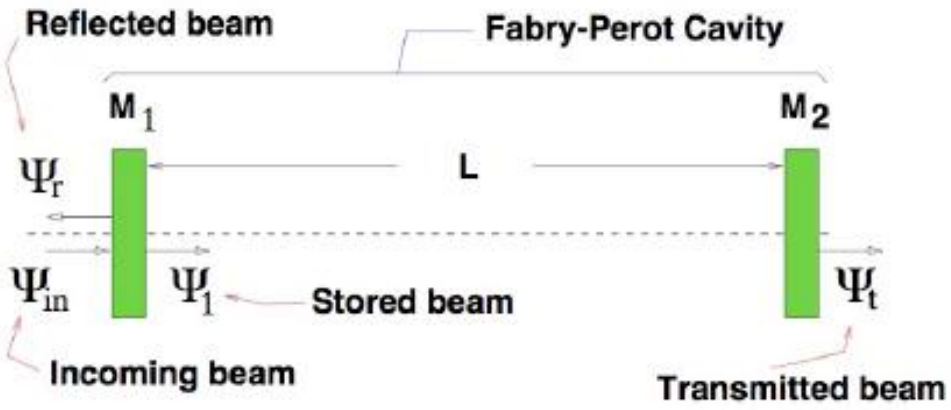

Figure 1.10: Schematic representation of the transmitted and reflected beams in the Fabry-Pérot of a Virgo-like interferometer.

where G is the gain between the stored and the incoming power. It is defined as

$$G = \frac{t_1^2}{(1-r_1r_2)^2}, \tag{1.71}$$

where the coefficients of reflection of the input mirrors and the end mirrors are different $r_1 \neq r_2$. Then the *finesse* can be written:

$$\mathcal{F} = \pi\left(\frac{\sqrt{r_1r_2}}{1-r_1r_2}\right). \tag{1.72}$$

In particular in Virgo the reflectivity of the input mirrors (R_1) and end mirrors (R_2) are $R_1 = 0.88$ and $R_2 = 0.9999$. Therefore the gain G is proportional to the *finesse* according to the relationship

$$G = \sqrt{F} = \frac{2\mathcal{F}}{\pi}. \tag{1.73}$$

In the output interference pattern of the Fabry-Pérot, the phase shift around the resonance induced by the perturbation of the cavity length δL, at the first order, is

$$\varphi(L+\delta L) - \varphi(L) \simeq 2kG\delta L \tag{1.74}$$

i.e. it is directly proportional to the gain in power G.
Recalling from the eq.(1.65) that the ***finesse*** is defined as

$$\mathcal{F} = \frac{FSR}{FWHM} \approx \frac{\pi\sqrt{r_1 r_2}}{1 - r_1 r_2} \tag{1.75}$$

where the $FRS = \frac{c}{2L}$ and the $FWHM$ is equal to

$$FWHM = \frac{FSR}{\mathcal{F}} = \frac{c}{2L\mathcal{F}}. \tag{1.76}$$

The cavity is a low-pass filter for all frequencies, with a cut-off frequency

$$\omega_c = 2\pi\nu_c = 2\pi\frac{FWHM}{2} = \pi\frac{c}{2L\mathcal{F}} = \frac{1}{\tau_s}, \tag{1.77}$$

where τ_s is the storage time of the light beam inside the cavity. Therefore, the optical path length, also called effective optical length, is increased with respect to L and equal to

$$L_{eff} = \mathcal{F}L\frac{2}{\pi}\frac{1}{\sqrt{1+(\omega/\omega_c)^2}} \tag{1.78}$$

which is modulated by the cut-off frequency and proportional to the finesse. For frequencies lower that the cut-off frequency it is

$$L_{eff} = LG \tag{1.79}$$

thus equal to the cavity length multiplied by the gain G. Then, this choice not only raises the level of the signal by the gain G, but it contributes to reduce the shot noise (see sec. 1.3.3).

In order to describe the frequency response of the interferometer, it is considered the case of a simple Michelson interferometer. From the equations (1.8) and (1.24) it is possible to deduce the output power detected by the photodiode, after the passage of the GW of intensity $h \ll 1$,

$$\begin{aligned} P_{out} &= P_{in} r_{BS}^2 t_{BS}^2 (r_1^2 + r_2^2)\Big[1 + Ccos(\Delta\phi_L + 2k_L hL)\Big] \\ &= P_{in} r_{BS}^2 t_{BS}^2 (r_1^2 + r_2^2)\Big[1 + C[cos(\Delta\phi_L)cos(2k_L hL) + sin(\Delta\phi_L)sin(2k_L hL)\Big] \\ &\approx P_{in} r_{BS}^2 t_{BS}^2 (r_1^2 + r_2^2)\Big[1 + Ccos(\Delta\phi_L) + C2k_L hLsin(\Delta\phi_L)\Big] \end{aligned} \tag{1.80}$$

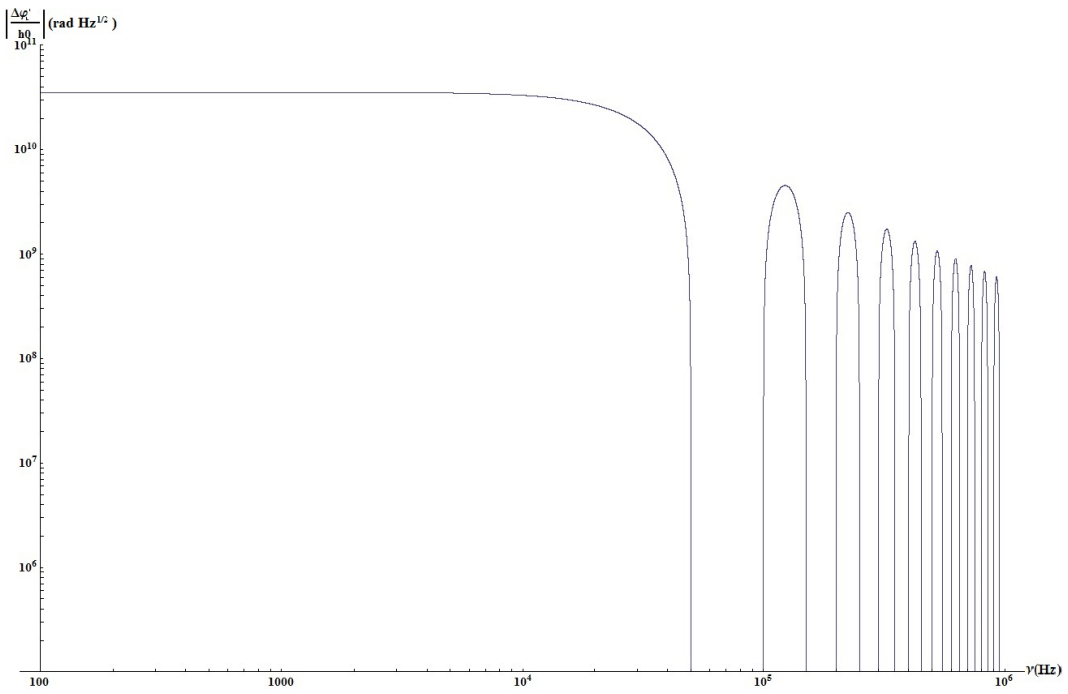

Figure 1.11: Frequency response of an interferometer with arms length $L = 3km$ and laser wavelength $\lambda_L = 1.064\mu m$.

in which, since $h \ll 1$, it has been possible to do the approximation $cos(2k_L hL) \approx 1$ and $sin(2k_L hL) \approx 2k_L hL$.
The plot of the phase shift $\Delta\varphi'_L$ (eq.(1.39)) normalized by the amplitude of the gravitational signal, in function of the frequency, shows that the response of the interferometer is not linear (see figure 1.11). It exists a cut-off frequency above which the response of the interferometer is attenuated. This frequency, $2\pi c/L$, corresponds to the travel time of the light beams in the arms. In fact, for signals with lower period, the effect of the passing wave is averaged over more than one period. The phase shift is canceled for all the integer multiples of the cut-off frequency $2\pi c/L$. This means that the detector is blind to all the signal with these frequencies. Being the cut-off frequency inversely proportional to L, this phenomenon constitutes a limitation to the arm-length of the interferometer L.

Furthermore, if the gravitational wave does not arrive in the direction orthogonal to the plane of the interferometer and has not a defined polarization, the generic direction can be written in the spherical coordinate frame (see fig.1.12). And the phase shift associated to the length variation of the arms will be

$$\Delta\varphi'_L = 2\frac{2\pi}{\lambda_L}\Delta l' = \frac{4\pi}{\lambda_L}L\left\{\left[\frac{1}{2}(1+cos^2\theta)cos2\psi)\right]h_+(t) + (cos\theta sin2\psi)h_\times(t)\right\}. \quad (1.81)$$

Moreover, in this case the angular response of the interferometer is described by the antenna diagram pattern as in the figure 1.13, which shows that the detector has a wide field of view. Nevertheless, the response is attenuated along the plane of the

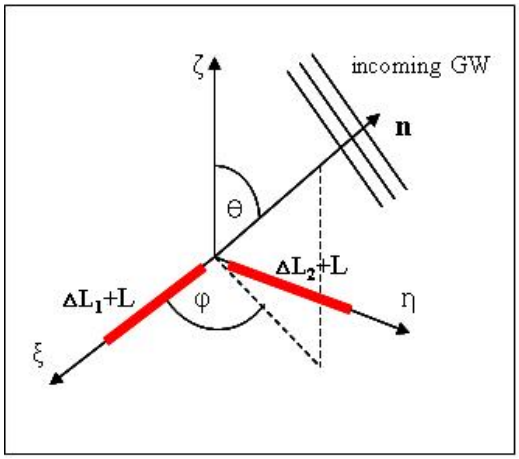

Figure 1.12: GW incident from the generic direction n in the reference frame with spherical coordinates.

interferometer and in particular it vanishes in the four points which corresponds to the bisectors of the axes x and y (the directions of the two arms).

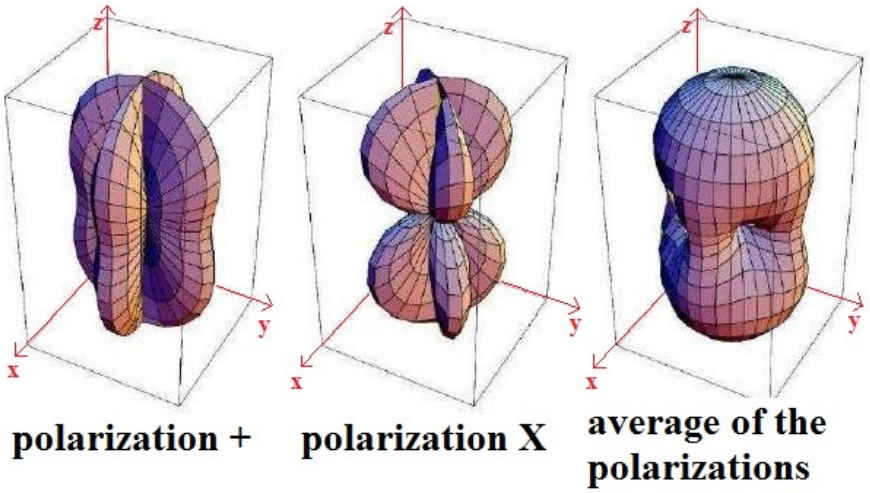

Figure 1.13: Antenna pattern diagram of the interferometer. It represents the response in function of the direction of the incoming wave having polarization h_+ (on the left) or $h_\times$ (in the middle). The last diagram on the right represents the response averaged between the two states of polarization.

1.3 Noise Sources in a Ground Based Interferometer

The word noise refers to any physical variable that randomly fluctuates over the time. There are many sources of noise that set limits to the sensitivity of the laser interferometer, as in any measuring instrument. These noises occur with random fluctuations of the measured signal. Depending on the type of process that they produce, they can be divided into:

NOT INSTRUMENTAL NOISES

- noises that cause an effective motion of the mirrors
  1. due to external disturbances
     - newtonian noise
     - seismic background
     - civil or industrial noise

INSTRUMENTAL NOISES

- noises that cause an effective motion of the mirrors
  2. intrinsic noise $\longrightarrow$ thermal noise
  3. technical noise $\longrightarrow$ control noise
  4. back-action noise $\longrightarrow$ radiation pressure noise
- noises that alter the measurement
  5. noise of the laser source, with amplitude and phase variations
  6. intrinsic noise $\longrightarrow$ shot noise
  7. technical noise $\longrightarrow$ stray light

The dominating noises in an interferometer are the seismic and civil-industrial noises, in the low frequency range, (lower than $5Hz$, i.e. below the detection band), the thermal noise in the range (5-500)Hz and the shot noise above the $500Hz$.

In the following treatise on the different noises and on the phenomena that originate them, each noise is characterized by its power spectral density [117], defined as

$$X_A^2(\nu) = \lim_{T\to\infty} \frac{2}{T}\left| \int_{-T}^{T} A(t)e^{-2\pi\nu t}dt \right|^2, \tag{1.82}$$

where $A(t)$ represents the time evolution of the physical quantity taken into account. The corresponding linear spectral density is

$$\tilde{x}(\nu) = \sqrt{X_A^2(t)} \tag{1.83}$$

whose unit of measurement is $[A]/\sqrt{Hz}$. The amplitude of the fluctuations of the

position noise can be calculated from its spectral density $X_A^2(\nu)$ as

$$A_{rms} = \sqrt{\int_0^\infty X_A^2(\nu) d\nu}. \tag{1.84}$$

The noise in an interferometer, in general, occurs as a variation of the apparent or actual position of the mirrors, producing an output signal on the detector. In order to compare and distinguish the noise from the gravitational signal it is useful to define the equivalent spectral density $\tilde{h}_n$

$$\tilde{h}_n(\nu) = \frac{\tilde{x}(\nu)}{L} \tag{1.85}$$

which represents the amplitude of the gravitational signal that would have generated a displacement equal to that one associated to the oscillations induced by the stochastic noise process n. In order to extract the gravitational signal from those generated by the various types of noise it is therefore necessary to study the effects produced by each of them.
Separated chapters are devoted to the radiation pressure and thermal noise, where they will be discussed in more detail.

1.3.1 The Seismic Noise

A ground based interferometer is firstly subject to the environmental noise: **seismic** and **civil-industrial**. Indeed, an interferometric antenna fixed to the ground suffers from permanent ground vibrations induced by the seismic activity, the wind, the oceans motion and the human activity. These vibrations are transmitted to the optical components of the apparatus by means of the suspension system and the resulting signal is the main limit to the sensitivity of the detector in the low frequencies, i.e. below 10Hz. Typically the spectral displacement amplitude generated by the seismic noise is [40]:

$$\tilde{x}_{seism}(\nu) = \frac{10^{-7}}{\nu^2} \qquad [m/\sqrt{Hz}] \qquad \text{for } \nu > 0.01Hz, \tag{1.86}$$

and in Virgo (since $L = 3km$), this amplitude corresponds to a strain sensitivity

$$\tilde{h}_{seism}(\nu) = \frac{2\sqrt{2}}{L}\tilde{x}_{seism}(\nu) \approx \frac{10^{-9}}{\nu^2} \qquad [1/\sqrt{Hz}]. \tag{1.87}$$

Hence, the only way to detect GW in the low frequency band (lower than $0.01Hz$) is to go on space. Therefore, it is undergoing an ESA L3 mission called eLISA, former LISA (Laser Interferometric Space Antenna) [3]. Anyway, it is possible to at least damp these vibrations on Earth. Therefore, the optics must be isolated and suspended by suitable mechanical filters. The chain of filters in Virgo is called superattenuator. Their working principle is described in the following. Let k be the recall constant of a suspended pendulum, defined as $k = mg/l$, β is the dissipative coefficient, which for

simplicity is supposed to be viscous, and let $F(t)$ be an external force which modifies the equilibrium position of the suspended mass m. The equation of motion of the mirror is then

$$m\ddot{x}(t) + \beta\dot{x}(t) + kx(t) = F(t). \tag{1.88}$$

In the frequency domain it is:

$$-\omega^2 X(\omega) + i\frac{\beta}{m}\omega X(\omega) + \omega_0^2 X(\omega) = F(\omega), \tag{1.89}$$

where $\omega_0^2 = \frac{k}{m}$ is associated to the resonant frequency $\nu_0 = \frac{\omega_0}{2\pi}$ of the suspended pendulum. The transfer function associated to the equation of motion (1.88) is

$$H(\omega) = \frac{X(\omega)}{F(\omega)} = \frac{\omega_0^2}{\omega_0^2 - \omega^2 + i\frac{\beta}{m}\omega}. \tag{1.90}$$

From the transfer function of eq.(1.90), note that, for seismic perturbations:

- below the resonant frequency, $\omega \ll \omega_0$, the transfer function is

$$H(\omega) \approx 1 \tag{1.91}$$

  i.e. the noise is totally transferred to the suspended mass;

- in the proximity of the resonance, $\omega \approx \omega_0$, the noise is amplified of an amount equal to the quality factor $Q = \omega_0 m/\beta$

- above the resonance, $\omega \gg \omega_0$, the vibrations are attenuated as

$$H(\omega) \approx \frac{\omega_0^2}{\omega^2}. \tag{1.92}$$

In the case of a system of N coupled oscillators, the transfer function becomes

$$H(\omega) = \prod_{i=1}^{N} \frac{\omega_i^2}{\omega_i^2 - \omega^2 + i\frac{\beta}{m}\omega}. \tag{1.93}$$

where ω_i is associated to the resonant frequency $\nu_i = \frac{\omega_i}{2\pi}$ of the i-th oscillator. Hence, above the resonances, $\omega \gg \omega_i$, the vibrations are attenuated as

$$H(\omega) \approx \left(\frac{\prod_{i=1}^{N} \omega_i^2}{\omega^{2N}}\right). \tag{1.94}$$

This brief treatise shows that suspending the optics by a series of N identical pendulums, with the same quality factor Q, hence the same resonance $\omega_0 = \beta Q/m$, it is realized a

low-pass filter with cut off frequency equal to $\frac{\omega_0}{2\pi}$. Thus, the seismic vibrations on the mirrors are damped by an amount

$$\left(\frac{\omega_0}{\omega}\right)^{2N}. \tag{1.95}$$

Referring to the Virgo case, it has been designed in such a way that its sensitivity is limited only by intrinsic noise sources starting from $10Hz$. This condition translates into the need to reduce the seismic noise of at least 10 orders of magnitude. Such a condition is obtained by the so called **superattenuator**. Anyway, despite the presence of this sophisticated suspension system, the achievement of the nominal sensitivity is partially limited by other sources of noise, such as the residual environmental noise, that are not filtered by the suspensions.

1.3.2 The Newtonian Noise

The Newtonian noise is caused by the fluctuations of the mass density distribution in the vicinity of the interferometer, and in particular close to the mirrors.

Variations in the density of the atmosphere or of the ground, or the motion of close bodies, like the oceans or the Earth's crust, produce a fluctuation of the local gravitational field. These variations are directly detected by the mirrors, independently from the isolation system. Therefore, the displacement of the mirrors due to the newtonian noise can not be corrected or damped by a superattenuator system.

The equivalent spectral density associated to the newtonian noise for a ground based interferometer like Virgo is [122, 40]

$$\tilde{h}_N \approx \frac{3 \cdot 10^{-11}}{\nu^2} \tilde{x}_{seism}(\nu) > 10^{-19} \qquad \left[1/\sqrt{Hz}\right] \qquad \text{for } \nu < 4Hz. \tag{1.96}$$

Nevertheless, the newtonian noise does not constitute a significant limit to the sensitivity, since generally it determines a density perturbation significantly lower than the detection threshold, which is due to other noise sources.

1.3.3 The Shot Noise

The shot noise is an intrinsic noise of the interferometer which is related to the quantum nature of light. It is caused by the statistical fluctuations in the number of photons incident on the detector, and consequently causes a spurious phase shift. It may be dominant when the finite number of particles which carry energy is small enough so that the uncertainties due to the photon distribution are significant.
Due to the presence of the Fabry-Pérot cavity along the arms, the shot noise grows linearly with the frequency and dominates the sensitivity starting from few hundreds Hz.
The number N of photons emitted by the laser, as well as from any source of light, follows a Poisson's distribution, whose standard deviation is

$$\sigma_N = \sqrt{N}. \tag{1.97}$$

The output power on the photodiode, related to this phenomenon, can be expressed as the average energy carried by the photons $\overline{E}$ in the time Δt, multiplied by the quantum efficiency of the photodiode η

$$P_{out} = \frac{\overline{E}}{\Delta t}\eta = \frac{\overline{N}\hbar\omega_L}{\Delta t}\eta, \tag{1.98}$$

where $\overline{N}$ is the average number of incident photons and ω_L the laser's angular frequency. Recalling the equation (1.98) for the $\overline{N}$, and the standard deviation of a Poisson's distribution from the equation (1.97)), the fluctuation of the number of photons associated to the shot noise is then [40]:

$$\Delta N_{shot} = \sqrt{\overline{N}} = \sqrt{\frac{P_{out}\Delta t}{\hbar\omega_L\eta}}. \tag{1.99}$$

The power fluctuation at the output photodiode is obtained by making the derivative of the eq. (1.98) with respect to the $\overline{N}$ and then by multiplying by the fluctuation of the number of impinging photons ΔN_{shot} (eq.(1.99))

$$\Delta P_{shot} = \left|\frac{\partial P_{out}}{\partial \overline{N}}\right|\Delta N_{shot} = \sqrt{\frac{P_{out}\eta\hbar\omega_L}{\Delta t}}. \tag{1.100}$$

Assume to be in the ideal case, the output power at the detector is given by the equation (1.9)

$$P_{out} = \frac{P_{in}}{2}\big(1 + cos\phi\big), \tag{1.101}$$

where, for the sake of simplicity, the phase with no gravitational signal $\Delta\phi_L$, has been written as ϕ. When a GW passes by, the output power varies of an amount equal to

$$P_{out}^{GW} = \frac{\partial P_{out}}{\partial\phi}\Delta\phi_{GW} = -\frac{P_{in}}{2}sin\phi\Delta\phi_{GW}. \tag{1.102}$$

In order for the event to be detected, the signal to noise ratio (S/N) must be greater than or at least equal to 1. If we consider only the shot noise, it is [54, 111]

$$\left|\frac{S}{N}\right| = \left|\frac{P_{out}^{GW}}{\Delta P_{shot}}\right| = \frac{\frac{P_{in}}{2}sin\phi\Delta\phi_{GW}}{\sqrt{\frac{\hbar\omega_L}{\Delta t}}\eta\sqrt{\frac{P_{in}}{2}\left[1 + cos\phi\right]}} \geq 1. \tag{1.103}$$

The minimum detectable phase variation $\Delta\phi_{GW}$ is obtained in the dark fringe, i.e. when it is in the condition of destructive interference ($\phi = \pi$) [54, 111]

$$\Delta\phi_{GW} \geq \Delta\phi_{GW_{min}} = lim_{\phi\to\pi}\sqrt{\frac{2\hbar\omega_L}{P_{in}\Delta t}}\eta\frac{\sqrt{1 + cos\phi}}{sin\phi} = \sqrt{\frac{\hbar\omega_L}{P_{in}\Delta t}}\eta. \tag{1.104}$$

The equivalent spectral density $\tilde{h}_{shot}$ associated to the minimum phase shift due to the shot noise $\Delta\phi_{GW_{min}}$, can be derived from the relationship $\Delta\phi_{GW} = \frac{4\pi}{\lambda_L}\Delta l_{GW}$, where $\Delta l_{GW} = hL$ [129]:

$$\tilde{h}_{shot} = \frac{\lambda_L}{4\pi L}\Delta\phi_{GW_{min}} = \frac{1}{L}\sqrt{\frac{\lambda_L \hbar c}{8\pi P_{in}\Delta t}}\eta. \tag{1.105}$$

From the previous expression note that the spectral density associated to shot noise decreases as the input power of the laser increases, i.e. $\tilde{h}_{shot} \propto P_{in}^{-1/2}$.

It follows that to increase the sensitivity of the interferometer, it is necessary to decrease the minimum detectable phase difference $\Delta\phi_{shot_{min}}$, given by the eq. (1.104). This is possible by increasing the P_{in} and the arm-length L. The former operation is limited by the radiation pressure noise which increases with $\sqrt{P_{in}}$ (see sec. 1.3.4). Moreover, on the Earth surface is not possible to build interferometers with arms longer than some km, because of the curvature of the earth. Nevertheless, it is possible to build interferometers longer than a $few\ km$ underground or partially underground, but the expensive cost is the limitation. Therefore Fabry-Pérot optical cavities (see sec. 1.2.2), inside the arms, allow the light beam to undergo multiple reflections, thus lengthening the optical path up to a much greater effective length. For Advanced Virgo, the finesse is supposed to be 450, so that the effective optical path in the arms is about $860km$. Moreover, in Advanced Virgo, the input power P_{in} will be artificially increased by the recycling technique, which consists in placing the all interferometer in a resonant cavity by adding a power recycling mirror before the beamsplitter [39]. Therefore, the presence of the recycling mirror increases the circulating power of a factor equal to the recycling gain G_{PR}, while the Fabry-Pérot cavities acts as a high pass filter with cut frequency $\nu_{FP} = \frac{c}{4L\mathcal{F}} = 500Hz$ (with $\mathcal{F}$ finesse). Hence, the shot noise has the following profile [40]:

$$\tilde{h}_{shot,Virgo} = \frac{\nu_{FP}}{2}\sqrt{\frac{4\pi\hbar}{\omega_L \eta G_{PR} P_{in}}}\sqrt{1 + \frac{\nu}{\nu_{FP}}}. \tag{1.106}$$

1.3.4 The Radiation Pressure

As the input laser power P_{in} grows, the interferometer turns to be sensitive to the fluctuations of the radiation pressure. This one, as well as the shot noise, is related to the quantum nature of the light, and it is discussed in detail in a devoted chapter (see chapt. 2). The photons impinging on the mirror exchange momentum with it, thus perturbing the mirror position. For a mirror of mass m, given an input power P_{in}, the power spectral density of the fluctuations of the position associated with the radiation pressure is

$$\tilde{x}_{RP}(\omega) = \frac{2}{\omega^2 m}\sqrt{\frac{2\pi\hbar P_{in}}{c\lambda_L}}\eta. \tag{1.107}$$

The associated equivalent spectral density is

$$\tilde{h}_{RP}(\omega) = \frac{2}{\omega^2 mL}\sqrt{\frac{2\pi\hbar P_{in}}{c\lambda_L}\eta}, \tag{1.108}$$

in which L is the arm-length of the interferometer.
As already mentioned in the section on the shot noise, from the eq. (1.108), it can be noticed that the equivalent spectral density associated to the radiation pressure $\tilde{h}_{rad}$, increases together with the laser input power P_{in} as $P_{in}^{1/2}$, contrary to the shot noise which is proportional to $P_{in}^{-1/2}$. This implies that it is possible and necessary to find an optimal value for the power $P_{in} = P_{opt}$, for which the two noises, at a given frequency, are equivalent $\tilde{h}_{shot}(P_{opt}) = \tilde{h}_{rad}(P_{opt})$ [129].

1.3.5 The Residual Gas Pressure Fluctuations

Inside the interferometer, can occur laser beam phase fluctuations due to the residual gas pressure. These fluctuations appear because of the relation existing between the refraction index and the residual gas pressure value [122]. In fact, even in the ultra high vacuum condition, inside the instrument are present residual gas molecules. For example not ideal mirrors determine only a partial reflection of the light. It follows that some photons are diffused inside the optical cavities and can combine with the laser beam, giving rise to spurious phase shift. This effect causes a change in the refractive index n, according to the equation [122]

$$n = 1 + \epsilon\frac{P_{res}}{P_{atm}} = 1 + \epsilon\frac{N_{res}}{N_{atm}} \tag{1.109}$$

in which P_{res} is the residual pressure, and P_{atm} the atmospheric pressure. N_{res} and N_{atm} are the respective molecular densities. ϵ is a constant whose value is $\epsilon \sim 1.2 \cdot 10^{-4}$.
The related equivalent spectral density is [122]

$$\tilde{h}_{gas}(\nu) = \frac{\epsilon}{N_{atm}}\sqrt{\frac{w_{beam}}{v_{H_2}}\frac{N_{res}}{V_{beam}}\sqrt{\pi}}, \tag{1.110}$$

where v_{H_2} is the velocity of the H_2 molecule, w_{beam} is the beam waist at the far mirror distance ($\sim 0.1m$ in the starting Virgo) and V_{beam} is the corresponding 'volume' of the beam $V_{beam} = \pi w_{beam} L$. From the eq. (1.110) notice that the equivalent spectral density associated to the fluctuations of the refractive index depends on the characteristics of the gas molecule. In the ultra high vacuum condition, like in Virgo, the limits on the partial gas pressures are different and equal to $10^{-9} mbar$ for the molecular hydrogen and $10^{-10} mbar$ for all the other gases. In Virgo the residual gas pressure effect is of the order $\tilde{h}_{gas}(\nu) \sim 2.5 \cdot 10^{-26} 1/\sqrt{Hz}$ [122].

1.3.6 The Thermal Noise

The Thermal Noise consists on the random fluctuations of a macroscopic observable of a given system, at the thermodynamic equilibrium, due to the thermal motion of the

microscopic constituents.
The thermal noise, is one of the intrinsic noise of the system. It is present in all the experimental apparatus and constitutes one of the intrinsic limitations on their sensitivity [73, 74, 79].
The thermal noise of a suspended interferometer can be distinguished in two different types. The thermal noise of the suspensions, and the thermal noise of the mirrors. They are described through the Fluctuation Dissipation Theorem (FDT) [93].

Before introducing the FDT is necessary to make some assumptions. Consider a one-dimensional system at the thermodynamic equilibrium at the temperature T. The system is also linear, i.e. its response is linear with respect to an external applied force $F(t)$, and dissipative, i.e. it dissipates energy by irreversible processes. Then its linear response, in the frequency domain, to an external force $F(\omega)$, is $X(\omega)$, i.e. the fluctuation of the coordinate $x(t)$:

$$X(\omega) = H(\omega)F(\omega) \tag{1.111}$$

where $H(\omega)$ is the transfer function of the system.
From the equation of motion it is possible to derive the velocity $V(\omega) = \dot{X}(\omega) = i\omega X(\omega)$ which is related to the impedance of the system $Z(\omega)$ through the

$$V(\omega) = \frac{F(\omega)}{Z(\omega)}. \tag{1.112}$$

It follows that the $H(\omega)$ and $Z(\omega)$ are related as

$$H(\omega) = \frac{X(\omega)}{F(\omega)} = \frac{X(\omega)}{i\omega X(\omega)Z(\omega)} = \frac{1}{i\omega Z(\omega)} \tag{1.113}$$

therefore, in order to calculate the thermal noise, it is enough to know one of them.
Then, the Fluctuation Dissipation Theorem states that, giving an external force $F(t)$, the power spectrum of the fluctuations of $x(t)$ is

$$w_X(\omega) = X^2_{therm}(\omega) = \frac{4k_BT}{\omega}\big|\Im[H(\omega)]\big| \tag{1.114}$$

and the power spectrum of the external force $F(t)$ is

$$w_F(\omega) = F^2_{therm}(\omega) = 4k_BT\big|\Re[Z(\omega)]\big|. \tag{1.115}$$

These show that the energy of the fluctuations is distributed along the frequency band.

A different approach is usually applied when the mechanical loss is not homogeneously distributed on the system, i.e. the Levin approach [97]. This is the case of real mirrors, where structural defects and stress within the bulk material are localized and the mechanical loss associated with the polished surfaces is higher than the levels typically associated with bulk effects [127]. Therefore, Levin suggested a direct application

of the FDT to the optically-sensed position of the mirror substrate surface [97]. This technique uses a notional pressure, of the same spatial profile as the intensity of the sensing laser beam, to the front face of the substrate and calculates the resulting power dissipated in the substrate on its elastic deformation under the applied pressure [127]. Using this approach the power spectrum of the effective displacement of the mirror's face can be described by the relation [97, 16]

$$X^2_{mir}(\omega) = \frac{8k_B T}{\omega} U\phi(\omega) \tag{1.116}$$

where T is the temperature, k_B is the Boltzmann's constant, $\phi(\omega)$ is the loss angle and U is the static strain energy stored in the mirror when a pressure distribution $p(r)$, due to the laser impinging on the mirror, is applied on the mirror surface.

The thermal noise will be discussed in more detail in the chapter 3.

Chapter 2

Quantum Pressure Radiation Noise and the QURAG

A gravitational signal arriving on Earth has an amplitude whose order of magnitude is typically $h_0 \simeq (10^{-20} - 10^{-22})1/\sqrt{Hz}$. This infers that a ground based km-scale GW interferometer needs to be able to measure arm-length differences smaller than $10^{-18}m$, which is like measuring a length even smaller than the diameter of an atom with respect to the Earth Moon distance! Therefore, all the noise sources, already discussed in the previous chapter (see sec. 1.3), which limit the sensitivity must be identified and removed [128]. Ground based GW detectors have sensitivity in the audio-

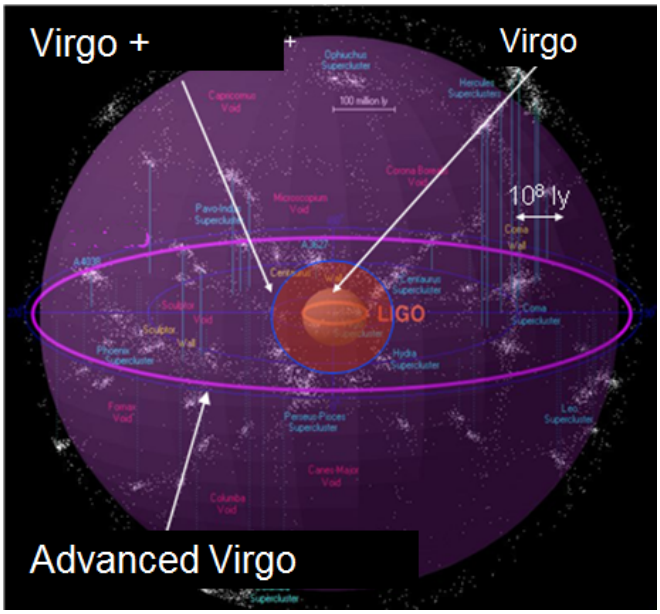

Figure 2.1: Volume of Universe observable by Advanced Virgo, compared to Virgo and Virgo+ (Virgo after substitution of steel wires by fused silica ones to reduce thermal noise of the suspensions).

band frequency range, i.e. Virgo could detect GW signal in the range $10Hz - 10kHz$. In the present status, the main limitation to the sensitivity is the thermal noise of

the suspensions and of the mirrors for frequencies lower than 200Hz and for higher frequencies is the shot noise of the light, as it is shown in the fig. 2.2. The limited

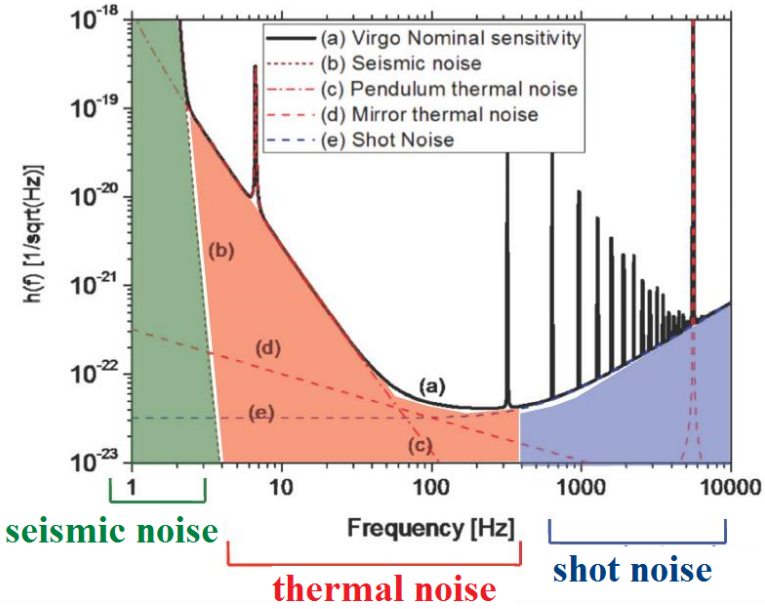

Figure 2.2: Main noise limitation in Virgo sensitivity curve.

sensitivity of GW detectors reduces the detection distance of observable gravitational events. For instance, signal such as coalescing binaries are limited to few megaparsec[1] with a very low expected detection rate in current configuration (0.01 events/year or few events/ 100years). Therefore, a large international effort is ongoing to improve the sensitivity, realizing the so called second and third generation of GW detectors, which are expected to make the first GW detection. In this program of enhancement Virgo will become Advanced Virgo, reaching a sensitivity 10 times higher than the starting Virgo, thus being able to observe a volume of universe 1000 times higher (see fig. 2.1) [39].

Nevertheless, in order to reach such improvement in sensitivity, an increasing of the laser power circulating inside the Fabry-Pérot cavities is necessary. This will lead the GW detectors to face the limit imposed by the quantum nature of light: the so called Standard Quantum Limit (SQL). Therefore, it is crucial to develop table top experiments to study this effect, to verify the theory and to test and develop methods that circumvent this limit. This is the primary aim of our experiment QuRaG.

2.1 Quantum noise in GW interferometers

The gravitational wave interferometer works in the dark fringe condition, which means that all the light incident on the beamsplitter returns back to the photodiodes, called the dark port, and it is only sensitive to the differential length between the two arms.

[1] $1 Megaparsec(Mpc) = 3.0857 \times 10^{22} m$

The other port is called the bright port. From the dark port the vacuum fluctuations of the light fields enter in the interferometer, as explained by Caves [34]. They are then coupled inside the Fabry-Pérot cavities and they make the suspended mirror fluctuates. This effect is called radiation pressure noise, and together with the shot noise constitutes the quantum noise, i.e. the limit in the sensitivity of GW detectors due to the quantum nature of light. The photon shot noise is a sensing noise and the photon radiation pressure noise is a back-action noise, as represented in the figure 2.3. The former

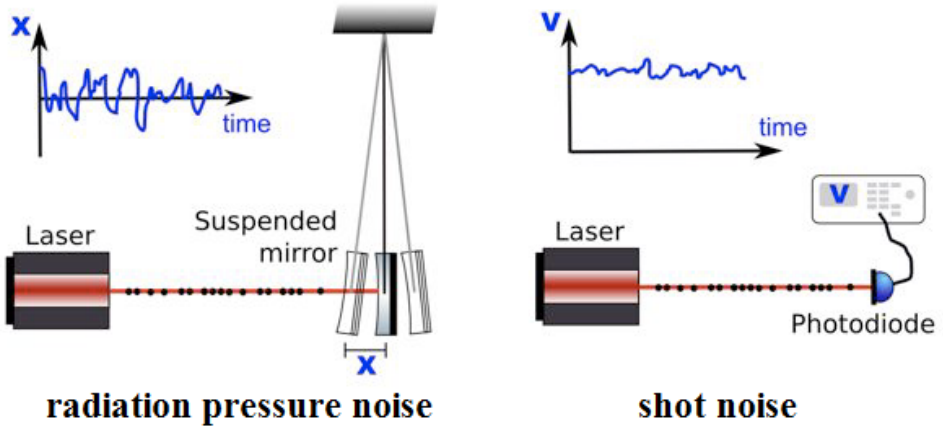

Figure 2.3: Photon shot noise is a sensing noise, photon radiation pressure noise is a back-action noise [85].

dominates in the high frequencies (higher than 200Hz), the latter will dominate, in the low frequencies, the sensitivity of next generation of GW detectors as it is shown in the sensitivity curve of fig.2.4. As already discussed in sec.1.3.3 and 1.3.4

- the **shot noise** derives from the fluctuation of the output power caused by the quantum fluctuations in the number of the photons at the interferometer output (see the figure on the right in fig.2.3).

- the **radiation pressure** arises from the uncertainties in the mirror position due to quantum fluctuations of the internal field inducing radiation pressure fluctuations that drives the mirrors (see figure on the left in fig.2.3).

In fact, when reflected back, the photons exchange momentum with the mirrors. Therefore, the fluctuations of the light field inside the Fabry-Pérot cavity affect the suspended mirrors by a random transfer of momentum to the mirrors, as represented in the figure on the left in fig.2.3.

It was already shown in the '80 by C. M. Caves [34, 35] that this radiation pressure force can be attributed to quantum fluctuations of the vacuum optical field that enters the unused port of the interferometer, the antisymmetric port [45].

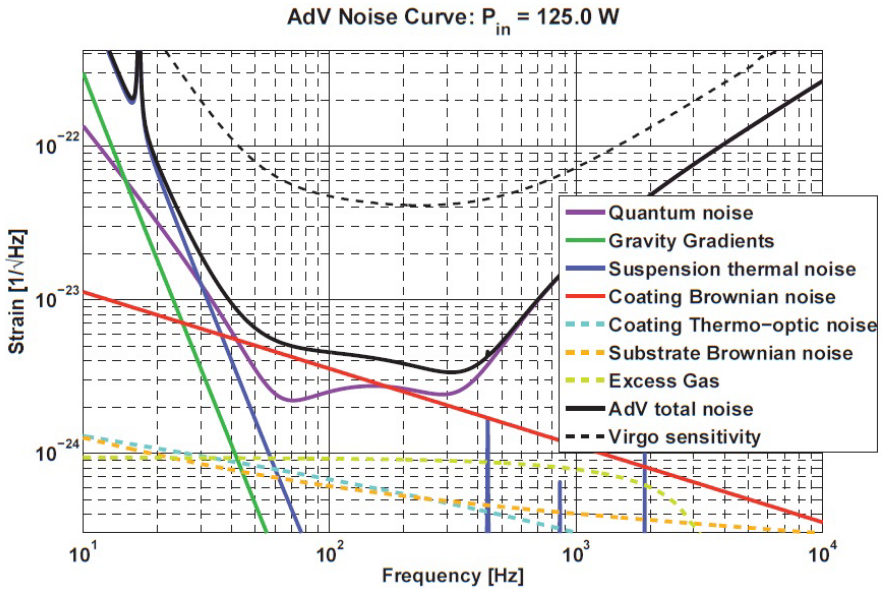

Figure 2.4: Sensitivity curve of Advanced Virgo.

2.2 Standard Quantum Limit

The standard quantum limit (SQL) for gravitational wave detectors, where the photons are used to measure the positions of the test mass mirrors, is obtained when the uncertainty in position measurements due to radiation pressure induced fluctuations is equal to the position measurement uncertainty due to fluctuations in the number of photons (or shot noise) [45, 17]. This equality can be seen as a statement of the Heisenberg uncertainty principle [82] for the position and the momentum of the particle. An initial measurement of the particle position imparts an unknown momentum to it via radiation pressure, which prevents one from predicting the outcome of a later position measurement, since the momentum and position do not commute [45]. This is known as quantum back-action noise.

Therefore, the gravitational wave interferometer can be consider as an observer of the dynamics of the suspended end mirrors, as depicted in figure 2.3. In this context, the radiation pressure noise and the shot noise can be seen as the displacement and momentum fluctuation of the mirror. It should be evident that the more precisely one needs to know the state of a macroscopic object like a mirror of a GW interferometer, the more it will behave quantum mechanically. Thus, the two noises are linked to the quantum uncertainty given by the Heisenberg principle:

$$\Delta x \Delta p \geq \frac{\hbar}{2}, \tag{2.1}$$

therefore the greater is the accuracy on the position Δx, the lower will be the accuracy on the momentum Δp and the best condition achievable corresponds to the equality in the eq.(2.1). To express this limit for a GW interferometer it is necessary to recall the

expressions for the linear noise spectral density of the photon shot noise (see sec. 1.3.3) and for the radiation pressure noise (see sec. 1.3.4):

$$h_{shot}(\nu) = \frac{1}{L}\sqrt{\frac{c\hbar\lambda_L}{8\pi P_0}} \tag{2.2}$$

$$h_{RP}(\nu) = \frac{1}{mL\nu^2}\sqrt{\frac{\hbar P_0}{2\pi^3 c\lambda_L}}, \tag{2.3}$$

which are derived independently and are therefore uncorrelated. Moreover, the square root of their square sum gives the total quantum noise of the GW interferometer:

$$h_{quantum}(\nu) = \sqrt{h^2_{shot}(\nu) + h^2_{RP}(\nu)}. \tag{2.4}$$

From the equations 2.3 it is straightforward noticed that while the noise contribution of the photons decreases with the input laser's power, the contribution of radiation pressure grows. However, it exists an optimal value for the laser's power for which at a given frequency the quantum noise is minimized. This condition is called the Standard Quantum Limit (SQL) and it corresponds to the minimum achievable quantum noise, h_{SQL}. It is reached when the two contributions, hence the two terms of equation (2.4), are equal

$$h_{SQL}(\nu) = \sqrt{2h^2_{shot}(\nu)} = \sqrt{2h^2_{RP}(\nu)}. \tag{2.5}$$

The SQL and the optimal laser power, for a given frequency ν_{SQL}, are then

$$h_{SQL}(\nu_{SQL}) = \frac{1}{L}\sqrt{\frac{\hbar}{2m\nu^2_{SQL}\pi^2}} \tag{2.6}$$

$$P_{SQL} = m\lambda_L c\pi\nu^2_{SQL}/2. \tag{2.7}$$

The fig. 2.5 shows how the quantum noise of a GW Michelson interferometer varies as the input laser power changes. As the input laser power increases the radiation pressure noise increases, and if the laser power decreases the shot noise increases. Moreover, when the power changes, also the minimal value of the total quantum noise and the frequency at which the SQL occurs change. Nevertheless, even changing the laser power the SQL cannot be overcome, therefore the SQL establishes a fundamental limit for the measurement precision of classical GW interferometers. For Advanced Virgo, since $m = 40kg$ and $\lambda_L = 1.064\mu m$ the formula for the optimal power is:

$$P_{AdV} \simeq 2 \cdot 10^4 \nu^2_{SQL}. \tag{2.8}$$

Therefore, since several interesting gravitational signal are expected to be around $100Hz$, this will be the frequency for the SQL in Advanced Virgo, which corresponds then to a power inside the FP cavities of $2 \times 10^8 W$. The higher power inside the Fabry-Pérot cavities is possible thanks to the power recycling system [39], so that the input power does not need to be so high. The current value for the Advanced Virgo input laser power is set to be $\sim 175W$. However, several techniques are currently under study in order to test and build the suitable technology which will allow to overcome this limitation in sensitivity [45].

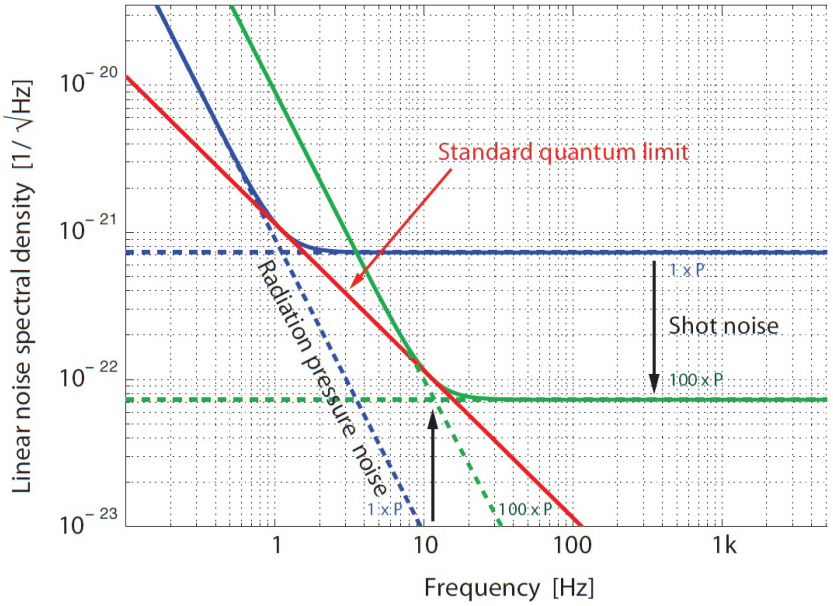

Figure 2.5: Quantum noise sensitivity curves of a GW detector by varying the input laser's power. When the power changes, also the minimal value of the total quantum noise and the frequency at which the SQL occurs.

2.3 Origin of the Standard Quantum Limit

The standard quantum limit is the limit on the accuracy with which any position sensing device can determine the position of a free mass in the absence of correlations between shot noise and radiation pressure noise. In fact the shot noise and radiation pressure noise enforce together the SQL only if they are uncorrelated. Therefore, it naturally follows that this limit can be overcome by creating correlations between radiation pressure noise and shot noise [45]. The devices, firstly proposed by Braginsky [23], that prevent their own quantum properties from demolishing the state of the system on which they are performing the measurement, are called quantum non-demolition (QND) devices. QND interferometers are then obtained by realizing correlations between radiation pressure and shot noise.

I previously spoke of shot noise as the fluctuations of the number of photons on the output port, and of the radiation pressure as the fluctuations of the vacuum field inside the arm cavities. Whereas, speaking in a quantized radiation field language, the shot noise represents the phase quadrature and the radiation pressure the amplitude quadrature of the input vacuum field [45]. The amplitude-phase commutation relation is analogous to the position-momentum commutation relation. In fact, the shot noise, i.e. the number of photons arriving at the detector at not equally spaced time intervals, can be seen as a not well defined phase of the radiation state associated with the laser [128]. On the other hand, the fluctuations of the number of photons exchanging momentum while exerting a real pressure on the mirrors, can be seen as the fluctuations of the amplitude of the radiation impinging on the mirrors.

2.3.1 Squeezed States

For both shot noise and radiation pressure noise as described in sec. 1.3.3 and 1.3.4, it has been assumed a Poisson statistics with the same mean value. In a quantized radiation field language, this means that we are dealing with radiation states with Poisson photon statistics and which have uncorrelated quantum noise equally distributed between phase and amplitude quadrature [128].

The non correlation of radiation pressure-shot noise expressed as non commutation of the amplitude quadrature X_1 and phase quadrature X_2 of the vacuum input field, in quantum mechanics formalism [148], is:

$$[X_1, X_2] = 2i. \tag{2.9}$$

The Heisenberg principle for the variances of the amplitude ΔX_1 and of the phase ΔX_2 quadrature can be written as

$$\Delta X_1 \Delta X_2 \geq \left|\frac{[X_1, X_2]}{2}\right|^2 = 1, \tag{2.10}$$

where the equal sign defines a family of minimum uncertainty states. The coherent states are a particular class of minimum uncertainty states with

$$\Delta X_1 = \Delta X_2 = 1. \tag{2.11}$$

The coherent state $|\alpha\rangle$ has the mean complex amplitude α and it is a minimum uncertainty state for X_1 and X_2, with equal uncertainties in the two quadrature phases. Therefore, a coherent state can be represented by an error circle in a complex amplitude plane whose axis are X_1 and X_2, as shown in the phase space plot of fig. 2.6 [148].

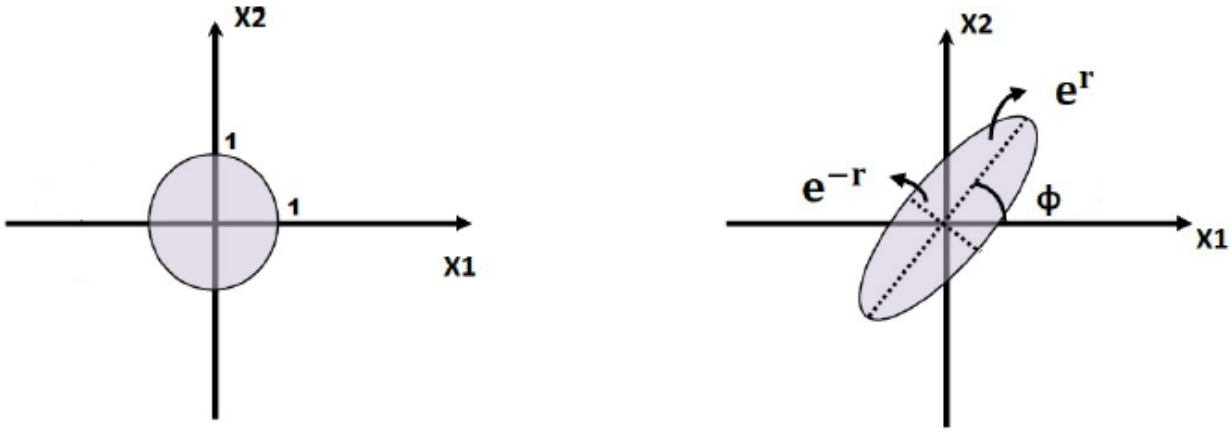

Figure 2.6: Phase-Space plot showing the uncertainty in a coherent state $|\alpha\rangle$ (left side) and in a squeezed state $|\alpha, r\rangle$ (right side).

The center of the error circle lies at

$$\frac{1}{2}\langle X_1 + iX_2\rangle = \alpha \tag{2.12}$$

and the radius $\Delta X_1 = \Delta X_2 = 1$ accounts for the uncertainties in X_1 and X_2. There is also the family of minimum uncertainty states defined by

$$\Delta X_1 \Delta X_2 = 1 \tag{2.13}$$

and by plotting the eq.2.13 in the plane $\Delta X_1 - \Delta X_2$, we obtain the hyperbola where the minimum uncertainty states lies on (see fig. 2.7). Only the points lying on the right

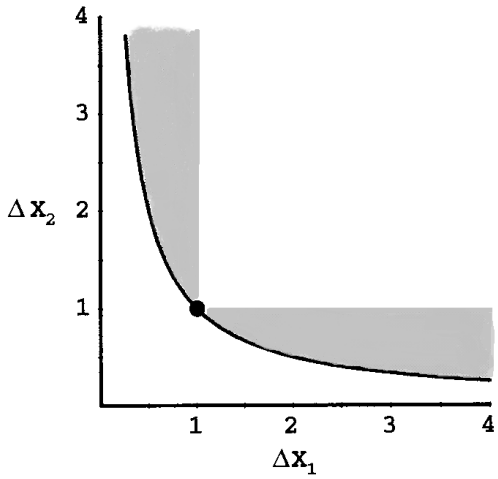

Figure 2.7: Plot of the ΔX_1 versus ΔX_2 which represents the hyperbola of the minimum uncertainty states. The dot marks the coherent state, while the grey region corresponds to the squeezed states.

of this hyperbola correspond to physical states. The coherent state is a particular case with $\Delta X_1 = \Delta X_2$ of a more general class of states which may have reduced uncertainty on one quadrature at the expense of increased uncertainty in the other $\Delta X_1 < 1 < \Delta X_2$. These states correspond to the grey region in the fig. 2.7 and they are called squeezed states [148].

The squeezed states can be generated by using the unitary squeeze operator

$$S(\epsilon) = exp\big(\frac{1}{2}\epsilon^* a^2 - \frac{1}{2}\epsilon a^{\dagger 2}\big), \tag{2.14}$$

where $\epsilon = re^{2i\phi}$, ϵ^* is its complex conjugate, and the annihilation operator a is defined as

$$a = \frac{X_1 + iX_2}{2}, \tag{2.15}$$

and $a^\dagger$ is its adjoint operator, the creation operator [148]. The squeeze operator obeys the relations

$$S^\dagger(\epsilon) = S^{-1}(\epsilon) = S(-\epsilon), \tag{2.16}$$

and has the following transformation properties

$$S^{\dagger}(\epsilon)aS(\epsilon) = a\cosh r - a^{\dagger}e^{-2i\phi}\sinh r \quad (2.17)$$

$$S^{\dagger}(\epsilon)a^{\dagger}S(\epsilon) = a^{\dagger}\cosh r - ae^{2i\phi}\sinh r \quad (2.18)$$

$$S^{\dagger}(\epsilon)(Y_1 + iY_2)S(\epsilon) = Y_1 e^{-r} + iY_2 e^{r} \quad (2.19)$$

where

$$(Y_1 + iY_2) = (X_1 + iX_2)e^{-i\phi} \quad (2.20)$$

is the rotated complex amplitude. The squeeze operator attenuates one component of the rotated complex amplitude, and amplifies the other (see eq.(2.19)) [148]. The degree of attenuation and amplification is called squeeze factor and it is determined by

$$r = |\epsilon| . \quad (2.21)$$

The squeeze state $|\alpha, r\rangle$ is obtained by first squeezing the vacuum $|0\rangle$ and then displacing it with the unitary displacement operator $D(\epsilon)$ ($D(\alpha) = exp(\alpha a^{\dagger} - \alpha^{*}a)$)

$$|\alpha, r\rangle = D(\epsilon)S(\epsilon)\,|0\rangle . \quad (2.22)$$

A squeezed state has the following expectation values and variances

$$\langle X_1 + iX_2\rangle = \langle (Y_1 + iY_2)\rangle\, e^{i\phi} = 2\alpha \quad (2.23)$$

$$\Delta Y_1 = e^{-r} \qquad \Delta Y_2 = e^{r} \quad (2.24)$$

$$\langle N\rangle = |\alpha|^2 + \sinh^2 r \quad (2.25)$$

$$(\Delta N)^2 = \left|\alpha\cosh r - \alpha^{*}e^{2i\phi}\sinh r\right|^2 + 2\cosh^2 r\sinh^2 r, \quad (2.26)$$

with N number of states. Thus the squeezed state has unequal uncertainties for Y_1 and Y_2 and it is represented by the error ellipse in the phase space plot of fig. 2.6. The principal axes of the ellipse lie along the Y_1 and Y_2 axes and the principal radii are ΔY_1 and ΔY_2 [148].

2.4 Beating the Quantum Limit

The Michelson interferometer operates at the dark fringe condition to minimize the coupling of the technical laser noise to the antisymmetric (dark) port. Since most of the light returns towards the laser, a partially transmitting power-recycling mirror (PRM) is placed between the laser source and the beam splitter to 'recycle' the light back into the interferometer [45]. The gravitational wave signal at a given frequency, due to asymmetric motion of the end mirrors, appears as a phase modulation on light. Upon mixing with a local oscillator field at the beam splitter, this phase modulation is converted into amplitude modulation that is detected by the photodetector. The gravitational signal appears only in a single quadrature. As well as for a

simple Michelson interferometer, in the power-recycled Michelson only the phase quadrature is detected. Therefore, the radiation pressure noise and the shot noise in this interferometers are uncorrelated. Vacuum fluctuations entering the antisymmetric port of the beamsplitter pass into each arm and return to the antisymmetric port with an uninteresting overall phase shift. Without injecting squeezing or a modified readout, there is no quantum non demolition at any operating power. Consequently, this configuration has been called 'conventional interferometer'. The conventional interferometer is a power-recycled interferometer with arm cavity half-linewidth of $100Hz$ and power input at the beamsplitter that gives the standard quantum limit performance at $100Hz$, i.e. $P_{in} = P_{SQL}(100Hz)$. The quantum non demolition (QND) interferometers can be

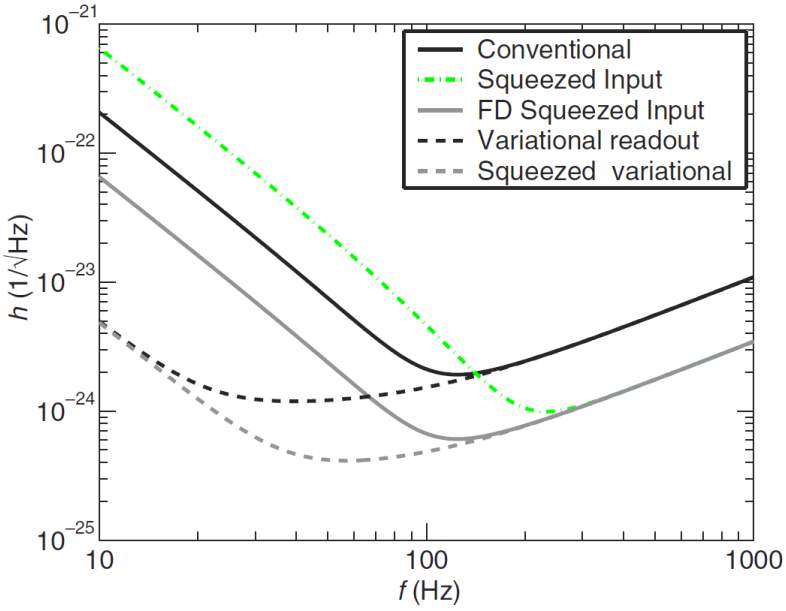

Figure 2.8: Spectral density of noise for a power-recycled interferometer. The solid (black) curve is the sensitivity for a conventional interferometer with $P_{in} = P_{SQL}(100Hz)$; the dash-dot (green) curve is for the same interferometer with *squeezed input* at a fixed, frequency-independent squeeze angle; the lighter solid (grey) curve has a squeezing injected at a *frequency-dependent* (FD) optimal squeeze angle; the dashed dark (black) curve is a frequency-dependent homodyne or *variational* readout that measures the optimal quadrature at each frequency; the lighter dashed (grey) curve uses a variational readout as well as $10dB$ of squeezing injected. Total fractional losses of 1% in the arm cavities and 5% in the output train are included in the noise curves plotted here [45].

realized in different manners, such as:

1. the injection of squeezed states which modifies the interferometer input fields;
2. the realization of dynamical correlations by coupling the optical field to the mechanical modes of the mirrors;
3. the direct measurement of a QND observable which satisfies the commutation relations for the measurement probe;
4. the variational readout method applied on the output fields.

The effect on the quantum noise reduction in the sensitivity curve of a Michelson interferometer are summarized in the figure 2.8 which compares the several methods, listed above, of beating the SQL.

The injection of squeezed states of light

The squeezed states of light, as already demonstrated in sec. 2.3.1, reduce the noise in one quadrature at the expense of additional noise in the orthogonal quadrature (see eq.(2.26)). The vacuum fluctuations entering in the interferometer from the unused port of the beamsplitter corrupt the measurement of the mirror position, with the amplitude quadrature X_1 responsible for the radiation pressure noise, and the phase quadrature X_2 responsible for the shot noise. Therefore, injecting the squeezed vacuum with the appropriate squeeze quadrature into the antisymmetric port of the interferometer will reduce the dominant optical noise by a factor e^{-2r}, which is then called the power squeeze factor (see eq.(2.21)). The squeeze angle describes the linear combination of input quadratures in which the fluctuations are reduced and it governs the degree of squeezing of each quadrature [45].

The Dynamical Correlations

Another method for the realization of a QND interferometer is to modify the mirror dynamics by coupling to the light. The basis of this process lies on the fact that the radiation pressure force not only causes random fluctuations of the mirror position, but also exerts a restoring force with a deterministic frequency dependent spring constant, called ponderomotive rigidity [29]. The resulting dynamical correlations of the shot noise and radiation pressure noise are manifestations of quantum non demolition in the sense that the correlations lead to go below the SQL [28].

The Measurement of QND observables

A general criterion of a QND measurement is that the measured observable $\tilde{q}$ commutes with the operator $O(\tilde{q})$ that describes the back action of the probe of the measurement, $[\tilde{q}, O(\tilde{q})] = 0$. In the Heisenberg picture this corresponds to $[O(t_0), O(t_1)] = 0$, so that momentum can be a good QND observable since it commutes with itself at different times. A measurement of the momentum perturbs the position of a test mass, as consequence of the Heisenberg uncertainty principle. This position kick does not influence the time evolution of the momentum, hence there is no back-action. Therefore, the position is not a good QND observable. In fact, a measurement of the position at a time t_0 disturbs a consequent measurement at a later time $t_1 > t_0$ due to the momentum kick from the first measurement [45]. Hence, momentum measurements are back-action evading if no position information is collected. Moreover, since the test mass speed is proportional to momentum, relative speed is also a good QND observable. Such kind of interferometers are called speedmeters [89] .

The Variational Readout

The ponderomotive squeezing derives from the natural correlation of the light intensity fluctuations, to the mirror position fluctuations upon reflection of light from a mirror. This process can be described taking into account the fact that when light, or vacuum, with fluctuations in the amplitude quadrature $\Delta A(=\Delta X_1)$ and in phase quadrature $\Delta\phi(=\Delta X_2)$, is incident on a mirror, the mirror position is influenced by ΔA due to the back-action force of the light on the mirror [45]. If the position signal is measured in the phase quadrature $\Delta\phi$, then the noise on that measurement is given by

$$\Delta\phi - \kappa(\omega)\Delta A, \tag{2.27}$$

where the $\kappa(\omega)$ is a measure of the back-action coupling and depends on the frequency of oscillation of the mirror ω. If a single quadrature is measured at the output of the interferometer, the noise on that measurement will depend on $\kappa(\omega)$ at each frequency ω. However, if it can be measured an admixture of quadratures with a frequency dependent homodyne angle that is function of κ, then it would possible to eliminate ΔA from the measurement at all frequencies [89]. Since the measured quadrature varies with the frequency, this method is generally called variational or equivalently frequency dependent homodyne readout [45].

2.4.1 Ponderomotive Squeezing

Next generation of gravitational wave detector will adopt the technique of injecting the squeezed light into the output port, in order to beat the SQL of the interferometer. This method has already been experimentally tested in few experiments [157]. In all these experiments, the effect of squeezing was measured in the few MHz frequency band, where the effect of classical noise sources, such as the laser frequency and intensity noise, can be reduced [128]. However, squeezed vacuum has been also produced in the detection band of ground based GW interferometers $10Hz-10kHz$, by using parametric processes [143]. Nevertheless, this method encounters some technical limitations, such as the photothermally driven fluctuations, which reduce the squeezing level.

An alternative method to produce squeeze vacuum is the ponderomotive squeezing, as already discussed in the previous section on the 'dynamical correlations'. The basis of this method is to take advantage of the radiation pressure to produce squeezing. In fact, whenever a carrier light with sidebands reflects off a mirror, the reflection ponderomotive squeezes the light's sidebands, creating correlations between their radiation pressure noise in one quadrature and shot noise in the other [89]. Although these correlations are not accessible by a conventional interferometer because of the particular quadrature that its photodiode measures, they can be accessed by conceptually simple modifications of the interferometer input and/or output optics. With these modifications the conventional interferometer becomes a QND device. These correlations were firstly presented implicitly by Braginsky in his earlier identification of the phenomenon of ponderomotive squeezing [19].

2.4.2 Other Experiments on Radiation Pressure Noise

Experiments for the observation of quantum radiation pressure noise are currently ongoing all over the world. Even if their sensitivity did not reach the sensitivity required for the Advanced generation of gravitational wave interferometers, they allowed to investigate the effects caused by classical radiation pressure, such as the optical spring or the cold damping. The graphics of figure 2.9 report and compare the sensitivity requirements of these experiments [109].

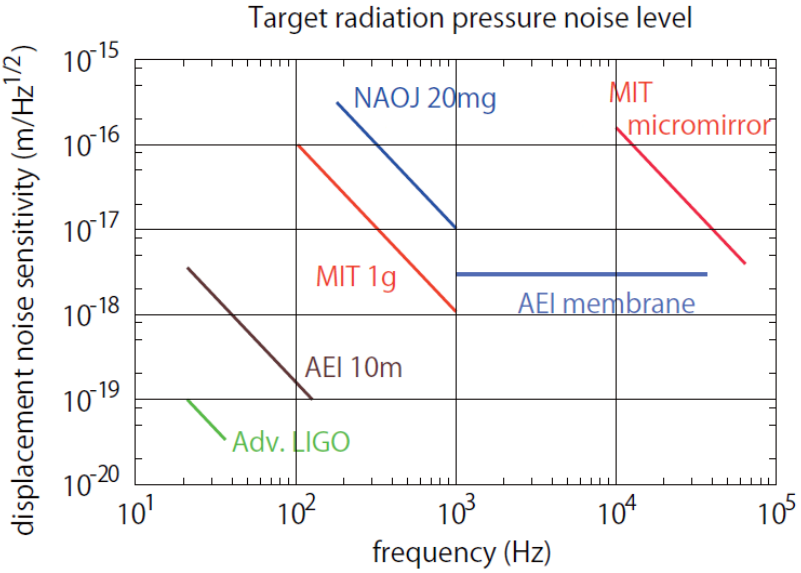

Figure 2.9: Comparison of the quantum radiation pressure noise limited design sensitivity of ongoing experiments.

Second Generation of Gravitational Wave Interferometers

The second generation of GW detectors are designed to reach a quantum radiation pressure noise level at few tens of Hz, and in figure 2.9 the value for Advanced LIGO is shown as representative of them. In order to detect gravitational wave signal these detectors require a sensitivity better than $10^{-19} m/\sqrt{Hz}$. For these instruments, the observation of quantum radiation pressure noise would be just the result of the pursuance of the ultimate sensitivity. Nevertheless, their goal is to observe gravitational waves, therefore, in order to contrast the effect of radiation pressure heavier mirrors with double mass ($40kg$) will be introduced.

$10m$ Prototype at the AEI, Hannover

A middle scale laser interferometer called Hannover 10m prototype is currently being set up at the Albert Einstein Institute (AEI) in Hannover [70]. The prototype interferometer will be used as a test bench for Advanced GW detectors. No recycling techniques,

such as power recycling or signal recycling, will be used in the initial round of experiments. Since high light power is required to approach the SQL regime, arm cavities of finesse $\mathcal{F} = 675$ are planned. In this way the resonantly enhanced light power does not travel through the beamsplitter, minimising the thermal load in the substrate. The end mirror of each interferometer arm will be formed by another Fabry-Pérot cavity, a so-called Khalili cavity, which is held on anti-resonance for the carrier light. Such a compound mirror can yield a high reflectivity while carrying only moderate coating thermal noise [1].

$1g$ Suspended Mirror at MIT, Massachusetts

Researchers at the Massachusetts Institute of Technology (MIT) intensively studied the effect caused by radiation pressure in optical cavities . They employed a small suspended mirror of $1g$ and they succeed in realizing the control of the cavity length only by the radiation pressure [43].

Thin Membrane at AEI, Hannover

A Michelson–Sagnac interferometer which senses the motion of a thin translucent silicon nitride (SiN) membrane with subwavelength thickness has been experimented at the AEI in Hannover. The researchers found that such an interferometer provides an operational point that is optimally suited for quantum opto-mechanical experiments with translucent oscillators. In the case of a balanced beam splitter of the interferometer, the membrane can be placed at a node of the electromagnetic field, which simultaneously provides the lowest absorption and optimum laser noise rejection at the signal port [64]. The power reflectivity of the membrane is about 30%. Moreover, since this membrane is very light, i.e. $\simeq 125ng$ and has a high mechanical factor ($Q \simeq 10^6$ in vacuum), it is quite sensitive to the radiation pressure and therefore very promising. A cryogenic environment is needed to reduce the thermal noise. The expected spectrum of quantum radiation pressure noise is flat, since the fundamental resonant frequency of the membrane is higher than the frequency range of observation [109].

Micromirror Resonator at MIT, Massachusetts

The MIT group is developing an interferometer with small mechanical oscillators realized with the MEMS (Microelectromechanical systems) technique. The mass of such mirrors is typically $250ng$. This mirror concept allows to have a control system simpler than a pendulum-type one. Nowadays, many experiments have been done using cantilever type mirrors, as for example for observing the radiation pressure cooling [33]. They succeed many optomechanical experiments, nevertheless these mirrors are not suited for the observation of quantum radiation pressure noise, since their resonant frequency is too high (order of 1MHz), owing to their small scale. However, the MIT oscillators have $1-5mm$ sticks, thus the target frequency range to observe the quantum

radiation pressure noise can be lower. Moreover, the mirrors should be cooled in order to thermally reduce excited fluctuations.

NAJO $20mg$, Tokyo

In this experiment a low mass $20mg$ mirror is suspended in such a way to optimize the radiation pressure noise at low frequencies (see fig. 2.9). However, this experiment pointed out problems in the alignment and control of a high power cavity [109].

2.4.3 Observed Radiation Pressure Effects

Quantum effects of radiation pressure have never been observed within the frequency band of ground based GW interferometers. The first experiments fell short off the quantum regime [77, 36] and even though recent experiments demonstrated a much larger optomechanical coupling between light and mirrors [67, 47, 142, 135], they were mainly focused on the demonstration of the quantum state of a very small mechanical resonator [90, 94] . However, several experiments studied physical phenomena derived from classical effects of radiation pressure, such as parametric instability [21, 22, 87, 161], optical spring [27, 20, 18], and optical cooling [156, 102]. In order to produce the dynamical effects of radiation pressure on the light or on the motion of the mirror in a Fabry-Pérot cavity, the phase change induced by the mechanical motion must be linearly coupled with the intensity fluctuations of the intracavity field. This mechanism consists in detuning the laser frequency from the cavity resonance, such that the stored power, and hence the radiation pressure force, has a linear dependence on the cavity length [11]. A blue-shift will corresponds to an restoring force, and a red-shift to an antirestoring force.

Optical Spring

This effect occurs when the optical restoring force on the cavity mirrors is no longer negligible with respect to the mechanical force. It produces, then, a frequency shift of the mechanical resonance [27, 20, 18]. The optical spring effect has been studied in a detuned Fabry-Pérot resonator in which one mirror is flexibly mounted [137] or suspended [146]. The optical spring effect has been observed in Virgo. A Fabry-Pérot cavity of $1cm$ is created with a concave mirror equal to a Virgo end mirror (VM) and a flat mirror (called auxiliary mirror AX) [145]. This high finesse (between $4 \cdot 10^3$ and $6 \cdot 10^3$) is isolated from the seismic noise with a system equal to the Virgo superattenuator. The control on the longitudinal motion is done by acting on the VM only, like in Virgo. The optical spring is modelled as a mechanical spring of elastic constant k_{opt}, acting between the two mirrors. Evidence of the optical spring effect emerged from the observation that it was possible to lock the cavity only for positive detuning (cavity longer than the closest resonance), corresponding to a positive value of k_{opt}. A static detuning, varying from run to run, ranging between $10^{-11}m$ and $10^{-12}m$

was measured, corresponding to a stiffness constant k_{opt} varying between $7 \cdot 10^4 N/m$ and $10^4 N/m$ [145].

Optical Cooling

The optical restoring force owns the important characteristic of having a radiation pressure force proportional to the velocity of the cavity mirrors which derives from the time delay of the cavity response [156, 102]. This feature has become accessible to the recent experiments thanks to the high finesse of the optical cavities. Radiation pressure cooling has been observed with several optomechanical devices, such as cm-scale mirrors, micromirrors, toroid microcavities and micromechanical membranes [67, 47, 142, 135]. The combined effect of optical spring and optical cooling has been used to trap a gram-scale mirror by using two laser beams inject in a single cavity [44]. The technique was to apply two different frequency offsets for the laser fields to simultaneously realize a stiff optical restoring force and a viscous damping force.

Parametric Instability

When the optical rigidity is much weaker than the mechanical rigidity, the optical spring effect is negligible and the mechanical resonant frequency is only slightly shifted. However, the viscous optical force may still have a strong effect if it is of the same order of magnitude of the mechanical viscous damping. The system behaviour at the resonance is then dominated by the damping. For a blue-shifted cavity, parametric instability occurs when the optically induced negative damping compensates the mechanical damping so that the total damping effect vanishes [21, 22, 87, 161]. The parametric instability effect has been observed with micromirrors [12] and in a high power optical cavity coupled to the pendulum mode of a suspended mirror [46].

2.5 The QuRaG interferometer

Although ubiquitous, quantum effects of radiation pressure are so weak that they have not yet been observed in the quantum regime, because they are hidden by thermal noise, and especially by the mirror coating thermal noise. Nevertheless, since the quantum noise will be the main noise limit of the next generations of GW, it is crucial to develop necessary tools to study this effect. A wide spread international effort, both in theoretical and experimental fields, is active at the present time. Our experiment, named the QuRaG interferometer, is framed within this scientific background, and our aim is to realize an instrument which will be able to experimentally observe the quantum radiation pressure effect in interferometric measurements such as gravitational wave detectors.

QuRaG will be a small scale suspended interferometer that will be sensitive to the quantum radiation pressure in the kHz frequency range of GW interferometers. A table

top experiment like QuRaG will allow to test the theory and find and test methods to beat the SQL.

2.5.1 The Preliminary Design of QuRaG

The observation of quantum effects of radiation pressure on the mirror displacements requires severe conditions on the system's characteristics. All noise sources must be controlled in accurate manner in order to be in quantum radiation noise regime in the frequency range desired, i.e. the audio frequency as the ground based GW detectors. At low frequency the main limitation comes from the seismic noise, that in Virgo is properly filtered by a complex chain of mechanical filters called superattenuator, as it has already been explained in the first chapter. For the frequencies up to few hundreds of kHz the main limitation comes from the thermal noise of the suspension thermal noise and mirror thermal noise. Therefore, the design of QuRaG takes advantage of the experience of Virgo, and reproduces its geometry optimizing it in order to be in regime dominated by the quantum radiation pressure effect. QuRaG will then be a suspended Michelson interferometer in which mechanical filters will attenuate the seismic noise in the low frequencies. The core of the experiment will be a monolithic interferometer made with fused silica, a low intrinsic losses material that is largely used in GW detectors to reduce the thermal noise both of the suspensions and of the mirrors. For this reason

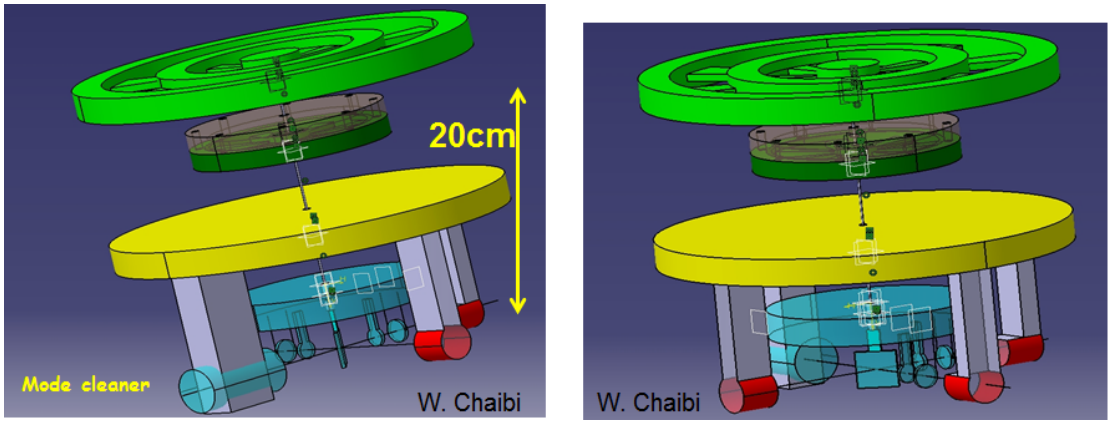

Figure 2.10: Preliminary Design of QuRaG.

it is necessary to further monolithically suspend the end mirrors of the interferometer, those which will be sensitive to the quantum radiation pressure effect. The design of the QuRaG interferometer has been develop during my doctorate thesis and I devoted my work on the optimization of the design for the last suspension system of the end mirrors. An electrostatic control will be further applied on these mirrors. In order to be more sensitive to the radiation pressure effect the end mirrors should be very light, only $0.1g$. Since, as it is evident from the formula of eq.(2.3), the spectral noise of quantum radiation pressure is inversely proportional to the mirror mass.

2.5.2 The Quantum Radiation Pressure Noise in QuRaG

The suspended mirrors of QuRaG will be those sensitive to the effect of the radiation pressure. We want them to be suspended in such a way to have a low pendulum resonance, around $3Hz$, in order to observe the radiation pressure noise, above the resonance, in the same detection band of the ground based gravitational wave detectors, i.e. $10Hz - 10kHz$. For realizing this, the suspension system should be optimized to be dominated by the radiation pressure in this frequency range and all the other noise contributions have to be reduced as much as possible.

The suspended mirrors can be considered free test masses above their pendulum resonance, ω_p, and this approximation is currently done for Virgo [122] (see sec. 1.3.4) and it has been done for the Japanese experiment [109]. Nevertheless, in order to have a more exact behaviour of the radiation pressure noise in the range of frequency $1Hz - 1kHz$, it should be taken into account the effect of the pendulum resonance ω_p, which should be around $3Hz$.

I will now derive the power spectrum of the radiation pressure noise for a suspended mirror in a Fabry-Pérot cavity, in the whole spectrum of frequency, where ω_p is the resonance of the suspended mirror. Consider a laser of power P_0 impinging on the mirror's surface, it has a momentum P_0/c and F_γ (the radiation pressure term) is the total force that it exerts on the mirror. In the elastic collision between them, the impinging laser will exchange momentum with the mirror, and the total momentum on the suspended mirror in one Michelson interferometer arm cavity will be equal to $2 \times P_0/(2c)$. The radiation pressure term F_γ, the force exerted by the laser on the mirror surface, is then

$$F_\gamma = 2\frac{P_0/2}{c}. \tag{2.28}$$

In the equation of motion of the mirror, I should also consider the gravitational (F_g) and elastic (F_{el}) terms, so that the equation of motion of the suspended mirror, along the optical path direction, is then

$$m\ddot{x} = F_\gamma - mg\frac{x}{l} - kx, \tag{2.29}$$

where

$$F_g = mg\frac{x}{l} \tag{2.30}$$

is the gravitational force and

$$F_{el} = -kx \tag{2.31}$$

is the elastic recall force exerted by the suspension onto the mirror. Moreover, in the eq.(2.29) the double dot stands for the second time derivative, m is the mirror mass, g the Earth's standard acceleration of gravity, l the length of the suspensions and k the elastic stiffness of the suspensions.

The force applied by the laser impinging on the mirror can be rewritten as

$$F_\gamma = \sqrt{\frac{8P_0\hbar\omega_0}{c^2}}, \tag{2.32}$$

because the square of the laser force can be expressed as [109]

$$F_\gamma^2 = \big(\frac{2}{c}\big)^2 < \delta P_0^2 >= \frac{4}{c^2} 2P_0\hbar\omega_0, \tag{2.33}$$

where $\hbar\omega_0$ is the energy of a photon of the laser. Now it is convenient to write the equation of motion eq.(2.29) in the domain of frequencies ω where the $X(\omega)$ is the Fourier transform of the $x(t)$

$$-m\omega^2 X(\omega) = \sqrt{\frac{8P_0\hbar\omega_0}{c^2}} - m\omega_g^2 X(\omega) - k(\omega)X(\omega) \tag{2.34}$$

where ω_g is the resonance corresponding to the gravitational term defined as

$$\omega_g^2 = \frac{g}{l}, \tag{2.35}$$

and $k(\omega)$ is the complex elastic stiffness of the suspension defined as [133] which considers the anelasticity degree of the suspension,

$$k(\omega) = k_{el}(1 + i\phi(\omega)), \tag{2.36}$$

where $\phi(\omega)$ is the **loss angle**, the term which takes into account all dissipative processes and depends on the frequency (see sec. 3.2.2).

Therefore, the power spectrum of the mirror fluctuations due to the radiation pressure can be written as

$$< X_{RP}(\omega)^2 >= \big(\frac{F_\gamma}{m}\big)^2 \frac{1}{\big[\big(\omega_p^2 - \omega^2\big)^2 + \big(\omega_p^2\phi_p(\omega)\big)^2\big]}, \tag{2.37}$$

where ω_p is the total pendulum resonance of the mirror suspension given by the sum of two contributions, the gravitational, ω_g, and the elastic one, ω_{el},

$$\omega_p = \sqrt{\omega_g^2 + \omega_{el}^2}, \tag{2.38}$$

where the elastic component is defined as

$$\omega_{el}^2 = \frac{k_{el}}{m}. \tag{2.39}$$

Moreover, in the expression of eq.(2.37), I considered the dilution effect due to the presence of a real pendulum, (see sec. 3.3.1) which allows me to introduce the so called pendulum loss angle $\phi_p(\omega)$ by imposing the following equivalence

$$\omega_{el}^2\phi(\omega) = \omega_p^2\phi_p(\omega), \tag{2.40}$$

so that the dilution factor is defined as [124, 127]

$$D = \frac{\omega_{el}^2}{\omega_p^2} = \frac{\omega_{el}^2}{\omega_{el}^2 + \omega_g^2} < 1. \tag{2.41}$$

The elasticity of the suspension has the positive effect of reducing the pendulum losses of the suspension, since the dilution factor is also

$$D = \frac{\omega_{el}^2}{\omega_p^2} = \frac{\phi_p(\omega)}{\phi(\omega)} \tag{2.42}$$

so that

$$\phi_p(\omega) = D\phi(\omega) < \phi(\omega). \tag{2.43}$$

The square root of the power spectral density of the mirror displacement due to the quantum radiation pressure effect, in the frequency range of QuRaG detection band is then

$$< X_{RP}(\omega) >= \sqrt{\frac{8P_0\hbar\omega_0}{c^2m^2}}\sqrt{\frac{1}{\left[\left(\omega_p^2 - \omega^2\right)^2 + \left(\omega_p^2\phi_p(\omega)\right)^2\right]}}. \tag{2.44}$$

I now rewrite the photon energy as $\hbar\omega_0 = h\nu_0 = h\frac{c}{\lambda_L}$, where λ_L is the laser wavelength, and in our case $\lambda_L = 1064nm$, and I call $P_{las} = P_0$ the laser power. Moreover, if I also consider the fact that the Fabry-Pérot cavity with finesse $\mathcal{F}$ has a gain $G = \frac{2\mathcal{F}}{\pi}$ (see eq.(1.73)), the eq.(2.44) of the square root of the power spectral density of the radiation pressure induced fluctuations for one suspended mirror becomes

$$< X_{RP}(\omega) >= \frac{2\mathcal{F}}{\pi}\sqrt{\frac{8hP_{las}}{\lambda c}}\sqrt{\frac{1/m^2}{\left[\left(\omega_p^2 - \omega^2\right)^2 + \left(\omega_p^2\phi_p(\omega)\right)^2\right]}}. \tag{2.45}$$

In order to observe the quantum radiation pressure noise in the audio frequency range, the design of the suspension is optimized in order to have the pendulum resonance at low frequencies, around $(3-5)Hz$. I will discuss this in more detail in the chapter 4 of the thermal noise optimization, where I explain the thermal noise calculations that I have done and which allowed to constrain the design of the suspensions in particular, and to consequently adapt the rest of the interferometer according to the configuration of the mirror's suspension.

Chapter 3

Thermal Noise in a Suspended Interferometer

The evaluation of the contribution of the whole QuRaG interferometer to the thermal noise [122, 125, 73, 74, 79] is necessary to obtain the sensitivity curve of QuRaG and then to establish constraints on its design and assembling. In fact, the thermal noise of the suspensions and internal to the mirrors is likely to limit the measure of the radiation pressure noise of the interferometer, since it is known to be one of the main limitation in the sensitivity of the current GW detectors [127]. The dissipations are mainly due to thermoelastic and clamping stages [125, 127] and to the mirror coatings [127]. Therefore, in this chapter I will introduce the theory of the thermal noise related to a Virgo like suspended interferometer, since it constitutes the starting point for my analysis of the QuRaG thermal noise which allowed to constrain the design of the suspension system.

3.1 The Thermal Noise

This section introduces the history of the physical interpretation of the phenomenon of the thermal noise. From the first half of the nineteenth century it was noticed that the motion of a small body in a fluid is extremely irregular and unpredictable. In such a system the strong relation between fluctuations of physical quantities and dissipative processes such as viscosity is evident. The viscosity of the fluid has the effect of slowing down the motion of the body in the same fluid. In fact it derives, at microscopic level, from the average of the collisions between the moving body and the molecules of the fluid. This average effect comes from a large amount of microscopic agents which are almost independent, and thus it can not be constant. Therefore, there should also be a fluctuating component of the force particularly evident in the case in which the body in motion is very small and light. This effect, called Brownian motion, owns its name to Robert Brown and it consists in the disordered motion of particles of micrometric diameter suspended in a fluid. The botanist Robert Brown, during his studies on the pollen behaviour inside water solutions, observed an extremely irregular

effect in the motion of those particles. Later he observed the same effect for dust particles, thus rejecting the hypothesis that the irregular movement was due to the fact that the pollen was alive. Hence he was the first to give a physical explanation of this phenomenon [25, 26]. Nevertheless, only in 1905 Einstein described theoretically the relation between the average dissipative effect, i.e. the viscosity of the fluid, and the fluctuations from the equilibrium position of the particles, i.e. the brownian motion [56]. Later, in 1908 Langevin used a different approach which uses the Newton's second law as representative of the Brownian motion [96]. In this way he invented the $F = ma$ of stochastic physics, now called the Langevin equation. After Einstein's publication of the theoretically explanation of the brownian motion of particles, Jean Perrin made out experiments about it, which confirmed Einstein's predictions. In 1926, thanks to these works and to those on the discontinuous nature of the structure of matter, Jean Perrin awarded the Nobel Prize for Physics. Nevertheless, the fluctuation-dissipation theorem was originally formulated by Harry Nyquist in 1928 [115], and later proven by Herbert Callen and Theodore A. Welton in 1951. It was with the contribution of Callen, Greene and Welton between 1951 and 1952 [32, 31, 72] and Kubo in 1957 [92] and 1966, that the concept which links fluctuations and dissipations has been developed and generalized in the Fluctuation-Dissipation Theorem (FDT) [93].

3.1.1 The Brownian Motion

Consider, as a simple example of Brownian motion, a set of colloidal particles moving in a fluid at the thermodynamic equilibrium. The molecules which compose the fluid fluctuate around their equilibrium position as effect of the temperature. In fact, observing the motion of the particles with a suitable contrast medium, it can be noticed that each of them follows a disordered motion independently from the nature of the particle itself. This effect is due to the fact that each particle undergoes a large number of collisions by the molecules of the fluid in which it is immersed. And there is one evidence: the lighter are the particles the faster is the Brownian motion. In fact from the principle of equipartition of energy at the dynamical equilibrium $m < v^2 >= k_B T$ and therefore $< v^2 >= \frac{k_B T}{m}$, with m molecular mass of the particles, k_B the Boltzmann constant and T temperature of the fluid. This motion is in contrast with the gravitational force and makes the colloidal solutions stable. In fact, the osmotic pressure of the fluid is $P_o = \rho \frac{RT}{m}$, with ρ density of the particles in the fluid and R ideal gas constant [126]. Suppose that an external force $F(t)$ is applied. If the particles are charged, the brownian motion can be guided by an external electrical field. Anyway, this forced motion is always affected by friction or by a resistive force. Although the molecular collisions are random, a part of them produces a systematic result proportional to the velocity of the particles. Thus the random collisions of the surrounding molecules generally determine two effects: firstly they act as a stochastic driving force on the Brownian particles in order to maintain their incessant irregular motion and secondly they give rise to the viscous friction force. The former constitutes the random part of the effect, the latter the systematic one. Therefore, it follows that the viscous friction force and the random force should be related as both coming from the same origin. This internal

relation between the systematic and random parts of the microscopic forces constitutes a more general issue, which is expressed by the Fluctuation-Dissipation Theorem [93]. The power spectrum of the fluctuation of the position of an extended body immersed in a medium at thermodynamical equilibrium is then related to the dissipative viscous mechanisms of the medium or internal to the body itself (but we can also imagine other mechanisms, like electromagnetic mechanisms [96]). These ones, as effect of thermodynamical irreversible processes, dissipate energy distributing it among all the available degrees of freedom. These fluctuations can be interpreted as the response of the system to the action of a generalized random force $F(t)$, whose effect is to drift the system away from the equilibrium, which on the contrary is promoted by the viscous force, or Stokes force. What has just been said can be illustrated and summarized by considering a particle of mass m moving with velocity v at thermodynamical equilibrium at temperature T [126]. The particle is subjected to

- the viscous friction $\vec{F} = -\beta\vec{v}$ or Stokes force, where β is the coefficient of viscous friction;
- the random force $F(t)$ resulting from the collisions with the molecules of the fluid.

The equation of motion is then

$$m\frac{dv}{dt} = -\beta v + F(t), \tag{3.1}$$

which is valid for a brownian free particle in one dimension. This equation eq.(3.1) therefore constitutes the starting point of the classical theory of brownian motion and represents the simplest case of Langevin equation [96]. In statistical physics Langevin equation is a stochastic differential equation which describes the temporal evolution of a subsystem of degrees of freedom. These degrees of freedom are typically macroscopic variables which slowly vary with respect to the other microscopic variables of the system. The microscopic (fast) variables are those responsible for the stochastic nature of Langevin equation. Therefore, the original Langevin equation describes the brownian motion. The degree of freedom interesting in this case is the position of the particle of mass m. The force acting on a particle is written as the sum of a viscous force (Stokes force) and a noise term, the one related to the stochastic process $F(t)$ (see eq. (3.1)). To simplify, it is usually assumed that the random force satisfies the following two conditions:

- the process $F(t)$ is Gaussian,
- and its correlation time is infinitesimal, i.e. the autocorrelation function of $F(t)$ has the form:

$$\langle F(t_1)F(t_2)\rangle = 2\pi G_F \delta(t_1 - t_2), \tag{3.2}$$

where G_F is a constant. The assumption of Gaussianity is reasonable for a Brownian particle having mass bigger than those of the collisional molecules of the fluid. In fact,

in this case the motion of the particle is the result of a great number of consecutive collisions, which is also the condition for the validity of the Central Limit Theorem. This condition also justifies the assumption of Gaussianity, because the correlation between consecutive collisions only lasts for the time of molecular motion, which is short with respect to the time scale of the Brownian motion [93].
As proceeding with the original argument of Langevin (1908), which started from the simple case stated in eq. (3.1), the relaxation time τ is defined as

$$\tau = \frac{m}{\beta}, \tag{3.3}$$

hence the equation of motion eq.(3.1) can be rewritten as

$$\frac{dv}{dt} + \frac{v}{\tau} = A(t), \tag{3.4}$$

where $A(t) = F(t)/m$ is the instantaneous acceleration applied on the body by the molecules of the fluid. Hence $A(t)$ satisfies the same condition as $F(t)$

$$\text{isotropy and centrality} \qquad \langle A(t) \rangle = 0, \tag{3.5}$$

$$\text{uncorrelation} \qquad \langle A(t_1) A(t_2) \rangle = 2\pi \frac{G_F}{m^2} \delta(t_1 - t_2), \tag{3.6}$$

$$\text{gaussianity} \qquad \left\langle A(t)^2 \right\rangle . \tag{3.7}$$

moreover, from the centrality of the process, the variance $\langle A(t)^2 \rangle$ is sufficient to characterize the probability distribution. From these conditions it follows that the collisions are assumed to occur rapidly with respect to the dynamics of the particle characterized by the relaxation time τ. Integrating the equation (3.4) the velocity is then

$$v(t) = v_0 e^{-t/\tau} + e^{-t/\tau} \int_0^t e^{u/\tau} A(u) du, \tag{3.8}$$

hence the mean square velocity is

$$\begin{aligned} \left\langle v(t)^2 \right\rangle = v_0^2 e^{-2t/\tau} + 2 v_0 e^{-2t/\tau} \int_0^t e^{u/\tau} \left\langle A(u) \right\rangle du \\ + e^{-2t/\tau} \int_0^t \int_0^t e^{(u+w)/\tau} \left\langle A(u) A(w) \right\rangle du dw. \end{aligned} \tag{3.9}$$

From the condition of centrality of the process the second term is zero. Moreover, with a suitable change of variable and using the condition of uncorrelation, the mean square velocity can be rewritten as

$$\left\langle v(t)^2 \right\rangle = v_0^2 e^{-2t/\tau} + \frac{k_B T}{m} \left(1 - e^{-2t/\tau} \right), \tag{3.10}$$

where k_B is the Boltzmann constant [53]. This equation quantitatively describes the transition from the chaotic to the deterministic motion. The following step is to proceed

towards the spectral analysis, which allows to study the distribution of the fluctuations in faster or slower components, i.e. in function of the frequency. For this reason it is necessary to introduce the function of autocorrelation of the random variable $v(t)$

$$\Psi_v(t) = \int_{-\infty}^{+\infty} v(t')v(t+t')dt'. \tag{3.11}$$

If we later apply the Wiener-Khintchine Theorem (1926) [153, 31], which states that the autocorrelation function $\Psi_v(t)$ and the power spectrum $w_v(\omega)$ of the stationary random variable $v(t)$ constitute a Fourier transform pair,

$$\Psi_v(t) = \frac{1}{2\pi}\int_{-\infty}^{+\infty} w_v(\omega)e^{i\omega t}dt = \frac{k_BT}{m}e^{-t/\tau}\ w_v(\omega) = \int_{-\infty}^{+\infty}\Psi_v(t)e^{-i\omega t}d\omega. \tag{3.12}$$

Therefore, we obtain that the power spectrum of the variable $v(t)$ is:

$$w_v(\omega) = \frac{4k_B\frac{T}{\beta}}{1+(\omega\tau)^2}, \tag{3.13}$$

and the autocorrelation function

$$\Psi_v(t) = \frac{k_BT}{m}e^{-t/\tau}. \tag{3.14}$$

Moreover, we can calculate the mean square of the variable $v(t)$ as:

$$\left\langle v(t)^2\right\rangle = \frac{1}{2\pi}\int_0^{\infty} w_v(\omega)d\omega. \tag{3.15}$$

Notice from the eq. (3.13), that for frequencies till $\nu \simeq 1/\tau$, the power spectrum of the velocity fluctuations in the Brownian motion is flat, i.e. a white noise, and it has the form

$$w_v(\omega) = 4k_B\frac{T}{\beta} \tag{3.16}$$

and for higher frequencies the velocities are damped. Therefore the power spectrum of the fluctuation of $x(t)$, i.e. the so called thermal noise, is

$$X^2_{therm}(\omega) = w_x(\omega) = \frac{4k_BT}{\beta\omega^2}\frac{1}{1+(\omega\tau)^2}, \tag{3.17}$$

since it is related to that one of the fluctuations of $v(t)$ by the relation

$$w_v(\omega) = \left|\dot{X}^2_{therm}(\omega)\right| = \omega^2 X^2_{therm}(\omega) = \omega^2 w_x(\omega). \tag{3.18}$$

Then, observe that the power spectrum of the fluctuation related to the thermal noise linearly depends on the temperature of the system T and on the inverse of the viscous friction coefficient β. Therefore it follows that by reducing the temperature and/or acting on the viscosity, the contribution of the thermal noise decreases [53].

The generalization to the case of any more complex physical system, like a crystalline solid in which it is not possible to write the instantaneous fluctuating force $F(t)$, or in which the dissipation is not caused by viscosity, can be obtained through the Fluctuation-Dissipation Theorem [93].

3.1.2 The Fluctuation-Dissipation Theorem

The Fluctuation-Dissipation Theorem (FDT) establishes the general relationship between the response of a given system to an external disturbance and the fluctuation of the particles constituting the system itself, i.e. its thermal noise. Such response is characterized by a response function (or transfer function), or, equivalently, by an admittance or by an impedance. The internal fluctuation is described by a correlation function of the relevant physical quantity of the fluctuating system at thermal equilibrium or, similarly, by the power spectrum of the fluctuations. The Fluctuation-Dissipation Theorem can be used in two ways. Firstly, it can predict the characteristics of the fluctuation or noise internal to the system from known characteristics of the physical system, such as the admittance or impedance. Secondly, it can be used as a general formula for deriving the impedance from the analysis of the thermal fluctuations of the system [93].
Before stating the theorem, it is necessary to make some assumptions. Consider a one-dimensional system at thermodynamic equilibrium at the temperature T. Such system is also linear, i.e. it linearly responds to an external force $F(t)$ and moreover it is dissipative, i.e. it looses energy through irreversible processes. Thus its linear response, in the frequency domain, to the external force $F(\omega)$, is $X(\omega)$, the linear fluctuation of the spatial coordinate $x(t)$

$$X(\omega) = H(\omega)F(\omega) \tag{3.19}$$

where $H(\omega)$ is the transfer function of the system.
From the equation of motion it is possible to derive the velocity

$$V(\omega) = \dot{X}(\omega) = i\omega X(\omega) \tag{3.20}$$

which is also related to the impedance of the system $Z(\omega)$ through the relation

$$V(\omega) = \frac{F(\omega)}{Z(\omega)}. \tag{3.21}$$

Hence, it follows that the two quantities $H(\omega)$ and $Z(\omega)$ are related as follows

$$H(\omega) = \frac{X(\omega)}{F(\omega)} = \frac{X(\omega)}{i\omega X(\omega)Z(\omega)} = \frac{1}{i\omega Z(\omega)} \tag{3.22}$$

therefore it is sufficient to know one of the two in order to derive the thermal noise. Finally it is possible to enunciate the theorem.
The Fluctuation-Dissipation Theorem states that the power spectral density of the thermal noise due to the square fluctuations of the coordinate $x(t)$ is

$$w_X(\omega) = X^2_{therm}(\omega) = \frac{4k_BT}{\omega}\big|\Im[H(\omega)]\big| \tag{3.23}$$

and the power spectral density of the Langevin stochastic force $F(t)$ is

$$w_F(\omega) = F^2_{therm}(\omega) = 4k_BT\big|\Re[Z(\omega)]\big|. \tag{3.24}$$

This means that the energy of the fluctuations is distributed along the frequency spectrum.
Note that from the relation of eq.(3.22) it follows the equivalence

$$\Im[H(\omega)] = \frac{1}{\omega}\Re[Z(\omega)^{-1}]. \tag{3.25}$$

The equations (3.23) and (3.24), hence the Fluctuation-Dissipation Theorem, affirm that it is not necessary to explicitly know the behaviour of the system at microscopic level, but it is sufficient to know how to deduce the macroscopic model of the impedance $Z(\omega)$ or, in an equivalent manner, of the transfer function $H(\omega)$, which both contain all the dissipative effects concerned in the system.
In the expression of eq.(3.23) of the power spectrum of the fluctuations of the coordinate $x(t)$, there is a dependence on the temperature and on the dissipations analogous to that of the brownian case. Therefore, also in this case, it is possible to conclude that, by reducing the temperature and/or acting on the dissipation, it is possible to decrease the contribution of the thermal noise.

Callen and Greene in their works in 1952 [31, 72] demonstrated that the FDT can also be applied to a n-dimensional system, by just defining the vectors force $F_i(t)$ and the coordinate $X_i(t)$ and the impedance matrix $Z_{ij}(\omega)$, where the three, in the domain of frequencies, are related by the matrix product

$$F_i(\omega) = Z_{ij}(\omega)X_j(\omega) \qquad \text{where } i,j = 1,...,n. \tag{3.26}$$

3.2 The Thermal Noise of a Real Simple Pendulum

A real harmonic oscillator does not have a point like mass, but it has a structure and it vibrates according to its proper modes. A pendulum has transverse modes of vibration in the suspension wire and longitudinal modes of vibration of the suspended mass. Those modes are held up by thermal noise. It follows that the suspended mass is set in motion by these vibrations and the measure of a position target chosen on the suspended mass, will always be affected by these fluctuations.
For a real pendulum it is therefore necessary to distinguish two different kinds of motion, due to the presence of a real non-ideal wire, which is thus deformable. The equation of motion is then

$$m\ddot{x}(t) + \beta\dot{x}(t) + kx(t) = F(t) \tag{3.27}$$

in which β is the coefficient of viscous friction and the stiffness k determines the resonant frequency ν_0, depending on the kind of motion that has been considered,

$$\nu_0 = \frac{1}{2\pi}\sqrt{\frac{k}{m}}, \tag{3.28}$$

and which is a constant for such motion.

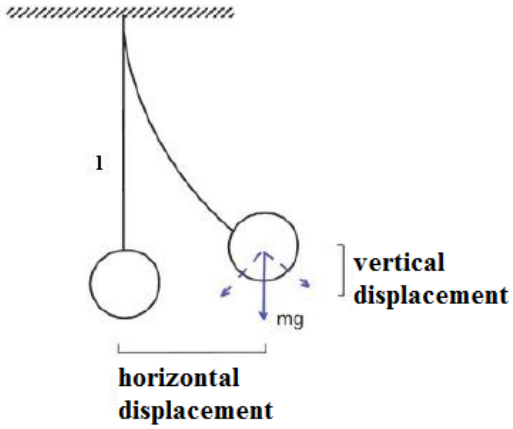

Figure 3.1: Schematic representation of the motion of a real pendulum with a bending of the wire. The weight is depicted in blue, with the two components in the directions tangent and perpendicular to the wire.

The deformability of the wire determines, in addition to the horizontal motion of the ideal pendulum, a motion in the vertical direction. See fig. 3.1.

1. The motion in the horizontal direction is due to the weight of the mass itself m. And the resonant frequency ν_0 (see eq. (3.28)) of the harmonic motion depends on the pendulum constant k_g

$$k_g = \frac{mg}{l} \tag{3.29}$$

   where g is the gravitational acceleration and l is the length of the wire.

2. The motion in the vertical direction is determined by the elastic force exerted with the bending of the wire on its bending point. The resonant frequency of the harmonic vertical motion depends on the elasticity of the bending point of the wire

$$k_e = n_w n_{fp} \frac{\sqrt{\Lambda Y J}}{2l^2} \tag{3.30}$$

   in which Y is the Young's modulus, characteristic of the material constituting the wire, $\Lambda = mg$ is the tension exerted on the wire, J is the moment of inertia of the section of the wire and n_w and n_{fp} are the number of wires and the number of flexural points (in this case are both equal to 1).

J is defined as the integral, over the section of the wire A, of the square of the distance y between the infinitesimal section dA of the wire and the axis with respect to which the moment of inertia is calculated

$$J = \int y^2 dA. \tag{3.31}$$

In this case the axis is that one of the wire, which is considered as a cylinder of radius r and length l. Then the momentum of inertia J with respect to its axis is

$$J = \frac{1}{4}\pi r^4 = \frac{1}{4\pi}A^2. \tag{3.32}$$

Notice that the second kind of motion is different from that one purely vertical. The purely vertical does not depend on the elasticity related to the bending point, but to the elasticity of the wire, which behaves as a 'spring' with stiffness $k = YA/l$, where A is the section of the wire.
Moreover, notice that the ratio

$$\frac{k_e}{k_g} \propto \frac{A}{l\sqrt{m}}, \tag{3.33}$$

depends on the ratio of the section over the wire length multiplied by the square root of the suspended mass. Therefore, the elastic component will dominate if the wire section is not thin enough with respect to the wire length and the suspended mass.
It is important to underline that the constant k_g is not associated to the dissipations, on the contrary the stiffness k_e, which depends on the properties of the material, contains the dissipative contribution. Indeed, the internal dissipations are mainly due to the imperfections in the structure of the crystal lattice of a solid body. Dissipations propagate inside the body and occur as a delay in the response to the external force $F(t)$. This effect is called anelasticity.

Q factor

The measure of a harmonic oscillator's resistance to disturbances to its oscillation period is a dimensionless parameter called the Q factor. The Q is proportional to the resonant frequency multiplied by the time τ_0 that the amplitude of the oscillation $A(t) = A_0 e^{-\frac{t}{\tau}}$ implies to be attenuated of a factor $1/e$ [60, 127]. For a given resonance ω_0, the associated Q mechanical quality factor is then

$$Q_0 = \frac{\omega_0 \tau_0}{2}. \tag{3.34}$$

Note that the Q is related to how long it takes for the oscillations of an oscillator to die out. Particularly, a high Q corresponds to a long relaxation time τ_0.

3.2.1 Viscous Dissipations

In this treatise on the different types of dissipation, the first kind to be discussed is the viscous dissipation.
Consider, as simple example, the thermal motion of an ideal harmonic oscillator [126]. Hence, consider a mass m attached to the end of a spring, as represented in figure 3.2. The equation of motion is

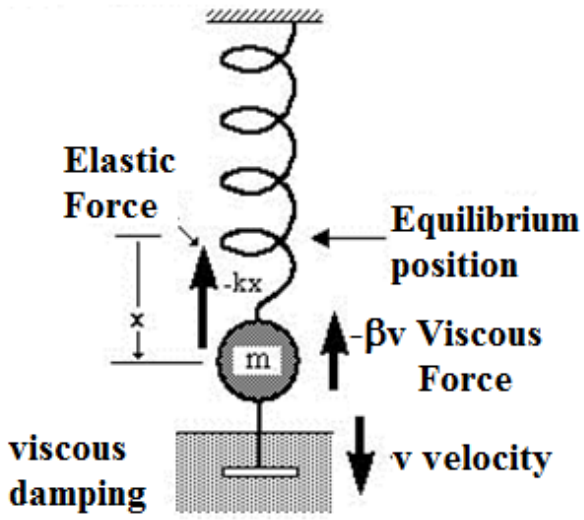

Figure 3.2: Scheme of an harmonic oscillator subject to viscous damping.

$$m\ddot{x}(t) + \beta\dot{x}(t) + kx(t) = F(t). \tag{3.35}$$

In the frequency domain it becomes then

$$-\omega^2 mX(\omega) + i\omega\beta X(\omega) + kX(\omega) = F(\omega). \tag{3.36}$$

The transfer function is therefore

$$H(\omega) = \frac{X(\omega)}{F(\omega)} = \frac{1}{m\left((\omega_0^2 - \omega^2) + \omega\frac{\beta}{m}\right)}, \tag{3.37}$$

where ω_0 is the resonance defined as

$$\omega_0 = \sqrt{\frac{k}{m}}. \tag{3.38}$$

It is then important to introduce the mechanical quality factor due to viscosity Q_v which is related to the resonance ω_0 through the relation

$$Q_v = Q(\omega_0) = \frac{\omega_0^2 m}{\beta\omega_0} = \frac{\omega_0 m}{\beta}. \tag{3.39}$$

Then replacing $\beta/m = \omega_0/Q_v$ in the eq. 3.37, the transfer function $H(\omega)$ becomes

$$H(\omega) = \frac{X(\omega)}{F(\omega)} = \frac{1}{m\left((\omega_0^2 - \omega^2) + \frac{\omega\omega_0}{Q_v}\right)}. \tag{3.40}$$

Once the transfer function is known, it is possible to apply the Fluctuation-Dissipation Theorem [93]. Therefore, the power spectrum of the thermal noise in presence of viscous

dissipations has the form

$$X^2_{therm}(\omega) = \frac{4k_BT}{m}\frac{\omega_0}{Q_v}\frac{1}{\left((\omega_0^2-\omega^2)^2+\left(\frac{\omega\omega_0}{Q_v}\right)^2\right)}. \tag{3.41}$$

Analysing now the behaviour of the power spectrum $X^2_{therm}(\omega)$ with respect to the frequency, it is possible to distinguish the three limiting cases shown in figure 3.3:

1. $X^2_{therm}(\omega) \propto \beta T = const$ below the resonance, i.e. for $\omega \ll \omega_0$;
2. $X^2_{therm}(\omega) \propto \frac{T}{\beta}$ in the vicinity of the resonance, i.e. for $\omega = \omega_0$;
3. $X^2_{therm}(\omega) \propto \frac{\beta T}{\omega^4}$ above the resonance, i.e. for $\omega \gg \omega_0$.

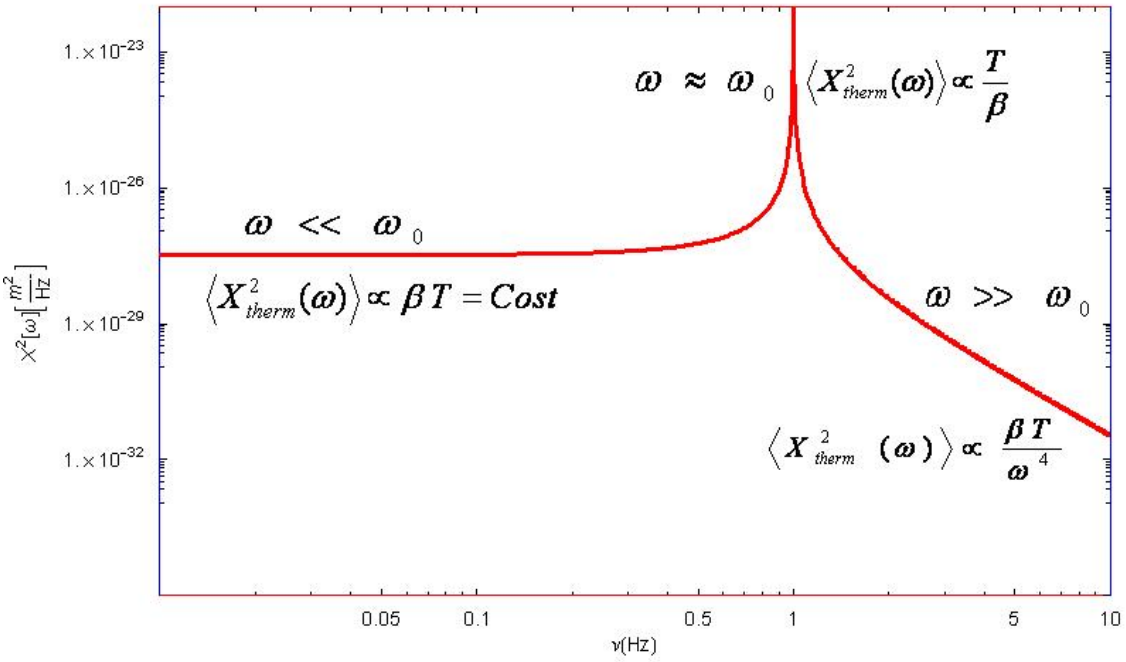

Figure 3.3: Power spectrum of the fluctuations of the spatial coordinate X in function of the frequency in the presence of viscous dissipations. Notice that the order of magnitude of the power spectrum of the fluctuations of X at the resonance and outside the resonance depends on the viscous coefficient β and the temperature T of the system. Moreover, below the resonance it is constant, while above the resonance it goes as $\frac{\beta T}{\omega^4}$.

The energy of the fluctuations is concentrated around the resonance, where the power spectrum of the thermal noise is inversely proportional to β, i.e. the viscous dissipations. On the contrary, far from the resonance, the power spectrum of the thermal noise is directly proportional to the coefficient of viscous friction β.
It follows that, in order to make the contributions outside the resonance negligible, and therefore the thermal noise, it is necessary to reduce dissipation and thus have a small value for β.

3.2.2 Internal Dissipations

As already said, a real pendulum has a wire with a proper structure and deformability and it is not just a point like mass. Therefore, a real wire, which is characterized by its proper internal dissipation, affects the thermal noise of the suspensions. This effect of the internal dissipation of an harmonic oscillator is described by a phenomenological model of anelasticity [24, 73, 40]. The pendulum can be seen as a system composed by an ideal spring, with stiffness k_{el}, placed in parallel with the series formed by a spring of stiffness Δk_{el}, and a piston, which quantifies the damping at constant speed, with coefficient C. Such kind of system is depicted in figure 3.4.

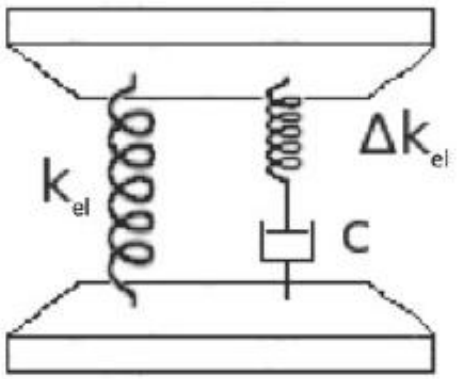

Figure 3.4: Graphic representation of the mechanical model of anelasticity: a real spring is in parallel with the series formed by a spring and a piston, the latter responsible of the dissipations.

This model, called Maxwell unity, or Debye solid, allows to calculate the effective stiffness k_{eff}, which depends on the frequency, by considering the system as an electric circuit and thus applying the rules for the components in series and parallel

$$k_{eff}(\omega) \approx k_{el}\left(1 + i\frac{\Delta k_{el}}{k_{el}}\frac{\omega\tau}{1+\omega^2\tau^2}\right) \tag{3.42}$$

where it has been introduced the time of response of the system $\tau = C/\Delta k_{el}$.
The expression of k_{eff} in eq. (3.42) can be rewritten in the compact form

$$k_{eff}(\omega) \approx k_{el}(1 + i\Phi(\omega)), \tag{3.43}$$

which is like adding to the stiffness k_{el} of an ideal suspension wire, an imaginary dissipative term $\Phi(\omega)$, called **loss angle**

$$k(\omega) = k(1 + i\Phi(\omega)). \tag{3.44}$$

It is important to underline that the resonant frequency of eq. (3.28), is a constant and does not change in presence of dissipation. Note also that, in this model for the internal dissipation, the dissipative term $ik_{el}\Phi(\omega)$ is added in the equation of motion in

the domain of the frequency and not in the expression of the resonant frequency. The loss angle $\Phi(\omega)$ represents the anelasticity degree of the wire in the pendulum. It can also be seen as the phase shift of the system's response to the external stress

$$k(\omega) = k_{real} + ik_{im}(\omega) = |k|e^{i\Phi(\omega)}. \tag{3.45}$$

Moreover, the addition of the imaginary dissipative term takes into account the effect of memory, typical of anelastic deformations [126]. In this case, in the equation of motion it appears a term called term of memory $F_M(t)$

$$F_M(t) = \int_{-\infty}^{t} k(t-s)x(s)ds. \tag{3.46}$$

The equation of motion then is

$$F(t) = m\ddot{x} + \int_{-\infty}^{t} k(t-s)x(s)ds, \tag{3.47}$$

where for simplicity the contribution of the viscous dissipation (as $\beta\dot{x}$) has been neglected. In the frequency domain the equation of motion becomes then

$$-\omega^2 mX(\omega) + k(\omega)X(\omega) = F(\omega), \tag{3.48}$$

and by expliciting the contribution of the internal dissipation of eq. (3.44), it becomes

$$[k - m\omega^2 + ik\Phi(\omega)]X(\omega) = F(\omega). \tag{3.49}$$

Therefore, the transfer function is

$$H(\omega) = \frac{X(\omega)}{F(\omega)} = \frac{1}{[k - m\omega^2 + ik\Phi(\omega)]} \tag{3.50}$$

and the power spectrum of the thermal noise is straightforwardly obtained by applying the Fluctuation-Dissipation Theorem [93]

$$X^2_{therm}(\omega) = \frac{4k_BT}{m\omega} \frac{\omega_0^2\Phi(\omega)}{\left((\omega_0^2 - \omega^2)^2 + \left(\omega_0^2\Phi(\omega)\right)^2\right)}. \tag{3.51}$$

The loss angle is usually very small, $\Phi(\omega) \ll 1$. We want now to observe the behaviour of the power spectrum of the thermal noise below, in the vicinity and above the resonance, in the case of internal losses and in we want to compare it with the case of pure viscous losses. Therefore, for the sake of simplicity we can consider $\Phi(\omega) \approx \Phi_0$. Therefore, the thermal noise $X^2_{therm}(\omega)$, when the internal dissipation dominates, in the three limiting cases seen before, has the behaviour described in fig. 3.5:

- $X^2_{therm}(\omega) \propto \frac{T\Phi_0}{\omega}$ below the resonance $\omega \ll \omega_0$;

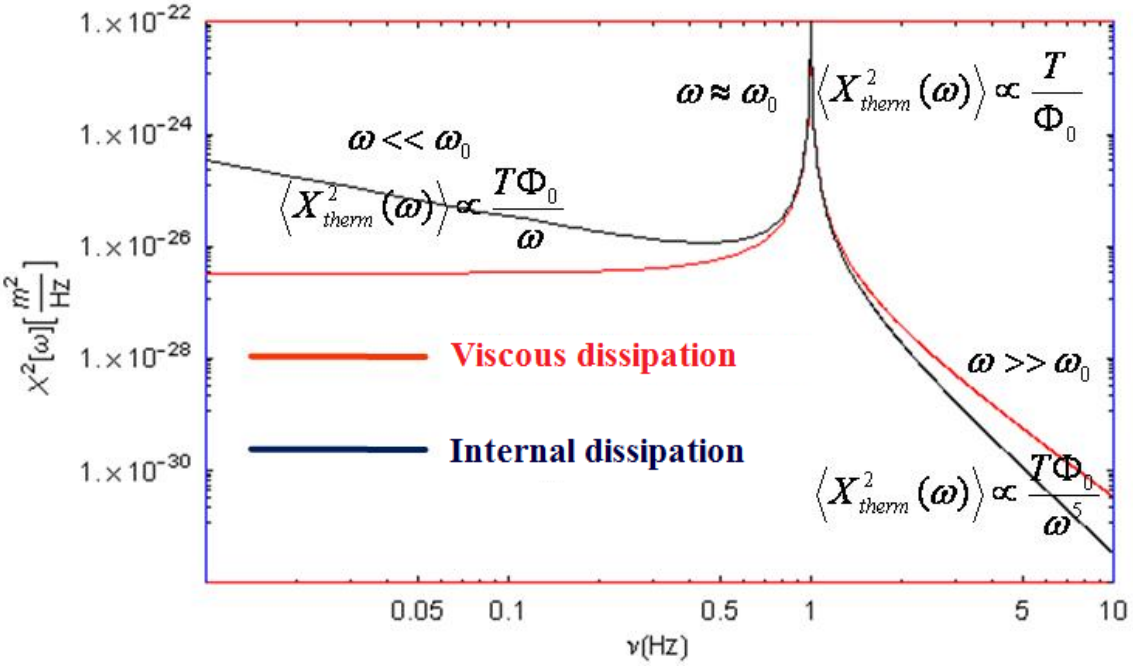

Figure 3.5: Power spectrum of the thermal noise in presence of internal dissipations (black curve) compared to the power spectrum in presence of only viscous dissipations (red curve).

- $X^2_{therm}(\omega) \propto \frac{T}{\Phi_0}$ in the vicinity of the resonance $\omega = \omega_0$;
- $X^2_{therm}(\omega) \propto \frac{T\Phi_0}{\omega^5}$ above the resonance $\omega \gg \omega_0$.

Compare now this case with the previous one, with the power spectrum of the thermal noise dominated only by viscous dissipations. The spectrum in the case dominated by internal dissipations has no more a flat trend under the resonance, but it grows like ω^{-1} as the frequency decreases, while above the resonance, as ω increases, it decreases more steeply, like ω^{-5}. Despite of a different behaviour in function of the frequency, however, it is evident an analogy in the dependence on dissipation. In fact, like for the viscous ones, also for the case of internal dissipation as the losses (the loss angle for internal and the viscous coefficient in the case of dominant viscous dissipation) decrease, the power spectrum of the thermal noise increases in the vicinity of the resonance and decreases outside the resonance.

So, the smaller the loss angle, the lower is the thermal noise contribution outside the resonance.

Therefore, in order to have the energy of the fluctuations concentrated around the resonance and negligible outside, thus to make the contributions of the internal dissipation negligible, it is necessary to have very small loss angles $\Phi_0 \ll 1$.

3.2.3 Thermoelastic Dissipations

Among the internal processes of dissipation, it is possible to find the thermoelastic dissipation. This kind of internal dissipation occurs in an elastic body in which the local variation of the state of deformation gives rise to the production of heat. In fact, in materials with thermal expansion coefficient $\alpha \neq 0$, the temperature is coupled to the local deformation.
If $\alpha > 0$:

- a volumetric expansion locally decreases the temperature,
- while a contraction causes an increasing of the temperature.

Consider the example of a metallic wire dynamically bended. For each bending, around the deformation one side is heated, while the other cools down, thus creating a temperature gradient. In order to restore the thermodynamic equilibrium, heat flows along the gradient, thus causing the dissipation that is sustained by the dynamic equilibrium of the system. Therefore, the elastic energy is dissipated owing to this irreversible heat flux in time-varying inhomogeneous deformations. The reaching of the equilibrium requires a characteristic time that has accurately been calculated by Zener [159, 160]. He started from the equation of the heat diffusion, which links the temperature T to the divergence of the strain ϵ:

$$\frac{\partial T}{\partial t} = \frac{k}{C}\nabla^2 T - \frac{Y\alpha T_0}{C(1-2\sigma)}\frac{\partial(\nabla\cdot\vec{\epsilon})}{\partial t} \tag{3.52}$$

where Y is the Young's modulus of the material, $\alpha = \frac{1}{L}\frac{\partial L}{\partial T}$ is the coefficient of linear thermal expansion, C is the specific heat, σ is the Poisson's ratio, and k is thermal diffusion coefficient [74, 126].

Solving this equation, Zener showed that this mechanism is well described by the Standard Anelastic Model [24] as a single relaxation process with a single peak. Hence, in this anelastic model, the corresponding loss angle has a frequency dependance:

$$\Phi_{te}(\omega) = \Delta\frac{\omega\tau}{1+\omega^2\tau^2}, \tag{3.53}$$

where τ represents the characteristic time of the heat diffusion inside the material. In the case of a wire with circular section, the parameters Δ and τ have the form [74, 126]:

$$\Delta = \frac{Y\alpha^2 T}{\rho C}, \tag{3.54}$$

$$\tau = \frac{C\rho(2r_w)^2}{2\pi k 2.16}, \tag{3.55}$$

where ρ is the volumetric density and r_w is the radius of the wire.
The curve of the thermoelastic loss of fig.3.6, i.e. the loss angle for thermoelastic

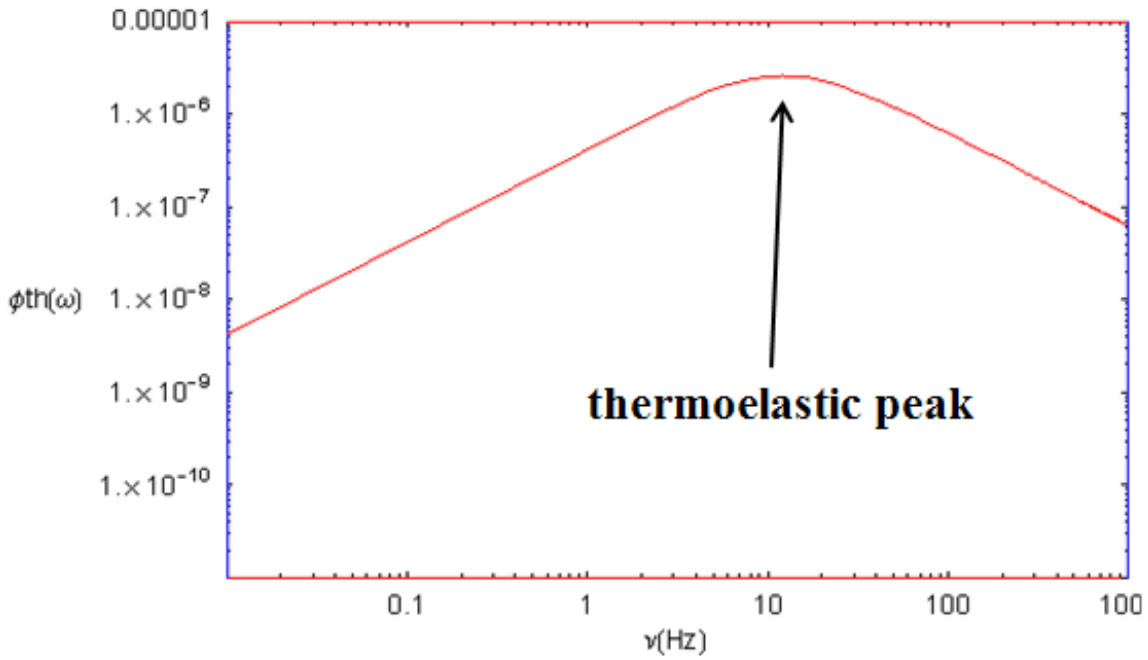

Figure 3.6: Thermoelastic loss curve. The thermoelastic loss angle as varying the frequency. Notice the maximum called thermoelastic peak.

dissipations in function of the frequency, shows a maximum called thermoelastic peak or Debye's peak, characteristic of the material. In fact, it is easily verified that the angular frequency of the peak is equal to the inverse of the time of heat diffusion τ and the maximum of the losses is equal to $\Delta/2$. Therefore, it follows that if we want to reduce the contribution of the thermoelastic losses it is reasonable to choose a material whose thermoelastic peak occurs outside the detection band. Both for ground based GW detector and QuRaG the detection band is the auto frequency band. Hence, the suitable material for QuRaG's suspensions already seems to be the same as for GW detectors: the fused silica. But this needed to be confirmed by more detailed analysis, as it is explained in the following chapter.
Then, given the expression of $\Phi_{te}(\omega)$ (3.53), it is possible to conclude that, in order to reduce the thermoelastic losses outside the peak, is necessary to choose a material with:

- small coefficient of linear thermal expansion α,
- a high specific heat C,
- a small Young's modulus Y.

For the third generation of GW detectors the material should have these characteristics also at cryogenic temperatures, because these interferometers will be cooled down to about $4K$, to further reduce the thermal noise contribution.
Note that for a ribbon suspension the characteristic time of the heat diffusion inside

the material has the form [74]

$$\tau = \frac{C\rho(t)^2}{\pi^2 k}, \tag{3.56}$$

where t is the thickness of the ribbon, which corresponds to the side of the ribbon section corresponding to the direction in which the temperature gradient is created by the bending of the ribbon.

3.2.4 Surface Losses

The imperfections and impurities in the crystal lattice are more frequently on the surface of a body. This depends on the fact that the surface is the region mostly exposed to the action of chemical agents or mechanical contacts. In particular, in a mirror, the surface is a zone full of defaults, cracks and impurities due to the polishing process. Therefore, it is assumed that the higher dissipation will mainly be in the zones of surface and contact. The mechanism of surface dissipation appears when, during the oscillations, mechanical friction occurs on the contact area between the two materials. This dissipation process is not only localized on the surface, but it can reach a more internal area, within the so called dissipation depth d_s, which I will define later. In Virgo+ it has been demonstrated [40] that these dissipations concern in particular the anchoring system of the test masses to the suspensions, where the contact tension is concentrated.

Suppose that the surface and structural dissipations dominate, the total loss angle is then [74]

$$\Phi_{tot} = \frac{\Delta E_{str} + \Delta E_{surf}}{E_{tot}} \tag{3.57}$$

where:

- ΔE_{str} is the energy lost in the volume of the wire for each oscillation cycle,
- ΔE_{surf} is the energy lost for each cycle in the surface dissipative layer,
- E_{tot} is the total energy of the oscillating wire.

It is reasonable to assume that

- $\Delta E_{surf} \propto S$, S contact surface or the area where the dissipation occurs
- $\Delta E_{str} \propto V$, V volume of the wire

then it is possible to write the ratio

$$\frac{\Delta E_{surf}}{\Delta E_{str}} = \frac{\mu d_s}{V/S} \tag{3.58}$$

where μ is a geometrical factor, and d_s is the dissipation depth. The latter is defined as

$$d_s = \frac{1}{\Phi_{str}} \int_0^h \Phi(\tau) d\tau \tag{3.59}$$

where τ is the depth starting from the surface and $\Phi_{str} = \Delta E_{str}/E_{tot}$ is the structural loss angle of the internal volume of the material. Suppose now that the dissipative layer on the surface has thickness h, and that the surface losses $\Phi(\tau)$ do not depend on the depth, we obtain that

$$d_s = h \frac{\Phi_{surf}}{\Phi_{str}}. \tag{3.60}$$

The total dissipation of the system can be rewritten then as

$$\Phi = \Phi_{str} \left(1 + \mu \frac{hS}{V} \frac{\Phi_{surf}}{\Phi_{str}} \right). \tag{3.61}$$

It follows that, for a fiber, the surface dissipations are described by the term

$$\Phi_e = \frac{\Delta E_{surf}}{E_{tot}} = \mu \frac{hS}{V} \Phi_{surf}. \tag{3.62}$$

From the eq. (3.62) we can conclude that by reducing the surface over volume ratio S/V of the suspension wire, it is possible to decrease the surface losses Φ_e. The geometrical factor μ, introduced in eq.(3.58), for a given fiber is defined as [74]

$$\mu = \frac{\int_{\mathcal{S}} \epsilon^2(\vec{r}) d^2 r}{\int_{\mathcal{V}} \epsilon^3(\vec{r}) d^3 r}. \tag{3.63}$$

where r denotes a point in the sample, $\epsilon(\vec{r})$ is the strain amplitude, V and S are the volume and outer surface of the sample, and $\mathcal{V}$ and $\mathcal{S}$ are the set of points comprising the volume and outer surface respectively. For transverse oscillations of a cylindrical fiber and of a ribbon and, the geometrical factor becomes:

$$\mu = 2 \qquad \text{for a cylindrical fiber,} \tag{3.64}$$

$$\mu = \frac{3+a}{1+a} \qquad \text{for a ribbon,} \tag{3.65}$$

where $a = t/w$ is the aspect ratio of the ribbon equal to the ratio of the thickness t in the bending direction (which is also the direction of the temperature gradient) over the width w of the ribbon [73, 74].

3.2.5 The Mechanical Quality Factor Q

Once the loss angle of each dissipative phenomenon is known, it is possible to obtain the associated impedance, or equivalently, the transfer function. Then, by applying the FDT, it is possible to calculate the power spectrum of the associated thermal noise,

and thus it is possible to estimate the contribution of each effect on the thermal noise. The dissipations, as already said, are also estimated through the mechanical **quality factor** of the system Q, which comes from the combination of two main effects:

$$\text{viscous dissipations} \qquad Q_{visc} = \frac{m\omega_0}{\beta}; \tag{3.66}$$

$$\text{structural dissipations} \qquad Q_{str} = \frac{1}{\Phi_{str}}. \tag{3.67}$$

The total mechanical quality factor Q is obtained from the equivalent loss angle [126]:

$$\Phi(\omega) = \frac{\omega}{\omega_0}\frac{1}{Q_{visc}} + \Phi_{str} = \frac{\omega}{\omega_0}\frac{1}{Q}. \tag{3.68}$$

Systems with high values for Q, therefore with low Φ, have the advantage of concentrating the main part of the fluctuation energy around the resonance. Note that since the Qs are inversely proportional to the Φs, they sum as the resistances in a parallel electric circuit. And the total Q is then given by the reciprocal of the sum of the reciprocals of the Qs.

3.3 The Suspension Thermal Noise

The pendulum thermal noise of the suspension can be distinguished in three kinds:

1. the thermal noise of the pendulum (horizontal modes of oscillation);
2. the thermal noise of the vertical modes of oscillation;
3. the thermal noise of the violin modes.

3.3.1 Pendulum Modes of Oscillation

If the systems operates in conditions of ultra high vacuum (UHV), like in Virgo, it is possible to consider the viscous damping due to the residual gas negligible with respect to the internal dissipations of the pendulum. In the Virgo vacuum chamber a UHV of $10^{-10}mbar$ ($10^{-8}Pa$) is reached [9]. In this case the internal dissipative forces are only due to the bending of the suspension wire. Moreover, it is very important having optical surfaces with a high degree of polishing and annealing, since the imperfections present on the surface are likely to undergo degassing process when the vacuum is activate. The degree of polishing and the annealing depends on the vacuum level needed.
To treat this argument, where the viscous damping contribution has been neglected, it is more convenient to describe the dissipation processes through the recall momentum of the suspension wire, which is the integral in the momentum equation:

$$mL\ddot{x} + mgx + \int_{-\infty}^{t} \tau(t-s)\frac{x(s)}{l}ds = lF_{ext}, \tag{3.69}$$

where l is the length of the wire, $\tau = k_e l^2$ is the torque and k_e is the stiffness.
Indeed, in the frequency domain, this term corresponds to the complex loss angle, which allows to introduce the loss angle for internal dissipations $\Phi_s(\omega)$

$$k(\omega) = k_e(1 + i\Phi_s(\omega)). \tag{3.70}$$

In this case the pendulum resonance effectively measured is not only that one given by the simple pendulum, i.e. the gravitational component $\omega_g = \sqrt{g/L}$, but it has an elastic component ω_e proportional to the stiffness k_e

$$\omega_p^2 = \left(\frac{g}{L} + \frac{k_e}{m}\right) = \omega_g^2 + \omega_e^2. \tag{3.71}$$

However, for a suspension in which the elastic restoring force is much lower than the gravitational restoring force $F_{el} \ll F_g$, the elastic contribution is almost negligible $\omega_e \ll \omega_g$. The stiffness depends on the characteristics of the fiber, the length l, the Young's modulus Y, the momentum of inertia of the section J

$$k_e = n_{fp} n_w \frac{\sqrt{\Lambda Y J}}{2l^2} \tag{3.72}$$

and on the suspended mass m, since the tension of the fiber Λ is $\Lambda = mg/n_w$, with n_w number of suspension wires and n_{fp} number of flexural points [54, 127]. Therefore, it is possible to make the elastic contribution negligible by choosing the suitable material, the suitable wire shape (length and section) and suspended mass, as in the case of Virgo [127]. Now we want to make an estimation of the elastic contribution on QuRaG's suspensions. Suppose for QuRaG the same material as for the suspensions of Virgo, hence with Young's modulus $Y_s = 72.8GPa$, and being two cylindrical wires with a radius of $20\mu m$ and length of $2cm$ and having a suspend mass of $\simeq 0.08g$, we obtain that the elastic contribution is about $\omega_e^2 = 59Hz^2$ smaller, but not negligible with respect to the gravitational contribution which is $\omega_g^2 = 490Hz^2$. Therefore, in the thermal noise estimation we should also take into account the elastic contribution.

Then, knowing the dissipations, it is possible to apply the FDT and thus to obtain the power spectrum of the pendulum thermal noise

$$X_{pend}^2(\omega) = \frac{4k_bT}{m\omega} \frac{\omega_e^2 \Phi_s(\omega)}{\left((\omega_p^2 - \omega^2)^2 + \left(\omega_e^2 \Phi_s(\omega)\right)^2\right)}. \tag{3.73}$$

It is preferable to express the thermal noise $X_{therm}^2(\omega)$ in terms of the measured quantities such as the pendulum resonance ω_p and the pendulum total loss angle Φ_p, which is defined as

$$\Phi_p(\omega) = \frac{\omega_e^2}{\omega_p^2} \Phi_s(\omega). \tag{3.74}$$

Then, the power spectrum of the pendulum thermal noise becomes

$$X^2_{pend}(\omega) = \frac{4k_BT}{m\omega} \frac{\omega_p^2 \Phi_p(\omega)}{\left((\omega_p^2 - \omega^2)^2 + \left(\omega_p^2 \Phi_p(\omega)\right)^2\right)}. \tag{3.75}$$

The mechanical quality factor Q has already been introduced to estimate the dissipations of the system. In the case of the pendulum Q is

$$Q_p = \frac{1}{\Phi_p(\omega)} = D\frac{1}{\Phi_s(\omega)} \tag{3.76}$$

where D is called dilution factor [126] and it is defined as

$$D \equiv \frac{\omega_p^2}{\omega_e^2}. \tag{3.77}$$

Therefore, recalling that $\omega_p^2 = \omega_g^2 + \omega_e^2$, if the elastic contribution is small compared to the gravitational one, as in the case of Virgo, $\omega_e \ll \omega_g$, then the dilution factor is a pure number much greater than 1

$$D = 1 + \frac{\omega_g^2}{\omega_e^2} \approx \frac{\omega_g^2}{\omega_e^2} \gg 1 \tag{3.78}$$

and then it increases the Q (or reduces the Φ), thus reducing the pendulum losses. Therefore, it is possible to state that, given the same structural loss angle, the pendulum has the lowest losses, lower of a factor D^{-1} with respect to those only given by the structural losses of the material. Anyway, even if the suspension has an important elastic contribution but still lower than the gravitational one, as for QuRaG, the dilution factor is still a pure number greater than one that allows to increase the pendulum Q.

3.3.2 Vertical Modes of Oscillation

As already largely discussed, for a real pendulum, such as the suspension system of the mirror of a GW detector like Virgo, it also exists a vertical component of the motion. These modes have resonances defined by the expression

$$\omega^2_{vert} = \frac{4\pi r^2 Y}{ml} \tag{3.79}$$

where m is the suspended mass, l, r and Y are respectively the length, the radius and the Young's modulus of the suspension wire. Usually their contribution to the total thermal noise of the suspensions is negligible.

3.3.3 Violin Modes of Oscillation

Suspension wires, if subject to tension, behave like vibrating strings and in the spectrum of the thermal noise of the suspension several resonances appear. The ideal string fixed in both ends has harmonics of ascending order according to the relation

$$\omega_n = n\omega_1. \tag{3.80}$$

This means that the frequency associated to the n-th harmonic is equal to n-times the frequency of the fundamental harmonic.
In the case of a real pendulum with elasticity, the relation among the harmonics is more complex. In fact, in this case the wires can not be considered as inextensible and one-dimensional. Moreover, their ends are not fixed but fluctuate. The frequency of the harmonics have been calculated by Saulson and Gonzalez and are related [69] as follows

$$\omega_n(\omega) = \frac{n\pi}{l}\sqrt{\frac{\Lambda}{\pi r^2\rho}}\left[1 + \frac{2}{lk_v(\omega)} + \frac{1}{2}\left(\frac{n\pi}{k_v(\omega)l}\right)^2\right] \tag{3.81}$$

in which l, r, ρ and Λ are respectively the length, the radius of the section, the density and the tension of the suspension wire. $k_v(\omega)$ is the wave number related to the flexural rigidity of the fiber [69] given by the expression

$$k_v(\omega) = \sqrt{\frac{\Lambda + \sqrt{\Lambda^2 + 4YJ\rho\pi r^2\omega^2}}{2YJ}} \tag{3.82}$$

where Y is the Young's modulus of the fiber and J is the moment of inertia of the section of the wire with respect to its axis. Φ_n, the loss angle related to the n-th harmonic, corresponds to the reciprocal of the mechanical quality factor of the same harmonic and is given by the relation [69]

$$\Phi_n(\omega) = \Phi(\omega)\frac{2}{lk_v}\left(1 + \frac{(n\pi)^2}{2k_v(\omega)l}\right) \tag{3.83}$$

where $\Phi(\omega)$ is the total loss angle which for the violin modes is given by the sum of the structural ϕ_s, thermoelastic $\phi_{te}(\omega)$ and surface losses Φ_e.

$$\Phi(\omega) = \phi_s + \phi_{te}(\omega) + \Phi_e. \tag{3.84}$$

The power spectrum of the thermal noise has peaks in correspondence of the resonances of the wire, as for the pendulum mode. Therefore, it is reasonable to consider the losses condensed around the resonances, and then to approximate the thermal noise associated to the violin modes of a wire, as the sum of the contributions of each single harmonic [133, 69]

$$\langle\tilde{X}_{viol}(\omega)\rangle^2 = 4\frac{4k_BT}{\omega}\frac{2\rho r^2}{\pi m^2}l\sum_n \frac{1}{n}\frac{\omega_n^2\Phi_n}{(\omega_n^2 - \omega^2)^2 + (\omega_n^2\Phi_n)^2} \tag{3.85}$$

where $\Phi(\omega_n)$ represents the value of the total loss angle in correspondence of the n-th harmonic.

3.4 Mirror Thermal Noise

In the frequency range between 30 Hz and 300 Hz, the thermal noise of the mirrors is likely to dominate, such as for the case of Virgo. The main internal mechanisms of dissipation in the mirrors are:

- structural dissipations Φ_{str},
- surface dissipations Φ_e,
- thermoelastic dissipations $\Phi_{te}(\omega)$.

The physical explanation of these three dissipation mechanisms has already been done for the case of the suspension wires, and it can straightforwardly be applied on the case of the mirrors. It is evident that the surface losses will be less important for the mirrors since they have a lower surface to volume ratio, while the thermoelastic losses can be neglected. In fact, if there is not a larger dimension with respect to the others, as on the contrary it is for a thin wire, there is no evidence of the bending causing the temperature gradient between the compressed and relaxed areas.
Two main approaches are used to model such noise: the Modal Approach and the Levin Approach. The former considers the complex solid system as a sum of harmonic oscillators, each one with its proper resonance, loss angle, and equivalent mass. The latter is preferred to be applied when the mechanical losses are not homogeneously distributed on the system, since in this case the direct application of the FDT is more complicated. This can be the case of real mirrors where the mechanical loss is know to be inhomogeneous.

3.4.1 The Modal Approach

For estimating the thermal noise of the mirrors, which are suspended test masses, each internal mode of the solid body can be considered as a one-dimension harmonic oscillator so that the effective spectral density of the mirror displacement can be expressed as the sum of all the mechanical resonances of the mirror. The total thermal noise will be the sum of all these modes. Nevertheless, it is possible to calculate the thermal noise, with great improvement in the computation time, by considering only those modes which affect more the mirror position, and which are coupled with the mirror displacement along the optical axis (the optical modes of the interferometer) [68]. Then, the thermal noise will be the sum of the contribution of the modes which influence more the mirror position along the optical axis. Therefore, the total thermal noise will have the following form

$$X^2_{modal}(\omega) = \frac{4k_BT}{\omega}\sum_{i=1}^{n}\left|\Re[Z_n(\omega)^{-1}]\right| = \frac{4k_BT}{\omega}\sum_{i=1}^{n}\frac{1}{M_i}\frac{\omega_i^2\phi_i(\omega)}{((\omega_i^2-\omega^2)^2+(\omega_i^2\phi_i(\omega))^2)}, \quad (3.86)$$

where each mode i is described by its proper resonance ω_i, its equivalent mass M_i and its loss angle $\phi_i(\omega)$ which contains all the dissipation mechanisms involved in the i-th

mode [127]. The equivalent mass M_i is related to the apparent motion measured by the laser beam, so that the mirror is modeled as a point like mass M_i vibrating at ω_i observed with the equivalent coordinate x_i^{eq} which is the mirror face displacement weighted by the beam shape. Let's consider a mirror, where the radial vector on the surface is $\vec{r}$, whose optical axis is on the direction z, and the beam shape profile $P(\vec{r})$, normalized over the mirror surface S such as:

$$\int_S P(\vec{r})dS = 1. \tag{3.87}$$

Then, for the i-th mode the deformation vector on the surface is $w_{i,z}(\vec{r})$ and the equivalent coordinate displacement [158] is defined as

$$x_i^{eq} = \int_{Surface} w_{i,z}(\vec{r})P(\vec{r})dS. \tag{3.88}$$

Then, the equivalent mass of the i-th mode can be calculated considering that each mode corresponds to a one-dimension harmonic oscillator having elastic energy equal to the strain energy of the corresponding mode

$$\frac{1}{2}M_i\omega_i^2(x_i^{eq})^2 = \frac{1}{2}\omega_i^2 \int_{volume} \rho|\vec{w_i}(\vec{r})|^2 dV \tag{3.89}$$

where ρ is the mirror density [127, 158]. The associated equivalent mass is then

$$M_i = \frac{\int_{volume} \rho|\vec{w_i}(\vec{r})|^2 dV}{\left|\int_{Surface} w_{i,z}(\vec{r})P(\vec{r})dS\right|^2}. \tag{3.90}$$

The modal approach is useful when dealing with modal Q measurements, since in fact the Q_i of the i-th mode is the reciprocal of the loss angle ϕ_i. Thus, knowing the losses associated to each mode, then the total thermal noise can be derived as the sum of the thermal noise of each mode as in eq. (3.86). Later, in chapter 4, I will demonstrate that this approach is useful to directly calculate the thermal noise of complex suspension system. Indeed, I extended the modal approach with appropriate modifications in order to study the thermal noise of the QuRaG suspension system in the more complex configuration.

3.4.2 The Levin Approach

When the mechanical losses are not homogeneously distributed on the surface of the mirror the FDT as expressed in the eq. (3.23) has a too complex form, and the Levin approach is usually applied. This is the case of solid mirrors where the localization of structural defects and stresses within the bulk material and the mechanical loss associated with the polished surfaces is higher than the levels typically associated with bulk effects. Therefore Levin suggested a direct application of the FDT to the optically-sensed position of the mirror substrate surface [97]. This approach is a low frequency

approximation, possible in the case of real mirror, since the resonances of the internal modes of the mirror are typically at frequencies much higher than the observed frequency range, and we are therefore in quasi-static regime $\omega << \omega_{1bulk}$, with ω_{1bulk} first of the internal (bulk) modes resonances. The Levin approach is based on calculating the strain energy accumulated by the mirror under the elastic deformation by applying a nominal pressure on the mirror surface normalized to $1N$ [127]. This pressure has the same spatial profile as the intensity of the sensing laser beam impinging on the front face of the mirror. Then, it is possible to calculate the resulting power dissipated in the substrate under the applied pressure. The power spectrum of the effective displacement of the mirror's face is thus described by the relation [97, 16]

$$X^2_{Levin}(\omega) = \frac{8k_BT}{\omega} U\phi(\omega) \tag{3.91}$$

where T is the temperature, k_B is the Boltzmann's constant, $\phi(\omega)$ is the loss angle for the dissipation of the bulk and U is the static strain energy stored in the mirror when a pressure distribution $p(r)$, due to the laser impinging on the mirror, is applied on the mirror surface. The beam intensity profile is typically a Gaussian, and thus the nominal pressure profile on the mirror is

$$p(r) = \frac{2}{\pi w_0^2} e^{-2\frac{r^2}{w_0^2}} \tag{3.92}$$

which is normalized and where w_0 is the beam radius on the mirror, i.e. the radius of the spot size on the mirror surface.[1] The analytical calculation of the strain energy is not always possible. Anyway there is a particular case in which there is an analytical expression for the strain energy: that one of a cylindrical mirror of infinite size. This can be the case in which the spot size of the beam is small compared to the size of the mirror. Therefore, the following expression for the strain energy U is obtained [16]

$$U = \frac{1-\sigma^2}{2\sqrt{\pi} Y w_0} \tag{3.93}$$

where σ and Y are respectively the Poisson's ratio and Young's modulus of the material. When the previous approximation of infinite mirror can not be done, it is more suitable to use the correction term for a finite cylindrical mirror, already calculated by Bondu Hello Vinet (BHV) [16] but with one error later corrected by Thorne [99]. In the strain energy of equation (3.91) appears a correction term ΔU [16, 99]

$$X^2_{Levin}(\omega) = \frac{8k_BT}{\omega} (U_0 + \Delta U)\phi(\omega), \tag{3.94}$$

where U_0 and ΔU are calculated in the Bondu Hello Vinet BHV approximation by Liu and Thorne [99].

[1] Note that the physical dimension of $p(r)$ is m^{-2}.

The error in [16] arises when BHV expand the Gaussian-shaped pressure as a sum over Bessel functions, where they omitted a uniform-pressure term from the sum. As a result, the pressure that they imagine impinging on the mirror face

$$P_{BHV}(r) = F_0 cos(\omega t) \sum_{m=1}^{\infty} p_m J_0(k_m r) \tag{3.95}$$

has a vanishing surface integral $\int_0^a P_{BHV}(r) 2\pi r dr = 0$ [99]. In other words, the desired pressure is equal to P_{BHV} plus an equal and opposite net force $F_0 cos(\omega t)$ uniformly applied over the mirror face:

$$P(r) = P_{BHV}(r) + p_0 F_0 cos(\omega t), \tag{3.96}$$

where F_0 is a normalized force amplitude coefficient, p_0 is equal to

$$p_0 = \frac{1}{\pi a^2}, \tag{3.97}$$

H is the mirror thickness, a the mirror radius, $J_0(\zeta_m)$ is the Bessel function of order zero calculated in $m\text{-}th$ zero (ζ_m) of the order-one Bessel function $J_1(x)$, and k_m and p_m are constant coefficients equal to

$$k_m = \frac{\zeta_m}{a}, \tag{3.98}$$

$$p_m = \frac{exp(-k_m^2 r_0^2/4)}{\pi a^2 [J_0(\zeta_m)]^2}. \tag{3.99}$$

The strain energy corrected is then given by the sum of U_0 and ΔU which are [99]

$$U_0 = \frac{(1-\sigma^2)}{\pi a Y} \sum_{m=1}^{\infty} U_m \frac{exp(-\zeta_m^2 r_0^2/2a^2)}{\zeta_m [J_0(\zeta_m)]^2}, \tag{3.100}$$

$$\Delta U = \frac{a^2}{6\pi H^3 Y} [\pi^2 H^4 p_0^2 + 12\pi H^2 \sigma p_0 s + 72(1-\sigma) s^2], \tag{3.101}$$

where s has the form [99]

$$s = \sum_{m=1}^{\infty} U_m \frac{exp(-\zeta_m^2 r_0^2/4a^2)}{\zeta_m^2 [J_0(\zeta_m)]}, \tag{3.102}$$

and U_m is

$$U_m = \frac{1 - Q_m^2 + 4k_m H Q_m}{(1-Q_m)^2 - 4k_m^2 H^2 Q_m}, \tag{3.103}$$

where the coefficient Q_m is equal to

$$Q_m = exp(-2k_m H). \tag{3.104}$$

3.4.3 The Thermal Noise of the Coatings

Interferometers for GW detections need to have highly reflecting end mirrors, and partially transmitting input mirrors, as already explained in the first chapter. This implies the presence of layers on the mirror surface, that should give the suitable values of reflection and transmission coefficients. Since, as for the interferometer Virgo, QuRaG requires totally reflective end mirrors and partially transmitting input mirrors, we suppose for QuRaG mirrors the same coating layers composition as for Virgo. Since in the expression of the mirror thermal noise, eq. (3.91), the loss mechanisms are included in the loss angle $\phi(\omega)$ term, therefore, we have to take into account the loss angle due to the coating losses.
The dissipation process due to the elastic deformation of a given surface layer *layer* of thickness h_{layer} is described by the loss angle

$$\Phi_{layer}(\omega_{mode}) = h_{layer}\frac{dU_{layer}/dh}{U_{tot}}\phi_{layer}, \tag{3.105}$$

which is given by the intrinsic loss angle of the material composing the layer ϕ_{layer} multiplied by the fraction of strain energy dU_{layer}/dh accumulated by the layer of thickness h_{layer} over the total strain energy U_{tot} accumulated by the whole mirror under the elastic deformation.

In the case of Virgo the coatings of the mirrors are composed of several alternate dielectric layers of high and low reflection index materials: the High Reflective (HR) Ta_2O_5 and the Low Reflective (LR) SiO_2. As already said, the reflection coefficient changes for input or end mirrors, and the number of high and low reflective layers is chosen in function of these conditions. Therefore, the overall thickness of the HR and LR layers for the input and end mirrors is different. In the case of the tiny end mirrors of QuRaG, it is reasonable to consider that the coating is circular shaped and almost covers the whole mirror front surface. While for the bigger input mirrors, I will consider just a circular area of the same radius as the circular coating shape of the end mirrors. This is a very good estimation of the losses since in the real case coatings do not cover the whole surface of the input mirrors.

The losses coming from the coatings are then the sum of the losses of each layer [127]:

$$\Phi_{coat}(\omega_{mode}) = S_{High}\frac{dU_{High}/dS}{U_{tot}}\phi_{High} + S_{Low}\frac{dU_{Low}/dS}{U_{tot}}\phi_{Low}, \tag{3.106}$$

of *High* and *Low* reflective material, tantalum pentoxide Ta_2O_5 and silica SiO_2 respectively [118, 127]. The coatings of Virgo, which are a priori chosen to be the same for QuRaG, have the properties summarized in the following table 3.1.
The same expression for the loss angle of a given layer eq.(3.105), can also be used for calculating the losses due to eventual layers of gluing material, like for layers of waterglass or for estimating the losses due to the silicate bonding technique.

	Materials:	High R Ta_2O_5	Low R SiO_2
Properties:			
density	$\rho\ (kg/m^3)$	8200	2200
Young's Modulus	$Y\ (GPa)$	140	72.2
Poisson's ratio	σ	0.26	0.167
loss angle	ϕ	$2 \cdot 10^{-4}$	$5 \cdot 10^{-5}$
thickness INPUT mirror	$h\ (\mu m)$	0.956	2.388
thickness END mirror	$h\ (\mu m)$	2.393	4.1086

Table 3.1: Characteristic parameters for the coatings of Virgo [127].

3.4.4 Internal Modes of Mirrors

The thermal noise fluctuations inside a solid object, generate the so called bulk modes of vibration. The internal or bulk modes of solids, like cylindrical mirrors, are characterized by the number of nodal diameters and nodal circumferences, which then define the shape of the mode. Thus, the order of bulk modes is conventionally described by the couple of numbers (n, m), where the former n refers to the number of nodal diameters and the latter m to the number of nodal circumferences. The modes which do not show nodal diameters ($n = 0$) are symmetrical with respect to the mayor axis [111, 40]. In the case of a cylindrical mirror inside an optical cavity, like for GW interferometers, this axis corresponds to the optical axis and, because of their shape, these modes are thus called Drum modes. Moreover, since in Drum modes the centre of the mirror is not a nodal point, but it moves. Therefore, the sensing of the mirror's position is significantly affected by these thermal noise fluctuations.

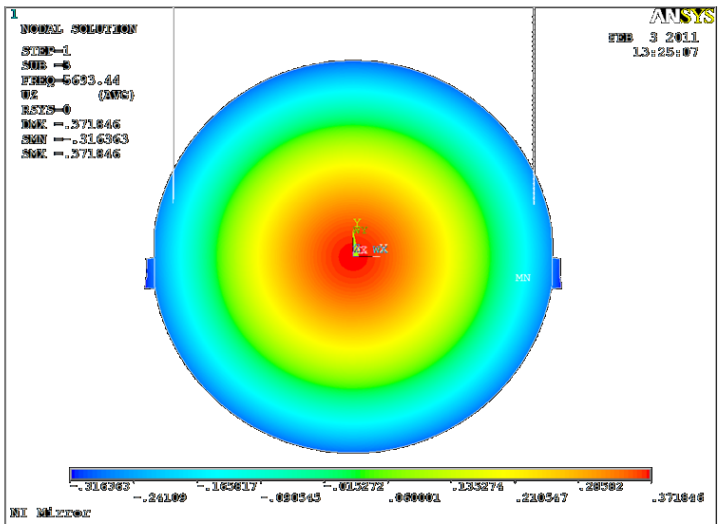

Figure 3.7: Example of Drum mode (1,0) of a suspended cylindrical mirror. The colors identify the deformations, i.e. the displacement of the mirror surface from the equilibrium. The red identifies the maximum deformation which is in the center, and the green indicates the minimal displacement, thus it represents the nodal circumference.

The modes with no nodal circumferences ($m = 0$), have nodal diameters which cross the center of the mirror, thus taking their name from their shape, they are called Butterfly modes. The center of the solid is a nodal point, hence, if the optical axis is well aligned with the mirror axis, the sensing of the mirror position is less influenced by Butterfly modes. Therefore Butterfly modes, as well as all the asymmetrical modes with respect to the optical axis, are negligible in the calculation of the mirror thermal noise.

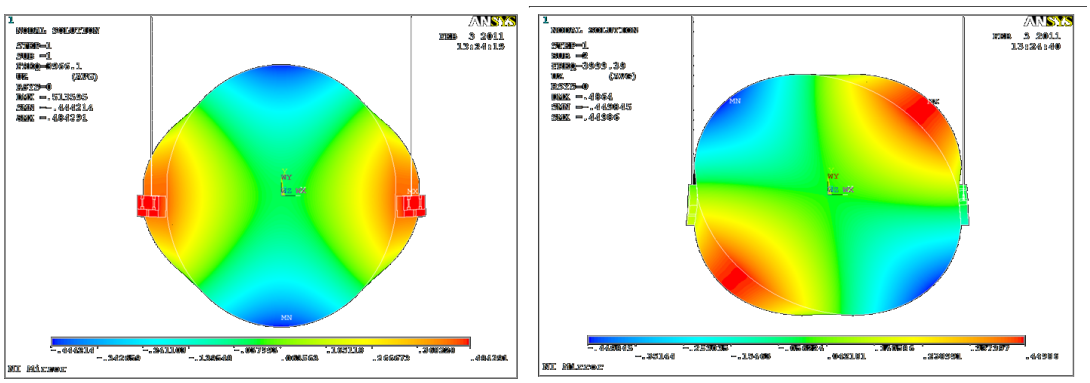

Figure 3.8: Example of Butterfly mode (0,2) of a suspended cylindrical mirror. The center of the mirror is a nodal point, which is the intersection of the two nodal diameters. Since the mirror is not exactly symmetric, the Butterfly (0,2) shows up in two slightly different modes: a mode "x" (image on the left) and a mode "+" (image on the right). This is valid also for higher order modes if the vibrating object is not perfectly symmetric.

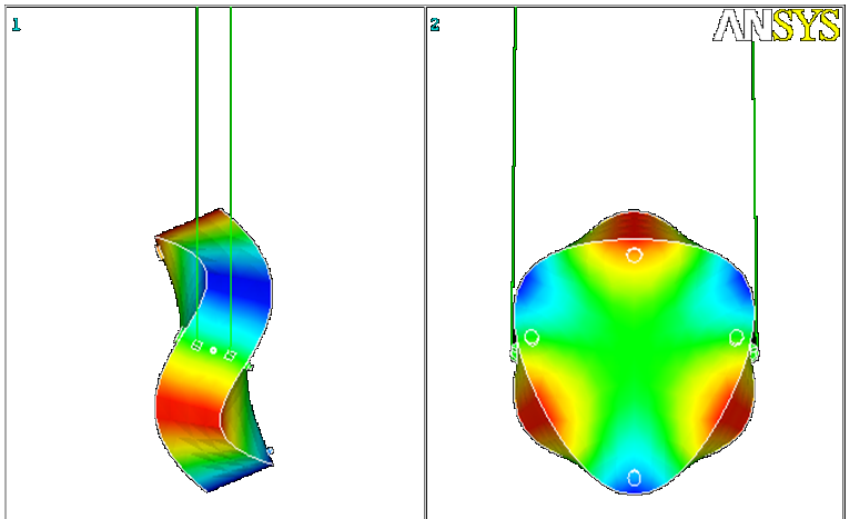

Figure 3.9: Example of Butterfly mode (0,3) of a suspended cylindrical mirror.

It is then intuitive that if the laser pressure impinging on the mirror surface has an intensity profile, like a Gaussian profile, with the maximum of energy concentrated in the center it will be more likely to induce drum modes. Thus, such a beam profile

is likely to affect the mirror thermal noise, as already pointed out. This issue will be discussed in more detail in a specific chapter.

Chapter 4

Thermal Noise Analysis to Constrain the Design of QuRaG

Starting from a preliminary design of the QuRaG interferometer, inspired from the current GW interferometers, a detailed study to constrain the design of the last suspension stage of the end mirrors has been done and it is described in this chapter. The guiding point for this analysis is that the best configuration should have a power spectrum of radiation pressure noise significantly higher than the thermal noise one, in order to be in quantum radiation pressure regime dominated. Therefore, several configurations for the suspensions have been conceived and tested through the estimation and then comparison between their thermal noise and radiation pressure noise.

I have done these analyses with the commercial software ANSYS® which makes a FEA (finite elements analysis) on the system. Therefore, several mechanical simulations have been done on each conceived configuration for the mirror's suspension. With this aim, this part of the work has been developed in collaboration with the Virgo group at La Sapienza University in Rome. My analyses confirmed that, in order to reduce the clamping losses, the suspension system should be monolithic, like in Virgo+, which means that the suspension wires and the mirror should be made with the same material. Moreover, this material should have very low internal losses. Therefore, the Suprasil® (a kind of fused silica), widely applied on GW interferometers, seems to be the best candidate [73, 125].

4.1 Finite Element Analysis with ANSYS®

As already explained in the previous chapter, the Modal Approach consists in considering the system as a sum of harmonic oscillators each one having a proper resonance, equivalent mass and loss angle. This assumption is always true, and it is particularly convenient in the case of a complex system as the core of the QuRaG suspended interferometer. In the modal analysis, the losses are estimated through the strain energies accumulated by each element while the mechanical stress occurs. ANSYS® subdivides

the system in finite elements and, with the suitable boundary conditions, solves the equations of motion on each element, each of them being connected to its neighbors. It then gives as output the characteristics of each mechanical mode, such as the resonant frequency, and the associated displacement. It is necessary to carefully choose the meshing, which means making the best choice of the finite elements shape and size before solving the equations of motion, in order to have a more precise solution within a finite computational time. Therefore, it should be done a trade off between the computational time and the quality of the meshing. For example, the best strategy is to make a more dense meshing around the bending points or the clamping stages, or anywhere a priori is supposed to be a more dissipative area, and a more sparse meshing as moving away from these areas. As example of meshing, see figures 4.3 and 4.4.

With the finite element analysis of ANSYS® it is possible to estimate how the internal modes of the whole interferometer can affect the mirror position. Therefore, this FEA allows to determine which are the modes that more contribute to the mirror displacement and then to the mirror thermal noise. This step is fundamental in order to choose the optimal suspension system for the final design, but also to constrain all the other parts of the design which strongly depend on the suspension configuration.

In figure 4.1 is shown the starting design of the QuRaG suspended interferometer. This is composed by a disk to which all the optical elements of the Michelson interferometer with Fabry-Pérot cavities are attached, and which is suspended to the upper stages through three wires occupying the vertices of an equilateral triangle around the center of the disk. For simplicity, the upper stages are schematized as a thick disk to which the three wires are suspended. The core of the interferometer is composed by a prism shaped beam splitter, two parallelepiped shaped input mirrors, two suspended end mirrors and a cylindrical shaped counterweight. The optic scheme of the suspended interferometer, already described in chapter 2, is shown in figure 4.2.

The figures 4.3 and 4.4 show how the meshing has been done on the Input and End mirror, respectively, in the case of the estimation of the mirror thermal noise with the presence of the coatings. As already explained, the meshing is more dense in the areas of the coatings where the laser pressure is supposed to impinge on. It is in those areas that is necessary to have meshing elements of smaller size, that are reasonably chosen to be at least two order of magnitude smaller than the dimension of the beam radius on the mirror surface.

4.2 Modal Analysis on the whole Suspended Interferometer

This preliminary analysis allows to make a complete mapping of the modes of the whole suspended interferometer thus to identify the modes which more affect the mirror position and therefore, its thermal noise. This analysis is also called mode mapping. As boundary conditions, the thicker disk, which represents all the upper stages, should be set as a fixed support. Moreover, at low frequency, it is necessary to do both the static

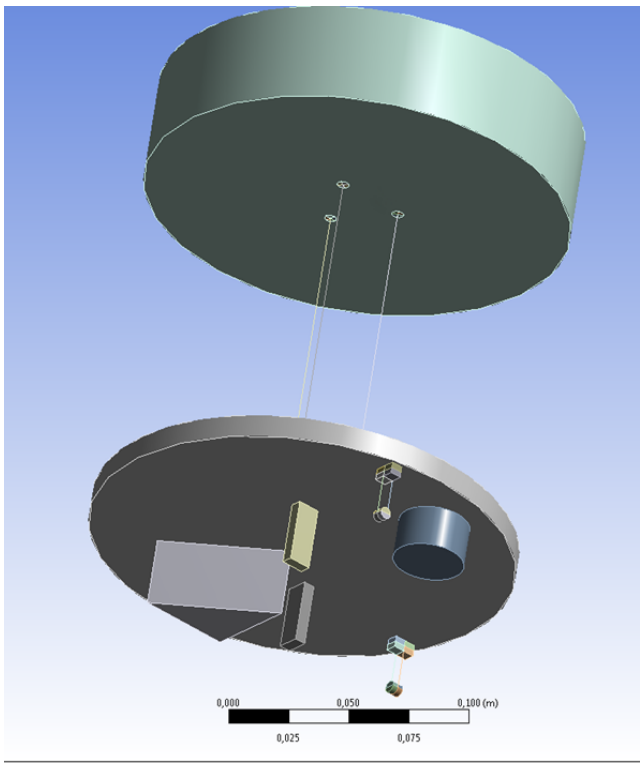

Figure 4.1: Scheme of the starting design of QuRaG for the FEA analysis with ANSYS®. The upper stages are schematized as a cylinder which suspend the rest of the system by three suspension wires.

with gravity as other constrain and floating analysis, because in this frequency range the effect of the gravity is not negligible. While going at higher frequency the mode mapping in the two conditions will converge. Since the pendulum mode resonance is around $3.5Hz$, I considered the effect of gravity negligible starting from $100Hz$, and I checked that this assumption was correct by comparing the frequencies of the normal modes obtained from the modal analysis with and without the gravity. This in ANSYS Workbench® interface translates in doing a modal analysis with pre-stress static analysis (that one which considers gravity) and a modal analysis in floating condition (without any pre-stress). Therefore, since I considered negligible the effect of gravity for frequencies higher than $100Hz$ in table 4.2, modes till number 14, which are within the $100Hz$, are taken from the pre-stress analysis, and starting from mode 15 are taken from the floating analysis.

For the mode description, it is necessary to set the cardinal axes. The x axis is along the arm of the suspended mirror 1, the y axis is along the direction of gravity but in opposite verse and the z axis is along the arm of the suspended mirror 2. For the sake of simplicity, ITF, m1, m2 respectively refer to the whole interferometer, the suspended mirror 1 and the suspended mirror 2 (see fig.4.2). CW refers to the counterweight and BS to the beam splitter. The ITF disk refers to the disk to which the ITF elements are directly attached and the upper disk refers to the disk which summarizes all the upper stages. M1 and M2 refer to the fixed mirror respectively along the x and z axis.

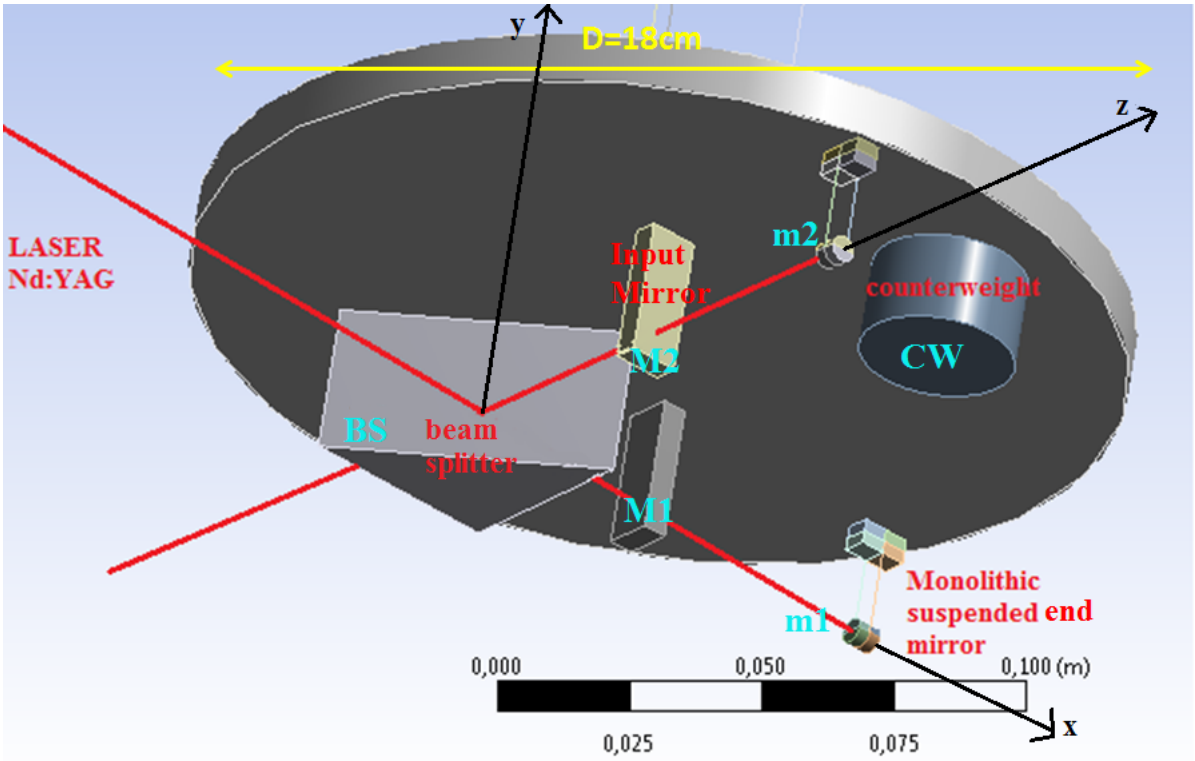

Figure 4.2: Optical scheme of the starting design of QuRaG.

Moreover tX, tY, tZ are short notations for the torsional modes along x, y, and z axis, and the notation pend stands for pendulum mode. The notation viol refers to the violin modes and LW stands for long wires which are the ITF disk suspension wires, while m2W and m1W stand for the m1 and m2 suspension wires respectively. The Roman numbers identify the order of the violin mode. All the acronyms explained above and used in the mode mapping tables tab.4.2 and tab.4.3, are summarized in table 4.1. The bulk modes like the Butterfly or Drum are explained in the section 3.4.4 at the end of the previous chapter 3 on the thermal noise. The torsional modes that do not affect the mirror position along the optical axis can be neglected, while it is necessary to evaluate the contribution of those which can affect the mirror position along the optical axis. The mode mapping showed that only the torsional mode of the mirror around the axis orthogonal to the optical axis and lying on the plane of the ITF optics affects the mirror position sensed by the laser. Therefore, in the thermal noise calculations I will neglect the contribution of the other torsional modes, while when applying the modal analysis I will take into account this torsional mode in addition to the pendulum and violin modes. The vertical mode of the system are also negligible a priori since it will not affect the mirror position along the optical axis. However, the effect of the vertical mode of the mirror will be studied in more detail while only applying the modal analysis to the mirror suspension system.
In the analysis I considered the whole system as made of Suprasil®, as the mirrors and mirror suspension of Virgo+, since at the present time it is the commercial fused silica

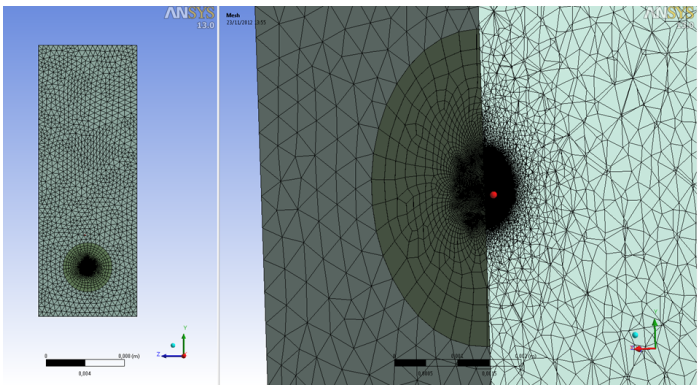

Figure 4.3: Example of the meshing of the Input Mirror with coatings.

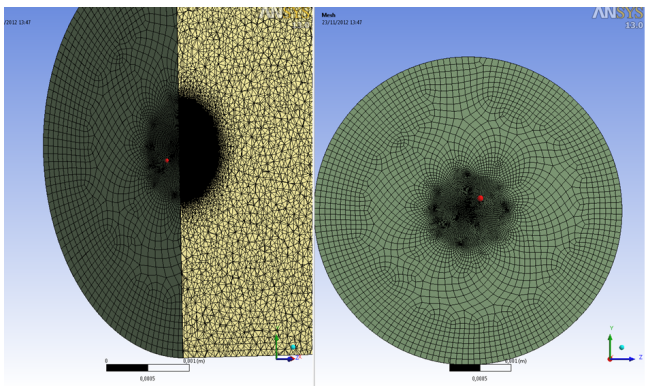

Figure 4.4: Example of the meshing of the End Mirror with coatings.

with the lowest losses [114].

I analysed all the modes of the system from 0 to $20kHz$, which should largely be within the frequency's window of observation of QuRaG.

This mode mapping on the preliminary design reported in the table tab.4.2, showed that, in order to reduce the contribution of the whole interferometer to the suspension thermal noise of the mirrors, it is necessary to have a thicker suspension disk. This will avoid the presence of many bulk modes of the interferometer suspension disk (ITF disk) in the detection band of QuRaG. Therefore, the first result I obtained from the modal analysis was the need to increase the thickness of the disk from $10mm$ to $40mm$. From the mode mapping, it also comes out that between the pendulum mode and the violin modes of the m1 and m2 suspension, there are some of the violin modes of the upper stage suspension. Nevertheless, the mirror position will not significantly be affected by these violin modes since the interferometer disk, much heavier than the suspended mirror, is a nodal point for these modes, so that the violin modes will not limit the thermal noise. Moreover the interferometer disk stage has the function of filtering the stresses transmitted to the mirror. This analysis also showed that around $5kHz$ there are some flexural modes of the fixed mirror M1 and M2. Therefore, an evaluation of the fixed mirror thermal noise has also been done in the following.

In order to verify that an ITF disk of $40mm$ is thick enough to not show internal

ACRONYM	DESCRIPTION
ITF	whole QuRaG suspended interferometer
m1	suspended end mirror along the x axis
m2	suspended end mirror along the y axis
M1	fixed input mirror along the x axis
M2	fixed input mirror along the y axis
BS	beam splitter
CW	counterweight
ITF disk	disk to which the whole interferometer is attached
upper disk	disk which simplifies all the upper suspension stages
m1W	suspension wires of the end mirror along the x axis, m1
m2W	suspension wires of the end mirror along the y axis, m2
LW	longer and thicker suspension wires which hold the ITF disk
tX, tY, tZ	torsional modes around x, y and z axis respectively
pendX, pendY	pendulum modes along x and y axis respectively
viol	violin mode
roman numbers	orders of the violin modes

Table 4.1: Descriptions of the acronyms used in the mode mapping tables.

modes within the frequencies of the QuRaG window of observation, I repeated the mode mapping, with the same boundary condition as before. This time I realized a more dense meshing on the wires, therefore the values of the violin frequencies are slightly different but more precise than in the previous mode mapping. In the table tab.4.3 I report the results of the mode mapping with the thicker disk. Some bulk modes of the ITF disk with thickness $10mm$ are depicted in figure 4.5. I prefer to report the images of the case with the thinner ITF disk, since here the internal (bulk) mode shapes are more accentuated.
After having increased the thickness of the interferometer disk all the bulk modes of the ITF disk have all successfully been shifted to higher frequencies. This is shown in the tables of the mode mapping (tab.4.2 and tab.4.3) and more in detail in the table 4.4 . Only few low order bulk modes are still within the $20kHz$ of the analysed spectrum, all the others disappeared from this frequency range.

4.3 First Set of Configurations of Suspension Tested

The first step is to verify that the whole system modes will not affect the mirror position, hence its thermal noise. In particular with the modal analysis on the whole interferometer, I demonstrated that a thicker ITF disk assures that the resonances of the internal modes of the ITF disk fall outside the detection band of QuRaG. The second step is to concentrate the attention on the design of the last suspension stage of the mirrors. Therefore, with the collaboration of the Virgo group of the university of Rome La Sapienza, I conceived several suspension configurations that I tested

N MODE	$\nu(Hz)$	DESCRIPTION OF THE MODE
1	0.44	tY ITF
2	1.38	pendX ITF
3	1.41	pendZ ITF
4,5	3.98	pendX m1, pend z m2 (along optical axis)
6	4.73	pendX m2
7	4.74	pendZ m1
8	9.99	tY m2
9	9.99	tY m1
10,11	21.0	tZ m1, tX m2
12	28.0	tZ ITF
13	30.0	tX ITF
14-19	113	I viol LW
20	117	vertical Y ITF
21-26	312	II viol LW
27-32	612	III viol LW
33-40	637	I viol m1W, m2W
41-46	1011	IV viol LW
47,48	1279	vertical m1, m2
49-54	1510	V viol LW
55-62	1757	II viol m1W, m2W
63,64	1810	tX m1, tZ m2
65	1855	Butterfly+2,0 ITF disk
66	1912	Butterfly$X$ 2,0 ITF disk (rotated of $\pi/4$ to mode 65)
67-72	2110	VI viol LW
73	2664	Drum 0,1 ITF disk
74-79	2809	VII viol LW
80-87	3445	III viol m1W, m2W
88-93	3610	VIII viol LW
94	4205	Butterfly 3,0 ITF disk
95	4259	Butterfly 3,0 ITF disk (rotated of $\pi/6$ to mode 94)
96-101	4512	IX viol LW
102	5422	flexural fixed mirrors in phase (along optical axis)
103	5465	flexural fixed mirrors in antiphase (along optical axis)
104-109	5515	X viol LW
110-117	5698	IV viol m1W, m2W
118	5945	Bulk 1,1 ITF disk
119	6400	Bulk 1,1 ITF disk (rotated of $\pi/2$ to mode 118)

N MODE	$\nu(Hz)$	DESCRIPTION OF THE MODE
120-125	6621	XI viol LW
126	6945	Butterfly 2,0 upper disk
127	6948	Butterfly 2,0 upper disk (rotated of $\pi/4$ to mode 126)
128	7198	Butterfly 4,0 ITF disk
129	7350	Butterfly 4,0 ITF disk (rotated of $\pi/8$ to mode 119)
130-135	7834	XII viol LW
136	8480	flexural M2 along x (coupled with disk ITF)
137-144	8525	V viol m1W, m2W
145-150	9157	XIII viol LW
151	9276	flexural M1 along z
152	9712	flexural M1 along z, M2 along x
153	9830	flexural M2 along x
154	10099	Drum 0,1 upper disk
154-160	10580	XIV viol LW
161	10721	flexural M1 along z (coupled with Butterfly 5,0 and XIV viol LW)
162	10783	flexural M1 along z (coupled with Butterfly 5,0 and XIV viol LW)
163	11151	Butterfly 5,0 ITF disk
164-171	11935	VI viol m1W, m2W
172-177	12133	XV viol LW
178-180	12628	long wires inflates (ANYS graphical resolution problem)
181	13600	Bulk 2,1 ITF disk (coupled with XV viol LW)
182-187	13791	XVI viol LW
188	14017	Bulk 2,1 ITF disk (coupled with XVI viol LW)
189	14031	Butterfly 3,0 upper disk
190	14170	Butterfly 3,0 upper disk (rotated of $\pi/6$ to mode 189)
191	14604	Butterfly 6,0 ITF disk
192-197	15588	XVII viol LW
198	15618	Butterfly 6,0 ITF (coupled with XVII viol LW)
199	15980	Squeezed$X$ ITF disk (coupled with XVII viol LW)
200-207	16050	VII viol m1W, m2W
208	16045	Squeezed+ ITF disk (rotated of $\pi/4$ to mode 199)
209	16089	Squeezed$X$ upper disk
210	16205	Squeezed+ upper disk (rotated of $\pi/4$ to mode 209)
211	16742	Bulk 4,1 ITF disk (coupled with XVII viol LW)
212-217	17496	XVIII viol LW
218	17667	Bulk 1,1 ITF Bean shaped (rotation around 2 nodal points)
219	17928	Bulk 4,1 ITF disk (coupled with XVIII viol LW)

N MODE	$\nu(Hz)$	DESCRIPTION OF THE MODE
220	18510	Bulk 1,1 upper disk Bean shaped (rotation around 2 nodal points)
221	18682	tX ITF disk (coupled with XVIII viol LW)
222	18731	tY upper disk (coupled with XVIII viol LW)
223	18753	tY ITF disk (coupled with XVIII viol LW)
224	18767	tZ ITF disk (coupled with XVIII viol LW)
225	19110	tx ITF disk (coupled with XVIII viol LW)
226	19241	Butterfly 7,0 ITF disk (coupled with XVIII viol LW)
227-232	19587	XIX viol LW
233	19795	tX upper disk (coupled with XIX viol LW)
234	19919	tZ upper disk (coupled with XIX viol LW)

Table 4.2: Mode mapping of the whole interferometer with ITF disk of thickness $10mm$. The acronyms are summarized in tab. 4.1.

through the ANSYS® modal analysis and thermal noise estimations. According to the preliminary design of QuRaG, the two mirrors to be suspend have a mass of around $0.2g$.

4.3.1 First Set of Configurations of Mirror Suspension

Some of the suspension configurations tested are depicted in the figure 4.6. The main guiding idea was to reduce the losses at the clamping areas of the wires. Therefore three of the proposed solutions are shown in the figure 4.6. In the configuration n.1 I suppose to preserve the preliminary idea of a cylindrical mirror by just introducing two lateral flats, like in Virgo, in order to fix two cylindrical ears to then weld the wires. Two ears should also be added to the parallelepiped that joints the mirror to the ITF disk. Nevertheless, realizing flat on such a tiny mirror can be risky for the possibility of causing cracks on the mirror's structure, and it will be difficult to realize the welding between the tiny wire and the thicker ears. Then I thought that using a cubic mirror as in configuration n.2, will avoid the problem of doing the flats. A cubic mirror suspended as in configuration n.2 needs to weld the corner point of the cubic mirror to the wire. Nevertheless, since the volume of the mirror is much higher than the wire's one, while heating the two points to weld, all the heat will flow into the wire and burn it, whereas the mirror corner will need a higher temperature to melt down (except if the process is carefully done with a CO_2 laser instead of with a flame). I then thought to introduce some cubes and pyramids that will simplify the end shape of a real fiber that could be directly glued on the sides of the cubic mirror, i.e. the configuration n.3.

Although they showed a thermal noise significantly lower than the radiation pressure noise, some of these configurations have been rejected for the impossibility to be realized, as explained above.

Therefore, the configuration n.3 seemed the best at that time, so that the final configuration has been conceived starting from it and just improving it by realizing some modifications.

N MODE	$\nu(Hz)$	DESCRIPTION OF THE MODE
1	0.38	tY ITF
2,3	1.33	pendX ITF, pendZ ITF
4,5	3.98	pendX m1, pendZ m2 (along optical axis)
6,7	4.73	pendX m2, pendZ m1
8,9	9.99	tY m2, tY m1
10	14.5	tZ ITF
11	14.7	tX ITF
12,13	21.0	tZ m1, tX m2
14	76.7	vertical Y ITF
15-20	113	I viol LW
21-26	312	II viol LW
27-32	612	III viol LW
33-40	637	I viol m1W, m2W
41-46	1011	IV viol X,Z LW
47,48	1279	vertical m1, m2
49-54	1510	V viol LW
55-62	1757	II viol m1W, m2W
63,64	1810	tX m1, tZ m2
65-70	2109	VI viol LW
71-76	2807	VII viol LW
77-84	3445	III viol m1W, m2W
85-90	3606	VIII viol LW
91-96	4505	IX viol LW
97-102	5504	X viol LW
103	5536	flexural M2 along z (optical axis)
104	5604	flexural M1 along x (optical axis)
105-112	5702	IV viol M1W, M2W
113	6416	Butterfly+ 2,0 ITF disk
114	6445	Butterfly$X$ 2,0 ITF disk (rotated of $\pi/4$ to mode 114)
115-120	6604	X viol LW
121	6937	Butterfly+ 2,0 upper disk
122	6946	Butterfly$X$ 2,0 upper disk (rotated of $\pi/4$ to mode 121)
123-128	7806	XXI viol LW
129-136	8527	V viol m1W, m2W
137	9084	Drum 0,1 ITF disk
138-143	9111	XIII viol LW

N MODE	$\nu(Hz)$	DESCRIPTION OF THE MODE
144	10077	Drum 0,1 upper disk
145	10105	flexural M2 along x
146	10186	flexural M1 along z
147-152	10517	XIV viol LW
153-160	11963	VI viol m1W, m2W
161-166	12039	XV viol LW
167	12497	flexural BS (coupled with Butterfly 3,0 ITF disk)
168-170	12641	long wires inflates (ANYS graphical resolution problem)
171	13094	Butterfly 3,0 ITF disk (rotated of $\pi/6$ to mode 167)
172-177	13650	XVI viol LW
178	13882	flexural BS (coupled with Butterfly 3,0 ITF disk)
179	14034	Butterfly 3,0 upper disk
180	14055	Butterfly 3,0 upper disk (rotated of $\pi/6$ to mode 167)
181-186	15373	XVII viol LW
187	15584	flexural BS (coupled with Butterfly 3,0 ITF disk)
188-189	16006	VII viol m1W, m2W
190	16028	Squeezed+ ITF disk (coupled with XVII viol LW)
191-193	16059	VII viol m1W
194	16066	Squeezed$X$ upper disk (coupled with XVII viol LW)
195-197	16074	VII viol m2W
198	16329	flexural BS (coupled with Drum 0,1 ITF disk and VII viol m1W,m2W)
199	17086	flexural BS and CW in phase (coupled with XVII viol LW)
200-205	17210	XVIII viol LW
206	17914	flexural BS and CW in anti-phase (coupled with XVIII viol LW)
207	18115	tY BS (coupled with Bulk 1,1 ITF disk)
208	18255	Bulk 1,1 upper disk Bean shaped (rotation around 2 nodal points)
209	18331	Bulk 1,1 upper disk Bean shaped (rotation around 2 nodal points)
210-215	19116	XIX viol LW
216	19197	tx ITF disk (coupled with XIX viol LW)
217	19523	tX upper disk (coupled with XIX viol LW)
218	19648	tZ upper disk (coupled with XIX viol LW)
219, 220	19686	tY ITF and upper disk (coupled with XIX viol LW)
221	19686	tX upper disk (coupled with XIX viol LW)
222	19805	tX ITF disk

Table 4.3: Mode mapping of the system with the thicker ITF disk of $40mm$. The acronyms are summarized in tab. 4.1.

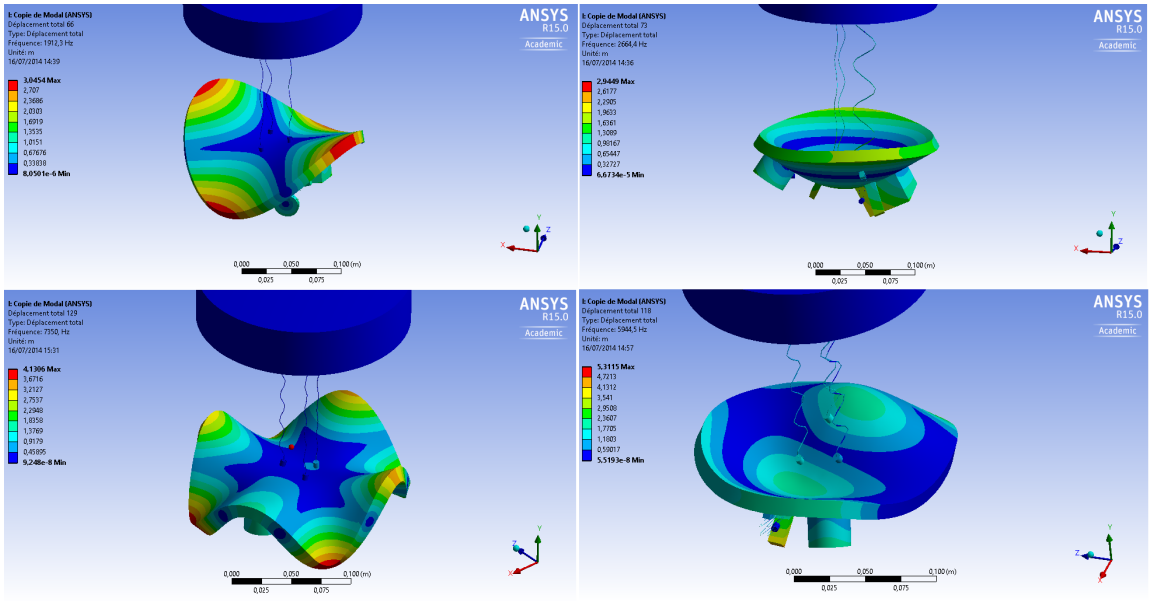

Figure 4.5: Some bulk modes of the interferometer disk of thickness $10mm$. On the upper left side there is the mode n.66 Butterfly 2,0, on the upper right side the mode n.73 Drum 0,1, on lower left side the mode n.129 Butterfly 4,0, on the lower right side the mode n.118 Bulk 1,1.

Nevertheless, I devote the following section to explain the thermal noise analysis that I made on these three configurations of figure 4.6.

4.3.2 Thermal Noise of the Suspensions

The estimation of the thermal noise of the suspensions is done starting by applying the fluctuation dissipation theorem and treating the three configurations as real pendulums. The formulas used are those explained in the chapter 3 and in particular the expression of the pendulum thermal noise of eq.(3.75). The thermal noise of the suspensions related to the pendulum mode of the suspended mirror is therefore

$$\langle X_{pend} \rangle (\omega) = \sqrt{2 \frac{4 k_B T}{m \omega} \frac{\omega_p^2 \Phi_p(\omega)}{((\omega_p^2 - \omega^2) - (\omega_p^2 \Phi_p(\omega))^2)}} \tag{4.1}$$

where m is the suspended mass, which slightly varies for the cylindrical or cubic mirror (see tab.4.5), as well as the pendulum resonance ω_p and the total loss angle of the suspension $\Phi_p(\omega)$. I recall that the loss angle of the wires depends on ω since it has a thermoelastic contribution which is frequency dependent (see section 3.2.3). The pendulum resonance is calculated as

$$\omega_p = \sqrt{\frac{g}{L_w} + \frac{k_e}{m}}, \tag{4.2}$$

CASE:	ITF DISK $10mm$ THICK	ITF DISK $40mm$ THICK
MODE DESCRIPTION	FREQUENCY $\nu(Hz)$	FREQUENCY $\nu(Hz)$
Butterfly + 2,0	1855	6416
Butterfly X 2,0	1912	6445
Drum 0,1	2664	9084
Butterfly 3,0	4205	13094
Bulk 1,1	5945	$> 2k$
Bulk 1,1	6400	$> 2k$
Butterfly 4,0	7198	$> 2k$
Butterfly 4,0	7350	$> 2k$
Butterfly 5,0	11151	$> 2k$
Butterfly 5,0	14604	$> 2k$

Table 4.4: Mode mapping: comparison between the internal modes of the ITF disk in the preliminary case having $10mm$ thickness and in the second proposed case having $40mm$ thickness. Increasing the disk thickness enable the system to shift all the bulk modes frequencies to higher frequencies, almost all outside the QuRaG detection band. The acronyms are summarized in tab. 4.1.

Mirror	Cylindrical	Cubic	Fixed
mass (g)	0.216	0.275	2.75
radius (mm)	2.5		
length (mm)		5	25
widht (mm)		5	10
thickness (mm)	5	5	5
beam radius (μm)	275	275	272

Table 4.5: Characteristic parameters of cylindrical vs cubic end mirror, and of the input fixed mirror. The last parameter is the beam radius of the laser's spot on the mirror surface.

in which the first term is the gravitational term and the second term is the elastic correction (see sec. 3.2). The elastic stiffness k_e is [127]

$$k_e = \frac{n_{fp} n_w \sqrt{\Lambda Y J}}{2L_w^2}, \tag{4.3}$$

where Λ is the tension of each suspension wire, Y the Young's modulus of the material, L_w the length of the wire, n_{fp} the number of flexural points (1 in all the three cases), n_w the number of suspension wires (2 all the three cases), and J is the momentum of inertia of the wire's section with respect to its axis (also called bending moment of inertia of the fiber [155]) [127]

$$J = \frac{1}{4}\pi r_w^4 \tag{4.4}$$

and r_w is the radius of the wire. The tension of the single wire is given by the ratio of the weight divided by the number of wires

$$\Lambda = \frac{mg}{n_w}. \tag{4.5}$$

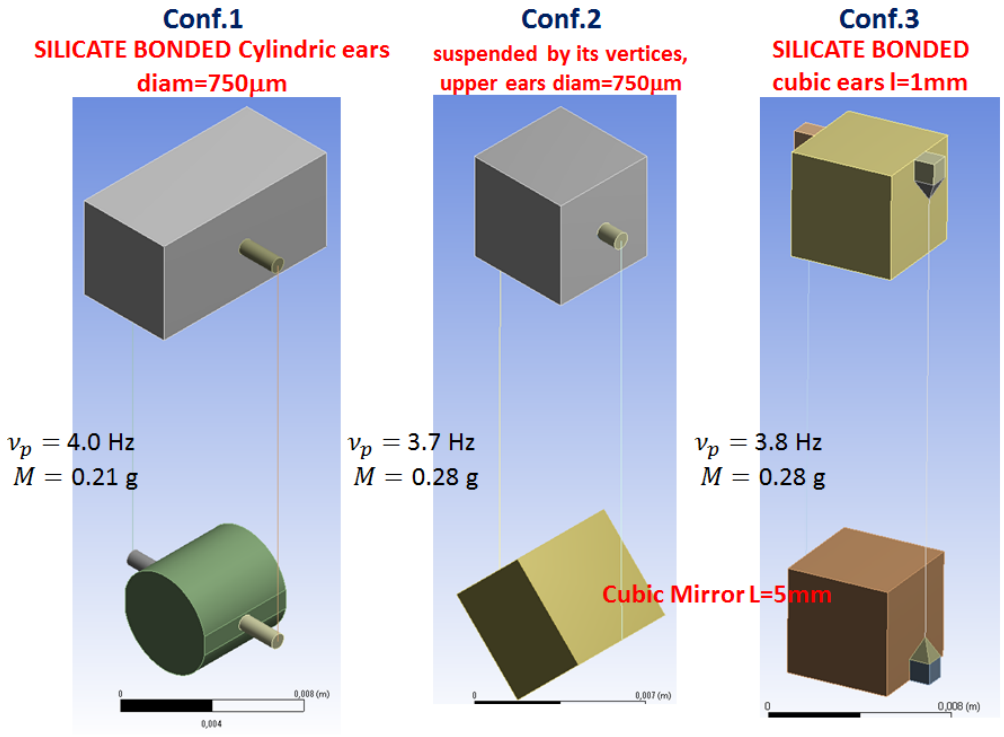

Figure 4.6: Three of the first configurations of the mirror suspension system analysed.

The suitable values for the wire's length, in order to have a pendulum resonance around $3-4Hz$, and then for the radius, to let the wire not to behave rigidly, are written in table 4.6.

wire's radius (μm)	25
wire's length (mm)	20(21for conf.3)

Table 4.6: Characteristic parameters of the suspension wires corresponding to the configurations of fig.4.6.

The pendulum total loss angle is given by the sum of all the internal, structural and thermoelastic losses, multiplied by a factor which is the inverse dilution factor (D_F^{-1}):

$$\phi_p(\omega) = D_F^{-1}(\phi_s + \phi_e + \phi_{te}(\omega)). \tag{4.6}$$

In particular ϕ_s is the structural loss angle of the suspensions material (Suprasil®), ϕ_e represents the surface losses of the wire and ϕ_{te} the thermoelastic losses. The factor D_F^{-1} is the inverse of the dilution factor and for the pendulum it has the form [127]

$$D_F^{-1} = \frac{n_{fp}}{L_w}\sqrt{\frac{2n_w Y_s J}{mg}}, \tag{4.7}$$

where Y_s is the Young's modulus of the fused silica (see table 4.12).

Surface Losses

The surface losses, also called excess losses, ϕ_e are calculated as explained in section 3.2.4 [124]

$$\phi_e = \frac{\mu_w d_s S_w}{V_w}\phi_s, \tag{4.8}$$

where μ_w is a form factor which for the cylindric wire is equal to 2, S_w and V_w are the lateral surface and the volume of the wire. d_s is the dissipation depth, already defined in equation (3.59), a parameter which expresses how deep from the surface the dissipations can spread. In this case, using equation (3.60) it follows that it is equal to

$$d_s = 1.5 \cdot 10^{-2} m. \tag{4.9}$$

Thermoelastic Losses

The thermoelastic loss angle has a more complicated form and, as already explained in the previous chapter (see eq.(3.53)), depends on the frequency. In the case of our fused silica fibers it takes the following form

$$\phi_{te} = \Delta_s \frac{\omega\tau_s}{(1-(\omega\tau_s)^2)}. \tag{4.10}$$

The factor Δ_s and the characteristic time of heat diffusion τ_s for the fused silica wires are

$$\Delta_s = \frac{Y_s T}{\rho_s C_s}\left(\alpha_s - \beta_s \frac{\Lambda_w}{A_w Y_s}\right)^2 \qquad \tau_s = \frac{C_s \rho_s (2r_w)^2}{2.16 \cdot 2\pi k_s} \tag{4.11}$$

where C_s, k_s and α_s are the specific heat, the thermal conductivity and the coefficient of linear expansion of the fused silica. In the second order therm in Δ_s, the β_s, is the relative coefficient of thermal gradient of the Young's modulus Y_s

$$\beta_s = \frac{1}{Y_s}\frac{dY_s}{dT}, \tag{4.12}$$

and Λ_w and A_w are the tension and the section area of the wire. All the characteristic parameters of the fibers material are listed in the table 4.12. The intrinsic loss angles of fused silica, as well as the calculated loss angle for the surface losses, and the Δ_s and τ_s parameters for the thermoelastic loss angle, are summarized in table 4.7. Note that the only value that slightly varies among the three configurations is the factor Δ_s.

Violin Thermal Noise

To complete the estimation of the thermal noise of the suspensions at high frequency, I should check the so called violin thermal noise (see section 3.3.3). The suspension wires are tighten under the weight of the suspended mass, hence they behave as a vibrating string [69], and these harmonics are also called violin modes. Therefore, it is better to

Conf.	ϕ_s	ϕ_e	Δ_s	τ_s
1	$4.1 \cdot 10^{-10}$	$9.84 \cdot 10^{-7}$	$3.22 \cdot 10^{-6}$	$0.23ms$
2	$4.1 \cdot 10^{-10}$	$9.84 \cdot 10^{-7}$	$3.21 \cdot 10^{-6}$	$0.23ms$
3	$4.1 \cdot 10^{-10}$	$9.84 \cdot 10^{-7}$	$3.21 \cdot 10^{-6}$	$0.23ms$

Table 4.7: Intrinsic loss angle of fused silica fibers, surface loss angle and thermoelastic loss angles factor Δ_s and time of heat diffusion τ_s, for the wires of the three configurations of fig. 4.6. Only the factor Δ_s slightly varies for the different configurations.

verify if some violin harmonics fall in the detection band of QuRaG and if they can affect the sensitivity of the instrument. A perfect vibrating string has its two ends fixed, so that its harmonics will not affect the position of the upper and lower end, whereas the suspension wires of QuRaG are not, since the mirror is suspended like a pendulum with the lower end free to oscillate. However, the low mass ratio between the wires and the suspended mass (mirror) allows to be close to the vibrating string case. Therefore, the violin harmonics of the wire can affect the mirror position so that they should be taken into account while estimating the thermal noise of the suspensions.

It is reasonable to consider all the losses condensed around the harmonic resonances [133, 69], therefore it is possible to approximate the thermal noise associated to the violin modes of a wire, as the sum of the contributions of each single harmonic [133]. Therefore, the violin thermal noise has the expression of equation (3.85), as described in the previous chapter (see section 3.3.3):

$$\langle X_{viol}(\omega) \rangle = \sqrt{4 \frac{4k_B T}{\omega} \frac{2\rho_s r_w^2}{\pi m^2} L_w \sum_n \frac{1}{n} \frac{\omega_n^2 \Phi_n}{(\omega_n^2 - \omega^2)^2 + (\omega_n^2 \Phi_n)^2}} \tag{4.13}$$

where the factor 4 stands for the total number of wires (2 wires $\times$ 2 suspended mirrors) and $\Phi(\omega_n)$ and ω_n are, respectively, the total loss angle and the resonance of the n-th harmonic (see eqs. (4.15) and 3.83) [133, 69]:

$$\Phi_n(\omega) = \Phi(\omega) \frac{2}{L_w k_v} \left(1 + \frac{(n\pi)^2}{2k_v(\omega) L_w} \right) \tag{4.14}$$

$$\omega_n(\omega) = \frac{n\pi}{L_w} \sqrt{\frac{\Lambda}{\pi r^2 \rho}} \left[1 + \frac{2}{L_w k_v(\omega)} + \frac{1}{2} \left(\frac{n\pi}{k_v(\omega) L_w} \right)^2 \right] \tag{4.15}$$

in which the parameter $k_v(\omega)$ is the wave number related to the flexural stiffness of the wire

$$k_v(\omega) = \sqrt{\frac{\Lambda_w + \sqrt{\Lambda_w^2 + 4Y_s J \rho \pi r_w^2 \omega^2}}{2Y_s J}}. \tag{4.16}$$

Moreover, the $\Phi(\omega)$ is the total loss angle of the wire which for the violin modes is given by the sum of all the contributions also present in the pendulum losses (see eq. 4.6)

$$\Phi(\omega) = \phi_s + \phi_e + \phi_{te}(\omega). \tag{4.17}$$

As already seen for the pendulum mode, since the mass and the wire length slightly vary for the three cases of fig. 4.6, the violin thermal noise also slightly varies and it has been calculated for each configuration.

Note that, by analogy with the case of the pendulum mode, the loss angle of the n-th violin harmonic can be seen as a total intrinsic loss angle of the fiber $\Phi(\omega)$, multiplied by the inverse of the dilution factor D_n^{-1} [155]:

$$\Phi_n(\omega) = D_n^{-1}\left(\phi_s + \phi_e + \phi_{th}(\omega)\right) \tag{4.18}$$

$$D_n^{-1} = \frac{2}{L_w k_v}\left(1 + \frac{(n\pi)^2}{2k_v(\omega)L_w}\right), \tag{4.19}$$

and in the expression of the violin thermal noise of eq. 4.13 the therm $\frac{\pi m^2}{2\rho_s r_w^2 L_w} n$ can be seen as an equivalent mass m_n of the n-th harmonic:

$$m_n = \frac{\pi m^2}{2\rho_s r_w^2 L_w} n. \tag{4.20}$$

4.3.3 Thermal Noise of the Mirror

At higher frequency, there is also the contribution of the internal modes of the mirror, the so called mirror thermal noise. For the evaluation of this thermal noise contribution, the Fluctuation-Dissipation Theorem (FDT) as expressed for the pendulum mode is too complicated and the Levin approach, a high frequency approximation of the FDT, is applied. The mirror thermal noise has been calculated for the Fabry-Pérot cavity mirrors, hence for the end suspended and for the input fixed mirror. According to Levin approach (valid for an homogeneous system) the thermal noise of 2 identical mirrors has the form

$$X_{Levin}(\omega) = \sqrt{2\frac{8k_B T}{\omega} U\Phi} \tag{4.21}$$

where Φ is the loss angle associated with the bulk motion of the mirror and U is the static strain energy accumulated by the mirror, as effect of a Gaussian profile pressure $p(r)$ representing the laser beam impinging on the mirror surface

$$p(r) = \frac{2}{\pi w_0^2} e^{-2\frac{r^2}{w_0^2}}. \tag{4.22}$$

The nominal pressure $p(r)$ is normalized such that it has physical dimension of m^{-2} and that it corresponds to a total impinging force of $1N$, and w_0 is the beam radius on the mirror (the radius of the spot size on the mirror surface).

The strain energy U, as well as the total loss angle Φ, have been calculated with ANSYS® FEA simulations. The strain energy has been also calculated with the Bondu

Hello Vinet approximation with Thorne correction as explained in sec. 3.4.2 and compared with the ANSYS® results. Nevertheless, for the final curve of thermal noise, the ANSYS® output values have been used, since they represent a better estimation of the real value. The total loss angle is essentially given by three contributions:

- the bulk modes loss angle of the material ϕ_{sb},
- the losses due to the coatings layers Φ_{coat} (see eq.(3.106)),
- the losses due to the layers of the material used to attach the ears to the mirror (in configuration n.1 and n.3) Φ_{SiBond}.

The surface to volume ratio is not remarkable for the cylindrical or cubic mirror, while it is for the wires. Hence the surface losses are neglected in this estimation. The value of the loss angle of the fused silica- Suprasil® for the internal modes is [127]

$$\phi_{sb} = 10^{-9}. \tag{4.23}$$

At present time one of the most convenient and low loss technique for bonding silica elements is the silicate bonding: a chemical process that enables the two elements to be bonded to reconstruct the crystalline structure of the material [76] . This process is largely used for bonding the ears of Virgo mirrors [100] [141, 51]. The silicate bonding layers are only present in the configuration n.1 and n.3 where they are supposed to have a thickness of $h_{sibond} = 60nm$, value that is currently well controlled for Virgo [127]. The losses due to the silicate bonding are evaluated as the ratio between the strain energy accumulated by the silicate bonding volume U_{SiBond} and the strain energy stored by the mirror plus the silicate bonding layer $U_{mirr+SiBond}$, under the elastic deformation, multiplied by the intrinsic losses of the material composing the silicate bonding which has been estimated to have an average value of $\phi_{sibon} = 0.1$ [51]. In fact, recalling the formula 3.105:

$$\Phi_{layer}(\omega_{mode}) = h_{layer}\frac{dU_{layer}/dh}{U_{tot}}\phi_{layer}, \tag{4.24}$$

the term $h_{layer}\frac{dU_{layer}/dh}{U_{tot}}$ here corresponds to the strain energy ratio $\frac{U_{SiBond}}{U_{mirr+SiBond}}$ between the strain energy of the silicate bonding layer of $h_{sibond} = 60nm$, and the strain energy of the total system composed by the mirror plus its silicate bonding layers. Hence, the equation 4.24 assumes the form

$$\Phi_{SiBond} = \frac{U_{SiBond}}{U_{mirr+SiBond}}\phi_{sibon}, \tag{4.25}$$

where from the static analysis on ANSYS® with the Gaussian pressure $p(r)$ as constraint, I calculate both the strain energies U_{SiBond} of the layer drown with a $60nm$ thickness and of the mirror plus the silicate bonding layer $U_{mirr+SiBond}$. The obtained values for the three configurations and for the fixed mirror are given in the table 4.9.

The bonding layer is not the only lossy layer to be considered in the mirror thermal noise, but on the mirror surface there are some dielectric layers called coatings which cause losses. The laser used for QuRaG will have the same wavelength of Virgo's one, while the Fabry-Pérot cavity will have a higher finesse. Hence, as over estimation of the coating losses I can consider the QuRaG mirrors having the same characteristics of the end and input mirrors of Virgo for the transmittivity and reflectivity, hence the same kind of coatings. The coatings of the mirrors will be composed of several alternated dielectric layers of high and low reflection index materials, i.e. Ta_2O_5 and SiO_2. The end and input mirrors require different values of reflectivity and transmissivity, since the end mirror should be totally reflective, while the input mirror should also be partially transmitting, so that the overall thickness of the coating layers of the input and end mirrors is different. In the evaluation of the coating losses this is usually modeled by considering for the end and input mirrors different thickness of the high reflective and low reflective layers, as shown in table 4.8 [127].

For sake of simplicity, the analytical computation of the related thermal noise can be performed supposing that the coating covers the whole mirror front surface in the case of the end mirror, while for the fixed input mirror the coating will cover just a radius equal to the cylindrical mirror of configuration n.1, as shown in the figures of the meshing fig. 4.3 and fig. 4.4.

From the formula of eq. (4.24) the losses coming from the coatings are then the sum of the losses of each layer

$$\Phi_{coat} = \frac{U_{HR}}{U_{mirr+HR}}\phi_{HR} + \frac{U_{LR}}{U_{mirr+LR}}\phi_{LR}, \tag{4.26}$$

made of high HR and low LR reflective material, tantalum pentoxide Ta_2O_5 and silica SiO_2 respectively [8, 118, 127]. The coatings of QuRaG have the properties summarized in the table 4.8.

	Materials	High R Ta_2O_5	Low R SiO_2
Properties			
density	$\rho\ (kg/m^3)$	8200	2200
Young's Modulus	$Y\ (GPa)$	140	72.2
Poisson's ratio	σ	0.26	0.167
loss angle	ϕ	$2 \cdot 10^{-4}$	$5 \cdot 10^{-5}$
thickness INPUT mirror	$t_I\ (\mu m)$	0.956	2.388
thickness END mirror	$t_E\ (\mu m)$	2.393	4.1086

Table 4.8: Characteristic parameters for the coatings of QuRaG end and input mirrors [127].

The total strain energies of the mirrors and the loss angles calculated according in the equations (4.25) and (4.26) for the suspended end mirrors of the three configurations and for the fixed input mirror, are listed in the table 4.9. I recall that for configurations n.1 and n.3 the total loss angle is

$$\Phi_{1,3} = \phi_{sb} + \Phi_{SiBond} + \Phi_{coat}, \tag{4.27}$$

	End mirror n.1	End Mirror n.2	End Mirror n.3	Input Mirror
U (J/N^2)	$2.2 \cdot 10^{-8}$	$1.97 \cdot 10^{-8}$	$2.23 \cdot 10^{-8}$	$9.72 \cdot 10^{-8}$
Φ_{coat}	$1.41 \cdot 10^{-6}$	$6.07 \cdot 10^{-6}$	$1.08 \cdot 10^{-6}$	$3.06 \cdot 10^{-9}$
Φ_{SiBond}	$1.82 \cdot 10^{-6}$		$3.26 \cdot 10^{-7}$	
Φ_{excess}				$1.03 \cdot 10^{-9}$

Table 4.9: Values calculated with ANSYS® simulations. The strain energies U are directly derived, while the other loss angles are calculated as explained in the relative formulas of eqs.4.25 and 4.26.

while in the configuration n.2 there is no silicate bonding, therefore

$$\Phi_2 = \phi_{sb} + \Phi_{coat}. \tag{4.28}$$

For the fixed input mirror the total loss angle is given by the bulk structural losses, the coating losses, the excess losses, and the thermoelastic losses

$$\Phi_{Fix}(\omega) = \phi_{sb} + \Phi_{coatfix} + \phi_{efix} + \phi_{tefix}(\omega), \tag{4.29}$$

since in fact the excess losses depend on the surface to volume ratio, and the thermoelastic losses are generated by the temperature gradient created by the flexural bending of the input mirror. For this reason the thermoelastic losses of the fixed mirror can be estimated by considering it as a cantilever beam [74].
Not only the excess and thermoelastic losses but also the strain energy of the fixed mirror can be calculated considering it as an oscillating cantilever beam [74]. In fact, when the laser beam is resonating within the FP cavity, on the intra-cavity face of the fixed mirror, close to its free end, it impinges a pressure that will excite the mirror flexural modes. The mode of order zero appears at about $5kHz$ according to the mode mapping results (see modes 102 and 103 of the table 4.2). Thus in order to compare the ANSYS® result to the analytical result, the parallelepiped fix mirror can be approximated as a cantilever beam. From Euler-Bernoulli beam theory [4, 80], the transverse displacement $w(x)$ of a cantilever beam placed along x direction, when a shear force F is acting on the free end, is

$$w(x) = \frac{F}{6YI}\left(3Lx^2 - x^3\right), \tag{4.30}$$

where L is the cantilever beam length, Y is the Young's modulus and I is the second moment of area, that for a beam of rectangular section is [74]

$$I = \frac{wt^3}{12}, \tag{4.31}$$

where t is the dimension in the direction of the displacement and w is the other dimension of the section area. In this case w is the width and t the thickness of the fixed mirror (see the table 4.5). Then the strain energy for a cantilever beam is [2]

$$U_{cb} = \int \frac{M^2 dx}{2YI}, \tag{4.32}$$

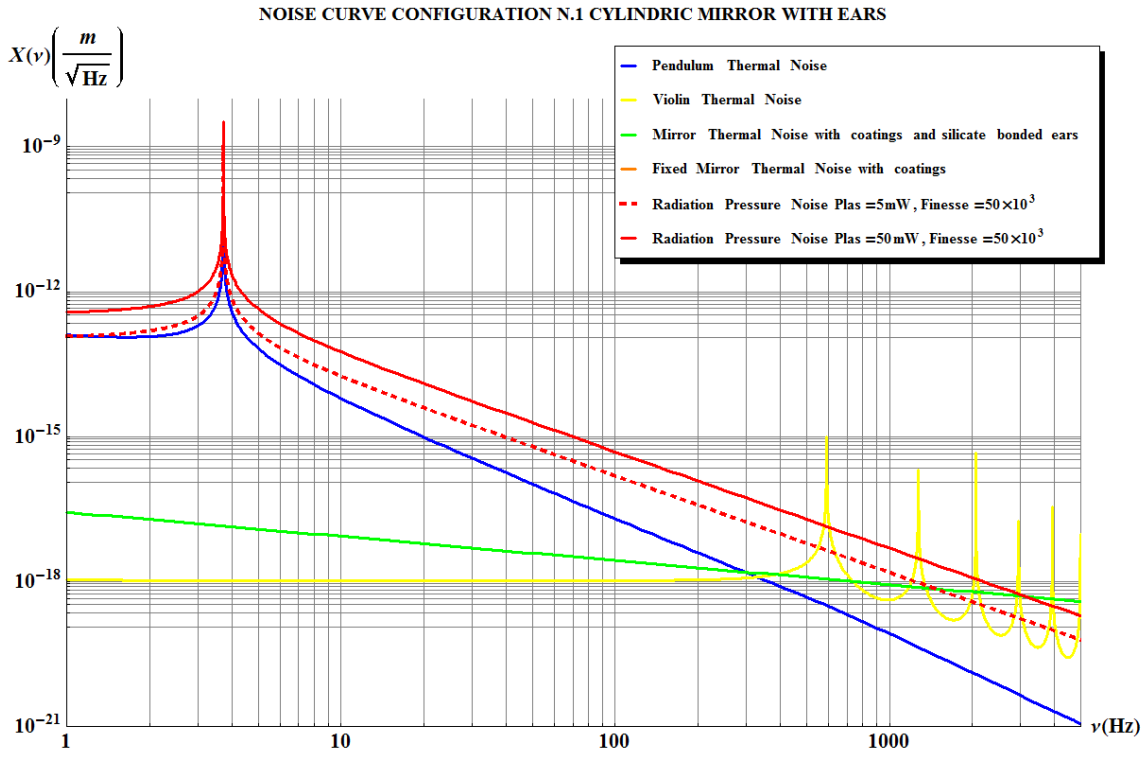

Figure 4.7: Noise Budget for the Cylindrical mirror with silicate bonded ears (configuration n.1). The Quantum Radiation Pressure Noise with laser power $5mW$ (red dashed curve) and $50mW$ (red curve) are higher then the Pendulum Thermal Noise (blue curve), the Violin Thermal Noise (yellow curve) and the Mirror Thermal Noise (green curve). The last one is much lower, but the pendulum thermal noise is not low enough compared to the radiation pressure noise in the detection band.

where M is the bending moment. Y and I can be considered constant along the beam axis x, but M is x dependent [4]

$$M(x) = -YI\frac{d^2w}{dx^2}, \tag{4.33}$$

so in this case the bending moment along the beam is

$$M(x) = -F(L-x). \tag{4.34}$$

In the case of the QuRaG fixed mirror on the ANSYS® static analysis the pressure profile impinging on the mirror is normalized, therefore the force F is equal to $1N$ and eqs. (4.30) and (4.34) become:

$$w(x) = \frac{1}{6YI}\left(3Lx^2 - x^3\right) \tag{4.35}$$

$$M(x) = -(L-x). \tag{4.36}$$

Moreover, I should take into account the fact that the shear force is acting at a distance $a = 5mm$ from the free end of the cantilever beam, so the strain energy is

$$U_{cb} = \frac{1}{2Y_sI}\int_0^{(L-a)}(L-x)^2dx = 3.40\cdot 10^{-7}J/N^2, \tag{4.37}$$

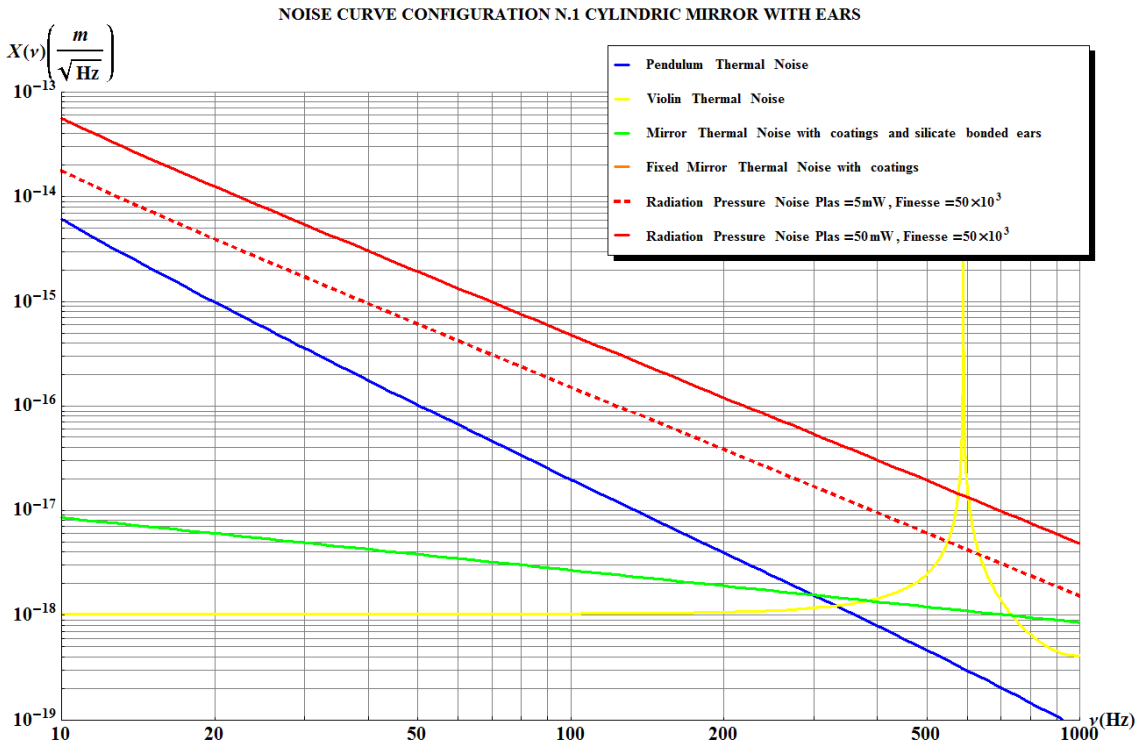

Figure 4.8: Zoom of the previous graphics (4.7) in the frequency range $(10 - 1000)Hz$.

where Y_s is the Young's modulus of the fused silica. The analytic result is 3.5 times greater than the result obtained from the simulations. This can be explained by the fact that the geometry of the parallelepiped input mirror is not very well approximated by a cantilever beam. Therefore, the value of strain energy estimated with the simulation (see tab. 4.9) is more accurate and it should be used in the estimation of the thermal noise associated with the flexural bending mode of the fixed mirror. Nevertheless, the loss mechanisms present in the bending motion of the cantilever can be approximated with those of a ribbon fiber, hence I used this approach for estimating the excess and thermoelastic losses of the fixed mirror. Therefore, the total loss angle is again given by the sum of the four contributions: the internal losses for bulk modes ϕ_{sb}, the excess losses ϕ_{efix}, the thermoelastic losses $\phi_{tefix}(\omega)$ and the coating losses $\phi_{coatfix}$. The first term is given by eq.(4.23). The loss angle due to the surface losses is [74]

$$\phi_{efix} = \mu \frac{t}{V_f/S_f} = 2L\frac{(3+a)(w+t)}{(1+a)(wt)}\phi_{si_{bulk}} \tag{4.38}$$

where V_f is the volume, S_f is the lateral surface of the fixed mirror and L, w, t are its dimensions respectively length, width and thickness (see table 4.5). I recall that the geometrical factor μ for a ribbon fiber is [74]

$$\mu = \frac{(3+a)}{(1+a)}, \tag{4.39}$$

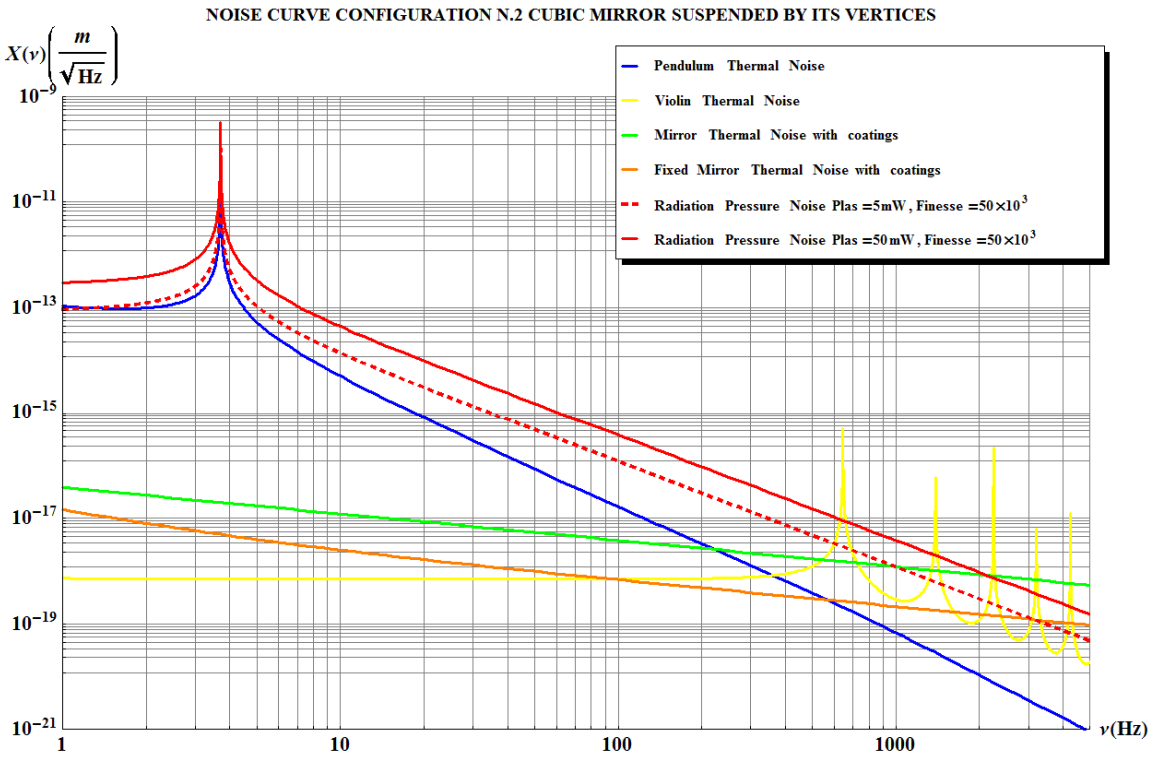

Figure 4.9: Noise Budget for the cubic mirror suspended by its vertices (configuration n.2). The Quantum Radiation Pressure Noise with laser power $5mW$ (red dashed curve) and $50mW$ (red curve) are higher then the Pendulum Thermal Noise (blue curve), the Violin Thermal Noise (yellow curve) and the Mirror Thermal Noise (green curve). The last one is much lower, but the pendulum thermal noise is not low enough compared to the radiation pressure noise in the detection band. The thermal noise of the fixed mirror (orange curve) is also lower than the radiation pressure noise.

where the term a is the aspect ratio given by the thickness over the width of the fiber section $a = t/w$, while the surface to volume ratio becomes

$$\frac{S_f}{V_f} = \frac{2(w+t)}{(wt)}. \tag{4.40}$$

Therefore, the loss angle related to the surface losses for the fixed mirror is equal to

$$\phi_{efix} = 1.03 \cdot 10^{-9}. \tag{4.41}$$

I also recall that the thermoelastic loss angle for a ribbon has the same form as for a cylindrical fiber [74]

$$\phi_{tefix}(\omega) = \Delta_f \frac{\omega\tau_f}{1+(\omega\tau_f)^2}, \tag{4.42}$$

where as first approximation the parameter Δ_f is the same

$$\Delta_f = \frac{Y_s T}{C_s \rho_s}\alpha_s^2 = 3.24 \cdot 10^{-6} \tag{4.43}$$

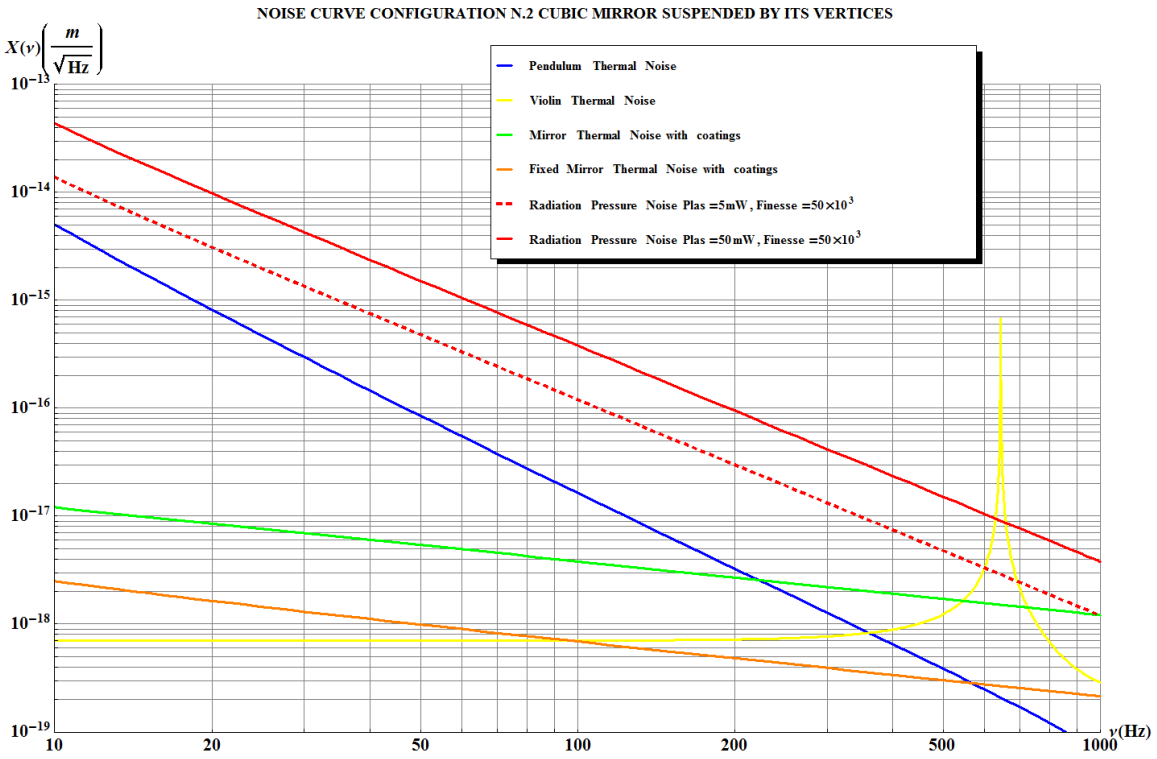

Figure 4.10: Zoom of the previous graphics (4.9) in the frequency range $(10 - 1000)Hz$.

but the time constant τ_f, at which the temperature gradient decays in the fundamental eigenmode differs [74]

$$\tau_f = \frac{C_s \rho_s}{\kappa_s} \left(\frac{t}{\pi} \right)^2 = 3.12s \tag{4.44}$$

where all the characteristic parameter of the silica are listed in the table 4.12.

From the power spectrum of the thermal noise in the Levin approach of eq. (3.91) the fixed mirrors fluctuations are described by

$$X_{Levin-fix}(\omega) = \sqrt{2 \frac{8 k_b T}{\omega} U_{fix} \phi_f(\omega)}, \tag{4.45}$$

where the factor 2 takes into account the fact that the fixed mirror are two.

4.3.4 Thermal and Quantum Noise Level Comparison

The thermal noise of each configuration, evaluated as explained in the previous sections, should be now compared with the quantum radiation pressure noise. In fact, in order to be compatible with our requirements, i.e. being sensitive to the effect of the quantum radiation pressure on the suspended mirror, the mirror suspension system must have the thermal noise level, both of the suspensions and of the mirror, lower than the radiation pressure noise in the detection band of QuRaG.

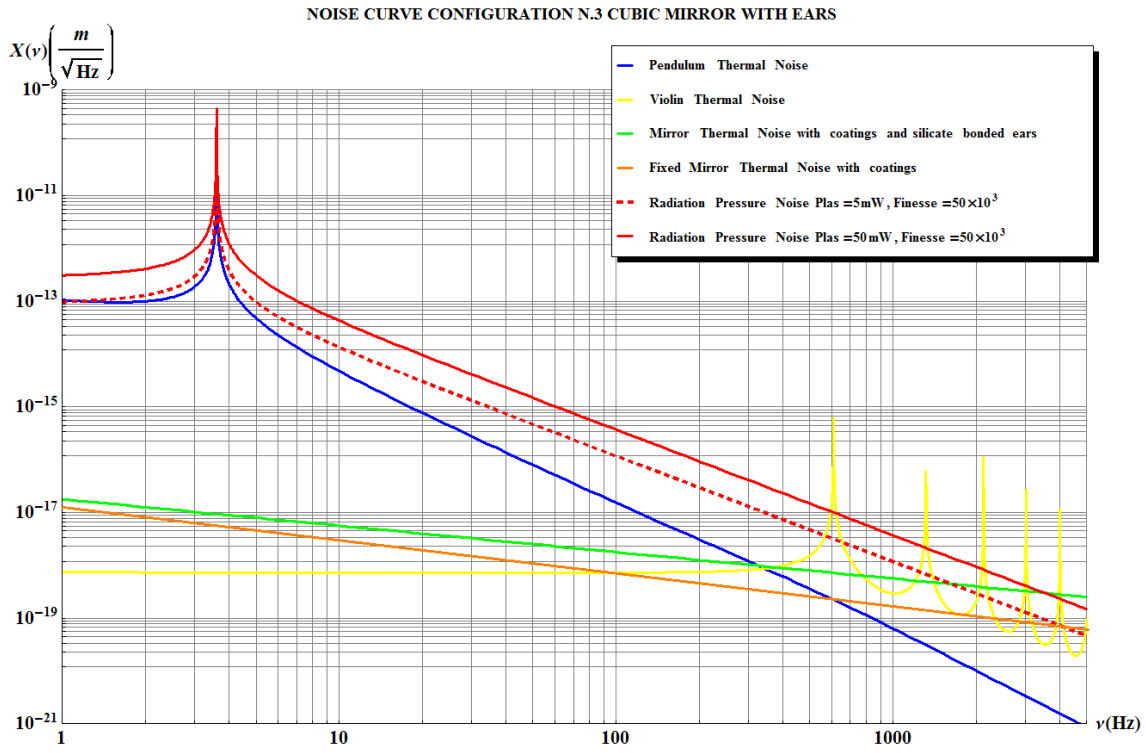

Figure 4.11: Noise Budget for the cubic mirror with silicate bonded ears (configuration n.3). The Quantum Radiation Pressure Noise with laser power $5mW$ (red dashed curve) and $50mW$ (red curve) are higher then the Pendulum Thermal Noise (blue curve), the Violin Thermal Noise (yellow curve) and the Mirror Thermal Noise (green curve). The last one is much lower, but the pendulum thermal noise is not low enough compared to the radiation pressure noise in the detection band. The thermal noise of the fixed mirror (orange curve) is also lower than the radiation pressure noise.

The radiation pressure noise of a suspended mirror as in the configurations proposed in the previous section, can be modeled as described in section 2.5.2 by the equation 2.37:

$$X_{RP}(\omega) = \sqrt{2}\frac{2\mathcal{F}}{\pi}\sqrt{\frac{8hP_{las}}{\lambda c}}\sqrt{\frac{1/m^2}{\left(\left(\omega_p^2-\omega^2\right)^2+\left(\omega_p^2\phi_p(\omega)\right)^2\right)}} \tag{4.46}$$

where m is the mass of the suspended mirror (see tab.4.5), $\mathcal{F}$ the *finesse* of the Fabry-Pérot cavity, P_{las} the power of the laser, λ the laser's wavelength (for a Nd:YAG is $\lambda = 1.064\mu m$), h the Planck's constant and c the speed of light. The values of the laser's power and the finesse of the cavity are reasonably set to be $P_{las} = 5mW$ or $P_{las} = 50mW$ and $F = 5 \cdot 10^4$. The noise budget of each configuration is shown in the figures 4.7, 4.8, 4.9,4.10, 4.11, 4.12, while all the three configurations are compared in figure 4.13. The pendulum and violin thermal noises constitute the total suspension thermal noise, and they sum as

$$X_{susp}(\omega) = \sqrt{X_{th}^2(\omega) + X_{viol}^2(\omega)}. \tag{4.47}$$

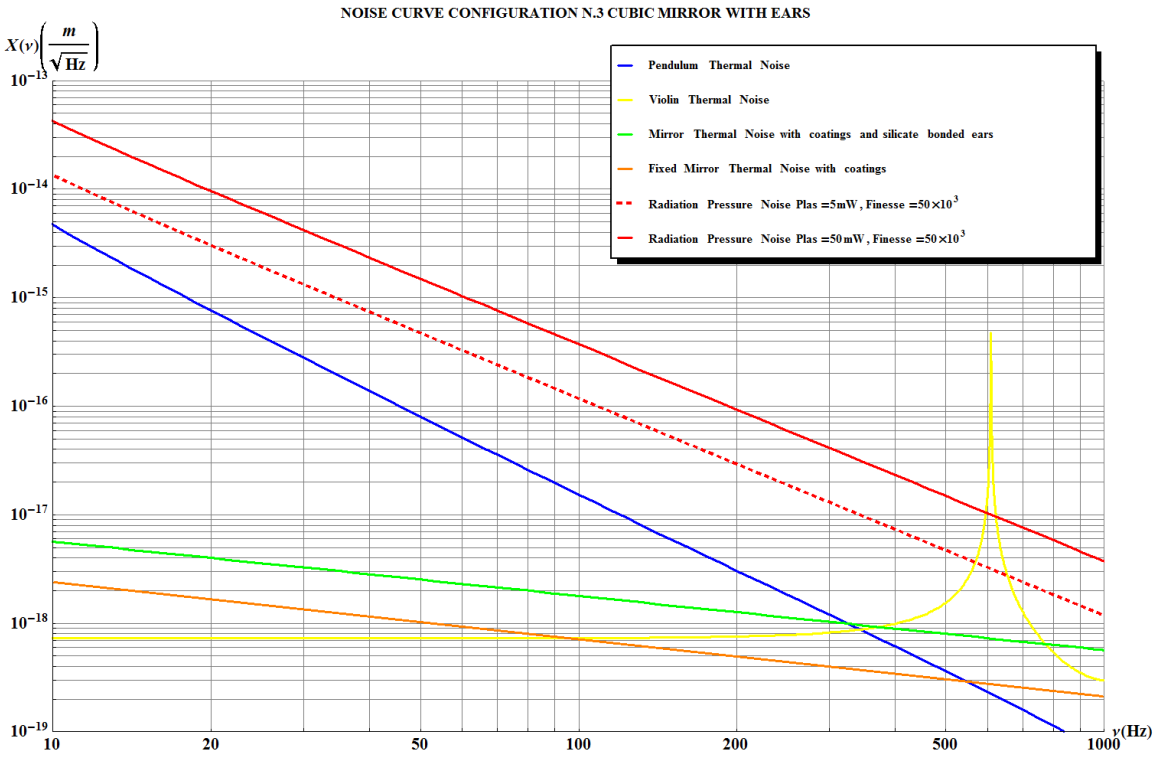

Figure 4.12: Zoom of the previous graphics (4.11) in the frequency range $(10 - 1000)Hz$.

This simplifies the graphic of the noise budget comparison of the three configurations (see fig. 4.13). The suspension thermal noise almost does not change in the three cases, but the radiation pressure noise is slightly more different, because the former depends on the inverse of the square root of the mirror mass, whereas the latter depends on the inverse of the mirror mass. Therefore, as expected, the radiation pressure noise increases as the mirror mass reduces. In the figure 4.13, it is also evident that the mirror thermal noise, which principally suffers from the coating and silicate bonding losses, varies for the three configurations. The configuration n.2 does not have silicate bonding, but the coating losses are higher than in case n.3, as shown in table 4.9. The best case among the three is the n.3, but, as already introduced at the beginning of this chapter, it seems almost impossible to realize it by silicate bonding such small ears to a such small mirror. Therefore, this result has been used as a guideline for the design of other configurations to test and that, little by little, let us approach to the final design.

A proposed solution for the realization of a configuration close to the case n.3, was a unique block, that I called cantilever, with an upper part, a thinner central ribbon having a cut in the middle thus to reproduce the two suspension wires, and a thicker end corresponding to the suspended mirror. In order to define the best dimensions for the central ribbon thickness and width of the cut (distance between the external corner of the central ribbon and the cut area), I made several ANSYS® modal analysis by changing these two parameters. I started with a thickness of $0.1mm$ and a cut width of $1mm$, but this gave a pendulum resonance at $19Hz$, too high for our requirements. In

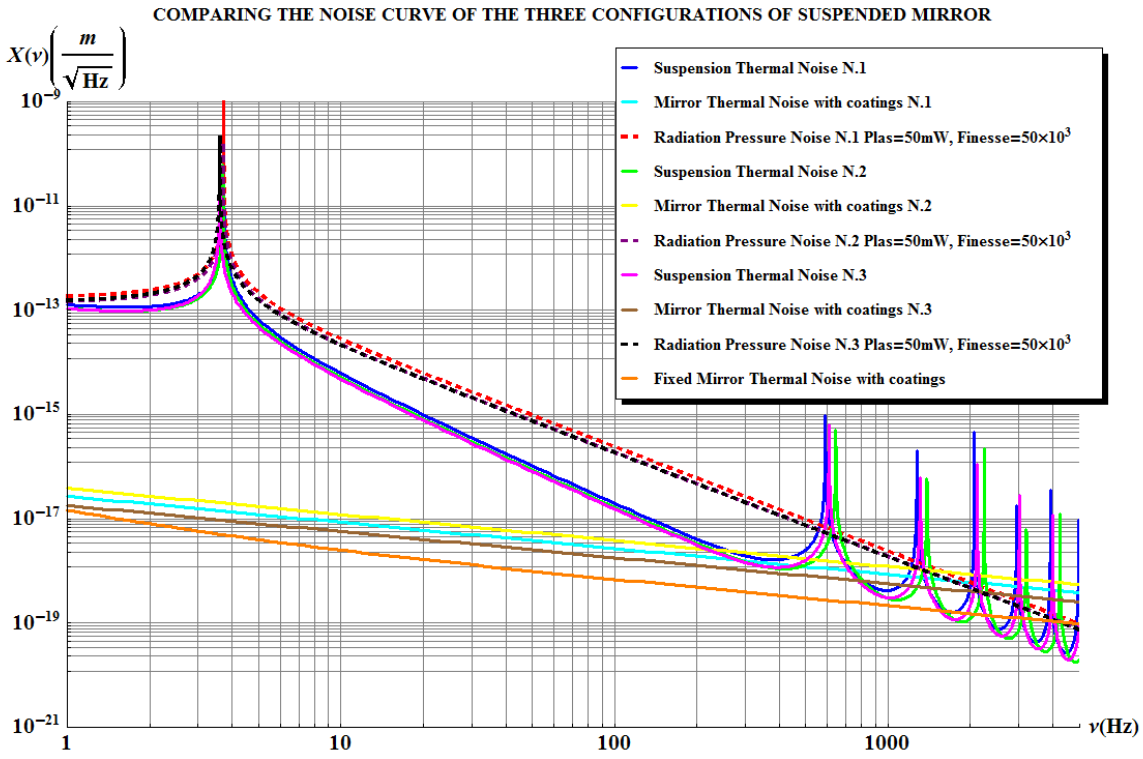

Figure 4.13: Comparison of the noise budget of the three configurations of suspension (n1, n.2 and n.3). The suspension thermal noise almost does not change in the three cases, but the radiation pressure noise is slightly more different, and the mirror thermal noise, cause it depends on the coating losses and silicate bonding. The best case among the three is the n.3.

fact QuRaG needs not to be dominated by thermal noise but only sensitive to radiation pressure noise in the frequency range $10Hz - 1kH$. Therefore, we thought to test in parallel the same configurations but made of an another material: the sapphire (see table 4.11). This material turned out to be more suitable for the cantilever configuration according to our requirements. In fact even increasing the length of the central ribbon from $20mm$ to $50mm$ the pendulum frequency is not enough reduced and the system whose pendulum frequency more approaches our requirements was made of sapphire (see table 4.10).

I obtained the best results for the configuration shown in the figure 4.14, having a thickness of $0.1mm$ and a cut with of $0.2mm$. This configuration, if made of suprasil has the pendulum resonance at $9Hz$. Whereas if made of sapphire, its pendulum frequency is lower, i.e. $6Hz$. Hence, the sapphire version better approaches the starting requirement of $3 - 4Hz$ for the pendulum resonance, that we set at the beginning in order to have a detection band starting from $10Hz$. Moreover, the first violin mode is at $855Hz$, which let QuRaG free from suspension thermal noise till almost $1kHz$. The most recent measurements of the mechanical losses of sapphire gave a mean value for the overall mechanical loss angle of about $\phi_z = 7 \cdot 10^{-7}$ at room temperature ($\simeq 300K$) [81]. I used this value as estimation of the sapphire ribbon losses (see fig. 4.15). This value is of course too much optimistic.

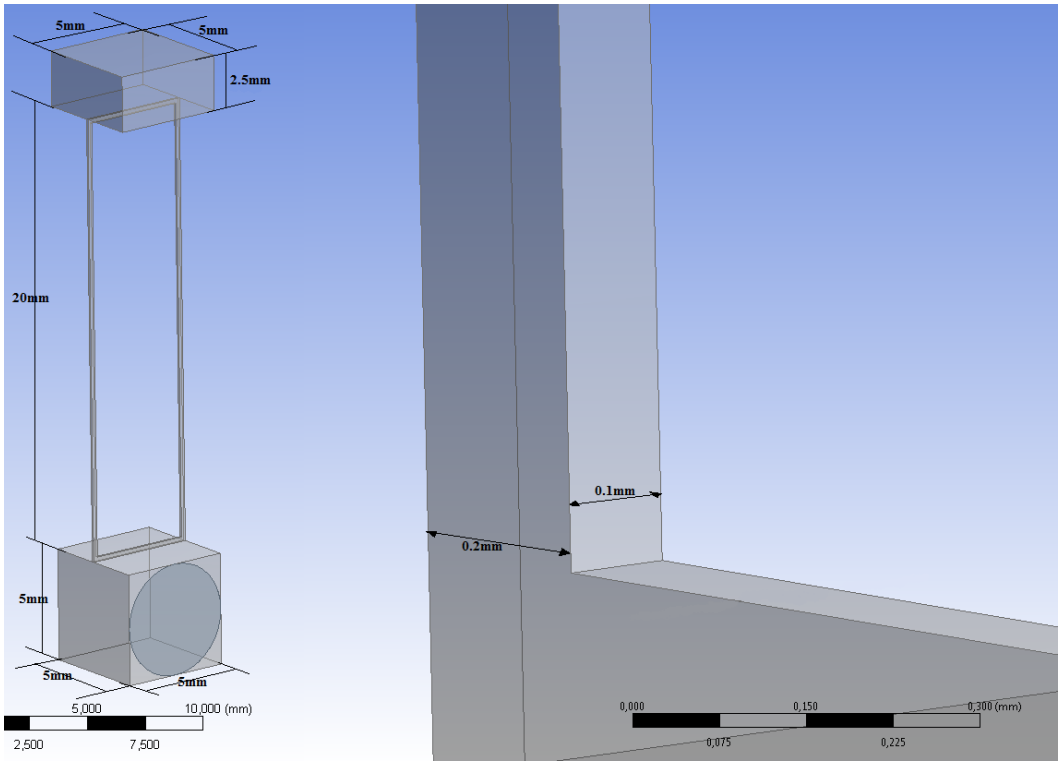

Figure 4.14: Suspension configuration proposed to IMPEX for a monolithic pendulum made of sapphire. The cut inside the central ribbon is necessary to lower the pendulum frequency. IMPEX rejected the configuration for the impossibility to realize the cut without an high risk of breaking the pendulum. They proposed other two configurations without cut (see fig. 4.17).

In fact further more detailed estimations gave a value for the total pendulum loss angle at the pendulum resonance a little higher, of about $2.47 \cdot 10^{-6}$, which implies a suspension thermal noise too high with respect to the radiation pressure noise with finesse $5 \cdot 10^4$ and laser power of $5mW$, and not low enough for the case with $P_{las} = 50mW$, as shown in fig.4.16. This estimation has been done according to the ribbon suspension excess and thermoelastic losses formulas of eqs. (4.38) and (4.42) for a ribbon suspension [74] made of sapphire [30], hence using the values of table 4.11. This kind of cut which realizes two suspension bars of section $0.1mm \times 0.2mm$ for $2cm$ length approaches a system of two wires having diameter of about $150\mu m$. More in detail, this configuration has an upper parallelepiped having sides of $5mm$ for $2.5mm$ height and a suspended cubic mirror of side $5mm$.

This cantilever system of figure 4.14 which gave the results shown in the graphics of fig. 4.15 has been submitted to the IMPEX Company [84] which answered that it would not be possible to realize the cut in a such thin sapphire ribbon without damaging it and thus breaking the monolithic block. Therefore, IMPEX proposed other two configurations (see fig. 4.17) without cut, but with central ribbon having width $2mm$ or $5mm$ and thickness $0.5mm$. But even the one with smaller ribbon of $2mm$ is still too thick and from ANSYS® modal simulations and thermal noise estimations resulted to be too rigid and not behaving has a pendulum, thus not sensitive to radiation pressure

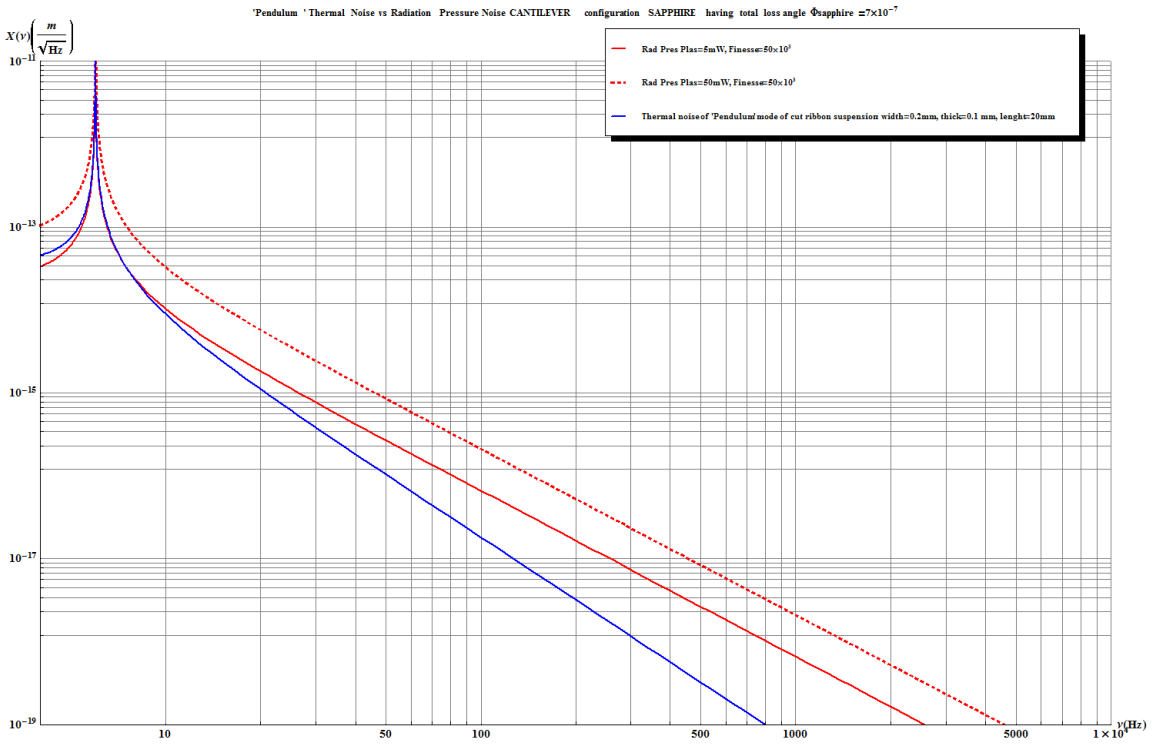

Figure 4.15: Comparison of the thermal noise of the cantilever system of fig. 4.14 (blue curve) vs its radiation pressure noise supposing a finesse of $5 \cdot 104$ and a laser power of $5mW$ (red curve), and $50mW$ (red dashed curve). The overall loss angle of the sapphire as been supposed to be $\phi_z = 7 \cdot 10^{-7}$ at room temperature ($\simeq 300K$) [81].

noise. In fact it has a 'pendulum' resonance at $302Hz$ and its suspension thermal noise budget vs the radiation pressure noise is too high, even supposing a too optimistic loss angle of $\phi_z = 7 \cdot 10^{-7}$, as shown in fig. 4.18. Therefore, we evolved the cantilever configuration to a double cantilever system in such a way to reduce the pendulum frequency, but the suspension system was still too rigid to be sensitive to radiation pressure noise. Thus, the cantilever configuration had to be abandoned and we moved to the idea of a double pendulum, where the first stage has the function of significantly attenuate the transmission of the vibrations to the mirror. In the following section I will describe in detail the double pendulum system since is the one that it has been validated by my thermal noise estimations with ANSYS® simulations.

4.4 The Best Suspension Configuration: the Double Stage Pendulum

After the study of a large number of configurations, the most promising one turned out to be a monolithic double pendulum system composed by a first suspension stage, called marionette, by analogy with Virgo, which then holds the light mirror by means of two fused silica wires of about $40\mu m$ diameter. This configuration, shown in figure

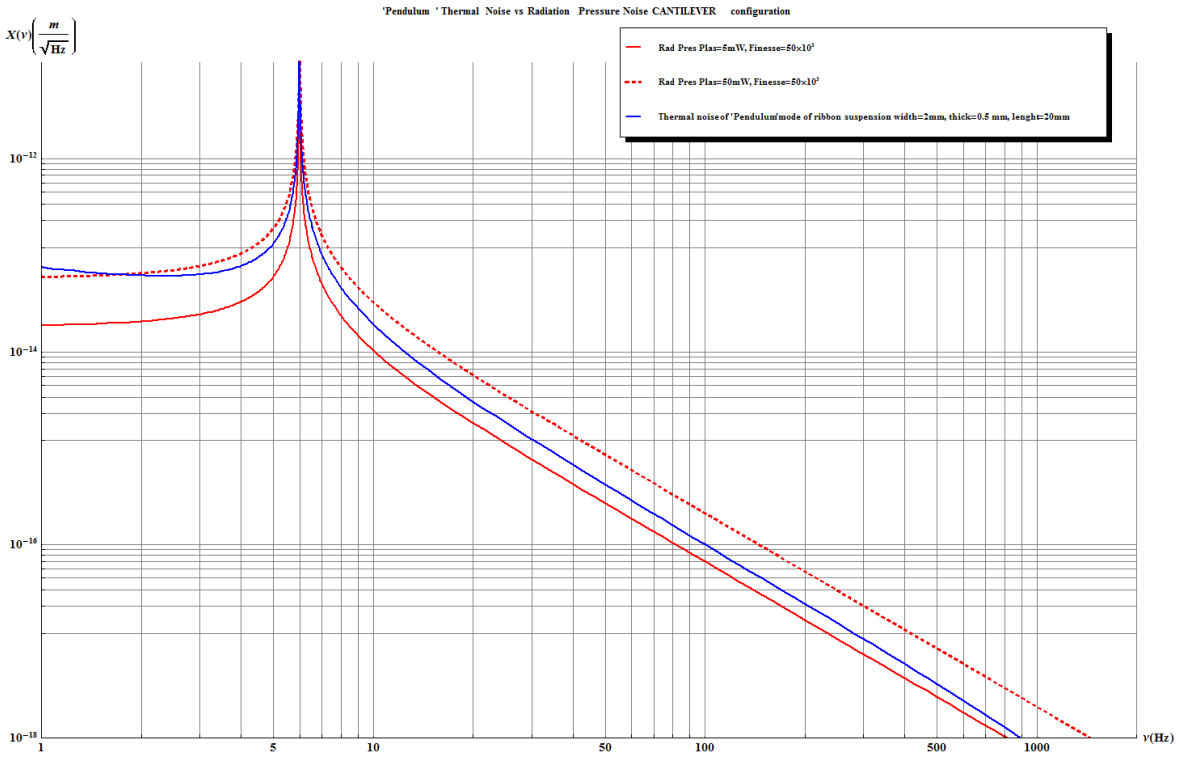

Figure 4.16: Comparison of the thermal noise of the cantilever system of fig. 4.14 (blue curve) vs its radiation pressure noise supposing a finesse of $5 \cdot 104$ and a laser power of $5mW$ (red curve), and $50mW$ (red dashed curve). The overall loss angle of the sapphire as been calculated considering a ribbon-like suspensions [74] and using the values of table 4.11, according to [30].

4.19, assures the desired detection band for QuRaG between $10Hz$ and $1kHz$. The marionette has a cross shape composed by two arms of $43mm$ length for $3mm$ thickness and $5mm$ height, and it is suspended to the interferometer disk by a suspension wire, that I will call marionette wire, having radius $100\mu m$ and length $22mm$. In reality, only one arm of the marionette is a unique block of $43mm$, and the other is composed by attaching to the long one two smaller arms of $20mm$ length each one by a waterglass layer of $60nm$ thickness. On the lower part of the marionette another layer of waterglass allows to attach a parallelepiped that is the twin of the mirror, which has square section of $3mm \times 3mm$ and height $4mm$. The mirror is then joined to his twin by two suspension wires having $40\mu m$ diameter and $20mm$ length always by means of waterglass layers of $60nm$. The tapered end parts of each wire are modeled as made of a pyramid of $1mm$ height and side on a cube of $1mm$ side. For the sake of simplicity all the upper stages are summarized in a parallelepiped of base area $10mm \times 10mm$ and height $5mm$, that I will call support.

Moreover, the advantage of a double stage is that the first stage will attenuate the vibrations transmitted by the interferometer disk to the suspended end mirror, and the clamping losses due to the attaching system to the big ITF disk will affect less the thermal noise. Only the clamping system of the last stage will affect the mirror thermal noise and the complexity of attaching the mirror to its suspension wires is not reduced.

thickness (mm)	cut width (mm)	length (mm)	material	$\nu_{pend}(Hz)$	$\nu_{Iviolin}(Hz)$
0.1	0.2	20	sapphire	6	855
0.1	0.2	20	suprasil	9	1640
0.1	1	20	suprasil	19	1750
0.2	1	20	suprasil	53	3424
0.1	no cut all width $5mm$	20	suprasil	27	1592
0.2	no cut all width $5mm$	20	suprasil	75	3365
0.5	no cut all width $5mm$	20	sapphire	471	15378
0.5	2	20	sapphire	301	13379
0.5	no cut all width $5mm$	20	suprasil	288	9334
0.5	2	20	suprasil	185	8183
0.5	2	30	suprasil	107	4282
0.5	2	40	suprasil	71	2816
0.5	2	50	suprasil	51	2025

Table 4.10: Characteristics used to test the cantilever configuration. By varying the thickness and length of the cantilever and eventually introducing a cut in the cantilever I tested which configuration and which material between suprasil and sapphire material better suit QuRaG requirements. The best one is described in the first line of the table.

Young's Modulus	Y_z	$392GPa$
Poisson's Ratio	σ_z	0.309
volume density	ρ_z	$3.99kgm^{-3}$
thermal conductivity	K_z	$70Wm^{-1}K^{-1}$
specific heat	C_z	$780Jkg^{-1}K^{-1}$
linear expansion coefficient	α_z	$5.59 \cdot 10^{-6}K^{-1}$
intrinsic loss angle	ϕ_z	$3.00 \cdot 10^{-9}$

Table 4.11: Elastic and thermodynamics parameters of the sapphire used for the ANSYS® modal analysis [30]. For the Poisson's ratio I used the value of [98].

Another advantage of having a double stage is that the electromagnetic control can be applied on the marionette, although the electrostatic control should be applied on the mirror. Nevertheless, the complexity of this system required the application of the modal analysis for the mirror's suspension thermal noise, that I opportunely adapted on the double pendulum system, starting from the modal analysis theory [158] [127]. Note that in this configuration I abandoned the silicate bonding for the waterglass, known to be more lossy than the silicate bonding, but a priori not limiting for this configuration and more easy to adapt to our experiment. I considered for the waterglass, the same thickness of the silicate bonding layer of the previous configurations, i.e. $60nm$, and I took into account the fact that it has the same intrinsic loss angle equal to 0.1.

4.4.1 The Modal Approach for the Thermal Noise Estimation

Although the modal approach discussed in sec. 3.4.1 was only referred to the thermal noise of the mirror, it is a very powerful method that allows to estimate the thermal noise of a generic complex system, as the suspension system of QuRaG. In fact, the modal analysis on ANSYS® allows us to get the internal modes of the whole system and to evaluate the relative mirror displacement associated to them. The total suspension thermal noise is then given by the sum of all these modes. Nevertheless, it is possible to approximate the suspension thermal noise by only taking into account the modes that more affect the position of the mirror along the ITF optical axis since those are the modes which give a greater contribution to the thermal noise. As already explained, the Fluctuation-Dissipation Theorem [93] states that the power spectrum of the thermal noise of the mirror suspensions is the sum of the contribution of all these modes

$$X^2_{modal}(\omega) = 2\frac{4k_BT}{\omega}\sum_{i=1}^{n}\frac{1}{M_i}\frac{\omega_i^2\Phi_i(\omega)}{((\omega_i^2-\omega^2)^2+(\omega_i^2\Phi_i(\omega))^2)} \tag{4.48}$$

where T is the temperature, k_B is the Boltzmann constant, and M_i, ω_i and $\phi_i(\omega)$ are respectively the equivalent mass, the angular frequency and the loss angle associated with the *i-th* mode and the factor 2 accounts for the fact that the whole QuRaG interferometer will have two suspended end mirrors.

The modal analysis on ANSYS®, calculated including gravity force, gives the modes of the system and the relative frequencies ω_i, while the evaluation of the equivalent mass and of the loss angle of each mode requires more calculations.

The Equivalent Mass of the *i-th* mode

In the modal approach the complex double pendulum system can be described as the discrete sum of harmonic oscillators, each one corresponding to a mode of the system. The elastic energy of each oscillator is equal to the strain energy of the corresponding mode

$$\frac{1}{2}M_i\omega_i^2(x_i^{eq})^2 = \frac{1}{2}\omega_i^2\int_{volume}\rho|w_i|^2dV \tag{4.49}$$

where ρ is the mirror density and w_i is the mirror deformation vector of the *i-th* mode [158] [127]. The integral of this equation gives the amplitude of the oscillation, that can arbitrary be normalized. By default, ANSYS® does the so called mass normalization, which means setting the integral equal to 1. Moreover the equivalent coordinate x_i^{eq} associated to the *i-th* mode can be calculated from the mirror displacement along the optical axis $u_i(S)$ in function of the surface S of the mirror since it is defined as

$$x_i^{eq} = \int_{Surface}u_i(S)P(\vec{r})dS = \Big|\frac{1}{S}\int_{Surface}u_i(S)dS\Big|, \tag{4.50}$$

where in the present modal analysis, which aims to calculate the thermal noise of the suspensions, no pressure is applied on the mirror surface, hence the weighting term in

the eq. 4.50 has then been set equal to 1. The associated equivalent mass is then

$$M_i = \frac{1}{\left|\frac{1}{S}\int_{Surface} u_i(S)dS\right|^2}. \tag{4.51}$$

For the observed modes of the mirror along the optical axis, in the modal analysis with ANSYS®, the mirror's surface displacement vector $u_i(S)$ can be approximated as $u_i(S) = h_\perp u_i(y)$, where $h_\perp = 3mm$ is the mirror dimension along the axis orthogonal to the vertical axis and to the optical axis. In fact, the mirror's surface deformation associated with these modes only occurs in the vertical direction y, i.e. the direction of the acceleration of gravity. Moreover, since the two end mirrors are identically suspended I only made the modal analysis on one double stage pendulum, the one which has the optical axis along z and which is represented in fig.4.19, hence $h_\perp = h_x$. The mirror dimension along z is $h_z = h_x = 3mm$, while the other dimension along the vertical y is $h_y = 4mm$. The integral for the estimation of the equivalent coordinate x_i^{eq} and of the equivalent mass M_i then simplifies as

$$M_i = \frac{1}{\left|\frac{1}{h_y}\int_0^{h_y} u_i(y)dy\right|^2}, \tag{4.52}$$

where I have set to 0 the coordinate y at the beginning of the mirror displacement profile in y.

The total loss angle of the *i-th* mode

The total loss angle for each mode is given by the sum of all the loss angles corresponding to the dissipation mechanisms which occur for the given mode [127]. Therefore, I model the total loss angle of the *i-th* mode as

$$\begin{aligned}&\Phi_i(\omega) = \\ &\phi_s + \phi_i^{WGmir} + \phi_i^{WGup} + D_i^{mir}\Big(\phi_{e_{mir}} + \phi_{te_{mir}}(\omega)\Big) + D_i^{up}\Big(\phi_{e_{up}} + \phi_{te_{up}}(\omega)\Big)\end{aligned} \tag{4.53}$$

which is essentially given by four kinds of contributions:

- the intrinsic losses of the material ϕ_s,
- the surface losses and the excess losses $\phi_{e_{mir}}$ and the thermoelastic losses $\phi_{te_{mir}}(\omega)$ of the mirror suspensions multiplied by the inverse of their dilution factor[1] D_i^{mir} for the *i-th* mode,
- the surface losses and the excess losses $\phi_{e_{up}}$ and the thermoelastic losses $\phi_{te_{up}}(\omega)$ of the marionette suspension wire multiplied by the inverse of their dilution factor D_i^{up} for the *i-th* mode,

[1]Note that the D_i are the inverse of the previously defined dilution factors, but for making the notation more 'light' I omitted the $^{-1}$.

- the losses due to the waterglass layers for attaching the mirror suspension wires ϕ_i^{WGmir} (which are 4 layers, 1 for each end of the wire),
- the losses due to the waterglass layers for attaching the marionette suspension wire ϕ_i^{WGup} (which are 2 layers, 1 for each wire's end).

This method allows to take into account in each mode the contribution of all the suspensions of the system opportunely weighted by their dilution factors. Note that the waterglass losses are already estimated as a strain energy ratio, therefore they should not be multiplied by any other dilution factor.

The dilution factor are calculated as the ratios between the strain energy of the considered suspensions for the *i-th* mode over the total energy of the mode

$$\begin{aligned} D_i^{mir} &= \frac{U_{mirw}}{U_{tot}}\Big|_i \\ D_i^{up} &= \frac{U_{upw}}{U_{tot}}\Big|_i \end{aligned} \tag{4.54}$$

which being more precise are the inverse of the dilution factor as defined in [125] and take into account the fraction of the strain energy accumulated by the considered suspension (at the upper or mirror stage) which is different for each mode.

The waterglass losses are calculated as the energy ratio between the strain energy of the waterglass layers and the total energy of the system multiplied by the intrinsic loss angle of the waterglass ϕ_{WG} which is known to be equal to 0.1 [127]. The thickness of the layer has also been supposed $t_{WG} = 60nm$, as for the anchoring system of Virgo+ [127].

$$\begin{aligned} \phi_i^{WGmir} &= \frac{U_{WGmirw}}{U_{tot}}\Big|_i \phi_{WG} \\ \phi_i^{WGup} &= \frac{U_{WGupw}}{U_{tot}}\Big|_i \phi_{WG} \end{aligned} \tag{4.55}$$

The internal loss angle of the Suprasil® fused silica is [125]

$$\phi_s = 4.1 \cdot 10^{-10}. \tag{4.56}$$

The surface losses for a cylindrical fiber, as already explained in this chapter, can be estimated by the eq.(4.8), and the thermoelastic losses using the eq.(4.10). Then, for the double pendulum mirror $\phi_{e_{mir}}$, $\phi_{te_{mir}}(\omega)$ and marionette $\phi_{e_{up}}$, $\phi_{te_{up}}(\omega)$ suspension surface and thermoelastic losses, I just take into account the fact that the mirror wires are two and have radius $20\mu m$ and length $20mm$, while the marionette wire has radius $100\mu m$ and length $22mm$. The fused silica parameter that are involved in the loss angle estimations are summarized in tab.4.12.

4.4.2 Mode Mapping of the Double Pendulum System

The first step for the modal analysis of the double pendulum suspension system is to do the mode mapping. The modal analysis on ANSYS® in presence of the acceleration

specific heat	C	$772 J/(kg \cdot K)$
volume density	ρ	$2.2 \cdot 10^3 kg/m^3$
thermal conductivity	κ	$1.38 W/(m \cdot kg)$
thermal expansion coefficient	α	$0.51 \cdot 10^{-6} m/(m \cdot K)$
relative thermal gradient coefficient	β	$1.86 \cdot 10^{-4} (1/K)$
Young's Modulus	Y	$7.29 \cdot 10^{10} Pa$

Table 4.12: Characteristic elastic and thermodynamics parameters of silica [122].

of gravity along the vertical axis y and the upper side of the support set as fixed, allows to obtain all the proper modes of the system. In order to optimize the computational time I have done the analysis in the frequency range 0-20kHz, which is largely within the detection band of QuRaG. For the description of the modes, it is important to fix the cardinal axis: the y axis is along the vertical, the z axis is the optical axis, the x axis is the orthogonal to the others two, as shown in figure 4.19. Since the thermal noise of the suspensions is related to the displacement of the mirror along the optical axis, in the thermal noise analysis I will only take into account the modes that more affect the mirror position along this axis. From the table of the mode mapping tab.4.13, the pendulum mode is at 5.29Hz, and since the system is a double pendulum, there is a second pendulum mode at 3.48Hz which corresponds to the pendulum mode of the whole double pendulum. In the observed frequency range appear the violin modes of the mirror wires till the order IX and the violin modes of the marionette wire till the order IV. Since for each wire there are two directions of oscillation for the violin modes (transverse to the wire), therefore, in the mode mapping, there are four modes for each order of the mirror wires violins, and two modes for each order of the marionette wire violins. However, in the analysis I only take into account the violin modes of oscillation along the optical axis direction, and in particular for the two mirror wires I consider the violin modes in which both wires oscillate in phase. In this manner I can have one mode for each violin order. There are also some torsional modes (2, $6-9$) and some internal modes of the marionette which are not important for the thermal noise estimations since they do not affect the mirror position along the optical axis. Nevertheless, it is necessary to evaluate the contribution of the torsional modes which can affect the mirror position sensed by the laser along the optical axis, like the torsional mode of the mirror along the x axis of fig.4.19, i.e. the mode 15.

The selected modes are therefore the pendulum modes along the optical axis (modes n.3 and n.5, shown in figure 4.20) the violin modes of the mirror wires (see fig. 4.22 and 4.23), the violin modes of the marionette wire, the torsional modes tX of the mirror and the vertical mode of the total system (mode n.14, see fig.4.21) and of the mirror (mode n.20). As effect of the elasticity of the suspensions, there is also a vertical mode of the total system induced by the marionette wire, and a vertical mode of the mirror induced by the mirror wires. These modes may affect the mirror position along the optical axis, therefore it is preferable to take into account those modes in the total suspensions thermal noise. As for the other modes, the coupling coefficient of these modes with

N MODE	$\nu(Hz)$	DESCRIPTION OF THE MODE
1	3.2565	double pendX
2	3.3653	tY marionette
3	3.4787	double pendZ
4	4.2513	pendX
5	5.2902	pendZ
6	13.23	tY mirror
7	14.006	tZ marionette
8	14.059	tX marionette
9	39.201	tZ mirror
10-13	611.11	I violin mirror wires
14	887.74	vertical total system
15	1038.2	tZ mirror coupled II violin mirror wires
16-19	1550.8	II violin mirror wires
20	1660.3	vertical mirror
21-22	1795.7	I violin marionette wire
23-26	2913.8	III violin mirror wires
27-30	4716.3	IV violin mirror wires
31-32	5122.5	II violin marionette wire
33	6315.5	cross marionette
34-37	6965.1	V violin mirror wires
38	7544.6	marionette 2 nodes in Z
39	7545.9	marionette 2 nodes in X
40-43	9658.9	VI violin mirror wires
44	9872.7	Butterfly 2,0 marionette
45-46	10338	III violin marionette wire
47-50	12800	VII violin mirror wires
51	15942	Drum 0,1 marionette
52-55	16387	VIII violin mirror wires
56-57	17485	IV violin marionette wire
58-61	20422	IX violin mirror wires

Table 4.13: Mode mapping of the double pendulum system. The acronyms are explained in tab.4.1.

respect to the mirror displacement along the optical axis is directly taken into account in the estimation of the mirror displacement $u_i(y)$ corresponding to those modes. In the table 4.14 I report all the selected modes and for each of them the corresponding total energy (strain energy + kinetic energy) U_{tot}, strain energies stored by the mirror wires U_{mirw} and by the marionette wire $U_{upw}(J)$, the strain energies stored by the waterglass layers of the mirror wires U_{WGmir} and by the waterglass layers of the marionette wire U_{WGup}. These values should then be used for the estimation of the loss angles. In particular in the table 4.15 I report the obtained value of the waterglass layers loss angles ϕ_{WGmir} and ϕ_{WGup} and the inverse of the dilution factors of the mirror wires D_{mir} and marionette wire D_{up}, calculated as explained in eqs. (4.55) and (4.54).

N MODE	$U_{tot}(J)$	$U_{mirw}(J)$	$U_{upw}(J)$	$U_{WGmir}(J)$	$U_{WGup}(J)$
3	238.87	9.3965	53.731	$1.48816 \cdot 10^{-8}$	$8.477 \cdot 10^{-6}$
5	552.43	176.0	30.539	$2.787 \cdot 10^{-7}$	$7.253 \cdot 10^{-6}$
10	$7.372 \cdot 10^{6}$	$5.067 \cdot 10^{6}$	0.52651	0.013051	$1.536 \cdot 10^{-6}$
14	$1.556 \cdot 10^{7}$	$2.585 \cdot 10^{5}$	$1.300 \cdot 10^{7}$	0.02266	38.941
15	$2.103 \cdot 10^{7}$	$2.079 \cdot 10^{7}$	$4.502 \cdot 10^{-5}$	$1.044 \cdot 10^{-8}$	$2.140 \cdot 10^{-13}$
19	$4.747 \cdot 10^{7}$	$3.858 \cdot 10^{7}$	$3.486 \cdot 10^{3}$	0.077428	$1.230 \cdot 10^{-2}$
20	$5.441 \cdot 10^{7}$	$5.234 \cdot 10^{7}$	$7.677 \cdot 10^{5}$	4.5772	2.8009
22	$6.365 \cdot 10^{7}$	$9.906 \cdot 10^{3}$	$3.725 \cdot 10^{7}$	0.00086836	19.676
26	$1.676 \cdot 10^{8}$	$1.480 \cdot 10^{8}$	10.14	0.33846	$7.786 \cdot 10^{-5}$
30	$4.392 \cdot 10^{8}$	$4.041 \cdot 10^{8}$	0.15289	1.20702	$3.508 \cdot 10^{-5}$
32	$5.180 \cdot 10^{8}$	0.2327	$3.849 \cdot 10^{8}$	$2.3198 \cdot 10^{-8}$	203.4
37	$9.576 \cdot 10^{8}$	$9.017 \cdot 10^{8}$	0.50928	3.4488	$1.275 \cdot 10^{-3}$
43	$1.842 \cdot 10^{9}$	$1.759 \cdot 10^{9}$	1.5712	8.3778	$2.200 \cdot 10^{-4}$
46	$2.110 \cdot 10^{9}$	2.7501	$1.750 \cdot 10^{9}$	$1.38602 \cdot 10^{-8}$	$1.076 \cdot 10^{3}$
50	$3.234 \cdot 10^{9}$	$3.117 \cdot 10^{9}$	0.62722	18.2872	$7.9624 \cdot 10^{-4}$
55	$5.301 \cdot 10^{9}$	$5.142 \cdot 10^{9}$	2.81990	36.152	$4.745 \cdot 10^{-4}$
57	$6.035 \cdot 10^{9}$	10.183	$5.309 \cdot 10^{9}$	$3.3606 \cdot 10^{-7}$	$3.986 \cdot 10^{3}$
61	$8.232 \cdot 10^{9}$	$8.023 \cdot 10^{9}$	2.4921	67.362	$1.057 \cdot 10^{-3}$

Table 4.14: Selected modes for the modal analysis for the thermal noise of the suspensions. I reported for each selected mode the total energy $U_{tot}(J)$, the strain energies of the mirror wires $U_{mirw}(J)$, the marionette wire $U_{upw}(J)$, the waterglass layers of the mirror wires $U_{WGmir}(J)$ and of the marionette wire $U_{WGup}(J)$.

For the estimation of the equivalent mass of each mode, I reconstructed the profile of the mirror displacement along the optical axis. After having checked that the mirror surface displacement could have been simplified in a one dimension displacement, as reported in eq. (4.52), I fitted the data of the one dimension mirror displacement along z, calculated with a specific command on ANSYS®. From the fits I obtained the one dimension mirror displacement profile along the optical axis for each mode $u_i(y)$, and then by applying the eq. 4.52 I obtained the equivalent masses that I report in the table 4.15. It is important to stress that the higher the equivalent mass is, the less will be the contribution to the thermal noise. In fact, a high equivalent mass of a given

N MODE	ϕ_{WGmir}	ϕ_{WGup}	D_{mir}	D_{up}	$M(kg)$
3	$6.22997 \cdot 10^{-12}$	$3.54882 \cdot 10^{-9}$	0.0393371	0.224937	0.000240257
5	$3.6204 \cdot 10^{-10}$	$1.31297 \cdot 10^{-9}$	0.318595	0.0552816	0.000132164
10	$1.77042 \cdot 10^{-10}$	$2.08432 \cdot 10^{-14}$	0.687371	$7.1423 \cdot 10^{-8}$	0.268345
14	$1.45666 \cdot 10^{-10}$	$2.50326 \cdot 10^{-7}$	0.0166179	0.835877	165439.
19	$1.63101 \cdot 10^{-10}$	$2.59119 \cdot 10^{-11}$	0.812788	0.0000734384	76.1352
20	$8.41196 \cdot 10^{-9}$	$5.14748 \cdot 10^{-9}$	0.961957	0.0141093	722.654
22	$1.36428 \cdot 10^{-12}$	$3.09129 \cdot 10^{-8}$	0.000155636	0.585202	903928.
26	$2.01957 \cdot 10^{-10}$	$4.64597 \cdot 10^{-14}$	0.882807	$6.05046 \cdot 10^{-8}$	7.84223
30	$2.748 \cdot 10^{-10}$	$7.98613 \cdot 10^{-15}$	0.920028	$3.48081 \cdot 10^{-10}$	7.91629
32	$4.47875 \cdot 10^{-18}$	$3.92697 \cdot 10^{-8}$	$4.49265 \cdot 10^{-10}$	0.743189	$5.01599 \cdot 10^{8}$
37	$3.6015 \cdot 10^{-10}$	$1.33187 \cdot 10^{-13}$	0.941676	$5.31829 \cdot 10^{-10}$	9.61554
43	$4.5493 \cdot 10^{-10}$	$1.19442 \cdot 10^{-14}$	0.955007	$8.53191 \cdot 10^{-10}$	11.8561
46	$6.57002 \cdot 10^{-19}$	$5.09809 \cdot 10^{-8}$	$1.3036 \cdot 10^{-9}$	0.829583	$1.39427 \cdot 10^{10}$
50	$5.65454 \cdot 10^{-10}$	$2.46204 \cdot 10^{-14}$	0.963924	$1.93941 \cdot 10^{-10}$	14.308
55	$6.8203 \cdot 10^{-10}$	$8.95155 \cdot 10^{-15}$	0.970033	$5.31992 \cdot 10^{-10}$	17.7025
57	$5.56873 \cdot 10^{-18}$	$6.60555 \cdot 10^{-8}$	$1.68739 \cdot 10^{-9}$	0.879818	$9.18189 \cdot 10^{9}$
61	$8.18255 \cdot 10^{-10}$	$1.28419 \cdot 10^{-14}$	0.974516	$3.02719 \cdot 10^{-10}$	160.595

Table 4.15: Selected modes for the modal analysis for the thermal noise of the suspensions. I report in this table for each selected mode the calculated loss angles of the waterglass layer of the mirror wires ϕ_{WGmir} and of the marionette wire ϕ_{WGup} and the inverse of the dilution factors of the mirror wires D_{mir} and marionette wire D_{up}. In the last column I report the calculated equivalent masses M.

mode means a small mirror displacement along the optical axis, thus less affecting the mirror suspensions thermal noise.

4.5 Thermal Noise of the Suspended Mirror

As already discussed in the section 3.4.2, the thermal noise of the mirror is well described by using the Levin's approach. It supposes a normalized Gaussian pressure profile $p(r)$ (see eq. 4.22) on the mirror surface which corresponds to the laser power profile impinging on the mirror and having a beam radius w_0. The mirror thermal noise of the 2 suspended mirror is then just given by

$$X^2_{Levin}(\omega) = 2\frac{8k_BT}{\omega}U_{mir}\Phi \tag{4.57}$$

where U_{mir} is the strain energy stored by the mirror under the pressure $p(r)$ and Φ is the total loss angle which takes into account all the dissipative mechanisms, such as those due to the coating layers, the waterglass layers, the loss angle of the material for the bulk modes $\phi_{sb} = 1 \cdot 10^{-9}$ [127]:

$$\Phi = \phi_{sb} + \Phi_{WG} + \Phi_{coat}. \tag{4.58}$$

For the ANSYS® static analysis I took into account that the only constraints are the support to be fix and the Gaussian pressure profile normalized, where I considered a beam radius of the laser on the mirror surface $w_0 = 275\mu m$. I then obtained that the strain energy of the suspended mirror under the pressure $p(r)$ is:

$$U_{mir} = 4.725 \cdot 10^{-7} J. \tag{4.59}$$

4.5.1 Coating and Waterglass Losses

The coating losses are calculated as explained in section 3.4.3, and the waterglass losses as explained in the previous section, but just considering the waterglass layers on the mirror (between the mirror and the end parts of the mirror wires). In this case, we are observing modes at high frequency, since the bulk modes are at much higher frequencies than the modes analysed in the modal analysis.

All the strain energies necessary for the evaluation of the losses are calculated by ANSYS® in a static analysis, where the only constraints consist in setting fix the parallelepiped support, which simplifies the ITF disk (see fig.4.20), and applying the Gaussian pressure $p(r)$ on the mirror face. As in the previous cases, the pressure is given with an opportune ANSYS® APDL command.

Coating Losses

The contributions of the coatings and of the waterglass should be separately evaluated. Firstly I add on the mirror surface the high reflective (HR) layer of Ta_2O_5 and I evaluate

the strain energy of the coating layer and of the mirror plus the HR coating, then I remove the high reflective and I add the low reflective (LR) layer of SiO_2 and I evaluate the strain energies of the coating layer and of the mirror plus the LR coating. For the coating layers I used the characteristics listed in tab. 3.1.

$U_{HR}(J)$	$U_{mir+HR}(J)$	$U_{LR}(J)$	$U_{mir+LR}(J)$
$1.359 \cdot 10^{-10}$	$2.467 \cdot 10^{-5}$	$2.075 \cdot 10^{-10}$	$2.437 \cdot 10^{-5}$

Table 4.16: Losses of the coating layers. I reported the obtained strain energies for the high reflective (HR) layer of Ta_2O_5 and the strain energy of the mirror plus the layer of Ta_2O_5, and the strain energies of the low reflective (LR) layer of SiO_2 and the strain energy of the mirror plus the layer of SiO_2.

From the values reported in table 4.16, and recalling that $\phi_{Ta_2O_5} = 2 \cdot 10^{-4}$ and $\phi_{SiO_2} = 5 \cdot 10^{-5}$, the loss angle for the suspended mirror due to the coating losses is:

$$\Phi_{coat} = \frac{U_{HR}}{U_{mir+HR}}\phi_{Ta_2O_5} + \frac{U_{LR}}{U_{mir+LR}}\phi_{SiO_2} = 1.528 \cdot 10^{-9}. \tag{4.60}$$

Waterglass Losses

For the estimation of the waterglass losses I supposed a layer of $60nm$, and I only took into account the layers that are used to attach the mirror to the mirror wires. The so obtained strain energies are reported in the table 4.17, where I also added the value of the waterglass loss angle Φ_{WG} calculated as

$$\Phi_{WG} = \frac{U_{WG}}{U_{mir+WG}}\phi_{WG} \tag{4.61}$$

$t_{WG}(nm)$	$U_{WG}(J)$	$U_{mir+WG}(J)$	Φ_{WG}
60	$1.2544 \cdot 10^{-9}$	$4.737 \cdot 10^{-7}$	$2.648 \cdot 10^{-4}$

Table 4.17: Losses of the waterglass layers for the mirror thermal noise. The calculation have been done for a thickness of the waterglass layers $t_{WG} = 60nm$.

4.6 Thermal Noise of the Fixed Mirror

Since the double pendulum system is much longer than the simple pendulum studied at the beginning of this chapter, also the fixed mirror should be adapted to it. I supposed that it should be composed by a longer cantilever bar of section $10mm \times 10mm$ and height $56mm$ to which it will be attached in longitudinal direction another silica bar of section $10mm \times 10mm$ and length $30mm$, as shown in the fig. 4.24. The fixed mirror will then need two layers of waterglass, i.e. one for being attached to the interferometer disk and one to attach the bar to the cantilever. I considered that the mirror surface

has disk-shape coating layers of diameter equal to a side of the mirror face, i.e. $10mm$. Moreover, since from the previous estimations we finally fixed the value of the finesse to be $5 \cdot 10^4$, for the thickness of the layers I supposed the same values as for the suspended end mirror which are listed in table 3.1. For the calculation of the strain energies on ANSYS® I considered that the beam radius will be slightly different then for the suspended mirror $w_0 = 272\mu m$. Following the same procedure as for the suspended mirror I obtained that

$$\Phi_{WG}^{fix} = 1.176 \cdot 10^{-5} \tag{4.62}$$
$$\Phi_{coat}^{fix} = 2.661 \cdot 10^{-7} \tag{4.63}$$

and that the strain energy of the fixed mirror under the Gaussian pressure $p(r)$ is

$$U_{fix} = 6.218 \cdot 10^{-7} J. \tag{4.64}$$

4.7 Noise Budget Curves

The suspended mirrors, in our Michelson interferometer with Fabry-Pérot cavities, should be sensitive to the effect of the quantum radiation pressure noise.

For the double pendulum system it is better to also write the radiation pressure noise as a sum of more than one mode each of them having its proper resonance ω_i, equivalent mass M_i and loss angle Φ_i as already calculated for the suspension thermal noise of eq.(4.48). The radiation pressure noise becomes

$$X_{RP}(\omega) = \sqrt{2}\frac{2\mathcal{F}}{\pi}\sqrt{\frac{8hP_{las}}{\lambda c}\sum_{i=1}^{n} K_i(\omega)} \tag{4.65}$$

where I defined the term in the sum $K_i(\omega)$ as

$$K_i(\omega) = \frac{(1/M_i)^2}{(\omega_i^2 - \omega^2)^2 + (\omega_i^2\Phi_i)^2}, \tag{4.66}$$

and where $\mathcal{F}$ the $finesse$ of the Fabry-Pérot cavity, P_{las} the power of the laser, λ the laser's wavelength (for a Nd:YAG is $\lambda = 1.064\mu m$), h the Planck's constant and c the speed of light. According to the results of the previous suspension configurations tested, the values of the laser's power and the finesse of the cavity are reasonably set to be $P_{las} = 50mW$ and $\mathcal{F} = 5 \cdot 10^4$.

I can simplify the sum in the eq. (4.65), by considering only the first 3 encountered modes occuring along the optical axis, i.e. the two pendulum modes 3 and 5 and the first violin mode 10 of the mirror wires. The eq.(4.65) then becomes:

$$X_{RP}(\omega) = \sqrt{2}\frac{2\mathcal{F}}{\pi}\sqrt{\frac{8hP_{las}}{\lambda c}(K_3(\omega) + K_5(\omega) + K_{10}(\omega))}. \tag{4.67}$$

In the final noise budget curve of QuRaG, it is important to also consider the shot noise contribution. The shot noise can be considered frequency independent in the

detection band of QuRaG, since in fact its cut frequency falls above $10kHz$. Therefore, the shot noise will be [122]:

$$X_{shot}(\omega) = \frac{1}{8\mathcal{F}}\sqrt{\frac{2h\lambda c}{P_{las}}}. \tag{4.68}$$

The evaluation of the suspension thermal noise (modal analysis) and of the mirror thermal noise showed that the double stage pendulum is a system compatible with our requirements, as it is clear from the graphics of fig.4.25 and fig. 4.26. The radiation pressure noise for this system is detectable in a frequency band $10Hz - 500Hz$, and even larger if we filter the violin peaks.

4.8 Conclusion on the FEA analyses

I have studied numerous configurations of suspension testing them by the evaluation of their thermal noise vs their radiation pressure noise. ANSYS® FEA analysis allowed me to estimate the thermal noise of simple, as well as complex configurations of suspension such as the double pendulum. The first configurations tested had a well optimized thermal noise such to be in quantum radiation pressure regime, but they were abandoned for feasibility reasons. Nevertheless, we tried a configuration close to the n.3, the 'cantilever', but made with sapphire instead of silica, that we submitted to the IMPEX® company, but it was still discarded for feasibility reasons. The IMPEX® company proposed some modifications to the cantilever design which did not satisfy our requirement for the mirror to be in quantum radiation regime in the band $10Hz-1kHz$. In fact, these systems are too rigid to behave as a pendulum, therefore they had a too high pendulum thermal noise.

The best configuration system turned out to be a double pendulum system, with a first stage marionette and a lower stage suspended mirror. The presence of the first stage allows to attenuate the eventual vibrations transmitted to the suspended mirrors, i.e. those sensitive to the radiation pressure, and the problem of attaching the suspended mirrors wires to the interferometer disk. The losses due to the waterglass layers used for attaching the first stage to the interferometer disk, will not influence the mirror thermal noise. Moreover, their contribution to the suspension thermal noise results to be not important, as I showed in sec. 4.4.1. For the evaluation of the suspension thermal noise of the double pendulum system, I decided to extend the Modal Approach analysis [127, 158]. This method allowed me to take into account in each mode of the system the contribution of all the suspension wires and all the possible losses, opportunely weighted. My calculations allowed us to conclude that the best configuration system should be as close as possible to the **Double Pendulum System**, requiring a very light mirror of $0.08g$ suspended by means of very thin fused silica wires having diameter $40\mu m$ and length $2cm$. Therefore, this strict requirement led us to develop the technique to produce such kind of fibers and to collaborate with the Virgo group of Perugia, expert in pulling silica fibers. I spent almost one month in the Virgo laboratory at the Perugia University, where I learned their technique of pulling

fused silica fibers with an oxy-hydrogen flame, since the laser machine used for Virgo+ was busy for the production of the suspension fibers for Advanced Virgo. In Perugia I also started to learn the technique of attaching silica elements with waterglass, a more simple process with respect to the silicate bonding technique, and which requires less drying time. For this reason in the analysis on the double pendulum system I decided to test the waterglass by using attaching layers made of waterglass instead of silicate bonding. The results of my analysis showed that the use of waterglass does not prevent the observation of the radiation pressure noise.

Moreover, my calculations showed that we are not limited by the structural loss angle of the silica composing the fiber and the mirrors, but the surface losses and losses in the coating and waterglass layers are dominant. In these analyses, I supposed the fibers and the optics made by the lowest losses fused silica available in commerce, which is the Suprasil-311® of the Heraeus® company, used for Virgo. This material has an intrinsic loss angle for fiber and surface losses of $\phi_s = 10^{-10}$ and for bulk losses of $\phi_{sb} = 4.1 \cdot 10^{-9}$. In 2002, measurements by Numata et al. [114] showed that the silica $Corning-7980$® produced by the Corning® company, has an intrinsic loss angle only a factor 2 higher than the Suprasil®, and is much cheaper. Therefore, since these analysis that I presented in this chapter showed that the intrinsic loss angle of the material is not limiting for the thermal noise of QuRaG, the use of silica $Corning-7980$® instead of the Suprasil-311®, will not reduce the sensitivity of our interferometer and its performances. Moreover, I have to stress that the estimations that I have done on the coating losses are also optimistic, since in fact with the silica $Corning-7980$®, they should be of the order of 10^{-6}. In addition, the most recent measurements in optical cavities constituted by tiny mirrors, show that the mirror thermal noise should be of the order of $10^{-17}m/\sqrt{Hz}$ at $1Hz$ [113]. Whereas in our case it is degraded to $10^{-15}m/\sqrt{Hz}$ at $1Hz$ because of the waterglass losses. At present time we are able to control waterglass layers of thickness of the order of $1\mu m$. Therefore, in order to verify how much the suspended mirrors thermal noise is degraded with thicker layers of waterglass, I did a simulation on ANSYS, considering a waterglass in contact with the mirror of $1\mu m$ thickness. In this case the waterglass loss angle is $\phi_{WG}^{1\mu m} = 4.039 \cdot 10^{-3}$, one order of magnitude higher with respect to the waterglass loss angle for a waterglass having thickness $60nm$, i.e. $\phi_{WG}^{60nm} = 2.648 \cdot 10^{-4}$. This implies that the suspended mirrors thermal noise is limited by the waterglass losses.

A specific chapter (chapter 5) is devoted to explain in detail the studies to develop the suitable technique to realize the required suspension wires for QuRaG and to measure the losses (loss angles) of the fibers.

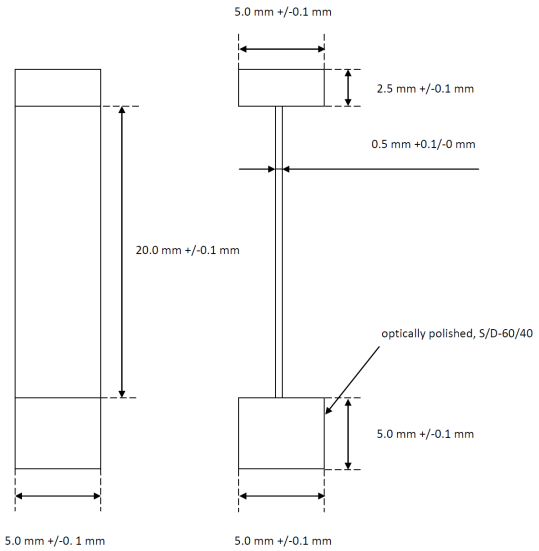

IMPEX HighTech

Sapphire pendant

091-086-5-5-27.5-03

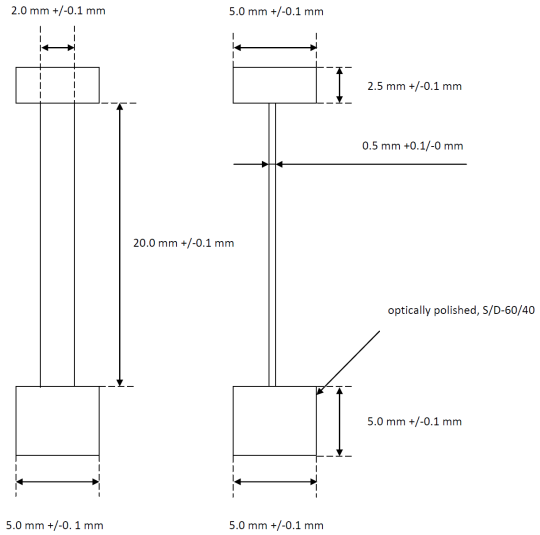

IMPEX HighTech

Sapphire pendant

091-086-5-5-27.5-04

Figure 4.17: Suspension configuration proposed back by IMPEX for a monolithic pendulum made of sapphire. They proposed two versions having a suspension ribbon without cut but with different width: 5mm (on the top) and 2mm (on the bottom). Even the 2mm width ribbon is too stiff to behave like a pendulum. Therefore, both configuration were rejected by us.

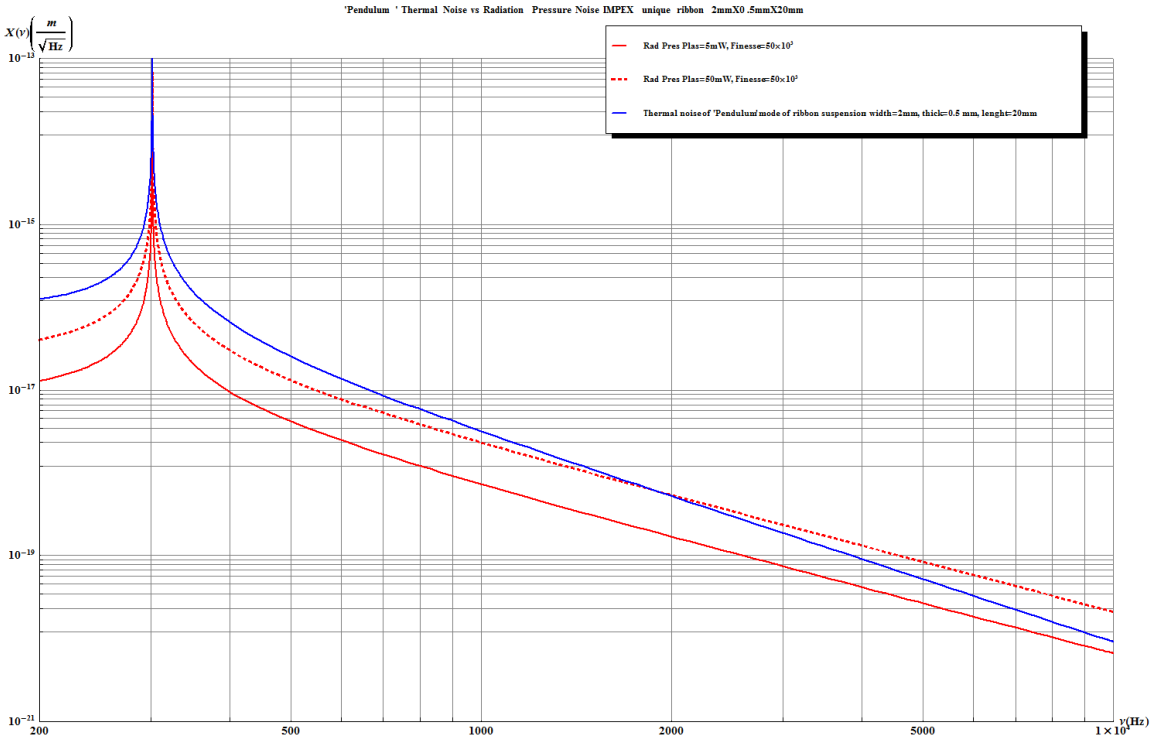

Figure 4.18: Noise budget curve for one of the two cantilever systems proposed by IMPEX having ribbon width $2mm$ for a thickness of $0.5mm$, i.e. the second of fig. 4.17. The suspension thermal noise (blue curve) is higher with respect to the radiation pressure noise even increasing the laser power from $5mW$ (red curve) to $50mW$ (red dashed curve). The finesse has been set equal to $5 \cdot 10^4$ and the overall loss angle of the sapphire as been supposed to be $\phi_z = 7 \cdot 10^{-7}$ at room temperature ($\simeq 300K$) [81].

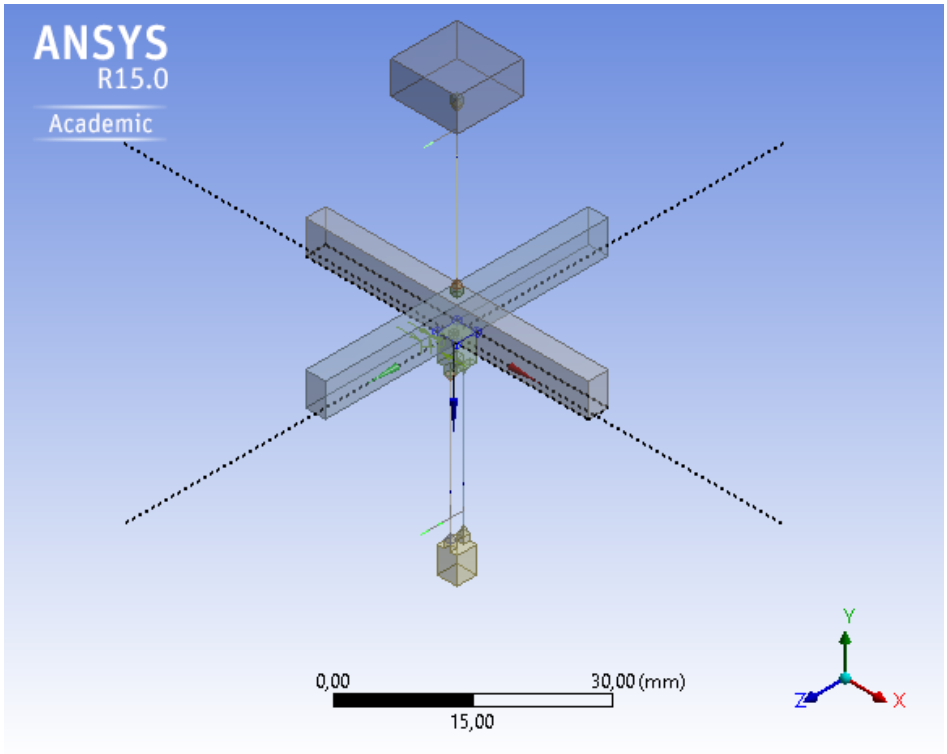

Figure 4.19: Double stage pendulum configuration. Starting from the upper element, there is a parallelepiped shape support of base area $10mm \times 10mm$ and height $5mm$ that summarizes all the upper stages. The support holds by means of a suspension wire (marionette wire), having radius $100\mu m$ and length $22mm$, a first stage marionette of cross shape composed by two arms of $43mm$ length for $3mm$ thickness and $5mm$ height. On the lower part of the marionette there is a parallelepiped, twin of the mirror, with square section of $3mm \times 3mm$ and height $4mm$. The suspended mirror is then joined to its twin by two suspension wires having $40\mu m$ diameter and $20mm$ length. The tapered end parts of each wire are modeled as made of a pyramid of $1mm$ height and side on a cube of $1mm$ side.

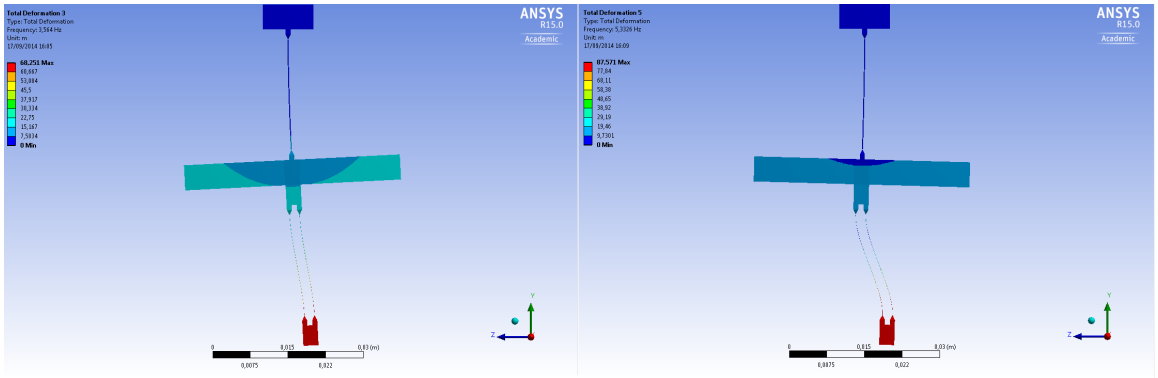

Figure 4.20: Pendulum modes of the double stage system. In the left side is shown the mode n.3 that represents the pendulum mode of the whole system along the optical axis z, having proper resonant frequency $3.4787Hz$. On the right side there is the mode n.5, which represents the pendulum mode of the mirror along the optical axis z and having proper resonant frequency $5.2902Hz$.

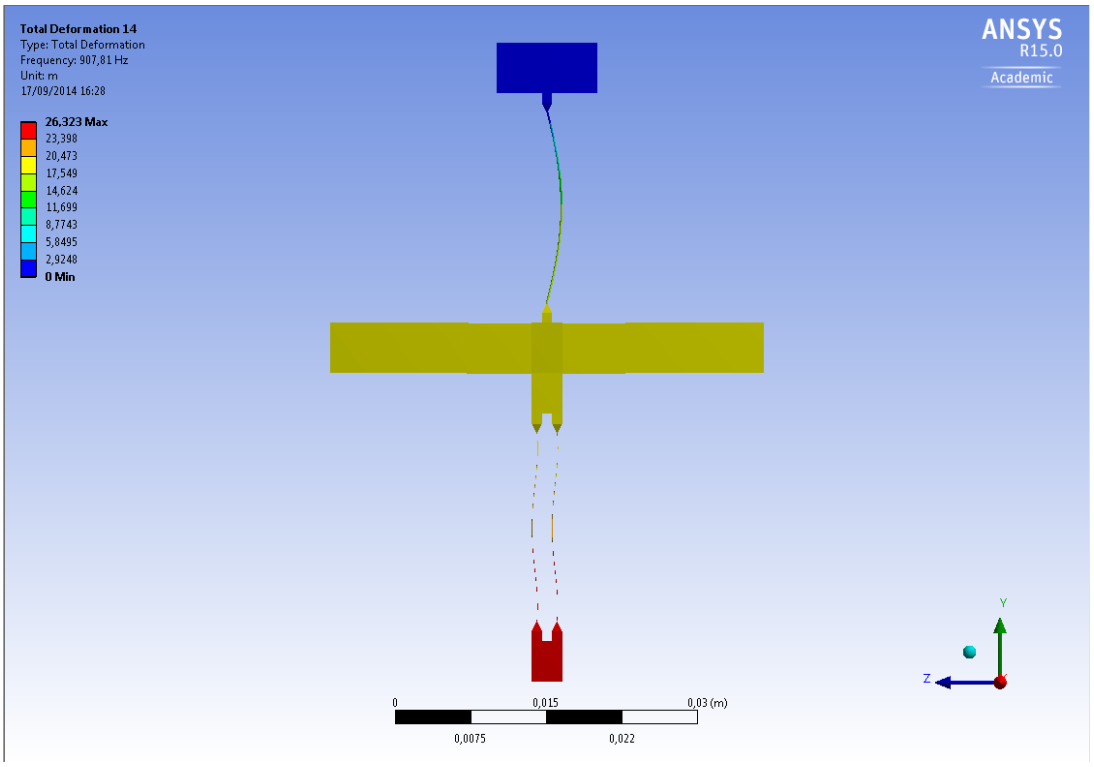

Figure 4.21: Double stage pendulum mode n.14 which represents the vertical mode of the whole double system and has proper resonance frequency $887.74Hz$.

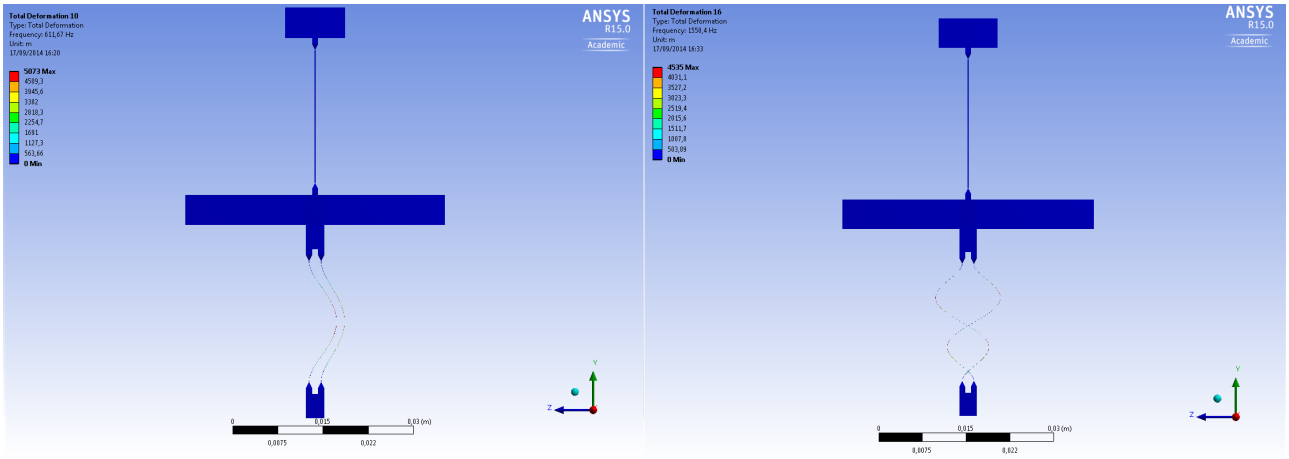

Figure 4.22: Double stage pendulum mode n.10 and n.16 which represent the I and II violin modes of the mirror wires along the optical axis z, and having proper frequency of $611.11Hz$ and $1550.8Hz$, respectively.

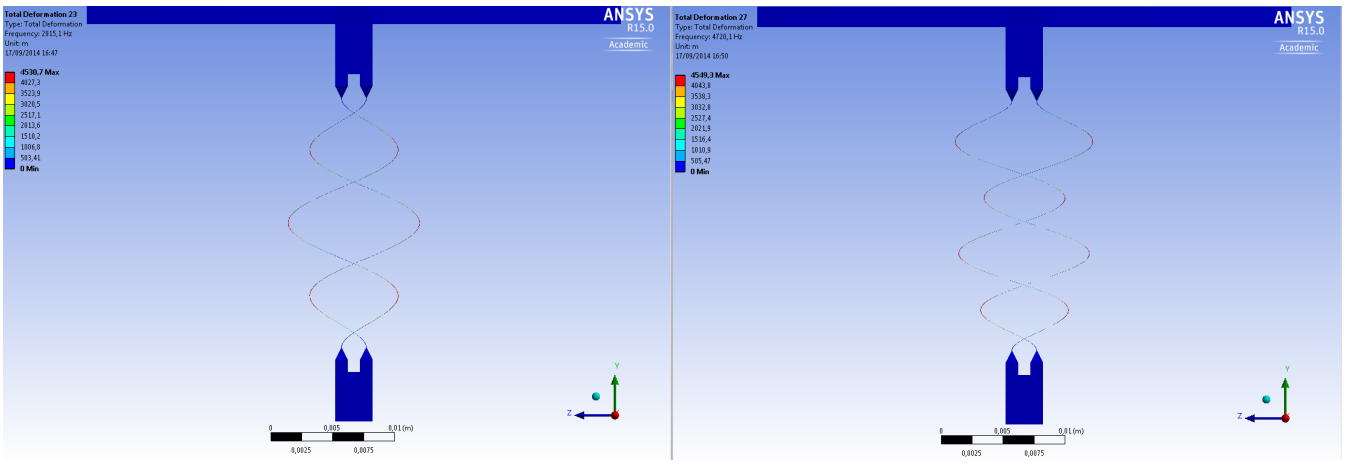

Figure 4.23: Double stage pendulum detail of the modes n.23 and n.27 which represent the III and IV violin modes of the mirror wires along the optical axis z, and having proper frequency of $2913.8Hz$ and $4716.3Hz$, respectively.

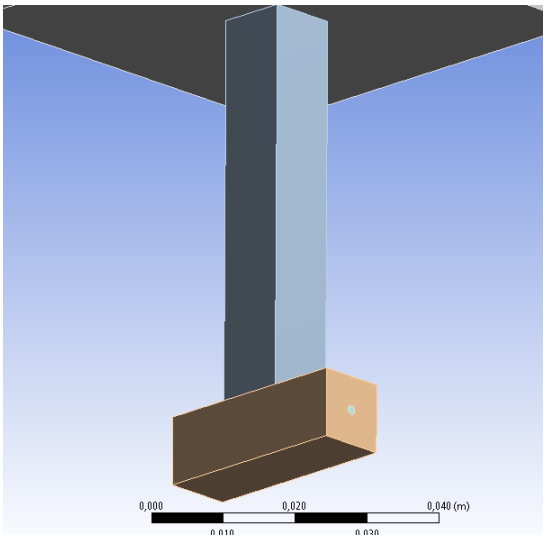

Figure 4.24: Fixed mirror for the new double stage pendulum design. It is composed by a long bar of section $10mm \times 10mm$ and height $56mm$ to which it is attached in longitudinal direction another silica bar of section $10mm \times 10mm$ and length $30mm$, the real fixed mirror of the cavity. The small circle identifies the center of the mirror surface where the laser beam is impinging.

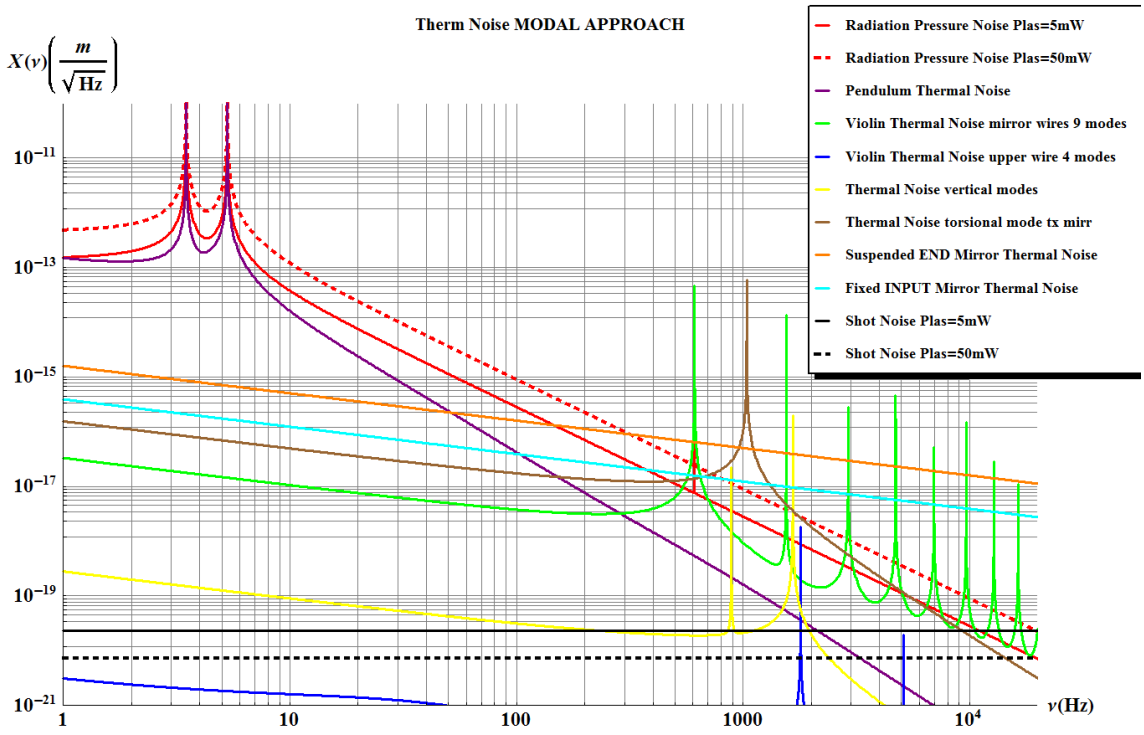

Figure 4.25: Noise budget curves for the modal analysis on the double pendulum system. The radiation pressure noise considering the laser power $P_{las} = 5mW$ (red curve) and $P_{las} = 50mW$ (red dashed curve) is higher than the suspension noises. This configuration satisfies our requirements. Moreover, note that the shot noise, both for $P_{las} = 5mW$ (black curve) and for $P_{las} = 50mW$ (black dashed curve) is negligible compared to the radiation pressure noise.

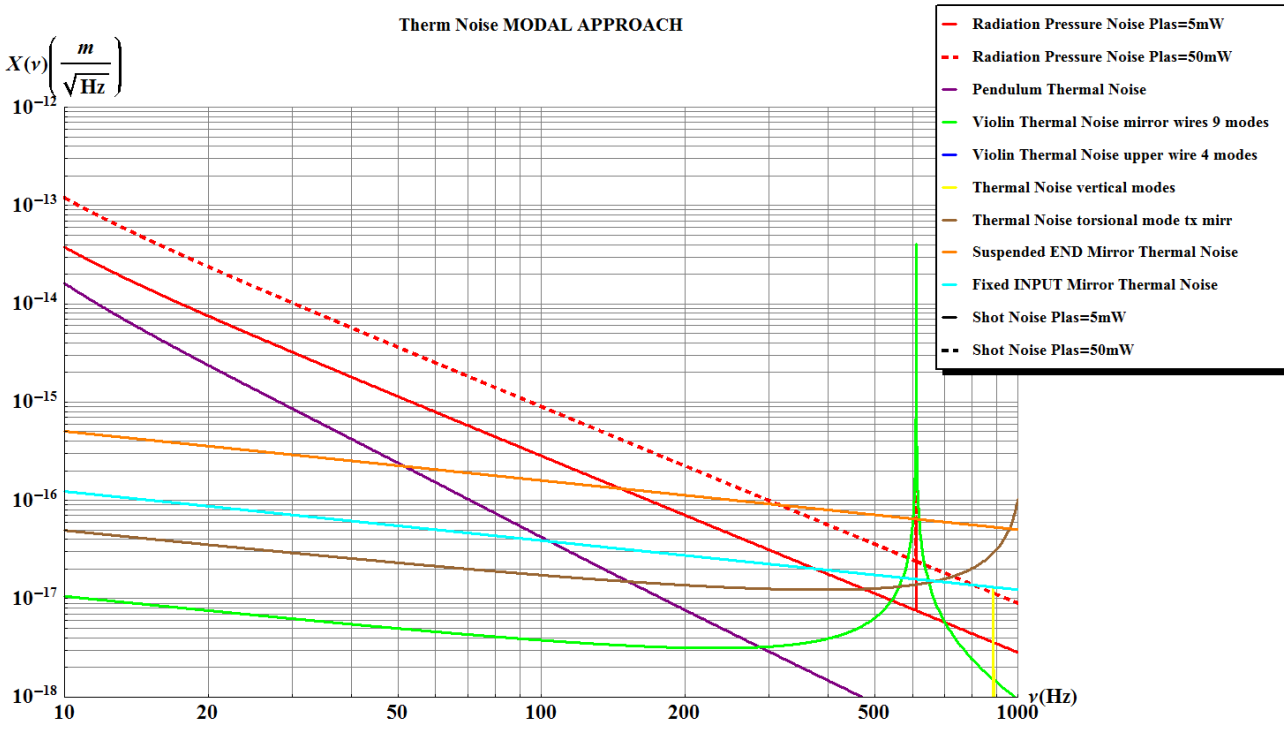

Figure 4.26: Zoom between 10Hz and 1kHz of the noise budget curves for the modal analysis of fig. 4.25.

Chapter 5

Production of the Suspension Fibers

In the present chapter I describe the study for the production of the suspension wires for QuRaG. The analysis that I have done by thermal noise estimation, presented in the chapter 4, demonstrated that the optimal suspension system should be a double pendulum with last suspension wire made of fused silica (see table 5.1) of $2cm$ length and $40\mu m$ diameter. The difficulty to realize such a thin suspension, and to attach it to the upper stage marionette and lower stage mirror, led us to collaborate with the expert of Virgo suspensions of the University of Perugia. The experience that I brought back to Nice allowed us to develop in Nice a similar process to realize the required wires. We bought a fiber splicer machine, that welds fibers by means of an electric arc generated by two electrodes. While doing some test for the welding of the fibers I discovered that it could also be used for pulling the thicker fiber of $400\mu m$ diameter into much thinner ones ($\approx 50\mu m$). Therefore, we decided to re-adapt the machine for producing the fibers and to develop a standard process for realizing them.

As I will explain more in detail in the following sections (see sec. 5.2.2), structural defects in the surface of the fiber are the primary cause of losses (surface losses). Therefore the production process should take care of a first step to uniform the surface by 'cleaning' it from imperfections. Currently, the pulled suspension samples realized in Nice, which are the closest to the requirements, have a central part of $1.5cm$ length and $40\mu m$ diameter and two tapering ends having a bigger diameter of $400\mu m$ for $1.45cm$ length which are connected to the central part by a cone of $0.05cm$ height.

5.1 The realization of the suspension wires for QuRaG

According to what has been said in the section on the thermoelastic dissipation (Sec. 3.2.3), it is necessary to choose, for the suspension fibers, a material whose thermoelastic peak falls outside the desired frequency band of observation. Furthermore, from the

formula of the thermoelastic loss angle (eq. 3.53), in order to decrease the losses outside the peak, it is optimal to use a material with:

- a small linear thermal expansion coefficient α,
- a high specific heat C,
- a low Young's modulus Y.

These conditions must be met even at cryogenic temperatures in the case of the third generation of GW interferometers. Moreover, as already explained, to reduce the contribution to the thermal noise due to the structural dissipation (Sec. 3.2.2), the use of materials with small structural loss angle (Φ_{str}) is mandatory. Therefore, these conditions should also be satisfied by the mirror suspensions of QuRaG, and since the window of frequencies of observation is the same as ground based GW interferometers, using the same material still seems to be the best choice. Moreover, this assumption has already been confirmed by the thermal noise calculations done on several configurations of suspension, as described in the chapter 4.

Before describing the technique learned in Perugia and the system used in Nice, a short section describes how the first monolithic suspensions of Virgo have been realized. The monolithic Virgo was named after Virgo+.

5.2 A similar case: the suspension of Virgo+

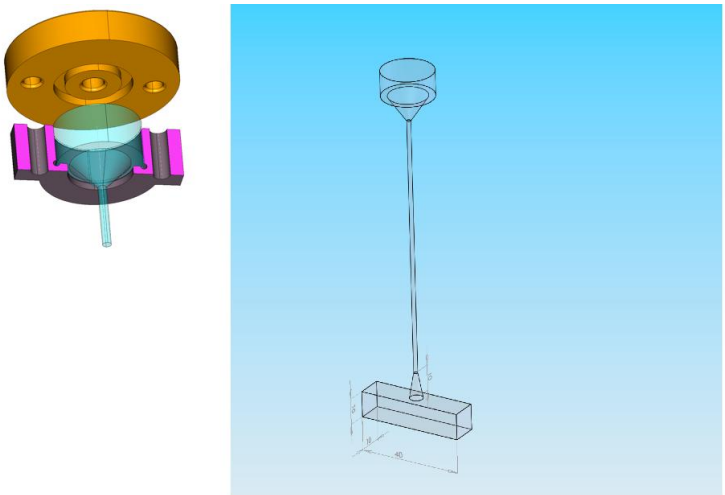

Figure 5.1: The Virgo case. Graphical representation of the silica fiber of suspension (right) and the coupling system of the upper end of the fiber to the marionette, the clamping system, (left).

The initial Virgo had test mirrors suspended by two loops of $C85$ steel wires, material that has an intrinsic loss angle of $\phi_{85} \approx 2 \cdot 10^{-4}$ at $100Hz$. This kind of suspension

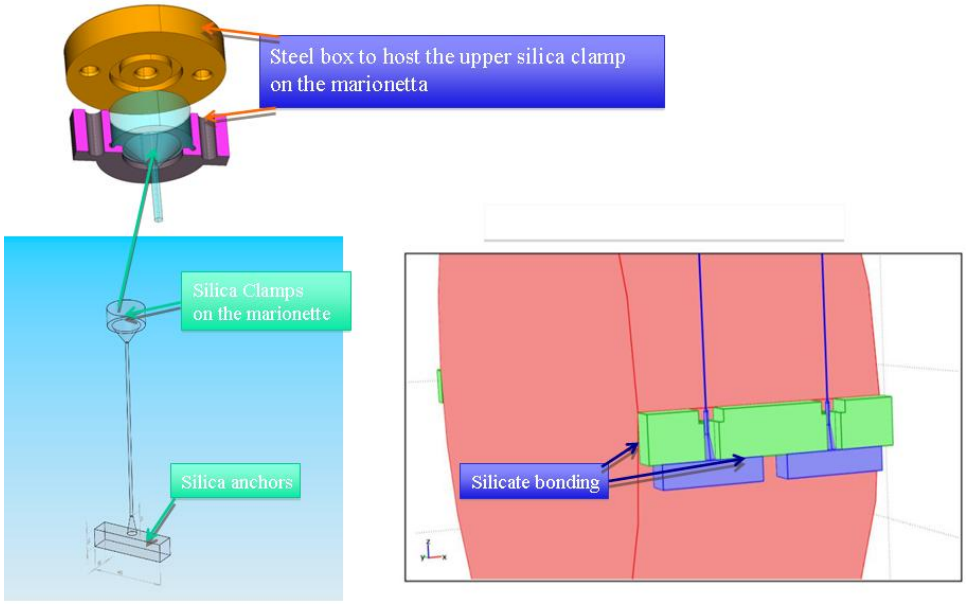

Figure 5.2: The Virgo case. Graphical representation of the silica fiber of suspension (right) and the coupling system of the upper end of the fiber to the marionette, the clamping system, (left). And lower clamping system of the silica fiber to the mirror (*silicate bonding*).

caused a too high friction on the contact area between the steel and the silica mirror, thus degrading the thermal noise performances. Therefore, it has been developed a deep study to test the possibility of realizing a monolithic suspension, in which the suspension wires and the clamps are made of the same material of the mirror. Fused silica is known to have a very low internal loss angle $\phi_{FS} \approx 10^{-9}$ and a low linear thermal expansion coefficient $\alpha_{FS} \approx 0.5 \cdot 10^{-6} K^{-1}$, thus reducing the thermal noise and satisfying the requirements listed at the beginning of this chapter.

specific heat	C	$772 J/(kg \cdot K)$
volume density	ρ	$2.2 \cdot 10^3 kg/m^3$
thermal conductivity	κ	$1.38 W/(m \cdot kg)$
linear thermal expansion coefficient	α	$0.51 \cdot 10^{-6} m/(m \cdot K)$
Young's Modulus	Y	$7.29 \cdot 10^{10} Pa$

Table 5.1: Mechanical and thermodynamical properties of fused silica [122].

Structural defects and surface imperfections are the most critical issues in the realization of the silica fibers, since they are the primary causes of losses. Therefore, the development of a technique of wire production made on purpose has been necessary, since fused silica has a glass structure and its tensile strength and losses strongly depend on cracks and defects present in the fiber structure and on ageing effects due to environment pollution [40]. It is then crucial to produce the fiber taking care of not introducing structural defects and by carefully protecting the fiber in a clean room under vacuum.

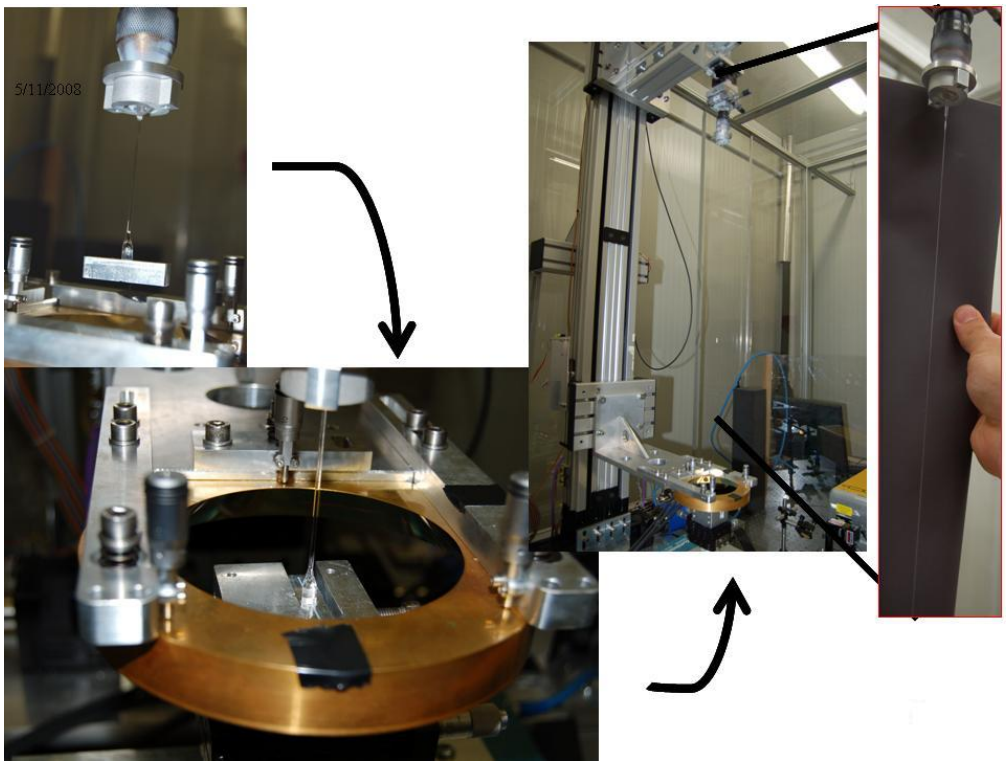

Figure 5.3: The Virgo case. Images describing the stages of pulling of the silica suspension fiber of Virgo+. On the left is shown the upper cylinder for the clamping to the marionette and the anchor in the lower part of the fiber for the clamping to the mirror. Continuing to the right, are shown the steps of fixing anchor for then pulling the fiber.

In particular, structural imperfections and impurities are found more frequently on the surface of a body. Hence, the dissipation are assumed to mainly take place in the surface areas and contact areas between surfaces.

5.2.1 The clamping system of Virgo+

The mechanism of surface contact dissipation occurs when, during the oscillations, there is mechanical friction on the contact area between the two materials. This concerns in particular the coupling system of the test masses of the pendulums in an interferometer like Virgo. The critical points are the upper ends of the suspension wires (see fig. 5.1), in the part clamped to the support of the pendulum, and the points of suspension of the mirror, where the load is attached.
In Virgo+, the attachment of the upper ends of the suspension, is done by clamping fasteners, called clamps (see fig. 5.1). The contact surface of the clamp has a groove for inserting the cylinder of the wire (see fig. 5.1). In this way the pressure of anchorage is exerted along the two tangent lines of the wire. The lower ends are fastened by means of some spacers which minimize the contact surface between the wires and the mirror (see fig. 5.2). It has been demonstrated that friction effects at the level of the

upper clamping stage of the Virgo+ suspension caused an increasing of the losses and a decreasing of the expected mechanical quality factors [127, 40].
The monolithic suspensions of Virgo+ are made of fused silica. In the figure 5.3 are visible, in the upper part of the fiber, the cylinder for the coupling to the marionette and, in the lower part of the fiber, the anchor for the attachment (by silicate bonding) to the grooves on the ears of the mirror. Moreover, the other images in sequence from left to right describe the steps of the realization of the silica fibers (fig. 5.3). The monolithic suspensions of Virgo have a $143\mu m$ radius for a $0.7m$ length and they are obtained by pulling a thicker and small cylinder of silica (called seed) of $3mm$ diameter for few cm length. This can be done by uniformly heating the central part of the seed and then by letting the lower part go down under the effect of gravity. Moreover, the diameter size and length of the pulled fiber can be controlled by a suitable choice of the heating time and of the load eventually applied on the lower end of the seed, thus controlling the pulling velocity. A good heating system was made by flames generated by the combustion of hydrogen and oxygen. A more precise and expensive system uses a CO_2 laser [100]. This has been chosen for the Virgo+ suspension and it is currently in use for the realization of the mirror suspensions of Advanced Virgo.

5.2.2 The production of Virgo+ suspensions

Virgo+ suspensions are made of fused silica which is a silicon compound SiO_2 of glass structure which glass transition temperature depends on the specific material history and vitrification velocity and it has an average value of $2000K$. The parameters of the fused silica are listed in the table 5.1.

Fused silica is currently used for optical fibers for telecommunications, nevertheless requirements for the the Virgo+ suspension wires of fused silica are different, and so the production process should be.

Virgo+ silica wires have been produced starting from cylindrical bars of $1.5mm$ radius for $10cm$ length, called *seeds* for their function, made of a commercially available high-purity material as the Suprasil® or Herasil®. The thinner wires are then obtained by melting the central region of the seed and subsequently pulling the two ends apart. Once melted at $2000K$, the Suprasil (or Herasil) seed becomes highly viscous and it can be plastically deformed. The melting and pulling process is done thanks to a high precision machine using a $100W$ CO_2 laser with $10.6\mu m$ wavelength, developed at the University of Glasgow [83], that has been assembled in a dedicated laser room at the site of the Virgo experiment. This machine allowed to produce fibers in a high controlled way and to get reproducible results. A schematic view of the functional parts of the machine is given in figure 5.4. The production of the fibers can be distinguished in four steps [40]:

1. The silica seed is cleaned with isopropyl alcohol. Then it is welded at its opposite ends to a silica anchor and to a silica cone (see fig. 5.3), that will be used for the integration in the Virgo monolithic design. The local welding is also assured by

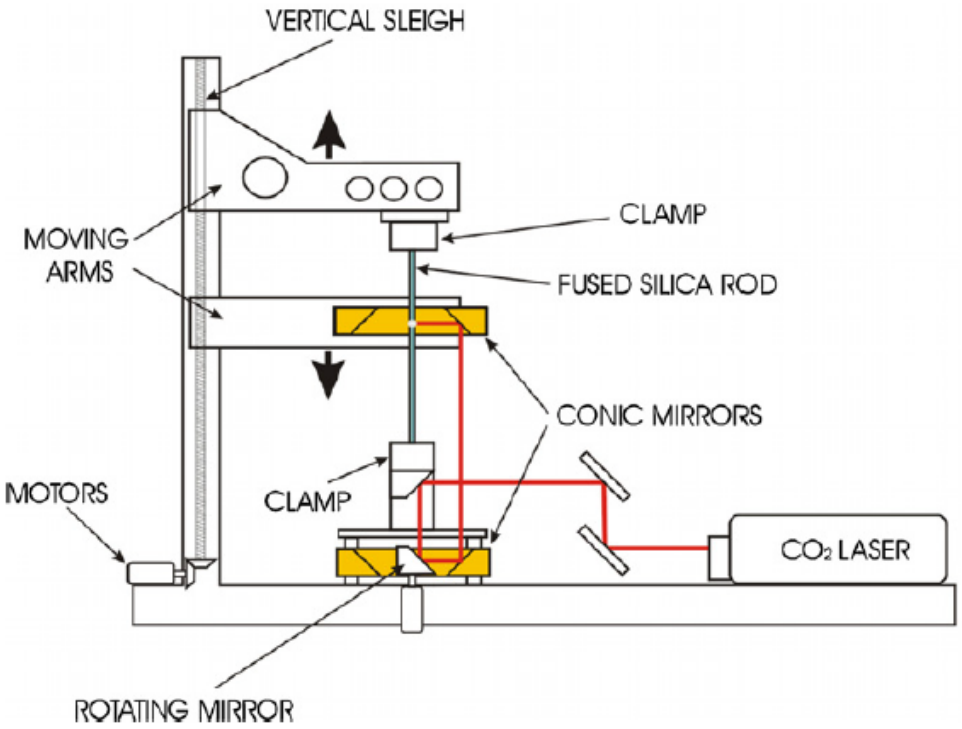

Figure 5.4: Schematic view of the CO_2 laser machine for pulling the silica fiber of Virgo+.

the CO_2 laser machine, in which case it can manually be operated to get accurate results. The silica rod is then clamped as in the figure 5.4. The lower end is then assured on a fixed clamp and the upper one is connected at the top of the moving arm of the CO_2 pulling machine.

2. The second step is the *annealing* (typically at a temperature of $900°C$), process necessary to prevent from the presence of imperfections that would reduce the quality of the fiber. The silica is heated by moving the laser spot along the rod axis without pulling, but just to melt all the structural imperfections and micro-cracks, that would decrease the breaking load of the fiber. Structural defects produce internal reflections within the fiber, clearly visible as diffuse light or spots. The annealing process is repeated until no more light diffusion is present inside the fiber and it appears perfectly transparent.

3. Then the laser beam is delivered onto the fused silica rod by a series of gold coated mirrors. The laser is directed on a rotating mirror and then reflected on the others so that the beam hits the rod continuously all around its axis, assuring a homogeneous local heating. The machine includes two arms connected to the vertical sleighs which are moved by software controlled motors [100]. The first motor guides the upper conic mirror along the vertical axis thus moving the laser spot along the silica bar. The second motor is used to control the moving clamp position. The alignment of the pulling machine axis and the bar axis is done by

precision slides and tilters, moving and orienting the clamps.

4. Once the rod is melted by the laser, the upper arm pulls it upward following a given velocity profile and the wire is produced. The geometry of the pulled wire critically depends on the chosen velocity profile. Since the melting involves a small volume of the rod, from which the material is driven away, new material must be melted in order to continuously feed the wire. Therefore, during the operation, the melting point must be shifted downward, and this is achieved by moving down the conic focusing mirror fixed to the lower arm.

The clamped ends of the rod are not melted, so the fiber profile has the thick ends showed in fig. 5.3. Moreover, two small bobs within the heads are produced before the pulling process by melting the rod near the clamps and then shrinking it [40]. These bobs are necessary for a good clamping process in all the sequence of operation of mounting and dismounting. It is also proven that for minimizing the thermal noise contribution, the best profile shape is a "dumbbell-shaped" fiber as shown in the figure 5.5 [50, 154].

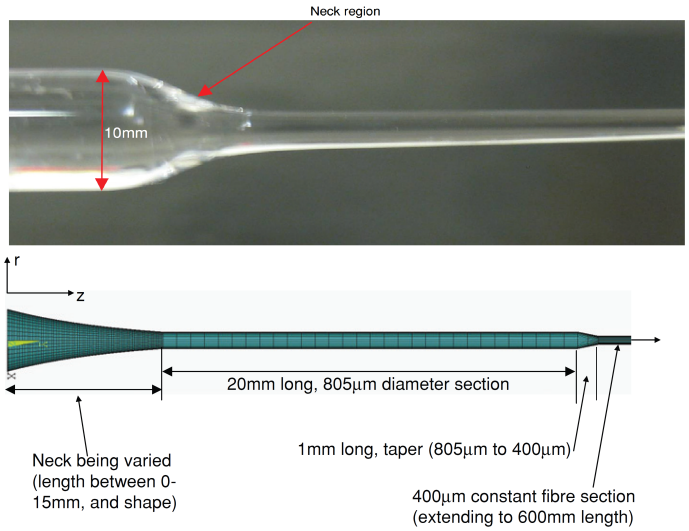

Figure 5.5: Dumbbell profile of fused silica fiber. The upper is the real profile, the lower is the one obtained analytically.

The profile of the obtained wire is very reproducible (within $10\mu m$), and its diameter ($285\mu m$) is remarkably constant along the $70cm$ of the wire. This high precision and reproducibility of the profile is assured by the two software controlled motors. This is confirmed from the graphics of figure 5.6 where are compared the fiber profiles of six different pulled samples [50, 154].

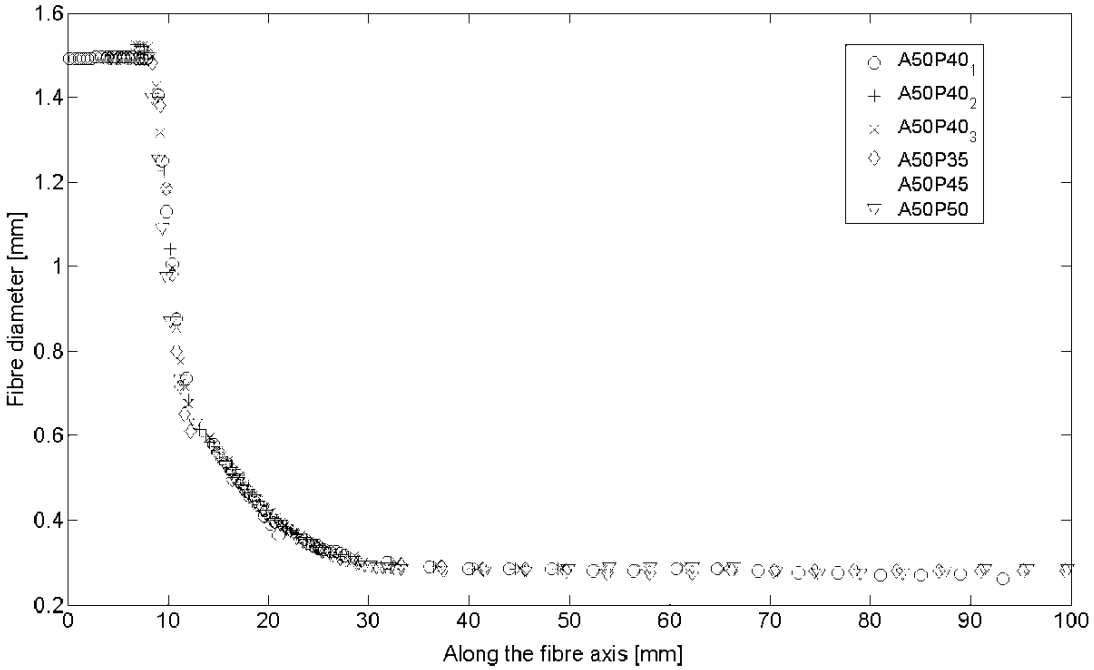

Figure 5.6: Comparison of the profile of six different fibers measured by a profiling tool within $10\mu m$ of precision.

5.3 Pulling Silica Fibers

At the time we wanted to start to realize the suspension fibers for QuRaG the $C0_2$ machine was busy for the realization the suspension fiber for Advanced Virgo. Therefore, for our first tests for QuRaG suspension the faster way was to use the oxyhydrogen flame machine, still operational in Perugia. Hence, for their long term experience on the Virgo suspensions, the collaboration with the Virgo group of the University of Perugia has been necessary to learn the technique of pulling silica fibers for the suspension system of QuRaG. During this collaboration, I learned how to use the oxyhydrogen flame machine for pulling the fiber and I could learn also the technique of measuring the intrinsic losses of the pulled fiber. I adapted the Perugia system to QuRaG's requirements, to realize some rough samples of suspension, of which I measured the loss angle. Then I brought back the acquired experience to Nice, where we adapted the techniques to the specifications and equipments of our laboratory.

The process of pulling silica fiber is one of the most crucial step in the realization of the monolithic suspension system. The material should remain as pure as possible, because the incoming impurities in the lattice of the silica will decrease the breaking load and will increase the internal dissipation. The fundamental idea for the production of silica fiber is to heat at 2000°C a cylinder of the same material and of a thicker diameter of few millimeters, that for its function is called seed. At this temperature, the fused

silica becomes a fluid with high viscosity and it looses its elastic behaviour. Therefore, under mechanical stress it responds with a plastic deformation [147]. The method used to reach such a high temperature with a sufficient level of pureness is the combustion of hydrogen through the oxyhydrogen flames. For the flames is used a machine that produces hydrogen and oxygen by electrolysis of distilled water shown in figure 5.7.

Figure 5.7: Machine for the production of the oxyhydrogen flames by electrolysis of distilled water, on the left. On the right the machine for the production of the silica fibers.

The gases in the machine have a degree of pureness higher than 95%, therefore the process is able to ensure the production of high pureness flames and a low level of incoming impurities during the fusion of the silica. The technique that better allows us to produce fibers with well controlled geometric characteristics and with high repeatability is the crown of flames shown in detail in figures 5.9 and 5.7. This system has been designed by the university of Perugia in collaboration with the group GEO600 of the university of Glasgow [147], whose prototype is still functional at the university of Perugia (see fig. 5.7). With this machine I realized some samples of fibers with the QuRaG requirements.

The first step to realize a pulled silica fiber with a flame is to learn to control a flame. This can be done by calibrating the expulsion of oxygen and hydrogen, and by choosing the suitable expulsion hole. A silica seed, a silica bar of thicker diameter, is used to realize the thinner wires, as already said. A sample is shown in figure 5.8. By using a unique flame is possible to manually pull the wire by holding the two ends of the silica seed (with appropriate gloves) and then pulling on opposite side and turning the seed while the flame is heating the central part. Anyway, in this way it is not possible to well control the wire geometry, and the risk of having a not uniform surface in the pulled fiber is very high. Moreover, the reproducibility is not assured. A better system is therefore a crown holding 6 equal hooks with nozzles for the flames, that can be pointed on the desired area of the silica seed. In this way, the silica seed, fixed in the center of the crown from the upper end, as shown in figure 5.9, can be uniformly

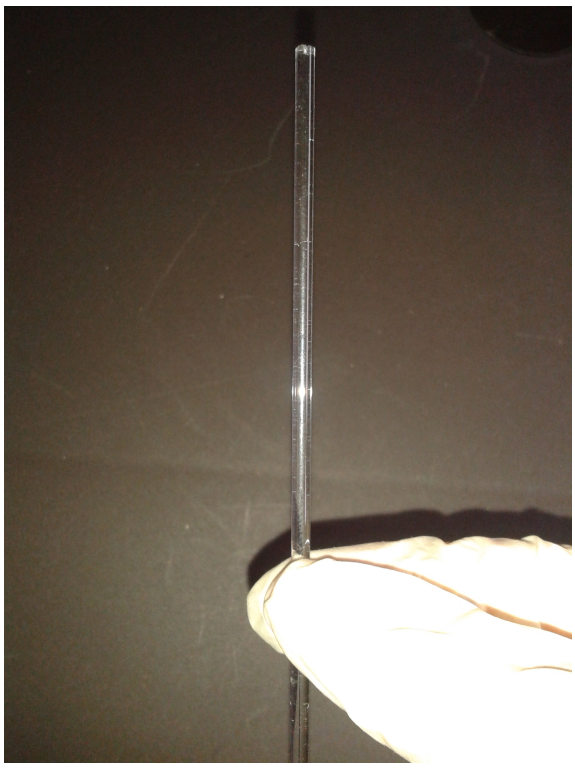

Figure 5.8: Silica seed having diameter of $3mm$.

heated in the circular area covered by the hooks of the crown. When the area of the seed starts to fuse, the lower part of the seed falls down under the effect of gravity. The flames must be turned off before the fiber breaks, and when it reaches the desired size and length. It is eventually possible to apply a load on the lower end of the seed. This process allows to well control the geometry and to have high repeatability since the fiber length and diameter depend on some parameters:

- the diameter of the starting seed of silica;
- the heating intensity and duration time;
- the load applied on the end part of the seed.

All these items can be controlled quite well with the system of figure 5.7. In the figure 5.10 is shown one of the fibers pulled with the system of crown of flames. After some tests, we realized that only 2 flames on opposite ends of a diameter of the crown were enough and no additional load was need to have fibers of $60\mu m$ radius and few cm length. The fibers realized with this system have a central part with a constant diameter (within 10% of the average diameter) and two tapering ends of few millimeters length. The best pulled samples have been used to learn to measure the intrinsic loss angle.

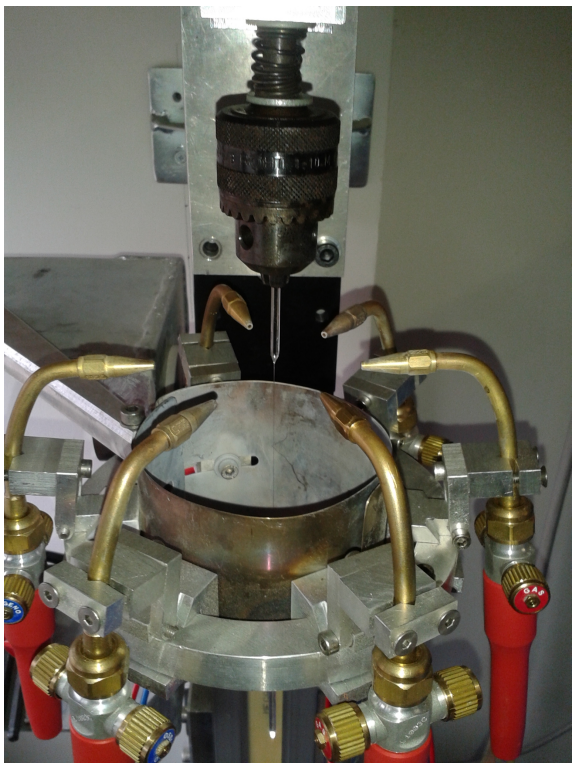

Figure 5.9: The system with the crown of 6 hooks with nozzle for flame. The pulled fiber is held in the middle of the crown. It is visible the thicker part of the original silica seed.

5.4 Loss Angle Measurements

This experiment done in Perugia, did not aim at making an accurate estimation of the loss angle, but only at learning the method of loss angle measurements. The used method is the ringdown technique [73, 147]. It is important to underline that the value of the loss angle that it is measured will be the sum of the several contributions: the intrinsic losses of the material, the thermoelastic losses, and eventual other excess losses [73]. These excess losses are caused by several effects, as for example the rubbing at the clamp-fiber interface between the fiber and its support for the measurements. This can be reduced by optimizing the support system. Other phenomena causing excess losses are the residual gas damping, or air damping, and the recoil damping. The air damping is a source of external dissipation which occurs when a body vibrates in a fluid [40]. Thus, this phenomenon is well modeled as a viscous friction proportional to the velocity. As already stated in the section 3.2.1, viscous dissipation is described by the viscous loss angle which is proportional to the viscosity coefficient β, appearing in the Langevin equation (3.35). Therefore, as in eq.(3.39) the air damping viscous friction is described by the loss angle due to gas friction

$$\phi_{gas}(\omega) = \frac{\beta\omega}{m\omega_0^2}. \tag{5.1}$$

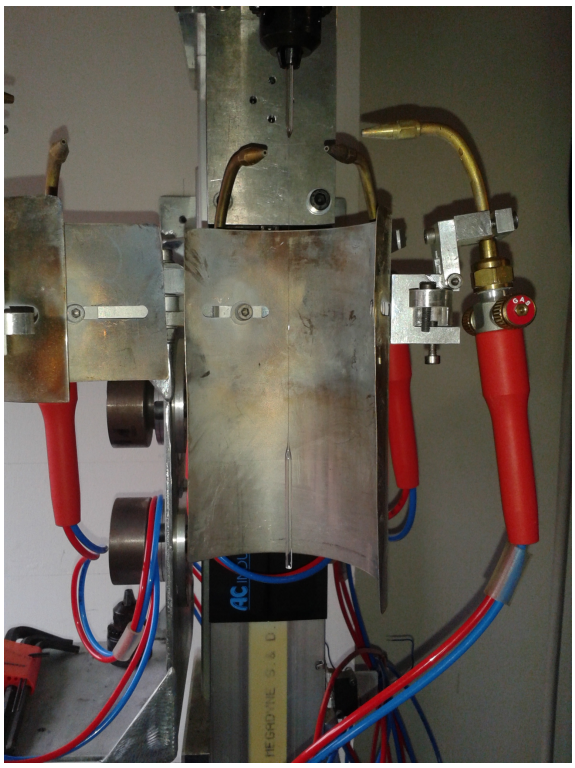

Figure 5.10: The pulled fiber is held in the middle of the crown. The thicker part of the original silica seed is visible.

In dense fluids the friction includes the effect of shear forces, whereas in a rarefied gas the dissipation is mainly due to the momentum transfer between the body and the gas molecules which are moving with a mean thermal velocity equal to

$$\bar{v} = \sqrt{\frac{k_B T}{m}}. \tag{5.2}$$

In this case the mean free path of molecules of mass m_{gas} is larger than the typical dimension of the oscillator and the viscosity coefficient can be written as [134]

$$\beta = \frac{1}{4}\rho_{gas} A \bar{v}, \tag{5.3}$$

where A is the cross sectional area of the body in which collisions with gas occur, and ρ_{gas} is the gas density deduced by the residual gas pressure P_{res} and temperature T through the thermodynamical equation of state of gas

$$\rho_{gas} = \frac{P_{res} m_{gas}}{k_B T}. \tag{5.4}$$

Hence, eq. 5.1 can be rewritten as

$$\phi_{gas}(\omega) = \frac{\rho_{gas} A \bar{v}}{4 m \omega_0^2}\omega. \tag{5.5}$$

Then, for a vibrating cylindrical wire, the gas loss angle is

$$\phi_{gas}(\omega) = \frac{\rho_{gas}\bar{v}}{\rho_w d_w \omega_0^2}\omega. \tag{5.6}$$

where ρ_w is the wire density, d_w its diameter and ω_0 the resonance of the harmonic oscillator. The corresponding quality factor of residual gas is [73, 86]

$$Q_{gas} = \frac{d_w \rho_w \omega_0}{n\sqrt{m_{gas} k_B T}}, \tag{5.7}$$

where n is the numeric density of the gas, or equivalently using equation 5.4

$$Q_{gas} = \frac{d_w \rho_w \omega_0}{P_{res}}\sqrt{\frac{k_B T}{m_{gas}}}. \tag{5.8}$$

Therefore, in the current case of the pulled fiber having a cylindrical mass suspended (which in reality is the end part of the silica seed that has preserved its original section) the residual gas quality factors are

- for the wire

$$Q_{gas-wire} = \frac{d_w \rho_w \omega_0}{P_{res}}\sqrt{\frac{k_B T}{\mu_{H_2}}} \tag{5.9}$$

  where I could approximate that the residual gas is just composed by the molecular hydrogen, so that $m_{gas} = \mu_{H_2}$

- whereas for the cylindrical mass

$$Q_{gas-pend} = \frac{4m\omega_0}{S_{lat} P_{res}}\sqrt{\frac{k_B T}{\mu_{H_2}}}. \tag{5.10}$$

  where I can approximate the cross sectional area A with the lateral surface of the cylindrical mass suspended (having diameter $d_s = 3mm$ and height $h_s = 3.5cm$) $A = S_{lat} = \pi d_s h_s$ and as before I considered $m_{gas} = \mu_{H_2}$.

Then, the gas pressure limiting quality factors can be calculated by considering that the lowest pressure reached inside the vacuum chamber is $P = 10^{-4} mbar = 10^{-2} Pa$, all the fibers characteristics, and by substituting in the eq.(5.10) the value of the pendulum resonance $\omega_0 = 2\pi\nu_0 = 2\pi \times 1.4Hz$:

- $Q_{gas-wire} = 2.0 \times 10^7$
- $Q_{gas-pend} = 5.9 \times 10^6$

which are higher than the expected value of the pendulum quality factor $Q_p = 10^6$. Equivalently, supposing a $Q_{gas-wire}$ and $Q_{gas-pend}$ of the order of the expected Q_p I can derive the limiting gas pressure from the equations (5.9) and (5.10). Therefore, we can state that the gas damping will not limit the losses if the gas pressure in the vacuum chamber is lower than the so obtained limiting gas pressure P_{res}:

- from the eq.(5.9) of the vibrating wire gas viscous quality factor I obtain

$$P_{res} = \frac{d_w \rho_w \omega_0}{Q_{gas-wire}} \sqrt{\frac{k_B T}{\mu_{H_2}}} = 2.7 \cdot 10^{-3} mbar \tag{5.11}$$

- and from eq.(5.10) of the gas viscous quality factor of the pendulum I obtain the limiting gas pressure value

$$P_{res} = \frac{4 m \omega_0}{S_{lat} Q_{gas-pend}} \sqrt{\frac{k_B T}{\mu_{H_2}}} = 0.97 mbar, \tag{5.12}$$

where for the $Q_{gas-pend}$ and for the $Q_{gas-wire}$ I used the values respectively of the measured pendulum and first violin mechanical quality factors, which are the inverse of the values reported in the tab. 5.3 and tab. 5.4. This condition is guaranteed thanks to a turbomolecular pump that assures a reached vacuum of few $10^{-4} mbar$.

The recoil damping, other effect causing excess losses, is given by the coupling between the resonant modes of the fiber and low-Q (highly dissipative) resonances of the support structure holding the fiber. Therefore, this effect can be minimized by isolating the fiber resonances from the support resonance. A simple technique is to realize a double pendulum structure in the fiber, by pulling a shorter and thicker fiber in the upper part (called isolation fiber) separated to the relevant fiber by a cylinder called isolation bob [73, 147]. The isolation bob will create a first stage pendulum acting like an attenuator of the recoil vibrations coming from the support structure of the fiber but also from the seismic excitations.

Another phenomenon causing excess losses is the eddy-current damping. The oscillating fiber carries a charge, induced by the exciter for the resonances, and the motion of the charges induces back eddy currents in the nearby of the conductors. Resistance in the conductors dissipates the mechanical energy stored in the currents, degrading the loss angle. In the measured fiber the moving charges on the surface are negligible, so the eddy current effect does not affect the system.

5.4.1 Experimental Set Up

The experimental set up was equiped of:

- a vacuum chamber;
- a pre-vacuum pump (dual stage rotary vane Alcatel Pascal® OME25-S);

- a turbo molecular pump (Pfeiffer® Vacuum Pump with single phase direct current motor (1500 Hz));
- a shadowmeter (alimented IR led HIRL5010, and a split photodiode);
- an exciter (made of two sharp ended screws);
- an HV amplifier (max 2kV, TREK® Model 677A);
- a generator (Agilent® 33220A);
- a filter (Stanford Research System, inc.® SR650 high-pass/low-pass programmable filter);
- a Data Acquisition (DAQ) board (National Instrument® NI USB 6221);
- LabView® interface on PC;
- a fiber support;
- a pulled fiber.

With the pre-vacuum pump a $few\ 10^{-2} mbar$ vacuum is reached and then the turbomomecular pump allows to reach $few\ 10^{-4} mbar$. The support for the fiber is an aluminum clamping system with a groove to place the upper end of the fiber. This one is then fixed by two screws, which should not be very tight so that no unwanted pressure is exerted on the fiber. The system is shown in the pictures of fig.5.12. The fiber profile with the isolation bob is schematized in the figure 5.11.

5.4.2 Measurements

For the loss angle measurements it is suitable to use the ringdown method [73]. The basic principle is to excite the resonances of the fibers and observe the amplitude decay. The exponential time constant of this decay is inversely proportional to the loss angle related to that resonance and directly proportional to the mechanical quality factor of that resonance. The used sensing device is a shadow sensor, called shadowmeter and the excitation of the modes is done with two electrodes, called exciter. The shadowmeter measures the displacement of the fiber by sensing the displacement of the fiber's shadow generated by an IR led on a split photodiode centered on the quiet position of the fiber, as shown in the picture of fig. 5.13. The resonances that should be observed are the pendulum and violin modes, so they implies a horizontal displacement of the fiber to be excited and sensed. The electrodes should be placed in the direction parallel to the 'sensing' direction of the shadowmeter. Therefore, the exciter and the shadow sensor are placed on a plane normal to the fiber, and in orthogonal directions between them. The fiber is placed at mid distance between the two electrodes, but as close as possible to the led, in order to have the biggest shadow on the photodiode, since the diameter

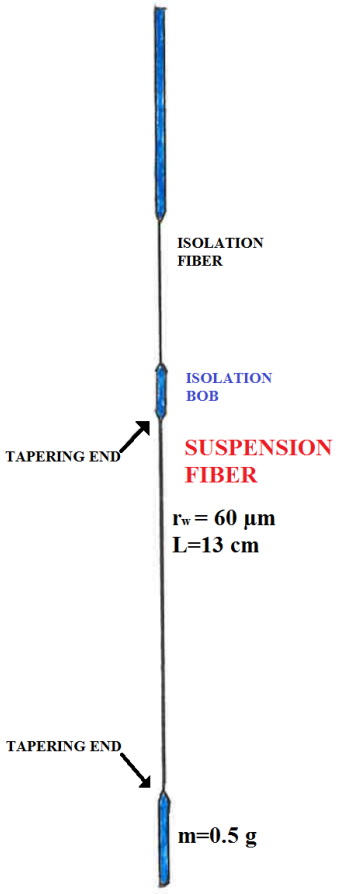

Figure 5.11: A scheme of the fiber profile. The isolation bob acts as the first stage of a double pendulum attenuating the vibration to the last stage. The fiber has a length of 13cm and a radius of $60\mu m$.

of the fiber is very small with respect to the gap between the two quadrants of the photodiode. The system around the fiber is shown in the picture of fig. 5.14.

An interface on LabView® software (see fig.5.15), programmed by the Perugia team, shows in real time the amplitude of oscillation as voltage (V) over time (graphics in the up left side of fig.5.15), and calculates the square root of the power spectral density ($V/sqrt(Hz)$) (graphics in the up right side of fig.5.15), thus allowing to directly identify the frequency of the excited resonances. The envelope of the exponential decay of the amplitude of the excited resonance is sampled in the lowest graphics in the LabView® script interface, as shown int the fig.5.15. This signal is called analytical signal. The analytical signal $z(t)$, associated to a physical signal $y(t)$, is defined as the sum of the signal $y(t)$ and its Hilbert transform $\tilde{y}(t)$ [40]:

$$z(t) = y(t) + \tilde{y}(t) \tag{5.13}$$

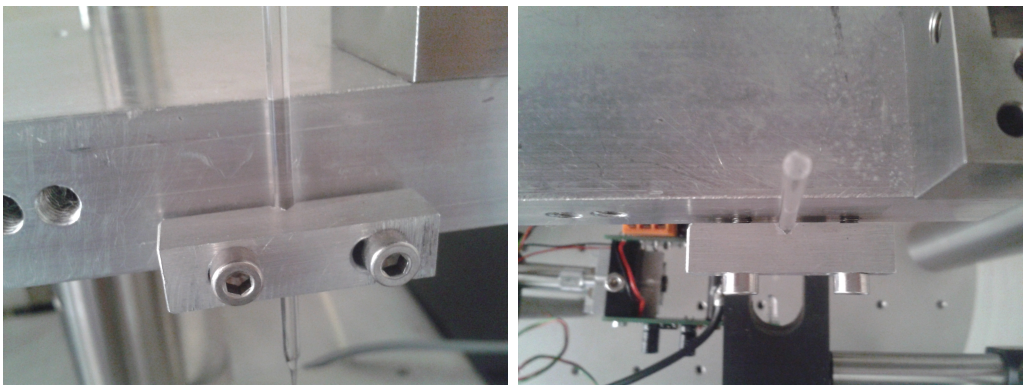

Figure 5.12: The clamping system to hold the fiber for the loss angle measurements. The support has a groove to place the upper end of the fiber. This one is then fixed by two screws, taking care to avoid unwanted pressure to be exerted on the fiber. Front (right) and upper (left) view of the system.

where the Hilbert transform of $y(t)$ is defined as:

$$\tilde{y}(t) = \frac{1}{\pi} \int_{-\infty}^{\infty} \frac{y(t')}{t - t'} dt'. \tag{5.14}$$

The amplitude of the analytical signal is therefore

$$|z(t)| = \sqrt{y(t) + \tilde{y}(t)} \tag{5.15}$$

and it corresponds to the envelope of the real signal $y(t)$. In the ring down method measurements, the analytical signal of the read-out of the physical quantity is an exponential function, as I will show in the following of this section.
In order to identify the resonances, the wire is firstly excited with a white noise coming from a function generator and amplified by a high voltage amplifier [40]. The applied voltage is of the order of few kV. Once the resonances are identified on the power spectral density, I analyse them one by one, from the analytical signal that is the lower signal displayed on the LabView® interface in fig. 5.15. The identified resonance is excited by sending a sine function with frequency corresponding to the resonance I want to excite. The fiber motion is detected by the shadowmeter: the fiber produces a shadow on the split photodiode, and the signal from each side is subtracted from the ground. Then, the output signal is filtered with a pass-band filter around the resonance and amplified. Once the resonance is excited, the driving signal is switched off and the fiber is let free to oscillate. The exponential amplitude decay of the resonance is recorded with a Data Acquisition Board and displayed on the LabView® interface (see fig. 5.15). The LabView® script allows to set the desired sampling frequency and the resolution. From the exponential time decay of the amplitude of the resonance, I can straightly derive the quality factor Q, which is the inverse of the loss angle ϕ, as I will explain in the following. Once identified the peak frequency among all the resonances in the power spectral density, an approximate value is given as input to LabView® together with a small incertitude range so that the program filters the data in this

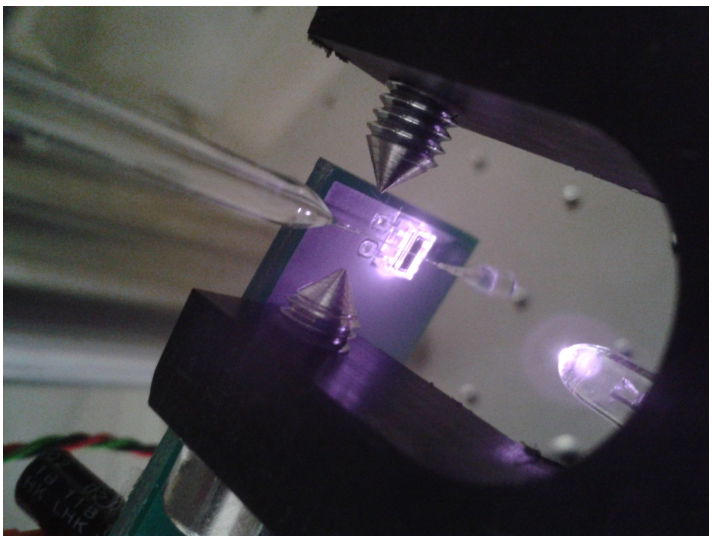

Figure 5.13: The picture shows how the shadowmeter works. It senses the displacement of the shadow of the fiber on a split photodiode, created by an IR led light placed on the opposite side of the fiber.

range of frequencies to then find the real value of the frequency and amplitude peak $A(t)$. The amplitudes are calculated along the time, until the curve displayed on the interface (see fig. 5.15) has enough points to calculate the time decay of the amplitude. This means having points on a time range comparable or higher than the expected time decay. The amplitude peak (the amplitude of the analytical signal, eq.(5.15)), as already outlined, has an exponential decay of the form

$$A(t) = A_0 e^{-t/\tau} \tag{5.16}$$

where τ represents the time in which initial amplitude A_0 decays of $1/e$. The exponential time constant, τ, can be therefore derived by measuring the slope of the linearized amplitude decay (eq. (5.16)) as follows

$$ln[A(t)] = -\frac{1}{\tau}t + ln[A_0] \tag{5.17}$$

since the eq.(5.17) can be rewritten as

$$y(t) = bt + a, \tag{5.18}$$

where the slope b and the intercept a are related to the time decay and the initial amplitude as

$$b = -\frac{1}{\tau} \tag{5.19}$$

$$a = ln[A_0], \tag{5.20}$$

and estimated by a linear fit. Moreover, given a mechanical system, the mechanical quality factor of the resonance frequency ν is $Q = 2\pi\nu\tau$ [60], and the Q corresponds

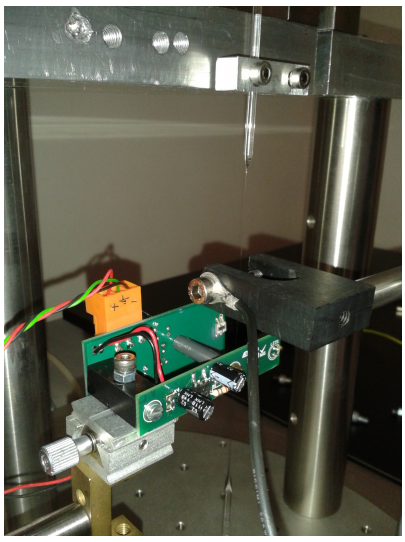

Figure 5.14: The picture shows the system for the loss angle measurements. The exciter (in black), the fiber holded by its clamping system (see fig. 5.12) and the shadowmeter with the alimented led and photodiode.

to the inverse of the associated loss angle. Therefore, from the slope obtained with the linear fit, the loss angle is

$$\phi = \frac{1}{2\pi\nu\tau} = \frac{b}{2\pi\nu}. \tag{5.21}$$

5.4.3 Results

The measurements done allowed to well identify only two fiber resonances: the pendulum and the first violin. The observed pendulum frequency is at $1.4Hz$, very close to the pure gravitational pendulum frequency $\frac{1}{2\pi}\sqrt{g/l} = 1.38Hz$, and the observed first violin frequency is at $120Hz$, while from the analytical formula for violin modes already discussed in the previous chapters, is expected at $110Hz$. I repeated the measurements with the same fiber, but with the lower mass cut and re-attached with the waterglass. This was to have an idea of how much losses the waterglass can introduce for such a thin fiber. From all collected data, for the pendulum resonance without waterglass there are three measures of the loss angle value, therefore the final value for this case is the average of the three and the error is the standard deviation. Whereas for the

$b(s^{-1})$	$\Delta b(s^{-1})$	$\tau(s)$	$\Delta\tau(s)$	$\phi(\times 10^{-3})$	$\Delta\phi(\times 10^{-3})$
-7.25	0.11	137.7	2.1	1.650	0.025
-7.38	0.15	135.5	2.7	1.678	0.034
-7.10	0.11	140.8	2.2	1.614	0.025

Table 5.2: Measured values of slope, exponential time constant, loss angle for the pendulum mode at $1.4Hz$ without the waterglass.

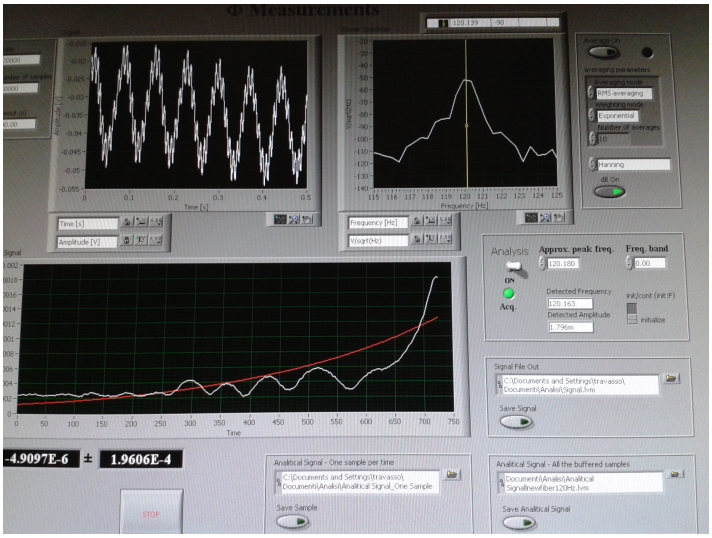

Figure 5.15: The picture shows the interface of Labview® for the loss angle measurements. The amplitude of oscillation as voltage (V) over time (up left side) is collected in real time, and the square root of the power spectral density ($V/sqrt(Hz)$) (up right side) allows to directly identify the frequency of the excited resonances. The lowest curve is the analytical signal, which represents the envelope of the exponential decay of the amplitude of the excited resonance (120Hz) that has been selected from the power spectral density. In the captured moment showed in this picture, the resonance is continuously alimented and does not decay.

case with waterglass, there is only one good sample of data. Therefore, the average value of the loss angle without waterglass is compared with the value obtained in the configuration with the introduction of the waterglass (see table 5.3). The similar value

no WG (average)	$\overline{\tau} \pm \sigma\tau = (138 \pm 2)s$	$\overline{\phi} \pm \sigma\phi = (1.65 \pm 0.03) \cdot 10^{-3}$
with WG	$\tau \pm \Delta\tau = (144 \pm 3)s$	$\phi \pm \Delta\phi = (1.50 \pm 0.02) \cdot 10^{-3}$

Table 5.3: Average values of exponential time constant and loss angle for the pendulum mode at $1.4Hz$ without the waterglass compared with the measured ones in the case with the waterglass used to attach the mass to the fiber.

obtained with and without waterglass for the case of the pendulum mode (see tab. 5.3), can be explained by the presence of other dominating excess loss, like for example the clamping of the fiber support structure.
For what concerns the first violin resonance, the obtained values without and with waterglass, for the loss angles are in table tab.5.4. The obtained values, shown in the table 5.4, state that the introduction of the waterglass increases the loss angle of two orders of magnitude. This can be reasonable since the known value of the intrinsic waterglass loss angle is of the order 10^{-1}. Moreover, the loss increases with increasing the amount of waterglass used and with the eventual presence of impurities introduced during the drying process of the waterglass. We suppose that the degrading of two orders of magnitude of the loss angles, after introducing the waterglass, can be explained by two main

no WG	$\tau \pm \Delta\tau = (1088 \pm 6)s$	$\phi \pm \Delta\phi = (2.44 \pm 0.01) \cdot 10^{-6}$
with WG	$\tau \pm \Delta\tau = (19.7 \pm 0.1)s$	$\phi \pm \Delta\phi = (1.344 \pm 0.007) \cdot 10^{-4}$

Table 5.4: Comparison between the exponential time constant and loss angle of the first violin mode at $120Hz$ in the case without waterglass (no WG) and with waterglass (with WG) used to attach the mass to the fiber.

causes. Firstly, an exceeding amount of waterglass placed to glue the fiber to the mass, and secondly the presence of impurities deposited during the drying process. In fact, since the experiment has just been a preliminary test, the waterglass was used without being diluted in water, thus to accelerate the process of drying. Whereas, on the other hand, this increases the percentage of impurities introduced during the drying process, not having the time to evaporates, thus not well reconstructing the glass structure.

5.5 Pulling Thin Silica Fibers for QuRaG

In Nice we developed a system to pull the suspension fiber that is a method that matches the oxyhydrogen flame method and the CO_2 laser method used for Virgo+ and uses a controlled electric arc as source of heating. The arc is produced by an old Portable Fiber Splicer machine of Power Technology Inc.® and the machine also has a support for holding the fiber. While making some tests for splicing fibers, I discovered that this machine could also work for pulling thicker fibers into thinner ones by just shifting the melting point along the seed. Within the first sample that I pulled, starting from a $400\mu m$ diameter seed, the best two had diameters of:

$$(98 \pm 5)\mu m, \tag{5.22}$$

$$(101 \pm 5)\mu m \tag{5.23}$$

Therefore, we fixed the machine on an optical table in order to have the fiber in vertical position, and we upgraded it with two motors (see fig. 5.16) to control the position of the fiber and of the melting point along the fiber.

An electronic motor is used to pull the fiber downward while the arc is heating the fiber, and a high precision position servo motor, placed on the upper part of the fiber, is used to follow the movement of the fiber and to continuously feed the arc with material to be fused. The best sample realized with this technique has a diameter of $(40 \pm 2)\mu m$ for $1.5cm$ length with two tapering ends having a bigger diameter of $400\mu m$ for $1.45cm$ length which are connected to the central part by a cone of $0.05cm$ height (see fig. 5.17). One crucial point of this technique is to well control all the involved parameters like the arc time duration and current (so the heating temperature) and the speed of the two motors, in particular the synchronization of the two speeds. These parameters are controlled on the computer through LabView® with programs realized on purpose. Nevertheless, the arc is not stable and not well controllable. Therefore, another technique is under test, without using the lower motor and just pulling the fiber in one time only under the effect of the gravity. In the fig. 5.16 is shown the

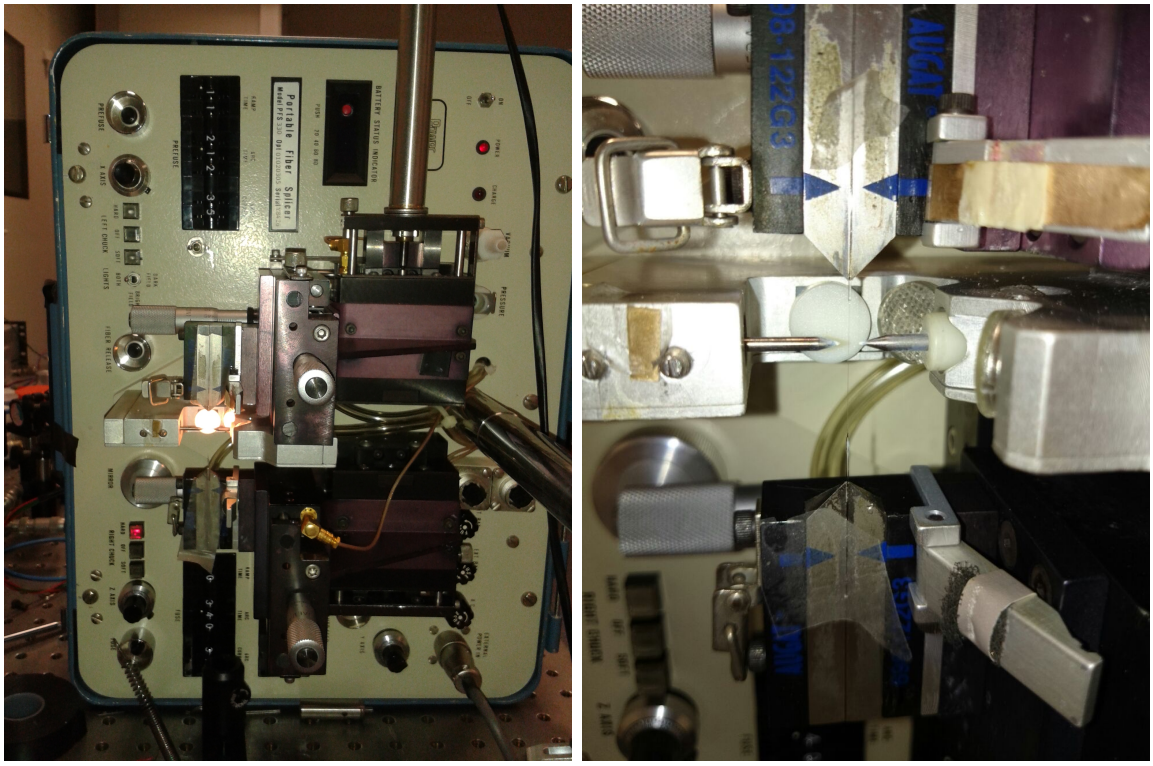

Figure 5.16: The picture on the left shows the machine used to pull fiber. Is an old Portable Fiber Splicer modified in order to place the fiber vertically and with a servo position motor to control the position of the fiber. The motor velocity and the arc intensity current and duration time are controlled on Labwiev. The picture on the right shows the detail of the best pulled fiber placed on the holding system of the pulling machine.

machine as is at present time with only the upper motor, and the detail of one of the best pulled fiber held on the machine. The figures 5.17 look more precisely into the best fiber with the microscope, showing a more detailed profile of the fiber. Its thinner part in the middle has a $40\mu m$ diameter and the taper ends have a cone shape, as described above.

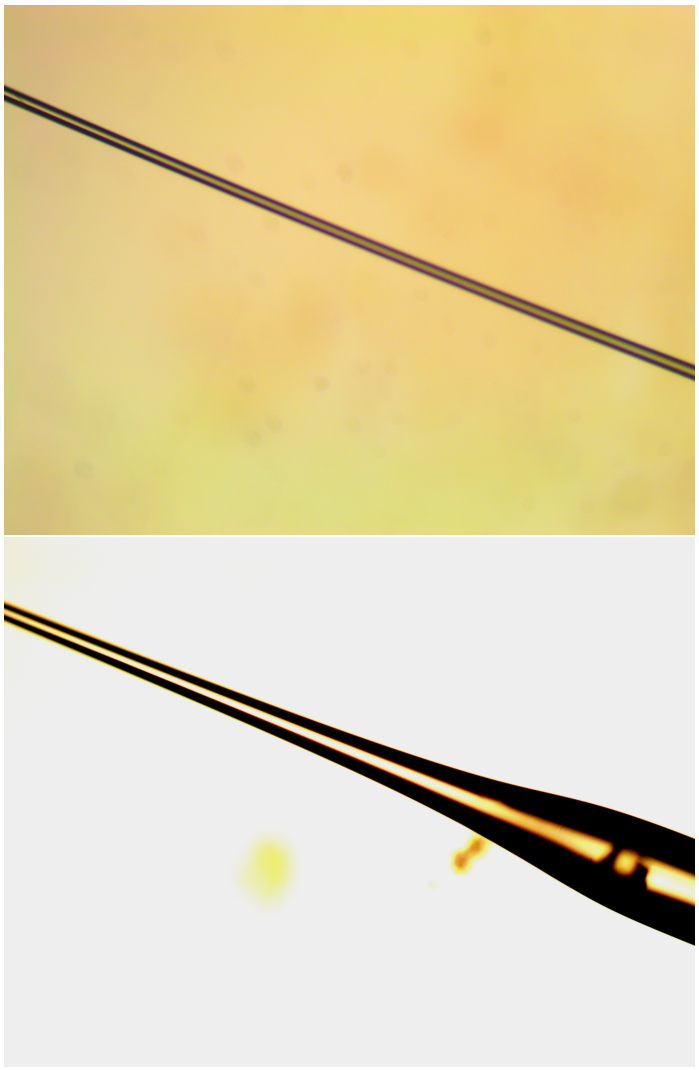

Figure 5.17: The picture shows the best pulled fiber. The image on the top is a detail of the middle part of the fiber which has a diameter of $(40 \pm 2)\mu m$, and the image on the bottom shows one of the tapering end of the fiber having a cone shape.

Chapter 6

Study of the Electrostatic Control

The control system of QuRaG interferometer foresees a last control stage of electrostatic actuation directly applied on the suspended mirrors, in order to damp the pendulum resonances. Therefore, part of my research has been devoted to the study of the electrostatic control on a suspended test mirror placed in a Michelson interferometer. The basic principle of this experiment is to deduce the mirror displacement by looking at the correction signal on the other mirror of the interferometer glued to a piezoelectric ceramic bar (PZT) after sending a voltage on the electrodes placed behind the suspended mirror, while the interferometer is frequency locked at half of the fringe wavelength (see fig. 6.10). The experiment was done in a clean room of class 100000 (or equivalently ISO 8) at a temperature of 19°C closing the interferometer in a box, thus to avoid unwanted effects of the air fluctuation (see fig. 6.1). Several systems for suspending the

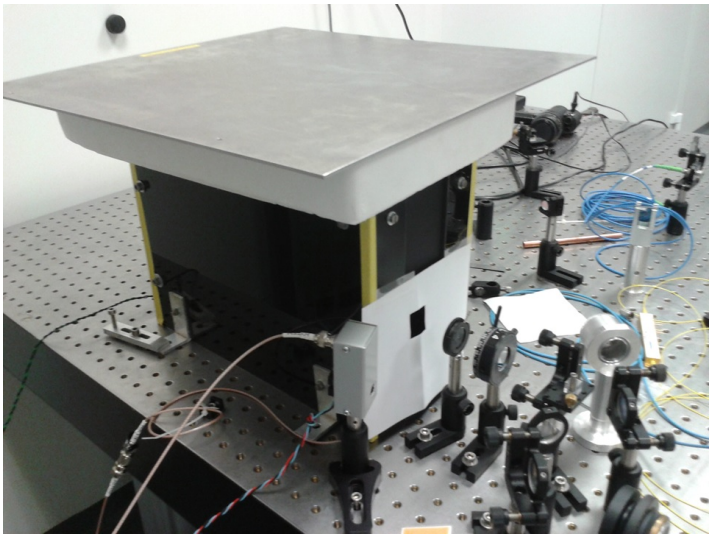

Figure 6.1: The picture shows the box fixed on a table used to protect the Michelson from air fluctuation of the air conditioning of the clean room of class ISO 8.

mirror have been tested. In fact, the electrostatic control has been applied on different kinds of suspensions, and their response to the applied voltage to the capacitor allowed to choose the more suitable suspension system to be adopted in these measurements.

6.1 Basic Principle

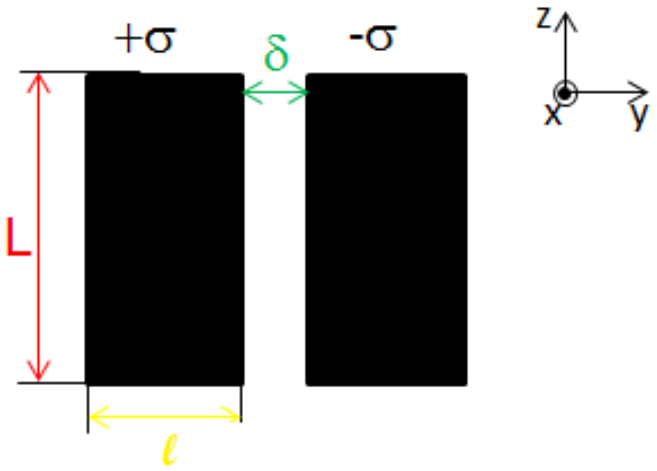

Figure 6.2: Scheme of the capacitor. It is made of two rectangular electrodes of dimensions $L \times l$, and spaced of an amount δ.

The capacitor is made of two rectangular electrodes of dimensions $L \times l$, and spaced of an amount δ, as shown in the figure 6.2.

A capacitor is placed behind a suspended mirror at a distance d. When a voltage ΔV is applied, the charged capacitor will exert on the dielectric mirror a force

$$F(x) = -\frac{1}{2}\frac{\partial C}{\partial x}\Delta V^2, \tag{6.1}$$

where the capacitance $C(x)$ depends on the distance between the capacitor and the mirror along the mirror axis x (which coincides with the optical axis) [104]. Moreover, since the recall force of the pendulum for the suspended mirror is

$$F_p(x) = \frac{mg}{L_p}\Delta x, \tag{6.2}$$

the displacement of the mirror Δx will be proportional to the square of the voltage

$$\Delta x = -\frac{L_p}{2mg}\frac{\partial C}{\partial x}\Big|_d \Delta V^2. \tag{6.3}$$

If the two electrodes have surface charge $\pm\sigma$ respectively and ΔV is the voltage between them, the capacitance is then given by:

$$C(x) = \frac{\sigma L \cdot l}{\Delta V}, \tag{6.4}$$

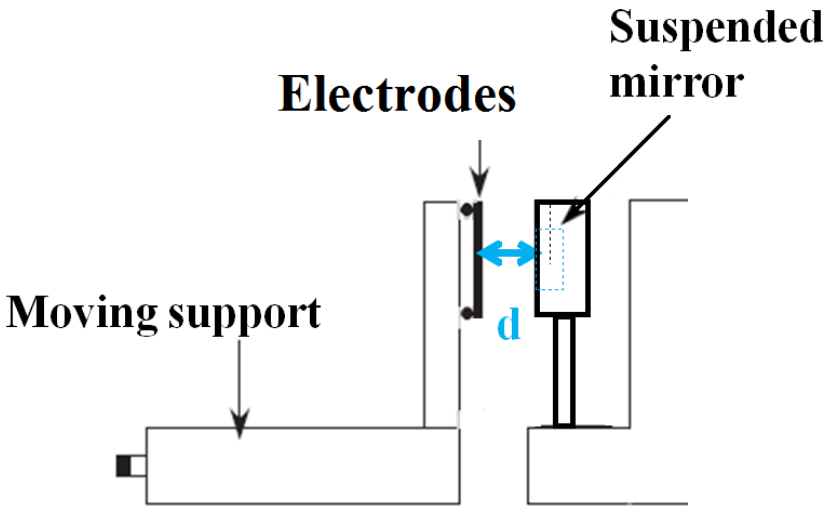

Figure 6.3: Schematic representation of the system electrodes-suspended mirror. The electrodes are placed on a moving support, thus allowing to change the distance d that separates them from the mirror.

where the dependence on x is implicit in the ΔV. In fact, as the distance between the capacitor and the mirror decreases, the voltage necessary to displace the mirror of the same amount Δx also decreases. Therefore, the derivative $\frac{\partial C}{\partial x}\Big|_d$ can be written as:

$$\frac{\partial C}{\partial x} = \frac{\partial C}{\partial \Delta V}\frac{\partial \Delta V}{\partial x} = -\frac{\sigma L \cdot l}{\Delta V^2}\frac{\partial \Delta V}{\partial x}. \tag{6.5}$$

Moreover, ΔV can be written as the difference between the average voltage on each electrode (1 and 2):

$$\Delta V = < V_1(2) > - < V_1(1) >, \tag{6.6}$$

$$< V_1(1) > = \int_{\delta}^{l+\delta}\int_{-\frac{L}{2}}^{\frac{L}{2}} V_1 dz dx \tag{6.7}$$

$$< V_1(2) > = \int_{-\delta}^{-l-\delta}\int_{-\frac{L}{2}}^{\frac{L}{2}} V_1 dz dx \tag{6.8}$$

where the expression of the potential V_1 generated by the electrodes in the zone between

them and the mirror is [119]

$$V_1(x,y,z) = \frac{\sigma}{4\pi\epsilon_0}\Big[f[(x-d)^2, y-\delta, z+\frac{L}{2}, y-l-\delta, z-\frac{L}{2}] - f[(x-d)^2, y+\delta+l, z+\frac{L}{2}, y+\delta, z-\frac{L}{2}]$$
$$+ r\ f[(x+d)^2, y-\delta, z+\frac{L}{2}, y-l-\delta, z-\frac{L}{2}] - r\ f[(x+d)^2, y+\delta+l, z+\frac{L}{2}, y+\delta, z-\frac{L}{2}]$$
$$+ \sum_{i=0}^{\infty}(-t^2)(-r)^{2i+1}\Big(f[(x+d+2(i+1)b)^2, y-\delta, z+\frac{L}{2}, y-l-\delta, z-\frac{L}{2}]$$
$$- f[(x+d+2(i+1)b)^2, y+\delta+l, z+\frac{L}{2}, y+\delta, z-\frac{L}{2}]\Big)\Big] \quad (6.9)$$

where

$$f(a, y_1, z_1, y_2, z_2) = \int_{y_1}^{y_2}\int_{z_1}^{z_2}\frac{1}{\sqrt{a+y^2+z^2}}dydz \quad (6.10)$$

and ϵ_0 is the vacuum permittivity, r and t are respectively the coefficients of reflection and transmission of the mirror, b is the thickness of the mirror, d the distance between the mirror and the capacitor. Therefore, if the plane capacitor (like the one showed in fig. 6.2 and fig.6.4) is placed at a distance of $d = 0.5mm$, supposing that the suspended mirror has a mass of $m \sim 1g$ and an ideal suspension wire of length $L_p \sim 2.5\ cm$ a voltage of about $\Delta V = 100V$ is necessary to let the mirror move of $1\mu m$ [119]. By varying the applied voltage ΔV on the electrodes, at a given distance d between the mirror and the capacitor, it is possible to reconstruct the expected behaviour of equation (6.3), in which the absolute value of the induced displacements proportionally increases to the square of ΔV. Moreover, the measurements are repeated by changing the distance d between the electrodes and the mirror (see fig. 6.3). In fact, we expect that as the distance d decreases, in order to produce the same amount for the mirror displacement, the necessary applied voltage ΔV will decrease. This effect can be seen as an increasing of the first derivative of the capacitance with respect to the direction of the mirror axis x $\frac{\partial C}{\partial x}\Big|_d$ with the decreasing of the distance d.

6.2 Suspension of the Test Mirror

This part of the work on the electrostatic control on the test mirror turned out to be closely related to the issue of suspending it. The test mirror is a cylindrical mirror having diameter of 1 *inch* and a weight of 1 g. The suspension system of the test mirror should be as close as possible to a pendulum system, as it is required for QuRaG suspended mirrors, and in order to observe, for the mirror displacement under the electrostatic force $F(x)$, the expected behaviour of eq. (6.3).
The first suspension system tested was composed of a ring support of plexiglass[1] surrounding the mirror to which were glued two stripes of tape having the function of

[1]Poly methyl methacrylate (PMMA) is a transparent thermoplastic often used as a lightweight or shatter-resistant alternative to glass.

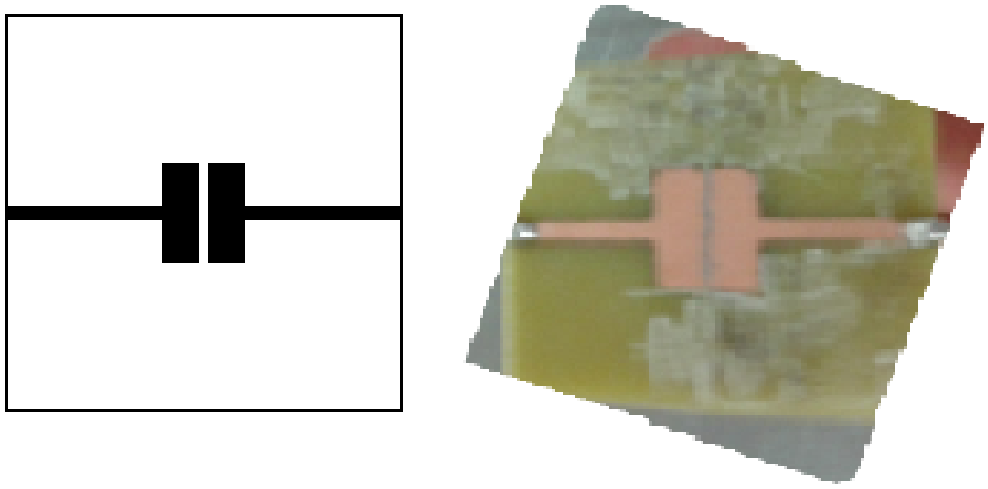

Figure 6.4: The capacitor is made of two rectangular electrodes of height $1cm$ and width $3.5mm$ spaced by $0.5mm$ (scheme on the left). The scheme is then printed on ceramic copper coated plaque in order to realize the real electrodes used, that are shown on the picture on the right.

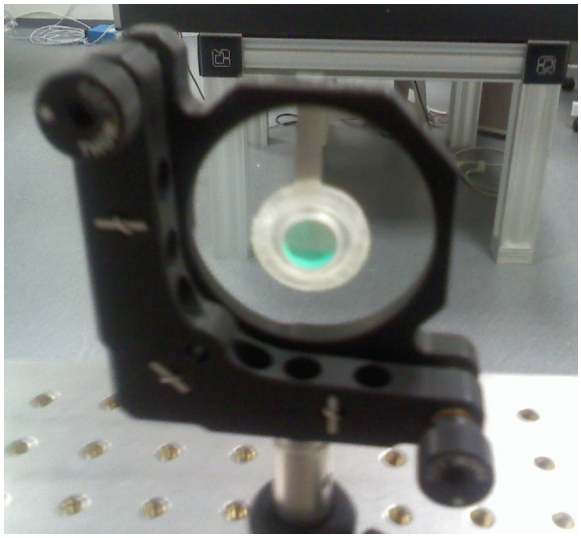

Figure 6.5: The picture shows the first suspension system tested. The mirror is held by two ribbons made with tape, and having dimension of $4mm$ width for $2.5cm$ length, attached to a ring support surrounding the mirror. With this system it was not possible to place the capacitor at a distance closer than $15mm$ because of the V-shape of the suspension ribbon.

two suspension ribbons (see fig.6.5). The two tape ribbons had a width of $4mm$ for $2.5cm$ length and were placed in a V-shape configuration on the plane orthogonal to the mirror as shown in fig.6.5. Nevertheless, the aperture angle created by the two tape ribbons did not allow to approach the capacitor at distances closer than $15mm$ from the mirror. Moreover, this suspension system did not let the mirror behave exactly like a pendulum and the first derivative of the capacitance with respect to the mirror axis

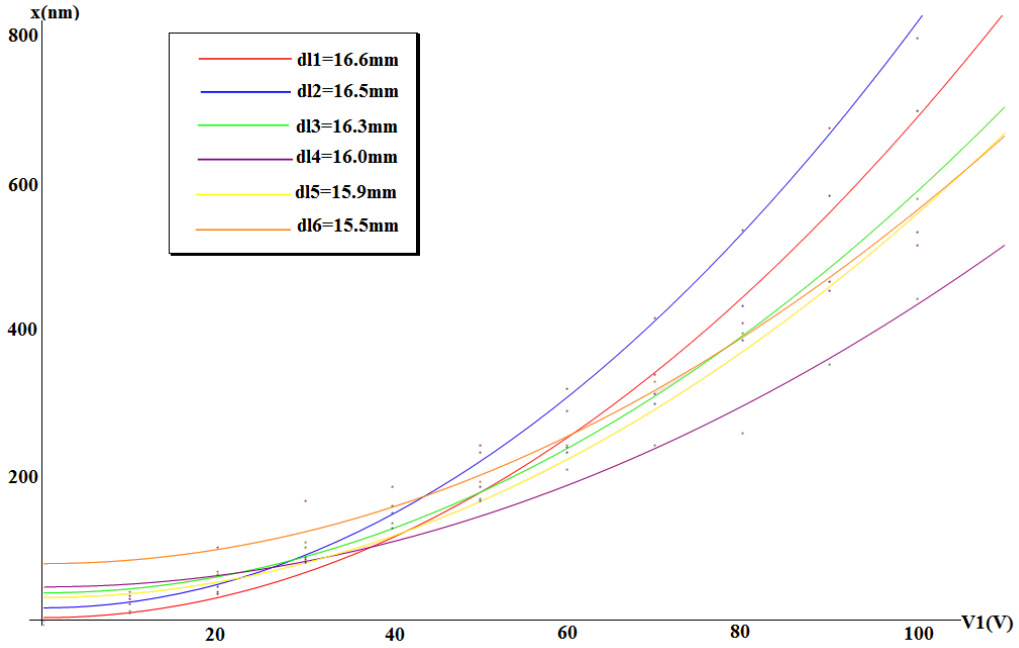

Figure 6.6: The graphics show the measurements done with the first suspension system tested of fig.6.5. The mirror displacements increase with increasing the applied voltage. Whereas, as the distance d decreases, the same mirror displacement is not regularly reproduced for a decreasing applied voltage ΔV. The maximal displacement is not obtained for the closest distance d.

x did not increase as the distance from the capacitor d decreased, as shown in fig.6.6. In fact, while approaching the capacitor to the suspended mirror, the mirror response to the applied voltage on the capacitor, did not show the expected behaviour. The displacement was proportional to the square of the applied voltage on the capacitor (eq.6.3), whereas the effect of the dependence on the distance d of the derivative $\left.\frac{\partial C}{\partial x}\right|_d$ was not clearly increasing as decreasing the distance. Thus the maximal displacement was not obtained for the closest distance d. We therefore passed to another suspension system which approached more a pendulum configuration. This system, shown in fig.6.9, uses a metallic ring that fits in the previous optic mount presented in fig. 6.5, with two screws on the top spaced of $1inch$ (the dimension of the mirror diameter) to hold up the suspension. Therefore, the suspension has to be a unique wire closed in loop in order to be placed on the screws, then fixed between two nuts and spaced by two washers in order to prevent from breaking the wire, which can be seen on the top of the metallic ring in fig.6.9. We extracted the mirror from the support of fig. 6.5, and we glued a wire with Araldite® [2] in only three points around the lower side of the lateral surface (one on the lowest point and two just before the intersection with the diameter). The Araldite® is an epoxy glue resin that sets its fixation by interaction of the resin and the hardener. It acts as a volume glue and is known to be very resistant.

[2] http://en.wikipedia.org/wiki/Araldite

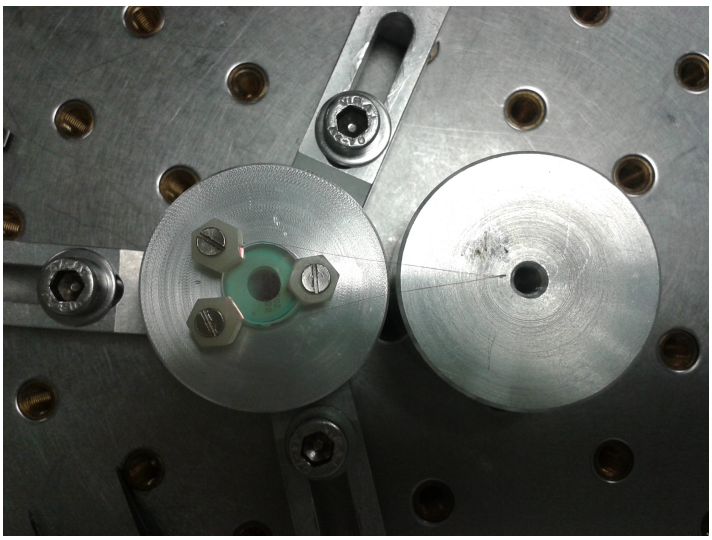

Figure 6.7: The picture shows the gluing of the copper wire of $40\mu m$ diameter on to the $1inch$ diameter test mirror.

A fourth point of glue was used to close up the wire (see fig. 6.7). The suspension wire used was a copper wire, extracted from an electric cable, having a diameter of $40\mu m$. Several tests have been done, by changing the positions of the points of glue or by increasing the glue drying time. The picture of fig. 6.7 shows the gluing process. The mirror is placed on a metallic support and fixed by three screws with nuts made of PVC[3] in order to preserver the mirror, since it is the plastic material in contact with the mirror which applies a low pressure on it. Nevertheless, this process showed a problem of perpendicularity of the suspension. This problem is due to the high dependency of this suspension system to the symmetry of the gluing points. In fact, even the minimal asymmetry in the amount of glue or in the position of the gluing points prevented the mirror from being parallel to the suspension wire, thus not being perpendicular to the optical axis and causing problems in the alignment of the Michelson interferometer.
To compensate this effect of deviation from perpendicularity, we added an L-shaped sustain in contact with the mirror. Once the mirror is suspended, the L-sustain slightly pushes it from the top and the back of the mirror in order to let it assume the correct vertical position, as shown in the figure 6.8. We also made some tests on adding a second wire by gluing with Araldite® the two suspension opportunely spaced, always in only three points. Anyway, it turned out to be impossible realizing a perpendicular suspension with this method. Therefore, such kind of suspension could not be introduced in the Michelson interferometer because it was not suitable to keep the mirror orthogonal to the optical axis and to assure the alignment, and no electrostatic measurements could have been possible with this suspension system.

We then decided to test a new system by gluing two ears on the mirror in order to have two small handles to tie the wire. The ears were made by cutting along the

[3]Poly(vinyl chloride), commonly abbreviated PVC, is the third-most widely produced polymer, after polyethylene and polypropylene.

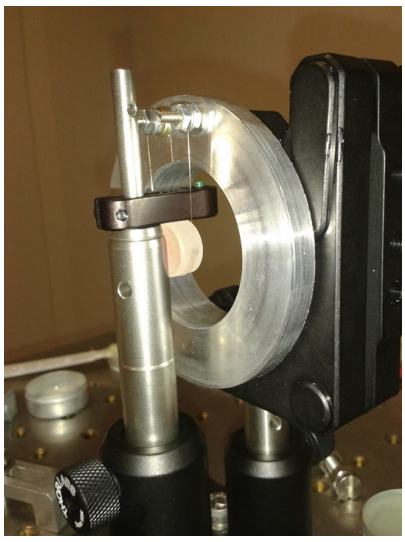

(a) The mirror suspends by one copper wire.

(b) The mirror suspends by one Niobium wire.

Figure 6.8: The pictures show two of the tested suspensions that could not be used for the electrostatic measurements. In the figure (a) on the left the mirror is suspended with the copper wire. Even the use of an L sustain, as shown in this picture, to try to let the mirror settle along the vertical did not solve the problem of perpendicularity. The picture (b) on the right shows the tentative to suspend the mirror with the niobium wire wrapped back on itself around the PVC ears. Nevertheless, this wire is too rigid and too thick to be tighten under the weight of the mirror.

diameter a PVC washer measuring $5mm$ and were then glued with Araldite on opposite side of the mirror with a small inclination upwards. We tried to tie around the ears the copper wire like the one used before, but it was too rigid and too thin so that it broke down when doing the knot.

We then tried a niobium wire of thicker diameter $(60 \pm 3)\mu m$. This material was too rigid to be tied with a knot but we could bent each end of the wire around the corresponding ear and we then fixed it by wrapping the wire on itself, as shown in the picture of fig. 6.8. Nevertheless, the wire was still too rigid and too thick to be tighten under the small weight of the mirror.

We then choose a more elastic material. The most easily available thin wire that could be elastic enough it was one of my hair. This suspension having a diameter of $(58\pm 3)\mu m$, showed a good elastic behaviour over the time of the electrostatic measurements and it was easy to tie on to the ears by two knots without breaking (see fig. 6.9).

This system solved the problem of perpendicularity, because even if the ears might be not glued in exactly symmetric position, once tied on the ears and placed on the screws of the metallic ring support, the wire adjusts itself along the vertical position under the weight of the mirror. Because the knotted wire can still move along the handles of the ears. Nevertheless, this system with the ears works only if the suspension wire is not too rigid and thin enough. For this reason the other materials (the copper and the niobium) were not suitable. This system proved to be even more resistant than

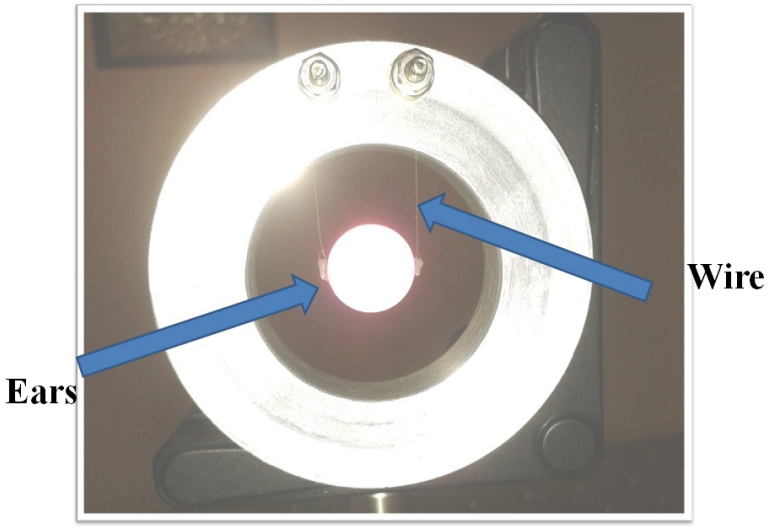

Figure 6.9: The picture shows the best suspension system used for the electrostatic control measurements. A metallic ring that fits in the previous optic mount (of fig. 6.5) has two screws on the top spaced of $1inch$ (the dimension of the mirror diameter) to hold up the suspension. The suspension is a unique wire closed in loop with two knots around two PVC ears glued to the mirror with Araldite. The wire is placed on the screws and fixed between two nuts and spaced by two washers which prevent from breaking the wire. The suspension wire is one of my hair, having a diameter of $\sim 60\mu m$.

the first with the ribbons and gave better results for the electrostatic control. In fact, the mirror suspended in this way behaves like a pendulum so it showed the expected response under the applied voltage on to the capacitor, as in equation (6.3). Moreover, this system allowed to approach the capacitor closer to the mirror, reaching a minimal distance of less than $4mm$. I will report in the following section 6.4 the results on the electrostatic control with the last suspension system used (see fig. 6.9).

6.3 Experimental Set Up

The laser used is a Nd:YAG of wavelength $1064nm$ (IR) as those used for ground based gravitational wave interferometer. The suspended mirror is placed in a Michelson interferometer where the other end mirror was glued to a PZT ceramic bar as shown in the fig. 6.10. All the Michelson elements are placed on the optic table and the capacitor is placed behind the suspended mirror at a distance d, as shown in the scheme of figure 6.3.

Once the mirrors and the beam splitter of the Michelson are aligned we optimize the contrast by manually moving the knobs of the support of two mirrors placed before the beam splitter, thus to adjust the inclination of the incident beam. When the contrast of the interference fringes reaches a value close to 98% the interferometer can be frequency locked at half of the fringe wavelength. The Michelson interferometer is then closed in the box as shown in figure 6.1 to protect from air fluctuation that could affect the

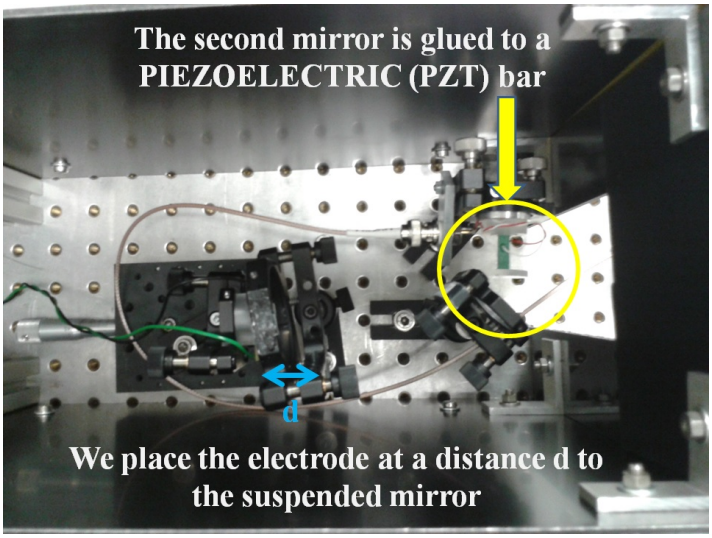

Figure 6.10: The picture shows the Michelson composed by the mirror glued to the PZT ceramic bar (upper on the right), the beam splitter (lower on the right) and the suspended mirror with the electrodes behind (on the left).

suspended mirror and thus the stability of the locking.

6.4 Measurements

The figure 6.11 represents a schematic view of the Michelson and of the procedure of the measurements. The laser enters in the Michelson interferometer from the beam splitter BS. The first mirror M_1 is suspended and the second mirror M_2 is attached to a PZT ceramic bar. A voltage is sent to the capacitor placed at a distance d from the suspended mirror M_1 and a force $F(x)$ as the one in eq.(6.1) will be exerted on the mirror. A high voltage amplifier multiplies by a factor 10 the voltage from the synthesizer before being applied on the capacitor. A second high voltage amplifier multiplies by 10 the correction signal before reaching the PZT (see fig.6.11). The correction signal, in order to keep the interferometer locked, changes the length of the PZT ceramic bar, and hence the position of M_2, thus compensating the displacement of M_1. Therefore, it is crucial to characterize the elongation parameter of the PZT bar k_d at each measurement, because the applied correction voltage to induce the same mirror displacement will vary in function of the distance d between the suspended mirror and the electrodes.

The correction signal on the PZT V_2 is read before being amplified 10 times and it needs to be filtered, as shown in the the scheme of fig. 6.11, with a low pass filter. In fact in the correction signal we formerly observed the modulation due to the pendulum resonance of the suspended mirror at $3Hz$. Therefore, in order to remove this modulation we decided to use a low-pass filter with a cut frequency at $0.16Hz$.

The elongation parameter of the PZT k_d represents its variation of length under a unitary voltage. It can be identify by sending a triangular signal modulated at $20Hz$

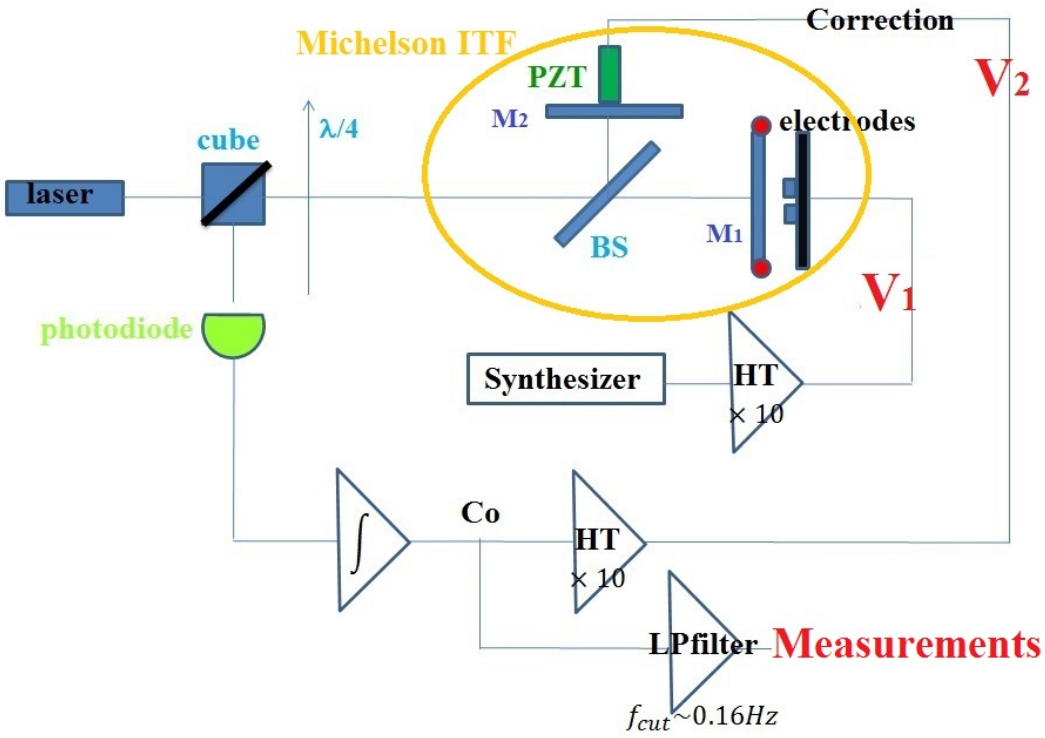

Figure 6.11: Scheme of the measurements. A voltage ΔV is given to the electrodes behind the suspended mirror so that a force is applied on the mirror. In order to keep the Michelson locked a correction signal act to the mirror attached to the PZT bar. By characterizing the PZT elongation over a unitary voltage applied is possible to deduce the mirror displacement by just knowing the voltage applied.

to the PZT and measuring on the oscilloscope the voltage ΔV_0 in the correction signal on the PZT bar, V_2, that corresponds to half fringe ($\lambda/4$) of the interferometer output signal on the photodiode. Thus with a simple proportion the elongation parameter k_d is:

$$\frac{\lambda}{4} : \Delta V_0 = k_d : 1V, \tag{6.11}$$

and since $\lambda = 1064nm$, hence

$$k_d = \frac{\lambda}{4}\frac{1}{\Delta V_0} = \frac{266nm}{\Delta V_0(V)}. \tag{6.12}$$

Once known k_d for a given configuration with a separation distance mirror-capacitor of d, the suspended mirror (M_1) displacement, corresponding to the PZT elongation (M_2 displacement), is directly obtained by multiplying the voltage on the PZT (V_2, correction signal) by the elongation parameter k_d.

Before starting with the measurements, the interferometer needs to be locked. A continuous signal is firstly given to the capacitor. Nevertheless, a d.c. signal turned

out to not be the best choice for the electrodes, because it leaves a residual charge on the capacitor, which alters the measurements. Although a square signal modulated at $8kHz$ has been used after, an effect of residual charge on the capacitors was still present, but much smaller. Hence, to cancel this effect, while increasing the amplitude of the signal from 0 to $100V$, each time the signal was brought back to zero before increasing the amplitude to the desired value for the measurements, and the corresponding zero voltage on the PZT bar is read in order to then be subtracted from the final value of V_2. This process of measurements had to be done very rapidly, in order to avoid drifting effects. For each given voltage to the capacitor (V_1), we read the corresponding V_2 on the PZT, and then by multiplying this value by k_d we obtain the mirror displacement. While the V_2 is a d.c. signal, the read voltage V_1 is the root mean square value of the square signal.
The figure 6.12 shows the best collected sample of measurements that has been obtained for the configuration of suspension with the PVC ears and the hair-wire of $(58 \pm 3)\mu m$ diameter of figure 6.9. The capacitor was at a distance $d = 4mm$ from the suspended mirror M_1 and the maximal displacement reached was of $(731 \pm 19)nm$ for an applied voltage $V_1 = (93.1 \pm 0.1)V$ on the capacitor. The elongation parameter of the PZT has been measured to be

$$k_d = (65.20 \pm 0.01)nm/V. \tag{6.13}$$

where it was measured $\Delta V_0 = (4.08 \pm 0.01)V$. The collected and elaborated data corresponding to this measurement are displayed in the graphic of fig.6.12. The errors on the displacements ΔX are calculated according to the theory of error propagation [15]

$$\Delta X(V_1, k_d) = \frac{\partial X}{\partial V_1}\Delta V_1 + \frac{\partial X}{\partial k_d}\Delta k_d, \tag{6.14}$$

where ΔV_1 and Δk_d are respectively the errors on V_1 and k_d. The same formula has been applied to calculate the error Δk_d on the k_d.
With the software *Origin*® all the data have been plotted and a polynomial fit of the second order has been applied. The so obtained curve that best fitted the data, with the method of least squares, gave a $R^2 = 0.993$ and it was, as expected, a second order curve in V_1 having parameters b, a_1 and a_2 as follows:

$$X = a_2V_1^2 + a_1V_1 + b \tag{6.15}$$
$$a_2 = (0.069 \pm 0.004)nm/V^2 \tag{6.16}$$
$$a_1 = (1.7 \pm 0.2)nm/V \tag{6.17}$$
$$b = (0.8 \pm 1.7)nm. \tag{6.18}$$

6.5 Conclusion

In the QuRaG interferometer there will be three control stages: a magnetic control, to control the position between the suspension disk and the first suspension stage of

the pendulum, a direct electrostatic control to damp the pendulum oscillation along the optical axis, and the thermal control to control the small Michelson interferometer. Therefore, at this stage of the QuRaG project it was necessary to carry out some experiment on the last control stage: the electrostatic control. This accurate study on the electrostatic control of a test mirror showed good results as expected from the analytical calculations mentioned at the beginning of this chapter in sec. 6.1 [119].

In the last configuration of suspension used the mirror correctly responded as a pendulum to the force applied by the capacitor. Therefore, both the choices of the capacitor and of the suspension system were confirmed by the measurements. Moreover, from these tests the procedure of the electrostatic measurements starting from the characterization of the PZT elongation parameter was correctly done and established. The locking system was stable, even if very sensitive to any seismic disturbance coming from the surrounding environment and the doors opening/closing of the neighbour clean rooms.

A maximal displacement of almost $800nm$ has been obtained with a square signal approaching $100V$ (see fig. 6.12). Consequently, the electronics have to be improved to increase the maximal signal up to $300V$. Preliminary results showed that with such a high voltage, the displacement of the mirror will increase of a factor 10, thus reaching the requirements announced in sec. 6.1 [119], of controlling mirror displacements within the order of $1\mu m$. In addition, these tests had been done with a Michelson protected only by a closed box (see fig. 6.1), whereas better results would be obtained by repeating the experiment in vacuum, condition that will decrease the effect of the residual charge on the capacitor.

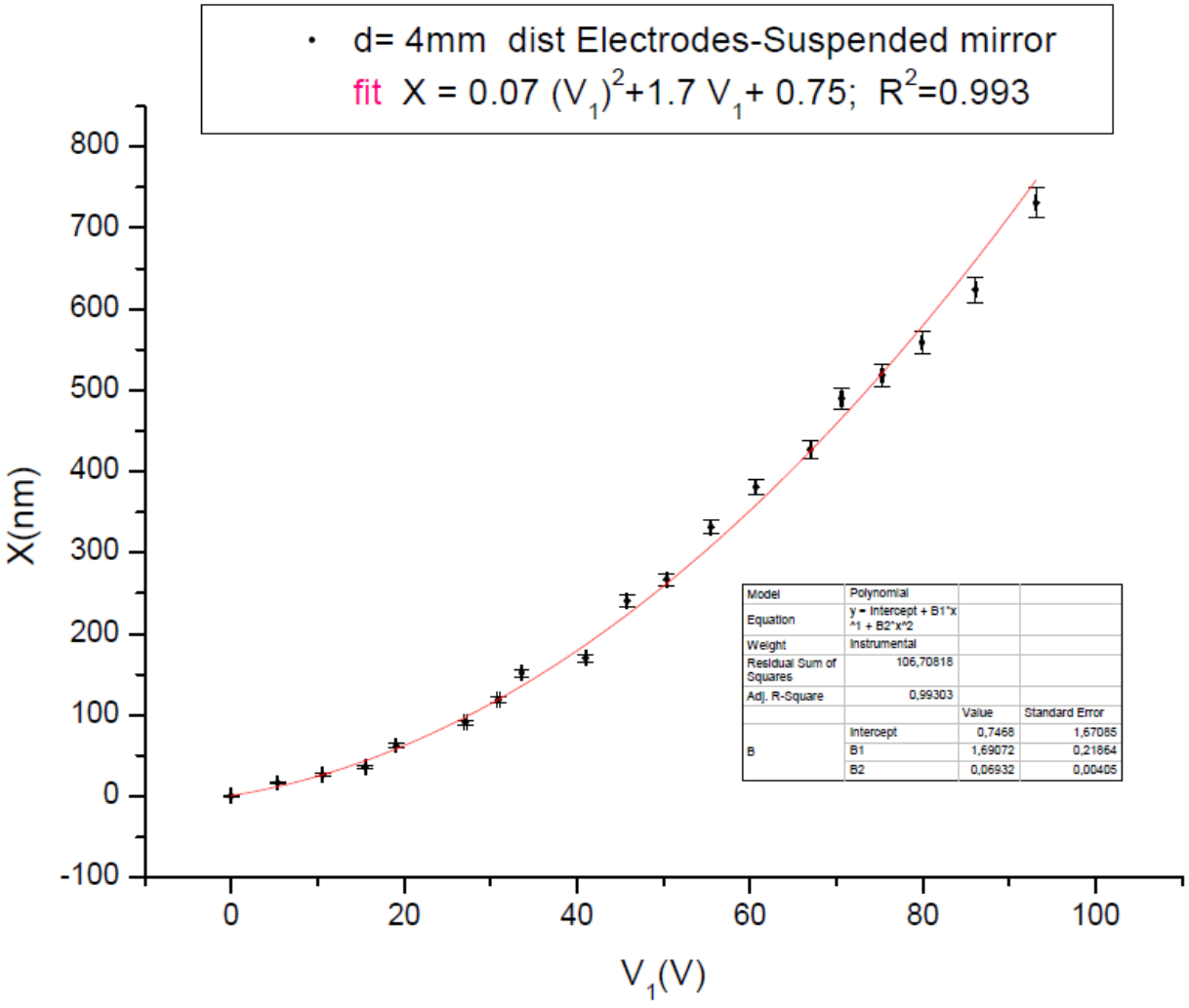

Figure 6.12: Graphic of the fit on the best collected sample. The data show a law $X \propto V_1^2$ as expected. The maximal displacement reached is $\sim 800nm$ for an applied rms voltage on the capacitor of $V_1 = 100V$ while the capacitor is at the closer distance $d = 4mm$ to the suspended mirror, as expected too. The mirror here is suspended with two ears and my hair as suspension wire (see fig.6.9).

Chapter 7

Hermite Gauss Modes of Higher Order: Generation and Optimization

My estimations on the thermal noise demonstrated that QuRaG sensitivity will not be limited by the thermal noise of the mirrors in the middle frequency. Nevertheless, the investigation on the optimization of the generation of the Hermite Gauss (HG) modes of higher order seems very interesting for the development of a tool that could help us, if needed, to further reduce the mirror thermal noise of QuRaG. Moreover, the use of these modes could also be applied to reduce thermal noise in GW detectors and for improving the sensitivity of optical clock experiments [150], which have also approached the mirror thermal noise limit. Within this aim, great part of my research work has been devoted to the problematic of the generation of high order HG modes and optimization of their coupling with a *mode cleaner* cavity. I explain this work and the best obtained results in the present chapter.

7.1 Higher Order Modes to Reduce Mirror Thermal Noise in GW Detectors

In the central region ($\sim 100Hz$) of the detection band of current ground based gravitational wave interferometers, the main limitation to the sensitivity comes from the fluctuations of the mirror surfaces under random motions of matter in the bulk material of the substrate [110]. Moreover, with the improvement of a factor 10 in sensitivity in the whole frequency band of the second generation of GW detectors, the mirror thermal noise fluctuation is expected to be, together with the radiation pressure noise, one of the major limiting noise sources [65]. In fact, from the second generation ahead, the advancements in other areas of the interferometers, such as the increasing of the laser power circulating inside the cavities and the improvement of the radiation pressure noise, also require the optimization of the mirror thermal noise, in order to make all the other enhancements effective around the $100Hz$ region of the detection band (see

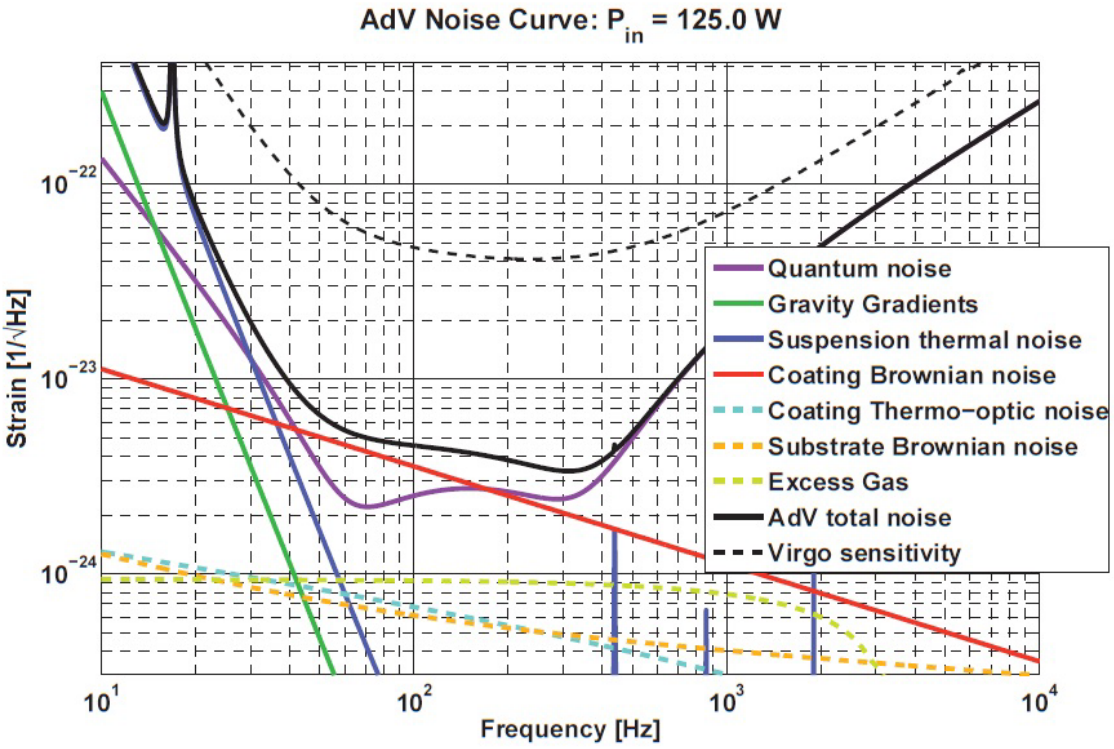

Figure 7.1: Advanced Virgo sensitivity curve. (See chapter 2).

fig. 7.1).

These fluctuations of the mirror surface are interpreted by the readout optical beam as a true motion of the mirror or a gravitational wave signal as well. One proposed method for thermal noise reduction is to use, in place of the Gaussian beam profile, a wider intensity distribution which, [144, 66, 65] can better average over the mirror surface distortions caused by the thermal motions. This method has been investigated for possible upgrades of second [144] and third generation of gravitational wave detectors [123].

It has been demonstrated that the use of beam profiles different from the fundamental Gaussian beam, like the Top-Hat and Laguerre-Gauss already investigated [110, 103, 71, 66, 65] and the Hermite Gauss, which have an intensity profile not concentrated in the center of the beam spot, can reduce the internal noise of the mirror, with an average gain in sensitivity of ~ 2 or even better [144], due to an average process on an area of the mirror's surface larger than with a fundamental Gaussian beam [110].

Nevertheless, the use of such beam profiles in GW interferometers will require no more spherical mirrors but with a suitable shape, i.e. for the 'flat top' profiles, a 'mexican hat' mirror's surface is needed, while for the Laguerre Gauss it is sufficient to replace the flat/spherical arm cavities with symmetrical spherical/spherical cavities [110].

However, the use of such modes has not yet been validated for the second generation of GW detectors, the potentiality of the Hermite Gauss modes still need to be further

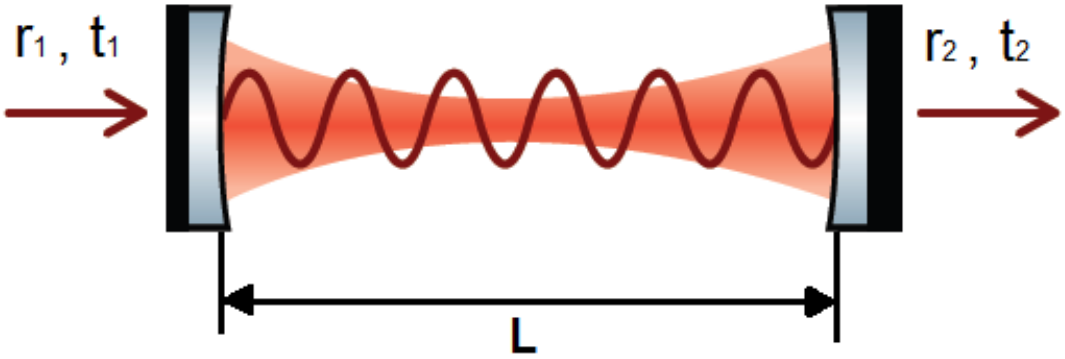

Figure 7.2: Graphical representation of an optical cavity with symmetrical spherical/spherical mirrors. The light field enters the input mirror from the left and resonates inside the cavity if its length is divisible by an integer number of half wavelengths. The sinusoid in brown represents the longitudinal mode properties, and the red shaded area the transverse mode properties.

investigated. The Hermite Gauss modes of higher order can have effects analogous to the Laguerre Gauss and Top Hat modes, by extending the power distribution on the mirror's surface. An important test for those modes is the compatibility with mode cleaner cavities technology [66], since these cavities are largely employed in GW detectors in order to 'clean' the beam intensity profile before being injected inside the interferometer. They are also applied to 'clean' the signal before reaching the output detector [10]. The advantage of mode cleaner cavities, which are usually triangular cavities, is to observe the output mode in transmission and without the need to use polarizing elements which are needed for linear cavities.

7.2 Spatial Laser Modes

Hermite Gauss modes, as well as Laguerre Gauss modes, represent a complete set of solutions to the paraxial wave equation and are well suited to model the eigenmodes of spherical optical resonators [66]. Before discussing on these solutions I introduce some concepts about light modes in resonant cavities.
An optical resonator, or cavity, is almost always used to predefine the geometric properties and the frequency of the light generated by a laser [65]. The light produced from the laser transitions in the lasing material circulates in an optical resonator, and the output beam is transmitted through a semi-transparent mirror. Consider a two mirror optical cavity as in figure 7.2, with light incident on one mirror. An optical resonator, as well as other resonators, owns the property of producing any of an infinite number of resonant modes. The mode operation of a laser is defined by the frequency of the light and the geometric properties of the beam. For an optical resonators these properties are known as the longitudinal mode order and transverse mode order.

For describing the longitudinal mode order of an optical resonator, let's consider

the response of an ideal optical resonator in the plane wave approximation (without considering the transverse properties of the light) [65]. The corresponding circulating power within an optical resonator for an input power of 1W is given by

$$P_{cav} = \frac{t_1^2}{1 + r_1^2 r_2^2 - 2 r_1 r_2 cos(2kL)} \tag{7.1}$$

where t_1 and r_1 are the transmitting and reflective coefficient of the input mirror and r_2 is the reflective coefficient of the output mirror, L is the cavity length and

$$k = \frac{2\pi}{\lambda_L} \tag{7.2}$$

is the wavenumber of the light having wavelength λ_L. Then, there is an infinite set of discrete light frequencies that give a maximum in the circulating light power P_{cav} of eq. (7.1), for a given cavity length L:

$$2kL = 2n\pi \qquad \text{with } n \in \mathbb{N} \tag{7.3}$$

or equivalently

$$\frac{2\pi\nu_n L}{c} = n\pi \qquad \text{with } n \in \mathbb{N}, \tag{7.4}$$

hence the maximum power is given by the frequencies:

$$\nu_n = n\frac{c}{2L} \qquad \text{with } n \in \mathbb{N}. \tag{7.5}$$

Moreover, each resonance can be easily seen as a case that fulfils the criterion that an integer number of half the wavelength matches the cavity length exactly, creating a standing wave inside the cavity [65].

The transverse mode of an optical resonator describes the geometry of a beam cross section, in a plane perpendicular to the propagation vector. An infinite set of transverse modes of an optical resonator with spherical mirrors can be found by solving the paraxial wave equation with the boundary conditions given by the parameters of the cavity, i.e. the cavity length and the curvatures of the mirrors [65]. The paraxial wave equation is the wave equation of the electric field with the additional approximation that the light field is beam-like, i.e. it varies much more rapidly along the transverse axes than the propagation axis (the paraxial approximation). The electric field can be described as the product of a function containing the spatial properties $u(x, y, z)$ and the oscillating function in the propagation direction z, i.e. e^{ikz}:

$$E(x, y, z) = u(x, y, z)e^{ikz}. \tag{7.6}$$

Then, substituting $E(x, y, z)$ of eq.(7.6) into the wave equation for the electric field, it is obtained

$$\frac{\partial^2 u}{\partial x^2} + \frac{\partial^2 u}{\partial y^2} + \frac{\partial^2 u}{\partial z^2} + 2ik\frac{\partial u}{\partial z} = 0, \tag{7.7}$$

and considering the condition that the variation on the beam shape is much slower in z than in x and y, i.e. the paraxial approximation:

$$\left|\frac{\partial^2 u}{\partial z^2}\right| \ll \left|\frac{\partial^2 u}{\partial x^2}\right|, \left|\frac{\partial^2 u}{\partial y^2}\right|, \left|2k\frac{\partial u}{\partial z}\right| \tag{7.8}$$

then the wave equation eq.(7.7) assumes the paraxial form:

$$\frac{\partial^2 u}{\partial x^2} + \frac{\partial^2 u}{\partial y^2} + 2ik\frac{\partial u}{\partial z} = 0. \tag{7.9}$$

There exist many solutions to the eq.(7.9), each representing a transverse mode of the electric field. The lowest order solution is the Gaussian beam, with transverse field distribution (normalized) given by

$$E(x,y,z) = \sqrt{\frac{2}{\pi}}\frac{e^{-i\psi(z)}}{\omega(z)} e^{i\frac{k}{2}\frac{x^2+y^2}{R(z)}} e^{-\frac{x^2+y^2}{w^2(z)}} e^{ikz}, \tag{7.10}$$

where $\omega(z)$ is the Gaussian spot size parameter, $\psi(z)$ is the Gouy phase, and $R(z)$ is the radius of curvature of the spherical phase front, and which are defined:

$$w(z) = w_0\sqrt{1 + \frac{(z-z_0)^2}{z_R^2}}, \tag{7.11}$$

$$R(z) = (z-z_0) + \frac{z_R^2}{(z-z_0)}, \tag{7.12}$$

$$\psi(z) = -\arctan\Big(\frac{(z-z_0)}{z_R}\Big), \tag{7.13}$$

where w_0 is the beam waist at z_0 and z_R is the Rayleigh length equal to

$$z_R = w_0^2\frac{\pi}{\lambda_L}. \tag{7.14}$$

The Rayleigh zone, for which $z - z_0 = z_R$, gives an idea of the area in which the wavefront curves.

The eq.(7.10) is the paraxial wave which represents a propagating wave along z with finite power, and that has a Gaussian profile in x and y, which is completely defined through its parameter w_0 (waist), and its source point z_0.

There also exist several infinite sets of solutions to the paraxial wave equation (7.9), each including the Gaussian mode as well as higher order solutions. The two sets of solutions which are more used are the Hermite Gauss (HG) and Laguerre Gauss (LG) modes. Both sets are a complete base, which means that they can be used to construct an orthonormal basis system in which all solutions to the paraxial wave can be

represented as linear combination of the basis modes [65]. Since all beam-like electric fields should satisfy the paraxial wave equation, it is always possible to use a linear combination of the HG or LG modes to describe any beam profile.

An important characteristic common to all transverse modes of spherical optical resonators is their self-reproducing intensity pattern, i.e. when they propagate, the overall scale of the transverse field distribution will change, but the shape remains constant.

7.3 High Order Hermite Gauss Modes

The Hermite Gauss modes represent a set of solutions to the paraxial wave equation in Cartesian coordinates, having rectangular symmetry. In fact, starting from a set of solutions in which the x and y component can be separated, i.e. having the form

$$u_{n,m}(x,y,z) = u_n(x,z)u_m(y,z), \tag{7.15}$$

we obtain that the solutions $u_n(x,z)$ and $u_m(y,z)$ exist and are independent if they simultaneously satisfy the reduced paraxial equation

$$\begin{cases} \frac{\partial^2 u_n}{\partial x^2} + 2ik\frac{\partial u_n}{\partial z} & = 0 \\ \frac{\partial^2 u_m}{\partial y^2} + 2ik\frac{\partial u_m}{\partial z} & = 0. \end{cases} \tag{7.16}$$

A set of such solutions is represented by the normalized Hermite Gauss modes which have the form [138]

$$E_{n,m}(x,y,z) = \sqrt{\frac{2}{\pi}}\left(\frac{e^{-i(2m+2n+2)\psi(z)}}{2^{n+m}m!n!w^2(z)}\right)^{1/2} H_n\left(\frac{\sqrt{2}x}{w(z)}\right)H_m\left(\frac{\sqrt{2}y}{w(z)}\right)e^{i\frac{k}{2}\frac{x^2+y^2}{R(z)}}e^{-\frac{x^2+y^2}{w^2(z)}}e^{ikz}, \tag{7.17}$$

of electric field distributions essentially given (apart from the phase term) by the product of a Gaussian function weighted by Hermite polynomials H_m and H_n with non-negative integer indices n and m, in the transverse beam pattern (transverse modes). I recall that the Hermite polynomials are:

$$\begin{cases} H_0(x) = 1 \\ H_1(x) = 2x \\ \vdots \\ H_{n+1}(x) = 2xH_n(x) - 2nH_{n-1}(x) \end{cases} \tag{7.18}$$

The $u_n(x,z)$ and $u_m(y,z)$ functions are then of the form

$$u_n(x,z) = \left(\frac{2}{\pi}\right)^{1/4}\left(\frac{e^{-i(2n+1)\psi(z)}}{2^n n! w(z)}\right)^{1/2} H_n\left(\frac{\sqrt{2}x}{w(z)}\right)e^{i\frac{k}{2}\frac{x^2}{R(z)}}e^{-\frac{x^2}{w^2(z)}}e^{ikz}, \tag{7.19}$$

and they describe the variation of amplitude in the orthogonal $x-z$ and $y-z$ planes and have an identical form. The indices n and m of the Hermite polynomials describe

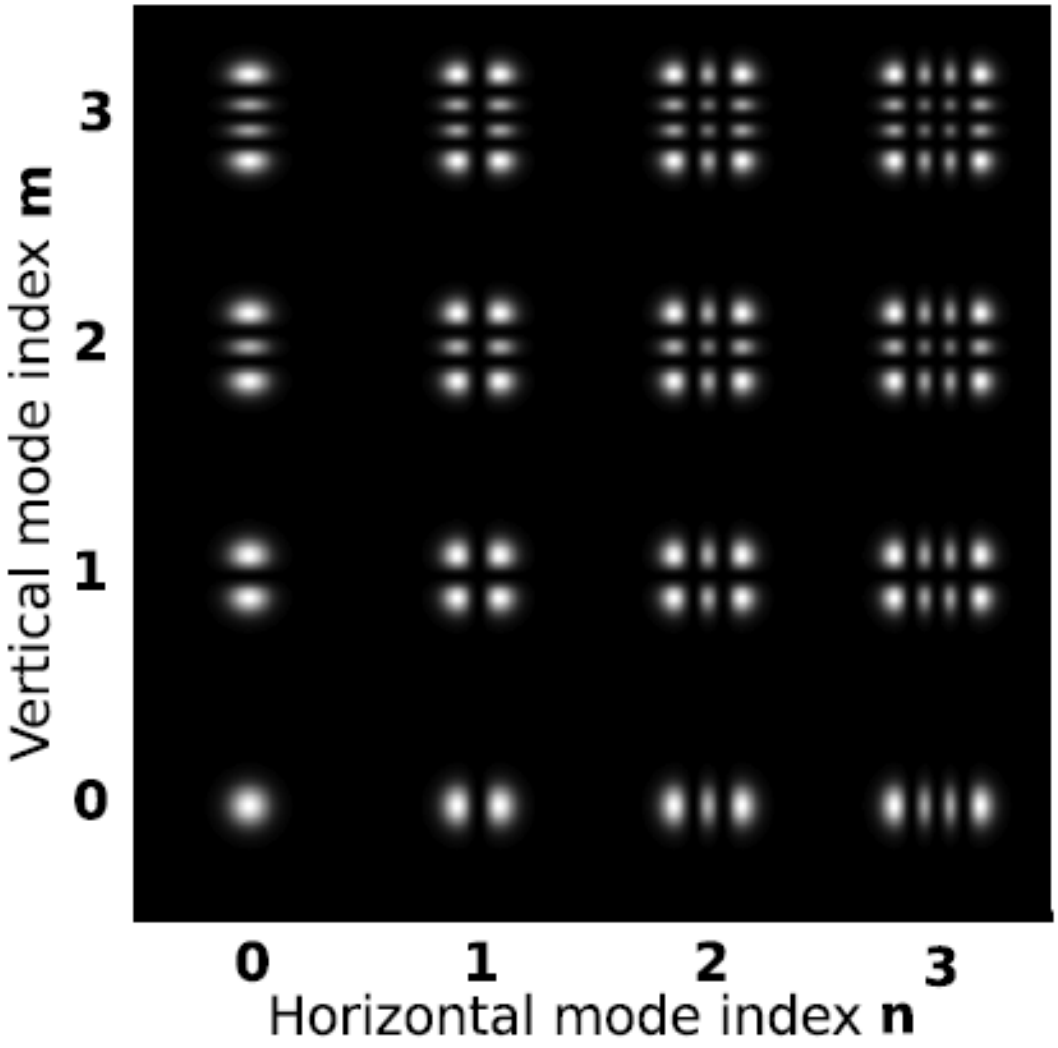

Figure 7.3: Intensity patterns of the Hermite Gauss modes $HG_{n,m}$ from the order $HG_{0,0}$ till the $HG_{3,3}$. The first index n is the horizontal mode index and the second index m refers to the vertical mode index.

respectively the order of the transverse mode in x and in y. Therefore, for $m = n = 0$ we find back the Gaussian beam of eq. (7.10). Note that the separability in x and y means that HG modes can be eigenmodes of astigmatic spherical optical resonators [65]. The intensity distribution of a $HG_{n,m}$ mode has n nodes in the horizontal direction and m nodes in the vertical direction. The order of a $HG_{n,m}$ mode is given by the horizontal index n and the vertical index m, and in figure 7.3 are shown some examples of modes from the $HG_{0,0}$ till the $HG_{3,3}$.

Observe from eq. (7.17) that the $HG_{n,m}$ modes have a Gouy phase which depends on (n, m). In fact the phase term $e^{-i(2m+2n+2)\psi(z)}$ can be rewritten as

$$e^{-i2(m+n+1)\psi(z)} = e^{-i2\psi_{n,m}(z)}, \tag{7.20}$$

where $\psi_{n,m}(z)$ is the new Gouy phase:

$$\psi_{n,m}(z) = (m + n + 1)\psi(z). \tag{7.21}$$

I want now to derive the resonance condition for the HG modes in an optical cavity. Let us define the parameters g_1 and g_2 for an optical cavity of length L composed by two mirrors having radius of curvature R_{c1} and R_{c2}:

$$g_{1,2} = 1 - \frac{L}{R_{c1,c2}}, \tag{7.22}$$

therefore the accumulated phase in the optical path between z_1 and z_2 is

$$\phi(z_2) - \phi(z_1) = kL + \frac{\pi}{2} + \psi_{n,m}(z_2) - \psi_{n,m}(z_1). \tag{7.23}$$

If we write the Gouy phase in function of the g_1 and g_2 parameters [136]:

$$\begin{cases} \psi(z_1) & = \arctan\left(\sqrt{\frac{g_2}{g_1}}\frac{1-g_1}{\sqrt{1-g_1g_2}}\right) \\ \psi(z_2) & = \arctan\left(\sqrt{\frac{g_1}{g_2}}\frac{1-g_2}{\sqrt{1-g_1g_2}}\right) \end{cases} \tag{7.24}$$

we obtain that

$$\psi(z_2) - \psi(z_1) = \arccos(\pm\sqrt{g_1g_2}), \tag{7.25}$$

and the resonance condition writes as

$$\frac{2\pi}{c}L\nu_{n,m} + \frac{\pi}{2}(m + n + 1)\arccos(\pm\sqrt{g_1g_2}) = q\pi. \tag{7.26}$$

Hence the HG modes do not have the same resonant frequency, since it depends on the mode order, i.e. $\nu_{n,m}$, and the optical cavity in which the HG mode resonates acts as a filter, and by changing the length of the cavity we can change the resonating mode. The effect of filtering disappears if $\arccos(\pm\sqrt{g_1g_2}) \to 0$, hence if $g_1g_2 \to 1$, moreover, if $\arccos(\pm\sqrt{g_1g_2}) \to \pm\frac{\pi}{2}$, hence if $g_1g_2 \to 0$, the odd modes are coincident with the fundamental and they can not be filtered by the cavity.

7.4 Laguerre Gauss Modes

The Laguerre Gauss (LG) modes are solutions to the paraxial wave equation in cylindrical polar coordinates and, unlike HG modes, the complex amplitude function is not separable in x and y, so LG modes are not eigenmodes for astigmatic optical resonators. LG modes are commonly expressed in two different forms, the sinusoidal mode set and the helical mode set, but only the helical set all have circularly symmetric intensity profiles [65]. The complex amplitude distribution of the sinusoidal LG mode set is given by

$$u_{p,l}^{sin}(r,\phi,z) = \frac{1}{w(z)}\sqrt{\frac{2p!}{\pi(|l|+p)!}}e^{i(2p+|l|+1)\psi(z)}\left(\frac{\sqrt{2}r}{w(z)}\right)^{|l|}L_p^l\left(\frac{2r^2}{w^2(z)}\right)e^{-ik\frac{r^2}{2q(z)}}\left\{\begin{array}{l}\sin(l\phi)\\ \cos(l\phi)\end{array}\right\} \tag{7.27}$$

where p, l and L_p^l are the radial mode index, the azimuthal mode index and the associated Laguerre polynomials. Moreover, the complex $q(z)$ can be decomposed in the sum of its real and imaginary part:

$$\frac{1}{q(z)} = \frac{1}{q_r(z)} + i\frac{1}{q_i(z)} = \frac{1}{R_c(z)} + i\frac{\lambda}{\pi w^2(z)}. \tag{7.28}$$

The complex amplitude of the helical LG modes differs from the sinusoidal in the azimuthal dependence which is given by $e^{il\phi}$:

$$u_{p,l}^{helical}(r,\phi,z) = \frac{1}{w(z)}\sqrt{\frac{2p!}{\pi(|l|+p)!}}e^{i(2p+|l|+1)\psi(z)}\left(\frac{\sqrt{2}r}{w(z)}\right)^{|l|}L_p^l\left(\frac{2r^2}{w^2(z)}\right)e^{-ik\frac{r^2}{2q(z)}}e^{il\phi}. \tag{7.29}$$

The radial mode index p determines the number of radial nodes appearing in the amplitude cross section of the beam and is equivalent for sinusoidal and helical modes. The azimuthal mode index l determines the number of azimuthal nodes for the sinusoidal modes. For the helical modes l determines the number of 2π phase shifts that appear around a circle of constant r. Helical modes can be seen as a linear combination of two sinusoidal LG modes with the same mode indices but with a phase shift of $\pi/2$ between them since from the Euler's formula $e^{il\phi} = \cos(l\phi) + i\sin(l\phi)$ [65, 66].

We recall that the generalized Laguerre polynomials are solutions of the differential equation:

$$xy''(x) + (\alpha + 1 - x)y'(x) + ny(x) = 0 \qquad \text{with } \alpha \in \mathbb{R}, \tag{7.30}$$

where $y'(x)$ and $y''(x)$ identify the first and second derivative of y in x. The generalized Laguerre polynomials are then:

$$\left\{\begin{array}{l} L_0^{(\alpha)}(x) = 1 \\ L_1^{(\alpha)}(x) = 2 + \alpha - x \\ \vdots \\ L_{k+1}^{(\alpha)}(x) = \frac{(2k+1+\alpha-x)L_k^{(\alpha)}(x) - (k+\alpha)L_{k-1}^{(\alpha)}(x)}{k+1} \end{array}\right. \tag{7.31}$$

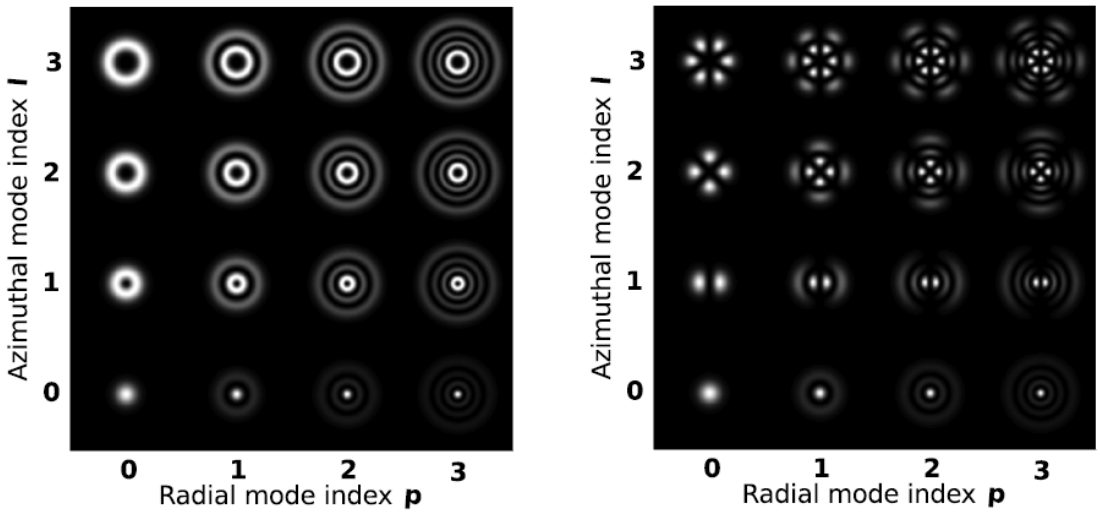

Figure 7.4: Intensity patterns of the Laguerre Gauss modes $L_{p,l}$. In the left panel are shown the helical LG modes up the $L_{3,3}$ and in the right panel the sinusoidal LG modes up to the $L_{3,3}$. The first index p is the radial mode index and the second index l refers to the azimuthal mode index.

or in a more compact form, the Rodrigues formula [6]:

$$L_n^{(\alpha)}(x) = x^{-\alpha}\frac{\left(\frac{d}{dx}-1\right)^n}{n!}x^{n+\alpha}. \tag{7.32}$$

7.5 Generation of Hermite Gauss Modes

Several methods have been demonstrated for the generation of Higher Order LG modes [88], and the optimization of higher-order LG modes has been carried out also with methods not suited for gravitational wave detectors. For example, in the cold atoms and optics fields the use of LG modes (or equivalently HG modes) requires high-speed manipulation of the beam parameters and positions, whereas for high precision interferometry the use of higher order modes relies on the mode purity and stability [66]. One of the leading candidate method for the conversion from $HG_{0,0}$ mode to higher-order modes in high precision interferometry is the use of diffractive optics, or phase plates, because of their stability, potentially high conversion efficiency and output mode purity [66]. Other examples of conversion methods use computer generated holograms [13] or spatial light modulators [103]. None of these methods is perfect since some unwanted light inevitably remains in the modes. Nevertheless, an effectively pure and stable higher order mode light source can be obtained with the implementation of mode cleaner cavities [66]. Mode cleaners are employed as medium to high finesse optical resonators which are feedback controlled to remain on resonance for the chosen laser mode. Gravitational wave interferometers use mode cleaner cavities in several locations. For example, the pre-mode cleaners are used in the initial frequency stabilization chain of

the laser, then the beam passes through the input mode cleaners, suspended optical cavities to filter beam geometry fluctuations (beam jitter noise). Current interferometers also include optical cavities in the main interferometer acting as additional mode cleaning cavities. Moreover, a small in-vacuum output mode cleaner is used to filter the light leaving the interferometer before reaching the photodetectors. Mode cleaners can be used to increase the spatial purity of any Gaussian mode. Therefore, the experimental verification of the compatibility of higher order modes with mode cleaner cavities is of great importance for validating the use of such modes in gravitational wave interferometers, or in any high precision interferometer.

For mode cleaner cavities the use of the triangular configuration is more frequent, since it allows to spatially separate the injected beam from the reflected one, enabling to measure the control error signal in reflection without the use of polarizing optics. It is important to underline that after one full round trip in a triangular cavity any beam is mirrored about the vertical axis, which means that the problem of the mode intensity patter symmetry is a fundamental issue to deal with while generating the higher order modes.

7.5.1 LCOS-SLM

The method using a spatial light phase modulator (SLM) is currently the most appropriate method for the generation of higher order modes, because of its universal, flexible and widely applicable scheme and because it allows a dynamical control of the higher order beam generation [75, 103]. In our experiment higher order HG modes are generated using a phase only type Liquid-Crystal-on-Silicon Spatial Light Modulator (LCOS-SLM). Our LCOS-SLM is a Hamamatsu® X10468 series, for $\lambda = 1064nm$ laser light source, whose active area consists of a rectangular screen of 792×600 pixels, with pixel size $20\mu m \times 20\mu m$ (see figure 7.5). The LCOS-SLM is a reflective light phase modulation device equipped with a monolithic silicon circuit for electrically controlling the orientation of parallel-aligned nematic[1] liquid crystal (LC) molecules. As a result, the LCOS-SLM device achieves easy and flexible use while special care is required in practical operations, particularly when precise phase setting is required [103].
The figure 7.6 shows a schematic cross sectional picture of the structure of the LCOS-SLM device. A LC layer is placed between a pair of alignment layers and attached to an optically flat glass substrate (thickness $3mm$) via a transparent electrode layer. A silicon backplane, equipped with an active matrix circuit directly connected to the pixelated metal electrodes, is mounted onto the other side of the LC layer to control the orientation of the LC molecules at each pixel [103]. This process allows to change the refractive index of the liquid crystal, but only for one polarization. For this reason it is important to assure that the incoming beam is horizontally polarized, i.e. the direction of polarization should be parallel to the plane including the incident and reflected light. Thus the phase is modulated by the LC layer and the amount of phase modulation varies according to the voltage level applied on the pixel electrodes. Moreover, the

[1] existing in or having a mesomorphic state in which a linear orientation of the molecules causes anisotropic properties.

Figure 7.5: Liquid-Crystal-on-Silicon Spatial Light Modulator (LCOS-SLM) device used. It is a Hamamatsu® LCOS-SLM X10468 series, for $1064nm$ light, whose active area consists of 792×600 pixels, with pixel size $20\mu m \times 20\mu m$.

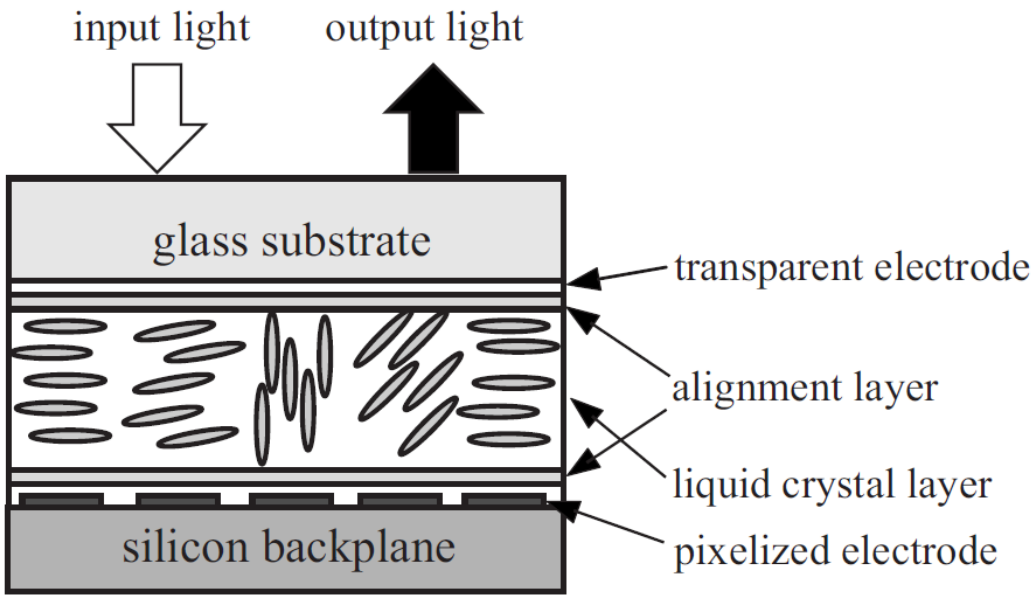

Figure 7.6: Cross sectional picture of the structure of the Liquid Crystal on Silicon Spatial Light Modulator (LCOS-SLM) device.

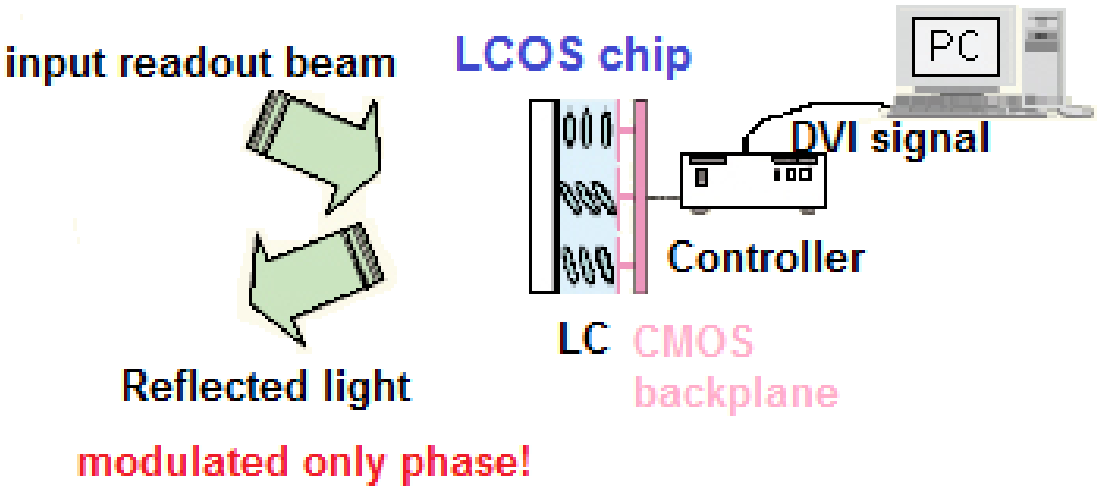

Figure 7.7: The controller processes image signals sent from the PC via the DVI-D cable and sends control signals to the LCOS-SLM.

diffraction efficiency depends on the spatial frequency, and in particular, it decreases with increasing spatial frequency from a maximum of 90% to $\geq$ 40% [2]. The LCOS-SLM controller contains circuits for supplying power and for generating data signals and control signals for driving the LCOS-SLM. The controller processes image signals sent from the PC via the DVI-D cable and sends control signals to the LCOS-SLM (see figure 7.7). The input light is projected onto the LCOS-SLM, where it is attached to a phase distribution of a required HG mode. The output light, which propagates in a slightly different direction with respect to the unmodulated input light, due to the blazed phase pattern, needs to be extracted by using a Fourier transform lens.

7.6 Experimental Set Up and Measurements

For the generation and optimization of the higher order HG modes, the fundamental elements that I used on the optical bench are in order:

- the light source, a *Innolight*® Nd:YAG 1064nm IR laser;
- an amplifier which assures an incident laser power of $few W$;
- the device to generate HG modes, a LCOS-SLM *Hamamatsu*®, X10468series;
- the Fourier lens, a plane-convex lens with $f = 300mm$;
- a spatial filter, which allows us to clean the beam from unwanted diffracted light;

[2]Hamamatsu®, LCOS-SLM X10468series, Hardware Instruction Manual

- the suitable optics (lens and mirrors) to obtain the adequate beam waist on the input mirror of the mode cleaner cavity (or the linear cavity), and to assure the resonance condition;
- a photodiode to read the output signal in transmission;
- a Camera to check the mode pattern;
- a CCD camera to capture the mode intensity pattern and measure the beam waist in x and y.

The phase maps displayed on the SLM screen are generated thanks to a program on $Matlab^{®}$. The interface of the program allows us to control the pixel area covered by the phase map, the order of the mode in x and y, the waist of the mode w_x in x in pixel, the ellipticity (which contains the information on the waist w_y in y), the positions z_x of the waist w_x and z_y of w_y, and the focal lengths f_x in x and f_y in y of a virtual lens to eventually correct mode's distortions. We separate the beam characteristics in x and y in order to compensate possible discrepancies in the beam size and position accumulated by the mode during the propagation on the optical bench, as for example due to eventual asymmetries of the lens curvatures in x and y, and/or to the fact that the SLM screen is rectangular. Moreover, in the last setting I substitute the normal spherical lenses with cylindrical lenses, in order to realize a more precise calibration in the two directions and manually correcting the differences in the beam waist position in x and y. This step of the experiment is fundamental, because in order to then obtain a mode that can be coupled in a mode cleaner cavity, it should firstly be properly generated. This requires to choose the suitable input parameter of the $Matlab^{®}$ program which gave a high quality mode, i.e. with an intensity pattern as poor as possible of any diffracted light nearby the mode area.

The LCOS-SLM used requires that the incoming light on the SLM has an incident angle $\theta \leq 10°$ and horizontally polarized (the polarization direction should be parallel to the plane including the incident and reflected light). The laser's power on the SLM should also be controlled around few Watt.
To convert the beam reflected from the SLM a Fourier lens (a plane-convex lens) with $f = 300mm$ is used. A spatial filter, after the Fourier transform lens, allows to clean the beam from unwanted diffracted light. The suitable optic elements are then chosen to send the beam with the required characteristics (waist and waist position) at the input mirror of the mode cleaner cavity. Before injecting the beam in the cavity, a Gaussian fit on the beam, with the help of the camera software $DataRay^{®}$ to measure the waist at a given position and then of the $GaussianBeam^{®}$ software to identify the beam waist and position, allows to verify the beam characteristics before being injected in the cavity, and to further act on the input parameters to be set on the $Matlab^{®}$ program interface.

To monitor the cavity length, the position of the concave mirror is controlled and adjusted thanks to the correction signal generated from the transmission signal on the

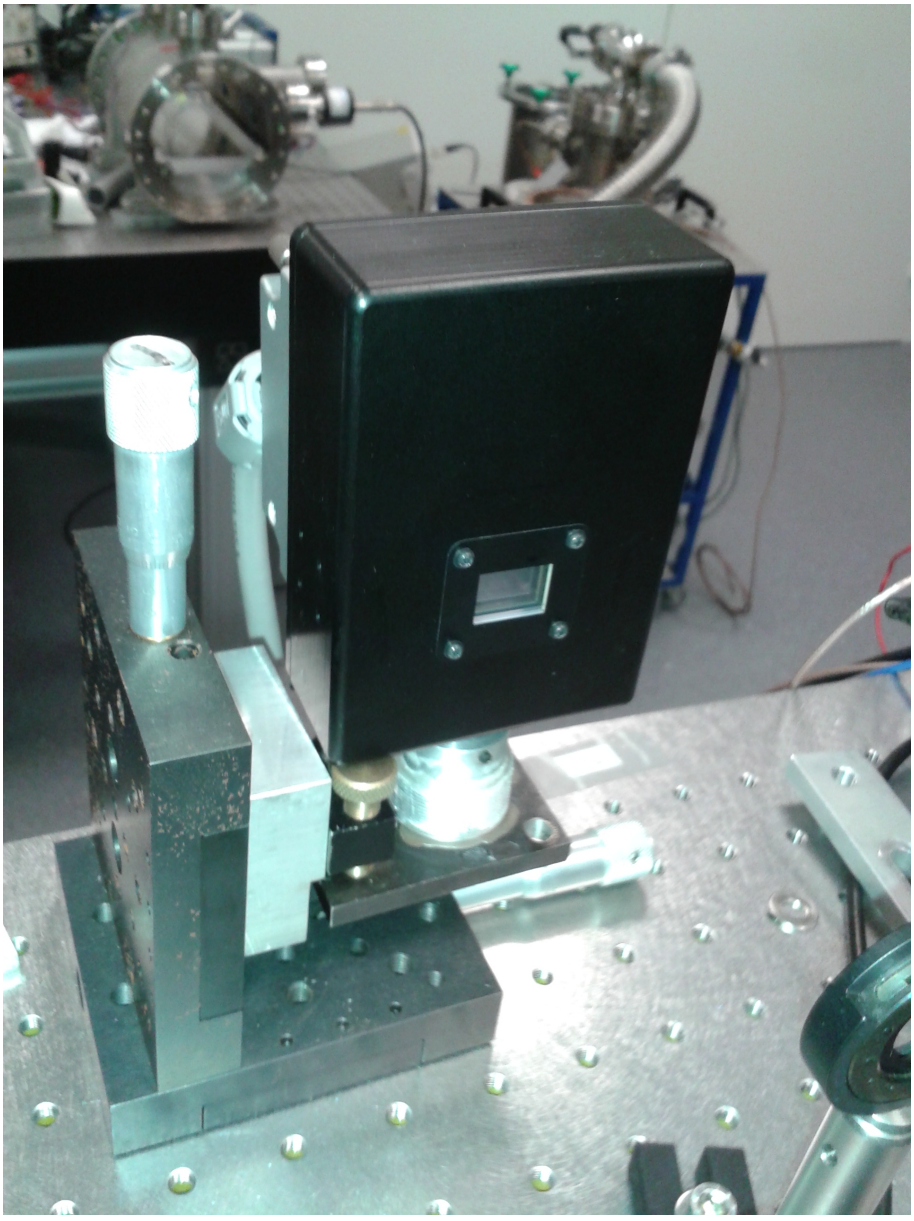

Figure 7.8: Photo of the used phase only spatial light modulator (SLM) a *Hamamatsu*®, X10468series, liquid crystal on silicon -SLM.

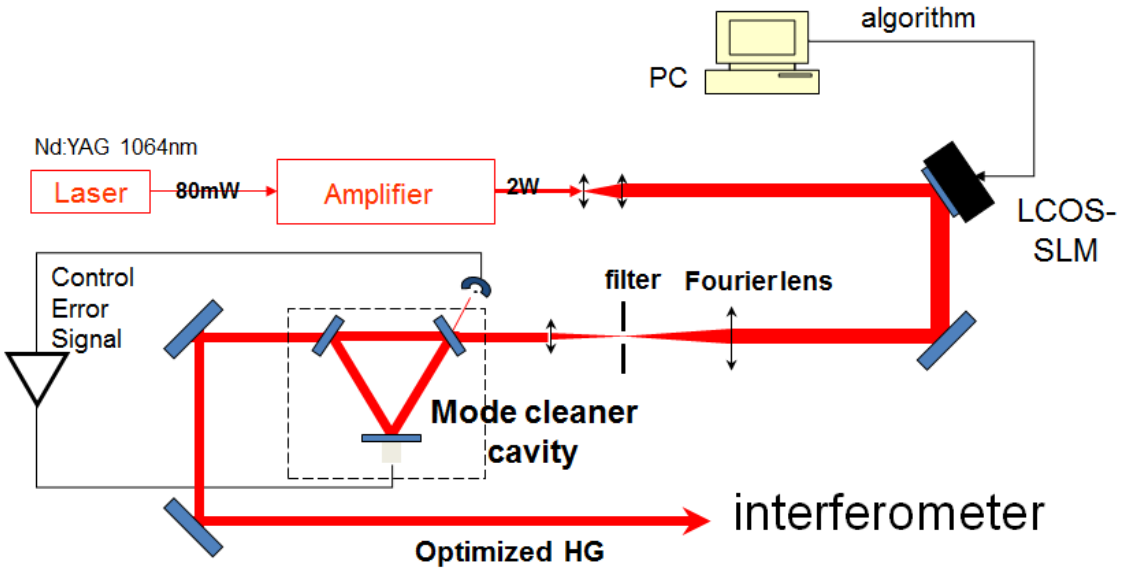

Figure 7.9: Experimental set up for the generation of the HG modes.

photodiode. Once the beam is coupled inside the mode cleaner cavity, I estimate the HG mode coupling with the cavity by measuring the contrast of the signal in reflection. Two movable mirrors, placed before the injection of the HG mode into the mode cleaner cavity, are manually adjusted to optimize the contrast, while always checking the order of the mode on a camera displayed on a screen. Once the contrast is optimized I observe the mode pattern with a CCD camera (for IR light at $1064nm$) controlled by the $DataRay^{®}$ software on the PC. I then compare the mode intensity pattern with the mode intensity pattern of the mode before the 'cleaning' in the cavity. The mode pureness is progressively increased by varying the input parameters on the $Matlab^{®}$ program interface.

The first mode cleaner cavity used has the characteristics described in figure 7.10. It has mirrors of diameter $1inch$, a length of $L = 150mm$, an aperture angle of $\alpha = 12°$, an end mirror with radius of curvature $R_c = 30cm$. In order to have a proper mode resonating in the cavity it requires a beam waist of $550\mu m$ at the entrance of the cavity (first plane mirror on the top-right of the figure 7.10). Then we had to move to a $2inches$ mirrors triangular cavity, shown in the picture of fig.7.12, for geometrical reasons. This cavity has been used as a test cavity, to verify the nature of the generated higher order mode. The effective area of the cavity mirrors of the first triangular cavity, is too small with respect to the beam size of modes higher than the $HG_{5,5}$, as explained in sec. 7.7. Therefore, we decided to use a linear cavity to avoid the geometrical problem related to the previous triangular cavity. The linear cavity used, as shown in figure 7.11, has a length of $150mm$ and mirrors of $1inch$. The cavity is locked by locking the laser on the cavity length. The two mirrors are one flat and one concave with a radius of curvature $R_c = 30cm$, and the beam waist of $273\mu m$ should coincide with the flat mirror.

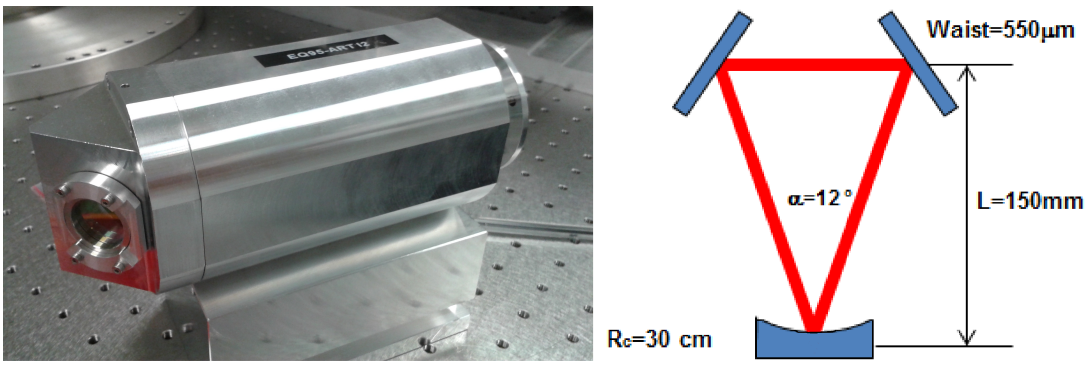

Figure 7.10: First Triangular Cavity with 1*inch* mirrors, used for the optimization and 'cleaning' of the higher order HG modes.

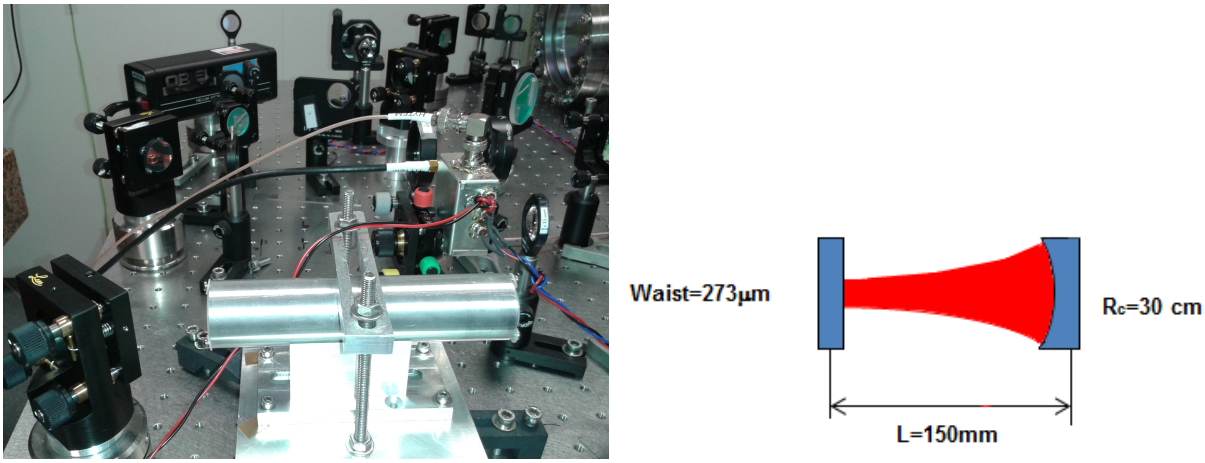

Figure 7.11: Real picture and scheme of the linear cavity used for the optimization and 'cleaning' of the higher order HG modes.

7.7 Results

The developed method of creating phase maps with the LCOS-SLM by communicating with the PC which produces the desired phase maps thanks to a *Matlab*® program interface, demonstrates that proper Hermite Gauss modes till the order $HG_{25,25}$ can be generated. For what concerns the coupling in mode cleaner cavities, the first triangular mode cleaner cavity used (see fig. 7.10) gives good results for HG modes until the $HG_{5,5}$ for which the geometry of the cavity was not suited. In fact, with respect to the beam size of HG modes of orders higher than $HG_{5,5}$, the size of the mirrors (1*inch* diameter) is too small because of the mechanical configuration of the cavity which prevents the possibility to use the whole mirror surface, thus reducing the effective mirror size. Therefore, we used as test cavity a triangular cavity with bigger mirrors having diameter of 2*inches*.

Anyway, with the first triangular cavity I obtained a coupling of $\geq 85\%$ for the modes

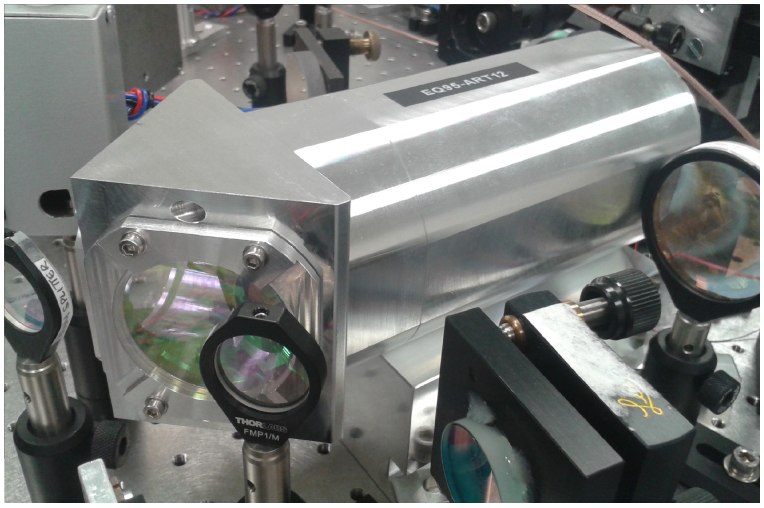

Figure 7.12: Second Triangular Cavity with 2*inch* mirrors.

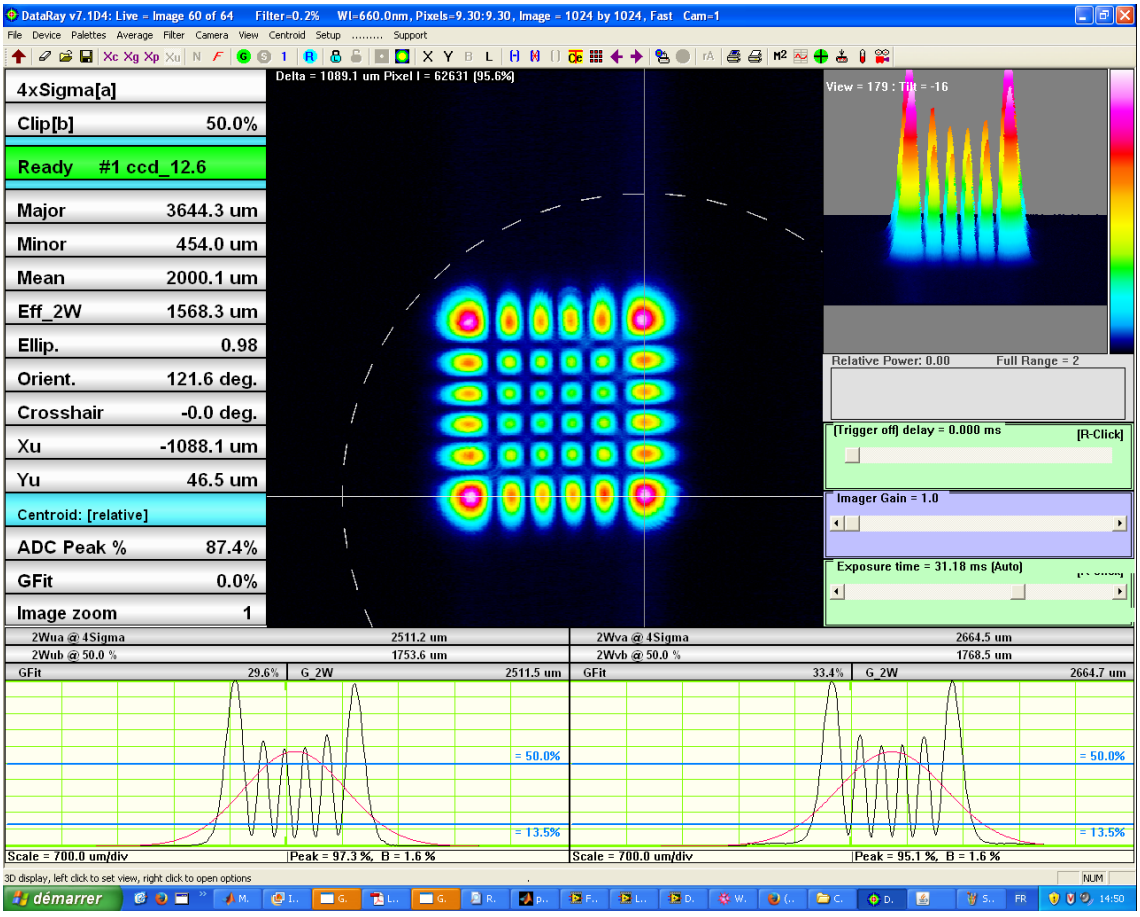

Figure 7.13: $HG_{5,5}$ with the best obtained coupling in the linear cavity, i.e. 80%.

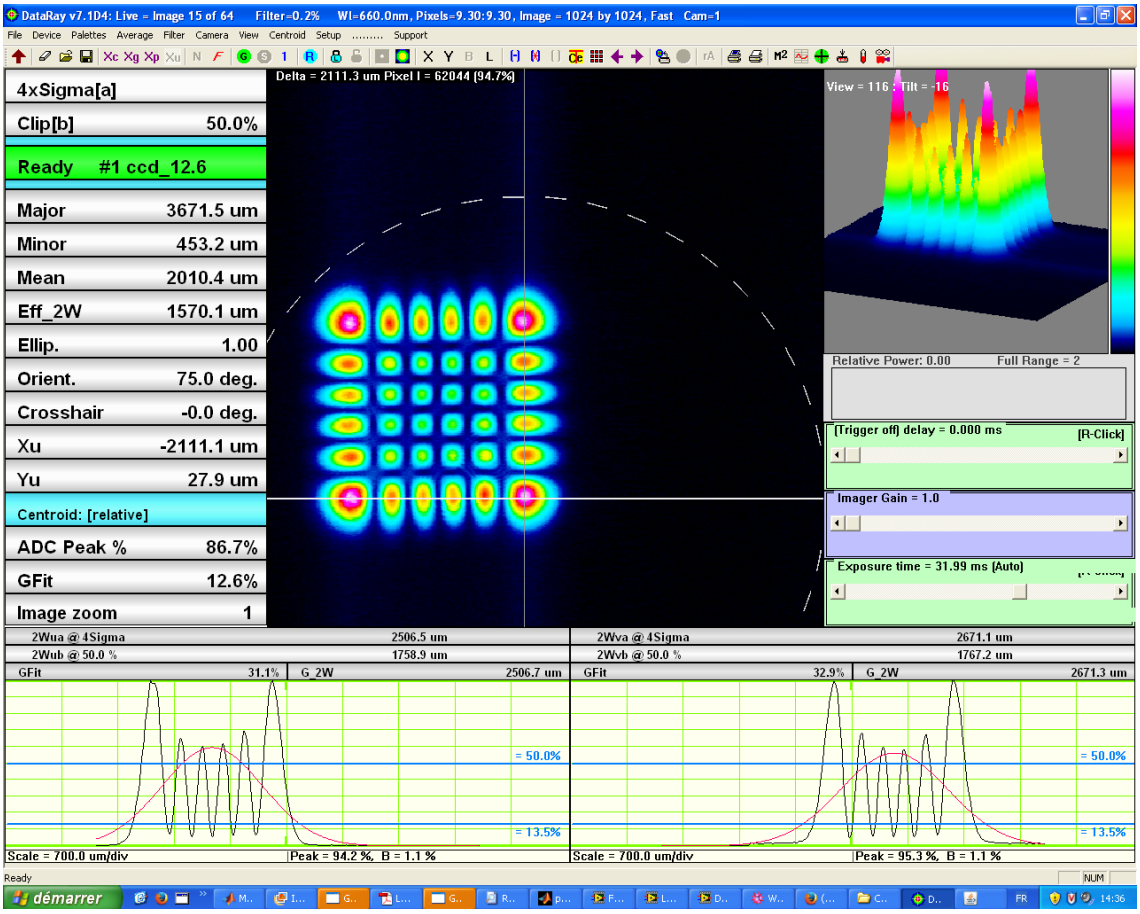

Figure 7.14: $HG_{5,5}$ with one of the best obtained coupling in the linear cavity, i.e. 78%.

$HG_{1,1}$ and $HG_{2,2}$, percentage which decreases to 75% for a mode $HG_{5,5}$. Then, in order to overcome the geometrical problem of the triangular cavity, we used a linear cavity, with same length ($150mm$) and $1inch$ mirrors, as shown in the figure 7.11.

Therefore, I tested the coupling of the higher HG modes with the linear cavity of figure 7.11. When using this cavity, we observed a small tilt angle in the mode coupled with the cavity due to the optics places before the cavity. We tried to compensate the tilt by acting on the optics before the cavity and also by slightly turning the cavity inside its support. Nevertheless, this effect could not be totally removed, and a small tilt of less than $\sim 2^{\circ}$ is still present and much more visible in higher order modes. This problem is due to the fact that while reflecting the generated higher order mode it can slightly change polarization, so that we also tried to compensate this effect by slightly turning the SLM, thus changing the direction of the polarization for which the SLM modifies the refractive index. Among the last best mode optimized with the linear cavity of figure 7.11 I obtained a coupling of 80% for a $HG_{5,5}$, which is shown in the *DataRay*® screen-shot of figure 7.13. In figure 7.14 I show an example of another optimized $HG_{5,5}$ with a contrast of 78% for a slightly different combination of input parameter in the *Matlab*® program interface. For the mode $HG_{10,10}$, I obtained a coupling of 50%, but we further reached the 70%. In figure 7.15 and 7.16 are shown two of the samples of the mode $HG_{10,10}$ for which I obtained the couplings 47% and 48% respectively.

Within all the problematic encountered during this experiment there is the stability of the SLM, a serious issue that prevents us to easily reproduce the results. In fact, for the same mode and the same input parameter on the *Matlab*® program interface, in the same environment conditions, in the same day, I did not obtain the same coupling percentage.

The experimental problematics which lie behind this work are numerous. The most important discussed in this chapter are the problem of polarization, the issue of generating a proper mode with no diffraction sparse around the mode intensity pattern and the problem of the coupling in the mode cleaner cavity. Other problems are related on the performance of the LCOS-SLM which are not constant along the time. Nevertheless, the work done till now allowed us to reach a good coupling of $\sim 90\%$ for modes $HG_{1,1}$ and $HG_{2,2}$, of 80% for a mode $HG_{5,5}$ and 70% for a $HG_{10,10}$. Although my calculations on the thermal noise of QuRaG showed that it will not be necessary to reduce the mirror thermal noise, the use of higher order Hermite Gauss modes could be later applied if further thermal noise reductions will be needed.

With the current state of the art, the use of these modes seems not very interesting for GW interferometers. In fact, while on one hand the use of such modes will give a gain of a factor $9 - 10$ in the thermal noise, on the other hand the light power that these modes will let circulate in the interferometer is too low that the shot noise will increase. These modes can also be applied to reduce the mirror thermal noise in the optical clock experiments, which, as already discussed at the beginning of this chapter, are currently limited in sensitivity by this noise.

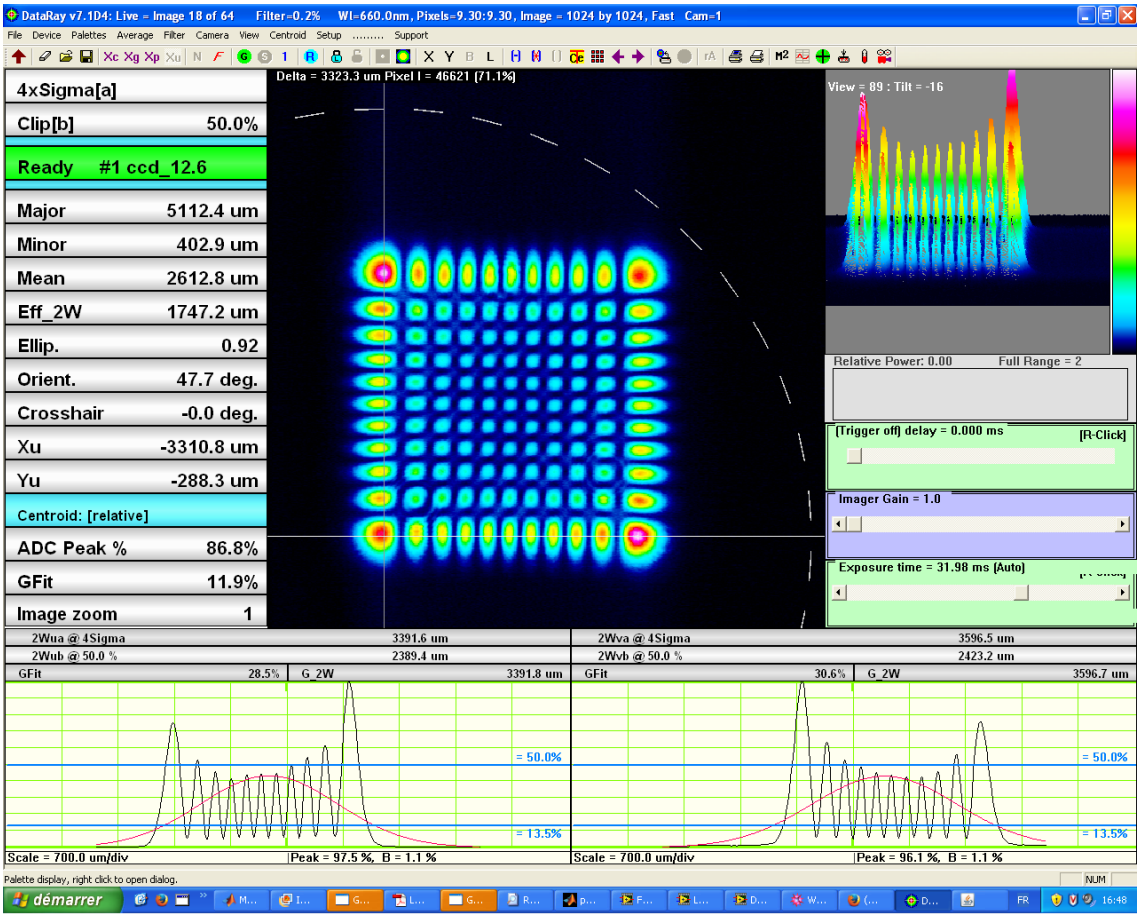

Figure 7.15: $HG_{10,10}$ with one the best obtained coupling in the linear cavity, i.e. 47%.

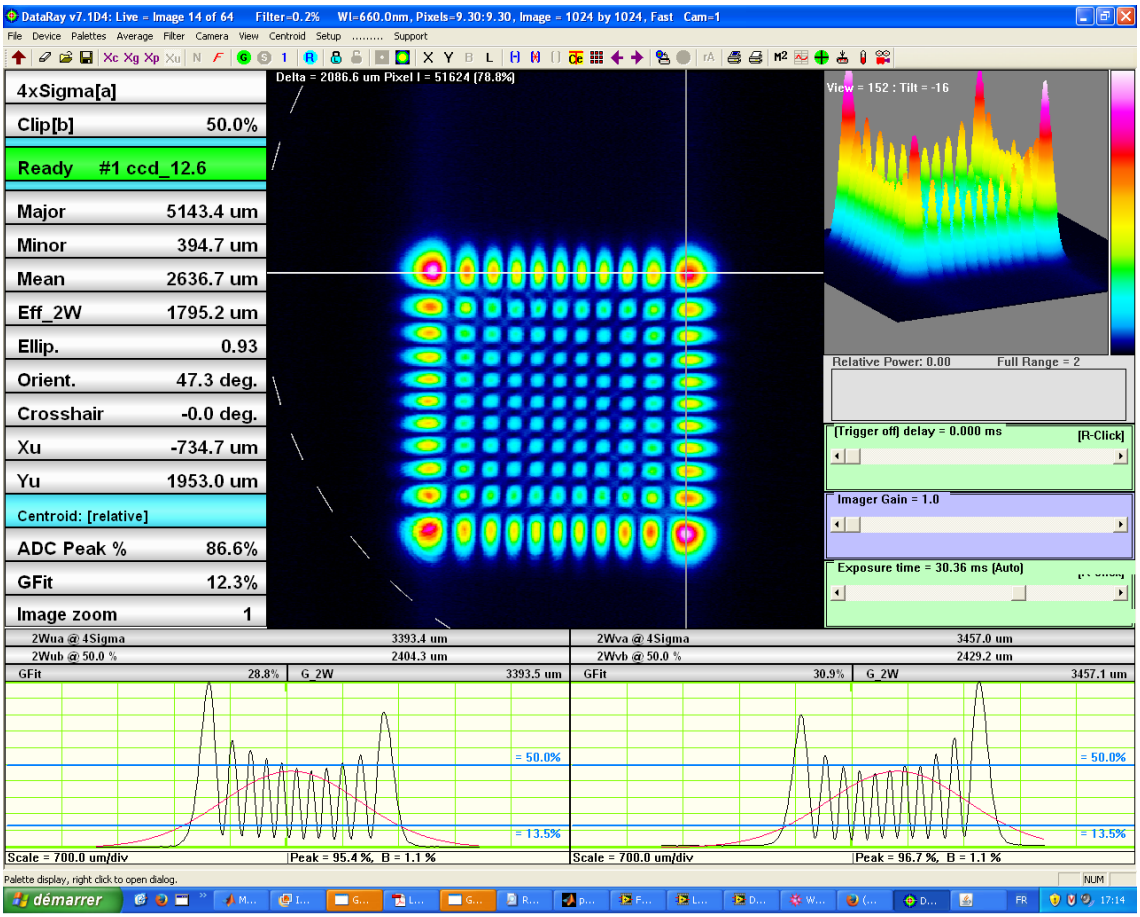

Figure 7.16: $HG_{10,10}$ with the best obtained coupling in the linear cavity, i.e. 48%.

Chapter 8

Conclusion

The work that I have done during my PhD thesis covers various aspects of the QuRaG project and then related issues belonging to different fields of Physics. Therefore, my thesis touches many themes from the operation of a ground based suspended interferometer for the detection of gravitational waves and the related noise sources which prevents its sensitivity, to the study of the construction of a small scale suspended interferometer (QuRaG) whose aim is to observe the radiation pressure noise. Hence, in the present thesis I analyse numerous suspension systems for the end mirrors of QuRaG interferometer by estimating and comparing their thermal noise budget with the radiation pressure noise, and I validate the best configuration as being the one which has the less thermal noise level with respect to the radiation pressure and that can practically be realized and employed in QuRaG.

My analysis shows that the last suspension stage of the suspended end mirror should be a **monolithic fused silica Double Stage Pendulum** with 2 suspension wires of $40\mu m$ diameter and $2cm$ length, and the suspended mass should be a parallelepiped mirror of $m \leq 0.1g$ and dimensions $5mm \times 3mm \times 3mm$. Moreover, the modal analysis on the whole optics of the suspended interferometer QuRaG, also shows that the interferometer disk which directly holds all the optics of the interferometer, should be thicker than what foreseen at the beginning, i.e. $40mm$ instead of $10mm$, to prevent the internal resonances of this disk to fall inside the detection band of QuRaG.

Hence, this analysis demonstrates that QuRaG will be not limited by the thermal noise of the suspensions and of the mirror, and it will be the first suspended interferometer capable to observe the radiation pressure noise in the same detection band of ground based gravitational wave interferometer (of Virgo in particular). More in detail, with a finesse of $5 \cdot 10^4$ and an input power of the Nd:YAG $\lambda = 1064nm$ IR laser equal to $P_{las} = 50mW$, the suspended mirror of QuRaG will be sensitive to the quantum radiation pressure effect of the order of $10^{-15}\ m/\sqrt{Hz}$ at $100Hz$.

The study on the realization of the mirror suspension wires, as required from the results of my thermal noise analysis, lead us to collaborate with the Virgo group of Perugia. Therefore, I worked there for few weeks, where I learned the technique of pulling thinner silica fiber from a thicker silica seed of $3mm$ diameter, by an oxy-hydrogen flame machine. Moreover, I learned the technique to measure the losses on

the so pulled fiber. I brought back all this expertise to Nice, where we set up a similar procedure for pulling silica fibers from $400\mu m$ diameter fibers with a Fiber Splicer Machine re adapted with two motors controlled on the PC, to very precisely control the melting point position and the heating time. The best pulled samples realized at the moment and closer to the thermal noise requirements have a central part of $1.5cm$ for $40\mu m$ diameter, connected by two cones of $0.05cm$ height, to two ends having a bigger diameter of $400\mu m$ for $1.45cm$ length.

My work also covers the problematic of how to realize the electrostatic control of the suspended mirrors, since the overall control system of the QuRaG interferometer foresees a last control stage directly applied on the suspended mirror. Therefore, I studied the issue on a prototype 1g mirror suspended in a simple Michelson interferometer. The electrostatic control on the prototype mirror is realized by placing a capacitor on a movable support behind the suspended mirror and by gluing the other mirror onto a piezoelectric bar. When a voltage is applied on the capacitor, a force acts on the suspended mirror and the mirror displacement is compensated thanks to the correction signal send back to the piezoelectric bar which moves the other mirror. The problematic of electrostatically control a suspended prototype mirror turned out to be directly connected to the problematic of suspending the prototype mirror. Thus, several techniques and kinds of wires have been tested. Nevertheless, the configuration of suspension which gave the best result is composed by two PVC ears glued to the mirror, with a unique suspension wire knotted in its two ends, around the ears and being one of my hair having $(58 \pm 3)\mu m$ diameter. With this suspension I obtained a maximal displacement of $(731 \pm 19)nm$ for an applied voltage $V_1 = (93.1 \pm 0.1)V$ on the capacitor. We suppose, and we already did some rough tests, that with an amplifier which allows to reach applied voltage till $300V$ will increase of a factor 10 the maximal displacement.

The other important topic covered by my work is the generation and optimization of the Hermite Gauss modes of Higher Order. These modes have a wider intensity distribution with respect to the fundamental Gaussian beam, thus they can average better over the mirror surface distortions caused by the thermal motions. Although my estimations of QuRaG thermal noise showed that its sensitivity will not be limited by this noise source, we could use these modes to further reduce the thermal noise level of the QuRaG mirrors, if during operation will result necessary. Moreover, these modes could also be applied for improving the sensitivity of next generation of gravitational wave interferometers as well as optical clock experiments, which approached the mirror thermal noise limit.

In fact, the thermal noise of the mirrors is one of the most important limit to the sensitivity of current gravitational wave detectors in the middle range of frequencies (around $100Hz$). Moreover, the enhancements required by the next generations of these detectors, such as the increasing of the laser power circulating inside the arm cavities, require also the optimization of the mirror thermal noise.

The work done on these modes demonstrates that the system that we implemented is able to generate proper Hermite Gauss modes till the order $HG_{25,25}$, that we can obtain a coupling percentage of $\simeq 90\%$ for the modes $HG_{1,1}$ and $HG_{2,2}$, values which

decreases to $\simeq 80\%$ for the $HG_{5,5}$ and to $\simeq 70\%$ for the $HG_{10,10}$.

The whole work demonstrates that it is possible to build a small scale suspended interferometer which is able to observe the radiation pressure noise in the same detection band of Earth based gravitational wave detectors. This interferometer should have two suspended end mirrors of $m \approx 0.08g$, those sensitive to radiation pressure effect, and its thermal noise is optimized if the last suspension system for the end mirrors is a Double Stage Pendulum, as required by the thermal noise estimations. Suspension wires very close to thermal noise estimation requirements have been realized, so we are confident to soon reach the goal. At the present time, we are able to control the amount of waterglass used to attach the suspension wires to the mirrors within a thickness of $1\mu m$, while in the thermal noise estimations I suppose a thickness of $60nm$, i.e. the same thickness of the silicate bonding layers for attaching the suspension wires to the mirror's ears in Virgo. Therefore, I have made a simulation on ANSYS® with a $1\mu m$ thickness layer of waterglass. This calculation showed that the waterglass losses increase of a factor 10 with respect to the $60nm$ layer. Nevertheless, while improving the pulling and waterglass gluing techniques, we can work on reducing the waterglass volume and with further thermal noise estimations it is possible to check if the state of the art on the fiber and on the waterglass thickness and diameter will significantly improve the suspended mirror thermal noise. This work also demonstrates that the electrostatic control can directly be applied behind the suspend mirror. Moreover, it demonstrates a powerful technique to generate and optimize high quality higher order Hermite Gauss modes with the coupling inside mode cleaner triangular and linear cavities. Although my thermal noise estimations demonstrates that the employment of higher order HG modes in QuRaG is not necessary since the mirror thermal noise does not dominate in the QuRaG detection band, they could be further used in next generation of ground based interferometer and in optical clock experiments. When the design will be finalized in all its aspects, we will be able to build the interferometer and QuRaG will be able to observe the radiation pressure noise.

Appendices

Appendix A

A brief treatise on Gravitational Waves

Einstein's Theory of General Relativity (GR) predicts the existance of ripples in the space-time frame due to accelerating massive objects, such as the electromagnetic waves are emitted by accelerated charged particles. These waves propagate at the speed of light and they carry energy and informations about their source. They can be derived from the field equation of GR: the Enstein's equations

$$G_{\mu\nu} = R_{\mu\nu} - \frac{1}{2} g_{\mu\nu} R = \frac{8\pi G}{c^4} T_{\mu\nu} \qquad \mu, \nu = 0, 1, 2, 3. \tag{A.1}$$

The solutions of eq.(A.1) describe the form of the metric tensor $g_{\mu\nu}$ in presence of a source of gravitational field, whose characteristics are enclosed in the energy-momentum tensor $T_{\mu\nu}$. Einstein's tensor $G_{\mu\nu}$ is symmetric since it is defined as the sum of two symmetric tensors $R_{\mu\nu}$ and $g_{\mu\nu}$ [59]. Ricci's tensor $R_{\mu\nu}$ is obtained by contracting Riemann's tensor $R^{\alpha}_{\mu\beta\nu}$ with the metric tensor $g_{\mu\nu}$

$$R_{\mu\nu} = g^{\alpha\beta} R_{\alpha\mu\beta\nu} = R^{\beta}_{\mu\beta\nu} \qquad \alpha, \beta, \mu, \nu = 0, 1, 2, 3. \tag{A.2}$$

The scalar curvature R is then derived by contracting Ricci's tensor $R_{\mu\nu}$ with the metric tensor $g_{\mu\nu}$

$$R = g^{\mu\nu} R_{\mu\nu}. \tag{A.3}$$

The metric tensor is defined by the line element ds, which is the distance between two points in the space-time frame

$$ds^2 = g_{\mu\nu} dx^{\mu} dx^{\nu} \tag{A.4}$$

where the x^{α} are the coordinates of a generic reference frame.
The Riemann curvature tensor $R^{\alpha}_{\mu\beta\nu}$ is constructed by linear combinations of second derivatives of the metric tensor

$$R^{\alpha}_{\mu\beta\nu} = \Gamma^{\alpha}_{\mu\nu,\beta} - \Gamma^{\alpha}_{\mu\beta,\nu} + \Gamma^{\kappa}_{\mu\nu} \Gamma^{\alpha}_{\kappa\beta} - \Gamma^{\kappa}_{\mu\beta} \Gamma^{\alpha}_{\kappa\nu} \tag{A.5}$$

since the Christoffel symbols $\Gamma^{\lambda}_{\mu\nu}$, symmetric by the lower index, depends on the first derivative of the metric

$$\Gamma^{\lambda}_{\mu\nu} = \frac{1}{2} g^{\lambda\kappa} \left[g_{\kappa\nu,\mu} + g_{\kappa\mu,\nu} - g_{\mu\nu,\kappa} \right]. \tag{A.6}$$

Commas represent the ordinary partial derivative with respect to the coordinates of the space-time

$$g_{\mu\nu,\alpha} = \frac{\partial g_{\mu\nu}}{\partial x^{\alpha}}. \tag{A.7}$$

The Riemann tensor contains information about the curvature of space-time since it expresses how the generic four-vector A_{β} varies when it is parallel transported along a closed path in a curved space-time

$$A_{\beta;\mu;\nu} - A_{\beta;\nu;\mu} = R^{\alpha}_{\beta\mu\nu} A_{\alpha}. \tag{A.8}$$

The semicolons represent the covariant derivatives with respect to the coordinates of space-time

$$A_{\beta;\mu} = A_{\beta,\mu} - \Gamma^{\alpha}_{\beta\mu} A_{\alpha}. \tag{A.9}$$

In eq. (A.8) the different order of the derivatives corresponds to the displacement of the vector A_{β} from P_1 to P_3 along two different paths. That is $A_{\beta;\mu;\nu}$ and $A_{\beta;\nu;\mu}$ represent respectively the displacements of A_{β} along the paths $P_1P_2P_3$ and $P_1P_4P_3$ (see the fig. A.1).

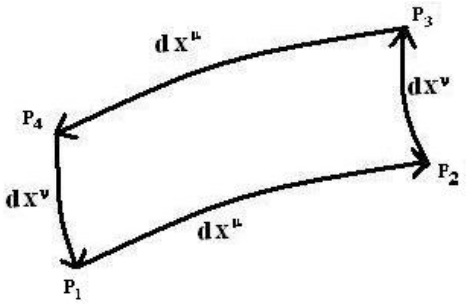

Figure A.1: The two points of the space-time P_1 and P_3, are connected by the two alternative paths $P_1P_2P_3$ and $P_1P_4P_3$.

The symmetric energy-momentum tensor $T_{\mu\nu}$, as already said, contains the information on the sources of the gravitational field, i.e. matter and energy.

Consider the simple case of a system of n non-interacting particles, each with coordinates $\xi^{\alpha_l}(t)$ (inertial reference system) and four-momentum p^{α_l}, with $l = 1, .., n$ and $\alpha = 0, .., 3$ [116]. Then the components of $T_{\mu\nu}$ are defined respectively:

- T_{00} as the energy density of the system,
- $\frac{1}{c}T_{0i}$, where $i = 1, 2, 3$, as the densities of momentum,
- T_{ik} where $i, k = 1, 2, 3$, as the momentum current of the i-th component through the unitary surface orthogonal to the k-th axis.

And in the limit conditions of:

- low velocities regime (non relativistic particles) $v \ll c$,
- weak gravitational field $g_{\mu\nu} \approx \eta_{\mu\nu}$ (flat space-time) and stationary $g_{\mu\nu,0} = 0$,

the equation of gravitational field takes the classical formulation, i.e. the Einstein equations are reduced to the equation of Poisson

$$\nabla^2\phi = 4\pi G\rho, \tag{A.10}$$

where ϕ is the gravitational potential and ρ the density.

Returning to the Einstein equations (A.1) it can straightforwardly be noticed that since it is symmetric, the Einstein tensor $G_{\mu\nu}$ has 10 independent components, so the equation (A.1) constitutes a system of 10 equations for 10 independent components of $g_{\mu\nu}$. However, the actual number of independent equations is equal to 6, since eq. (A.1) must comply with 4 conditions imposed by the equation $G^{\mu\nu}_{;\nu} = 0$ (demonstrable from the Bianchi identities) [108]. The remaining 4 degrees of freedom are fixed by the choice of the reference system in which is written the metric tensor, i.e. the $g_{\mu\nu}$, solution of the Einstein equations (A.1), is determined up to an arbitrary choice of the coordinate system. This implies the gauge invariance of the solution.

The Solution of the Gravitational Waves

The GWs are solutions of Einstein's equations, and they simultaneously describe the sources and the emitted waves. GWs, in fact, constitute both the propagating signal and the source of that signal, since the energy carried by the waves is also the source of the gravitational field. Two different approaches can be used to study GWs. The former consists on the search for the exact solutions of the Einstein's equations, and the latter is a perturbative approach. The former, called numerical relativity, results to be very complex and still uncompleted, a part for solutions of some case with particular conditions. The principal difficulties derive from the non-linearity of the equations to solve. The latter demonstrates how a weak perturbation of the space-time propagates as a wave.

The field of numerical relativity emerged from the desire to construct and study more general solutions to the field equations by approximately solving the Einstein equations numerically. A necessary precursor to such attempts was a decomposition of space-time

back into separated space and time. This was first published by R. Arnowitt, S. Deser, and C. W. Misner in the late 1950s in what has become known as the ADM formalism [14]. Although, for technical reasons, the precise equations formulated in the original ADM paper are rarely used in numerical simulations. Most or all practical approaches to numerical relativity use a "3+1 decomposition" of space-time into three-dimensional space and one-dimensional time that is closely related to the ADM formulation, because the ADM procedure reformulates the Einstein field equations into a constrained initial value problem that can be addressed encoded on a computer for solution. At the time that Arnowitt, Deser, and Misner published their original paper, computer technology would not have supported numerical solution to their equations on any problem of any substantial size. The first documented attempt to solve the Einstein field equations numerically appears to be those of Hahn and Lindquist in 1964 [78], followed soon thereafter by those of Smarr [139, 140] and Eppley [58]. These early attempts were focused on evolving Misner data in axisymmetry (also known as "2+1 dimensions"). At around the same time T. Piran wrote the first code that evolved a system with gravitational radiation using a cylindrical symmetry [120]. In this calculation Piran has set the foundation to many of the concepts used today in evolving ADM equations. Moreover, by applying the symmetry it was possible to reduce the computational and memory requirements associated with the problem, allowing the researchers to obtain results on the supercomputers available at the time [7].

However, in the present work I will not treat the numerical relativity, but the perturbative approach. Consider an unperturbed metric $g^0_{\mu\nu}$, exact solution of the Einstein's equations in presence of a source described by $T^0_{\mu\nu}$, in which is added a small perturbation $h_{\mu\nu}$, due to the source $T^{pert}_{\mu\nu}$. Summarizing, we have that the source of the total field is

$$T_{\mu\nu} = T^0_{\mu\nu} + T^{pert}_{\mu\nu} \tag{A.11}$$

and the perturbed metric tensor will be

$$g_{\mu\nu} = g^0_{\mu\nu} + h_{\mu\nu}, \tag{A.12}$$

where

$$|h_{\mu\nu}| \ll |g_{\mu\nu}|. \tag{A.13}$$

For the sake of simplicity we consider the case in which the unperturbed space-time frame is the Minkoski one

$$g^0_{\mu\nu} = \eta_{\mu\nu}. \tag{A.14}$$

Then

$$g_{\mu\nu} = \eta_{\mu\nu} + h_{\mu\nu}. \tag{A.15}$$

It is useful to underline that, under these conditions [59],

$$g^{\mu\nu} = \eta^{\mu\nu} - h^{\mu\nu}, \tag{A.16}$$

since

$$g_{\lambda\mu}g^{\mu\nu} = (\eta_{\lambda\mu} + h_{\lambda\mu})(\eta^{\mu\nu} - h^{\mu\nu}) =$$
$$= \delta^{\mu}_{\lambda} + h_{\lambda\mu}\eta^{\mu\nu} - \eta_{\lambda\mu}h^{\mu\nu} + O(h^2) \simeq \delta^{\nu}_{\lambda} + h^{\nu}_{\lambda} - h^{\nu}_{\lambda} \simeq \delta^{\nu}_{\lambda}. \tag{A.17}$$

GWs are then obtained as solutions of the linearized Einstein's equations (eq. (A.1)).

The flat space-time metric is described by the Minkowski tensor

$$\eta_{\mu\nu} = \eta^{\mu\nu} = \begin{pmatrix} -1 & 0 & 0 & 0 \\ 0 & 1 & 0 & 0 \\ 0 & 0 & 1 & 0 \\ 0 & 0 & 0 & 1 \end{pmatrix} \tag{A.18}$$

defined in such a way that

$$ds^2 = -(cdt)^2 + dx^2 + dy^2 + dz^2 = \eta_{\mu\nu}dx^{\mu}dx^{\nu} \tag{A.19}$$

and note that $\eta_{\mu\alpha}\eta^{\alpha\nu} = \delta^{\nu}_{\mu}$, where δ^{ν}_{μ} is the delta of Kronecker.

In the metric we use here (eq.(A.15)) the Ricci's tensor and the scalar of curvature become

$$R_{\mu\nu} = R^{\beta}_{\mu\beta\nu} = g^{\alpha\beta}R_{\alpha\mu\beta\nu} \simeq \eta^{\alpha\beta}R_{\alpha\mu\beta\nu} + O(h^2) \tag{A.20}$$

$$R = g^{\mu\kappa}R_{\kappa\mu} = R^{\mu}_{\mu} \simeq \eta^{\mu\kappa}R_{\kappa\mu} + O(h^2), \tag{A.21}$$

and since the derivatives of the flat metric are zero $\eta_{\mu\nu,\lambda} = \frac{\partial\eta_{\mu\nu}}{\partial x^{\lambda}} = 0$, the Christoffel's symbols become

$$\Gamma^{\lambda}_{\mu\nu} = \frac{1}{2}g^{\lambda\kappa}\left[g_{\kappa\nu,\mu} + g_{\kappa\mu,\nu} - g_{\mu\nu,\kappa}\right] \simeq \frac{1}{2}\eta^{\lambda\kappa}\left[h_{\kappa\nu,\mu} + h_{\kappa\mu,\nu} - h_{\mu\nu,\kappa}\right] + O(h^2) \tag{A.22}$$

Hence, from the expression of Christoffel's symbols eq. (A.22), the Ricci's tensor of eq. (A.20) is

$$R_{\mu\nu} \simeq \frac{1}{2}\eta^{\lambda\kappa}\left(h_{\kappa\nu,\mu\lambda} - h_{\mu\nu,\kappa\lambda} - h_{\kappa\lambda,\mu\nu} + h_{\mu\lambda,\kappa\nu}\right) + O(h^2). \tag{A.23}$$

Going back to Einstein's equations (A.1), it is likely to use another equivalent form

$$R_{\mu\nu} = \frac{8\pi G}{c^4}\left(T_{\mu\nu} - \frac{1}{2}g_{\mu\nu}T^{\lambda}_{\lambda}\right), \tag{A.24}$$

where $T^{\lambda}_{\lambda} = g^{\lambda\nu}T_{\nu\lambda}$. Moreover it is possible to make the approximation [59]

$$R_{\mu\nu} \simeq \frac{8\pi G}{c^4}\left(T_{\mu\nu} - \frac{1}{2}\eta_{\mu\nu}T^{\lambda}_{\lambda}\right). \tag{A.25}$$

From the eq. (A.23) it is straightforward verified that

$$R_{\mu\nu} \simeq \Gamma^{\lambda}_{\mu\nu,\lambda} - \Gamma^{\lambda}_{\mu\lambda,\nu}. \tag{A.26}$$

Therefore, the eq. (A.24) can be rewritten

$$R_{\mu\nu} \simeq \Gamma^{\lambda}_{\mu\nu,\lambda} - \Gamma^{\lambda}_{\mu\lambda,\nu} = \frac{1}{2}\left[-\eta^{\lambda\kappa}\frac{\partial^2 h_{\mu\nu}}{\partial x^{\lambda}\partial x^{\kappa}} + \left(\frac{\partial^2 h^{\lambda}_{\nu}}{\partial x^{\lambda}\partial x^{\mu}} + \frac{\partial^2 h^{\lambda}_{\mu}}{\partial x^{\lambda}\partial x^{\nu}} - \frac{\partial^2 h^{\lambda}_{\lambda}}{\partial x^{\mu}\partial x^{\nu}}\right)\right], \tag{A.27}$$

where we brought up the indices of the tensors by contracting it with the metric tensor $\eta^{\mu\nu}$

$$\eta^{\mu\nu}h_{\nu\lambda} = h^{\mu}_{\lambda}. \tag{A.28}$$

Moreover, it can be noticed that

$$\eta^{\lambda\kappa}\frac{\partial}{\partial x^{\lambda}}\frac{\partial}{\partial x^{\kappa}} = -\frac{1}{c^2}\frac{\partial^2}{\partial t^2} + \nabla^2 = \Box \tag{A.29}$$

which is equivalent to the operator of D'Alambert in the flat metric. Then the eq. (A.27) can be re-written

$$\Box h_{\mu\nu} - \left[\frac{\partial^2 h^{\lambda}_{\nu}}{\partial x^{\lambda}\partial x^{\mu}} + \frac{\partial^2 h^{\lambda}_{\mu}}{\partial x^{\lambda}\partial x^{\nu}} - \frac{\partial^2 h^{\lambda}_{\lambda}}{\partial x^{\mu}\partial x^{\nu}}\right] = -\frac{16\pi G}{c^4}\left(T_{\mu\nu} - \frac{1}{2}\eta_{\mu\nu}T^{\lambda}_{\lambda}\right). \tag{A.30}$$

Furthermore, in order to simplify the previous formulas, the following change of variable can be applied

$$h_{\mu\nu} = \tilde{h}_{\mu\nu} - \frac{1}{2}\eta_{\mu\nu}\tilde{h} \tag{A.31}$$

where the inverse transformation is

$$\tilde{h}_{\mu\nu} = h_{\mu\nu} - \frac{1}{2}\eta_{\mu\nu}h \tag{A.32}$$

and the equality between the scalars $\tilde{h} = -h$ is satisfied .
Then, imposing the following infinitesimal transformation of coordinates which leaves the field $h_{\mu\nu}$ weak

$$x^{\mu} \to x'^{\mu} = x^{\mu} + \epsilon^{\mu}, \tag{A.33}$$

and which corresponds to a new metric [59]

$$g'^{\mu\nu} = \frac{\partial x'^{\mu}}{\partial x^{\alpha}}\frac{\partial x'^{\nu}}{\partial x^{\beta}}g^{\alpha\beta} \tag{A.34}$$

it is obtained that

$$\tilde{h'}_{\mu\nu} = \tilde{h}_{\mu\nu} - \frac{\partial \epsilon_\mu}{\partial x^\nu} - \frac{\partial \epsilon_\nu}{\partial x^\mu}. \tag{A.35}$$

Hence, making the suitable *gauge* choice, called the **Lorentz gauge**:

$$\frac{\partial \tilde{h}^\mu_\nu}{\partial x^\mu} = 0, \tag{A.36}$$

Einstein's equations become

$$\eta^{\alpha\beta} \frac{\partial^2 \tilde{h}_{\mu\nu}}{\partial x^\alpha \partial x^\beta} = -\frac{16\pi G}{c^4} \left(T_{\mu\nu} - \frac{1}{2} \eta_{\mu\nu} T^\lambda_\lambda \right). \tag{A.37}$$

It is also important to notice that the Lorentz gauge condition (eq.(A.36)) implies that $\Gamma^\lambda = 0$. In fact, since it is

$$\tilde{h}_{\kappa\nu} = h_{\kappa\nu} - \frac{1}{2}\eta_{\kappa\nu} h^\lambda_\lambda \rightarrow \tilde{h}^\mu_\nu = \eta^{\mu\kappa}\tilde{h}_{\kappa\nu} = h^\mu_\nu - \frac{1}{2}\eta^{\mu\kappa}\eta_{\kappa\nu} h^\lambda_\lambda, \tag{A.38}$$

then being

$$\tilde{h}^\mu_{\nu,\mu} = h^\mu_{\nu,\mu} - \frac{1}{2}\delta^\mu_\nu h^\lambda_{\lambda,\mu} = h^\mu_{\nu,\mu} - \frac{1}{2} h^\lambda_{\lambda,\nu} = 0, \tag{A.39}$$

it is, therefore

$$\Gamma^\lambda = g^{\mu\nu}\Gamma^\lambda_{\mu\nu} \simeq \eta^{\mu\nu}\Gamma^\lambda_{\mu\nu} + O(h^2) \simeq \eta^{\lambda\kappa} \left(h^\mu_{\kappa,\mu} - \frac{1}{2} h^\nu_{\nu,\kappa} \right) = 0. \tag{A.40}$$

In the new frame it is then

$$\Gamma'^\lambda = g'^{\mu\nu}\Gamma^\lambda_{\mu\nu} \tag{A.41}$$

and while the metric tensor transforms as

$$g'^{\mu\nu} = g^{\tau\sigma} \frac{\partial x'^\mu}{\partial x^\tau} \frac{\partial x'^\nu}{\partial x^\sigma}, \tag{A.42}$$

the Christoffel's symbols Γ transform as follows

$$\Gamma^\lambda_{\mu\nu} = \frac{\partial x'^\lambda}{\partial x^\rho} \frac{\partial x^\tau}{\partial x'^\mu} \frac{\partial x^\sigma}{\partial x'^\nu} \Gamma^\rho_{\tau\sigma} + \frac{\partial x'^\lambda}{\partial x^\sigma} \frac{\partial^2 x^\sigma}{\partial x'^\nu \partial x'^\mu}, \tag{A.43}$$

hence in the new frame the Γ symbols become

$$\Gamma'^\lambda = \Gamma^\rho \frac{\partial x'^\lambda}{\partial x^\rho} + g^{\tau\sigma} \frac{\partial^2 x'^\lambda}{\partial x^\tau \partial x^\sigma} = g^{\tau\sigma} \frac{\partial^2 x'^\lambda}{\partial x^\tau \partial x^\sigma}. \tag{A.44}$$

This implies [59] that also in the new frame the $\Gamma'^{\beta} = 0$, if

$$g^{\beta\sigma}\frac{\partial^2 x'^{\lambda}}{\partial x^{\beta}\partial x^{\sigma}} = 0, \tag{A.45}$$

i.e. if the ϵ_{μ} satisfies the wave equation

$$\Box\epsilon_{\mu} = \eta^{\mu\nu}\frac{\partial^2\epsilon_{\mu}}{\partial x^{\mu}\partial x^{\nu}} = 0. \tag{A.46}$$

In fact, the following approximation can be done

$$\begin{aligned} g^{\tau\sigma}\frac{\partial^2 x'^{\lambda}}{\partial x^{\tau}\partial x^{\sigma}} &= g^{\tau\sigma}\left[\frac{\partial}{\partial x^{\tau}}\left(\frac{\partial x^{\lambda}}{\partial x^{\sigma}} + \frac{\partial\epsilon^{\lambda}}{\partial x^{\sigma}}\right)\right] = g^{\tau\sigma}\left[\frac{\partial}{\partial x^{\tau}}\left(\delta^{\lambda}_{\sigma} + \epsilon^{\lambda}_{,\sigma}\right)\right] = \\ &= \left(\eta^{\tau\sigma} - h^{\tau\sigma}\right)\frac{\partial}{\partial x^{\tau}}\delta^{\lambda}_{\sigma} + \eta^{\tau\sigma}\frac{\partial^2\epsilon^{\lambda}}{\partial x^{\tau}\partial x^{\sigma}} + O(h^2) \simeq \Box\epsilon^{\lambda}. \end{aligned} \tag{A.47}$$

The Einstein's equations in the approximated form of eq. (A.37) can be written in the more compact form

$$\begin{cases} \Box\tilde{h}_{\mu\nu} = -\frac{16\pi G}{c^4}T_{\mu\nu} \\ \tilde{h}^{\mu}_{\nu,\mu} = 0 \end{cases} \tag{A.48}$$

Moreover, the condition that outside the source the perturbation propagates in vacuum states that the components of the energy-momentum tensor are zero $T_{\mu\nu} = 0$, and the field equations (eq.(A.48)) in the new frame become

$$\begin{cases} \Box\tilde{h}_{\mu\nu} = 0 \\ \tilde{h}^{\mu}_{\nu,\mu} = 0. \end{cases} \tag{A.49}$$

The latter equation in the systems (A.48) and (A.49) represent the Lorentz gauge, also called **harmonic gauge**.
The simplest solution of the differential equation (A.49) is a monochromatic plane wave, which propagates at the speed of light in vacuum. In order to obtain the final solution it is important to observe that the degrees of freedom of the gravitational wave are 2. In fact, as it has already been underlined, the tensor $\tilde{h}_{\mu\nu}$ is symmetric, so it has only 10 independent components. Moreover, the Lorentz gauge (eq. (A.36)) gives 4 conditions and the eq.(A.46) implies other 4 conditions. Consequently, a gravitational wave has only 2 degrees of freedom. Consider, then, a wave propagating along the z axis. It follows that $\tilde{h}_{\mu\nu}$ is independent of x and y:

$$\left(-\frac{\partial^2}{c^2\partial t^2} + \frac{\partial^2}{\partial z^2}\right)\tilde{h}_{\mu\nu} = 0, \tag{A.50}$$

where $\tilde{h}_{\mu\nu}$ is an arbitrary function of the time $t \pm \frac{z}{c}$. The treatise is then restricted only to the case of a progressive wave $\tilde{h}_{\mu\nu} = \tilde{h}_{\mu\nu}[\chi(t,z)]$, where $\chi(t,z) = t - \frac{z}{c}$. Moreover, note that adding to the Lorentz gauge the conditions

$$\begin{cases} \frac{\partial}{\partial t} = \frac{\partial}{\partial\chi}\frac{\partial\chi}{\partial t} = \frac{\partial}{\partial\chi} \\ \frac{\partial}{\partial z} = \frac{\partial}{\partial\chi}\frac{\partial\chi}{\partial z} = -\frac{1}{c}\frac{\partial}{\partial\chi} \end{cases} \tag{A.51}$$

it follows that

$$\frac{\partial \tilde{h}^{\mu}_{\nu}}{\partial x^{\mu}} = \frac{1}{c}\frac{\partial \tilde{h}^{t}_{\nu}}{\partial t} + \frac{\partial \tilde{h}^{z}_{\nu}}{\partial z} = \frac{1}{c}\frac{\partial}{\partial \chi}[\tilde{h}^{t}_{\nu} - \tilde{h}^{z}_{\nu}] = 0. \tag{A.52}$$

Then, by integrating it is obtained

$$\tilde{h}^{t}_{\nu} = \tilde{h}^{z}_{\nu} \qquad\qquad \nu = t, x, y, z, \tag{A.53}$$

which reduces the degrees of freedom of the progressive wave. However, there are still 4 degrees of freedom coming from the conditions of eq. (A.46). Then it is convenient to set equal to zero the 4 quantities

$$\tilde{h}^{t}_{x} = \tilde{h}^{t}_{y} = \tilde{h}^{t}_{z} = \tilde{h}^{x}_{x} + \tilde{h}^{y}_{y} = 0, \tag{A.54}$$

from which it results also that

$$\tilde{h}^{z}_{x} = \tilde{h}^{z}_{y} = \tilde{h}^{z}_{z} = \tilde{h}^{t}_{t} = 0. \tag{A.55}$$

Then, the tensor $\tilde{h}_{\mu\nu}$ is traceless

$$\tilde{h}^{\mu}_{\mu} = \tilde{h}^{t}_{t} + \tilde{h}^{x}_{x} + \tilde{h}^{y}_{y} + \tilde{h}^{z}_{z} = 0. \tag{A.56}$$

Moreover, since it is

$$\tilde{h}^{\mu}_{\mu} = \eta^{\mu\nu}\tilde{h}_{\nu\mu} = \eta^{\mu\nu}(h_{\nu\mu} - \frac{1}{2}\eta_{\nu\mu}h) = h^{\mu}_{\mu} - \frac{1}{2}\eta^{\mu}_{\mu}h = h^{\mu}_{\mu} - \frac{1}{2}4h = h^{\mu}_{\mu} - 2h^{\mu}_{\mu} = -h^{\mu}_{\mu}, \tag{A.57}$$

then $h^{\mu}_{\mu} = 0 \rightarrow \tilde{h}_{\mu\nu} \equiv h_{\mu\nu}$. Hence, in the Lorentz gauge $h_{\mu\nu}$ and $\tilde{h}_{\mu\nu}$ coincide and they are traceless. Finally, from the conditions (A.54) and (A.55) the progressive wave $h_{\mu\nu}$ propagating at the speed of light in vacuum and along the z axis can be written

$$\tilde{h}_{\mu\nu} = \begin{pmatrix} 0 & 0 & 0 & 0 \\ 0 & h_{+} & h_{\times} & 0 \\ 0 & h_{\times} & -h_{+} & 0 \\ 0 & 0 & 0 & 0 \end{pmatrix} \tag{A.58}$$

that in the more compact form is

$$h_{\mu\nu}(z,t) = [h_{+}\epsilon^{\oplus}_{\mu\nu} + h_{\times}\epsilon^{\otimes}_{\mu\nu}]exp[j\omega(t - z/c)] \tag{A.59}$$

where the

$$\epsilon^{\oplus}_{\mu\nu} = \begin{pmatrix} 0 & 0 & 0 & 0 \\ 0 & 1 & 0 & 0 \\ 0 & 0 & -1 & 0 \\ 0 & 0 & 0 & 0 \end{pmatrix} \tag{A.60}$$

$$\epsilon^{\otimes}_{\mu\nu} = \begin{pmatrix} 0 & 0 & 0 & 0 \\ 0 & 0 & 1 & 0 \\ 0 & 1 & 0 & 0 \\ 0 & 0 & 0 & 0 \end{pmatrix} \tag{A.61}$$

are the **tensors of polarization**. They are transverse to the direction of propagation of the wave and they corresponds to the two different possible polarization of the GW. The Lorentz gauge it is also called **gauge TT**, which stands for transverse and traceless. Hence, the two degrees of freedom correspond to the two different polarizations $\epsilon^{\oplus}_{\mu\nu}$ and $\epsilon^{\otimes}_{\mu\nu}$ of the wave.

Appendix B

The Emission of Gravitational Waves

The Emission of Gravitational Waves

As the emission of electromagnetic radiation is associated to the acceleration of charged particles, the emission of GWs is related to the acceleration of a test mass, i.e. electrically neutral and subjected only to the gravity force. In the linear approximation, if the dimensions of the source are small with respect to the wavelength and the distance to the observer, the non homogeneous equations of Einstein can be solved by a multi-pole expansion of the emitted radiation.
The laws of conservation of momentum and angular momentum make the terms analogous to the electric dipole vanish

$$\vec{d} = \sum_{i=0}^{N} (m_i \vec{r}_i) \rightarrow \dot{\vec{d}} = \sum_{i=0}^{N} (m_i \dot{\vec{r}}) = 0. \tag{B.1}$$

Thus, the first term of the expansion that is not zero is the one associated to the variation of the tensor of quadrupole moment of a mass distribution, defined as [59]:

$$q^{kn}(t - z/c) = \frac{1}{c^2} \int_V T^{00}(t - z/c) x^k x^n d^3x, \qquad k, n = x, y, z. \tag{B.2}$$

From this definition it follows that the amplitude of the gravitational signal emitted at a distance d from the source is:

$$h^{ik}(t - d/c, d) = \frac{2G}{c^4 d} \left[\frac{\partial^2}{\partial t^2} q^{ik}(t - d/c) \right]. \tag{B.3}$$

Note that the factor

$$\frac{G}{c^4} \sim 10^{-44} s^2/(kg\ m) \tag{B.4}$$

justifies the initial assumption of weak field for the gravitational perturbation. In addition, GWs can not be emitted by a motion of radial symmetry in which the terms

$$\frac{\partial^2 q^{ik}}{\partial t^2} = 0.$$

In the quadrupole approximation, the luminous power emitted by a source of gravitational wave emission, or gravitational radiation, is then defined as [59, 108]:

$$L_{GW} = \frac{G}{5c^5} \sum_{k,n=1}^{3} \left(\frac{\partial^3 q_{kn}(t - d/c)}{\partial t^3} \frac{\partial^3 q_{kn}(t - d/c)}{\partial t^3} \right). \tag{B.5}$$

Note that, the emitted power L_{GW} depends on the third derivative of the quadrupole moment q_{kn} and by the coefficient

$$\frac{G}{5c^5} = 5.5 \cdot 10^{-54} m^{-2} kg^{-1} s^3 \tag{B.6}$$

For this low value of the coefficient $G/5c^5$ the observable sources of gravitational waves are astrophysical sources characterized by having high quadrupole moment, hence being highly massive and/or in high speed non spherical motion.

The Gravitational Signal

It is necessary to obtain information on the status of the metric tensor $g_{\mu\nu}$ in order to catch the gravitational signal. This in principle is possible by observing the motion of a free test mass with respect to another free test mass and not with respect to a reference frame, in which the body is stationary and therefore does not provide any information on the metric. Consider, then, the motion of two free particles with respect to the

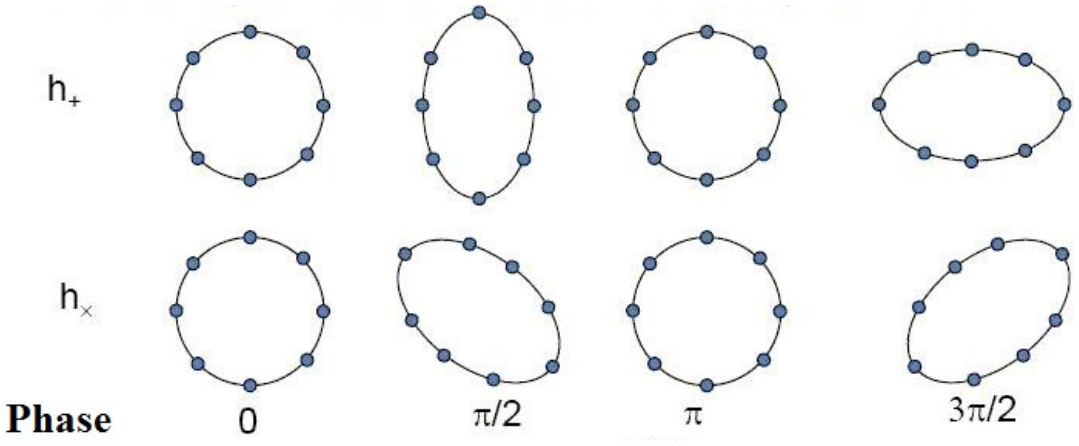

Figure B.1: Effect on a circular discrete distribution of test masses due to the two different polarization states, in function of the phase of the gravitational wave.

reference frame $g_{\mu\nu}$. This is described by the equation:

$$\frac{d^2 x^i}{ds^2} + \Gamma^i_{mk} \frac{dx^m}{ds} \frac{dx^k}{ds} = 0 \tag{B.7}$$

called the **geodesic equation** [108]. The eq. (B.7) is the explicit form of the covariant

derivative of the four-vector velocity of the particle having coordinate vector x^i, where s represents the curvilinear coordinate and the ds is proportional to the $d\tau$, and where τ is the proper time of the particle [59, 108]. However, the geodesic as written in equation (B.7) is not yet sufficient to shed light on the fundamental nature of the phenomenon under consideration.
Therefore, let us consider then two free particles A and B moving along two very close geodesics, with parameters τ and $\tau+d\tau$. For simplicity, the origin of the reference frame is chosen to be coincident with A, so that the vector that connects the two geodesics is just x^i_B. It is possible to obtain then that [59] the variation of the geodesic equation with respect to the parameter τ is:

$$\frac{d^2x^\alpha_B}{d\tau^2} = R^\alpha_{\beta\nu\mu}\frac{dx^\beta}{d\tau}\frac{dx^\nu}{d\tau}x^\mu_B \tag{B.8}$$

and it is called the **equation of the geodesic deviation**. This equation shows that the relative acceleration of two particles moving along nearby geodesics depends on the curvature tensor $R^\alpha_{\beta\nu\mu}$ (the Riemann tensor). Therefore, since the Riemann tensor is zero if and only if the gravitational field is null or constant and uniform (eq. (A.5)), the equation of geodesic deviation contains the information about the gravitational field and hence about the perturbation $h_{\mu\nu}$ to the flat metric.
In the reference frame chosen for the two free test masses A and B, and assuming to be in the case of small perturbation to the flat metric such as in eq.(A.15), the equation of geodesic deviation eq.(B.8) becomes [59]

$$\frac{d^2x^i_B}{d\tau^2} = \frac{1}{2c^2}\frac{\partial^2 h^{i(TT)}_k}{\partial t^2}x^k_B, \tag{B.9}$$

where the gravitational perturbation $h^{i(TT)}_k$ has been written in the Lorentz gauge (or TT gauge), of eq. (A.58). So, the motion of the particle B (as seen from the particle A) seems due to an acceleration field proportional to the second derivative of h. The solution of this equation is:

$$x^i_B(\tau) = x^k_B(0)\left(\delta^i_k + \frac{1}{2}h^{i(TT)}_k\right). \tag{B.10}$$

The eq.(B.9) gives in addition an intuitive idea of the polarization properties of the GWs. Assume that the wave propagates along the polarization axis z with polarization $h_\times$. In this case the percent change in the distance of separation between A and B due to the presence of the perturbation $h_{\mu\nu}$ is

$$\frac{\Delta l_{AB}}{l_{AB}} = \frac{h_\times}{2}. \tag{B.11}$$

This equation shows the effect of a gravitational wave on a system of two material points and allows to obtain a representation of the state of polarization of the wave.

Appendix C

Table of Acronyms

RP:	Radiation Pressure
GR:	General Relativity
GW:	Gravitational Wave
GWd:	Gravitational Wave detector
IR:	Infra-red
FDT:	Fluctuation Dissipation Theorem
PR:	Power Recycling
PRM:	Power Recycling Mirror
SQL:	Standard Quantum Limit
QND:	Quantum Non Demolition
ITF:	Interferometer
FP:	Fabry-Pérot
FEA:	Finite Element Analysis
BS:	Beam Splitter
FRS:	Free Spectral Range
FWHM:	Full Width at Half Maximum
PVC:	PolyVinyl Chloride
PZT:	piezoelectric
ISO:	International Organization for Standardization
DAQ:	Data Acquisition
WG:	Water-Glass
HG:	Hermite Gauss
LG:	Laguerre Gauss
LC:	Liquid Crystal
LCOS:	Liquid Crystal on Silicon
SLM:	Spatial Light Modulator

Appendix D

Physical Constants and Units of measurement

Units of measurement

Megaparsec	$1Mpc = 3.0857 \cdot 10^{22}\ m$

Physical constants

speed of light in vacuum	$c = 2.9979 \cdot 10^{8}\ m\ s^{-1}$
Newtonian constant of gravitation	$G = 6.6738 \cdot 10^{-11}\ m^{3}\ kg^{-1}\ s^{-1}$
Planck constant	$h = 6.6261 \cdot 10^{-34} J\ s$
reduced Planck constant	$\hbar = 1.0546 \cdot 10^{-34}\ J\ s$
vacuum permittivity	$\epsilon_0 = 8.8542 \cdot 10^{-12}\ F\ m^{-1}$
Boltzmann constant	$k_B = 1.3806 \cdot 10^{-23}\ J\ K^{-1}$
Earth's standard acceleration of gravity	$g = 9.8066\ m\ s^{-2}$
ideal gas constant	$R = 8.3145\ J\ K^{-1}\ mol^{-1}$
molecular mass of H_2	$\mu_{H_2} = 3.3452 \cdot 10^{-27}\ kg$

List of Figures

List of Tables

Bibliography

[1] Aei 10m prototype website. http://10m-prototype.aei.uni-hannover.de/.

[2] Complex stress tutorial 5 strain energy. http://www.freestudy.co.uk/statics/complex/t5.pdf.

[3] elisascience. https://www.elisascience.org/.

[4] Euler bernoulli beam theory. http://en.wikipedia.org/wiki/Euler_Bernoulli_beam_theory.

[5] International celestial reference frame. http://en.wikipedia.org/wiki/International_Celestial_Reference_Frame.

[6] Laguerre polynomials. http://en.wikipedia.org/wiki/Laguerre_polynomials.

[7] Numerical relativity. http://en.wikipedia.org/wiki/Numerical_relativity.

[8] Tantalum pentoxide. http://en.wikipedia.org/wiki/Tantalum_pentoxide.

[9] Vacuum in virgo. http://www.ego-gw.it/virgodescription/pag_5.html.

[10] B. Abbott, R. Abbott, R. Adhikari, A. Ageev, B. Allen, R. Amin, S.B. Anderson, W.G. Anderson, M. Araya, H. Armandula, F. Asiri, P. Aufmuth, C. Aulbert, S. Babak, R. Balasubramanian, S. Ballmer, B.C. Barish, D. Barker, C. Barker-Patton, M. Barnes, B. Barr, K. Bayer M.A. Bartona, R. Beausoleil, K. Belczynski, R. Bennett, S.J. Berukoff, J. Betzwieser, B. Bhawal, I.A. Bilenko, G. Billingsley, E. Black, K. Blackburn, B. Bland-Weaver, B. Bochner, L. Bogue, R. Bork, S. Bose, and P.R. Brady. Detector description and performance for the first coincidence observations between ligo and geo. *Nuclear Instruments & Methods in Physics Research, Section A: Accelerators, Spectrometers, Detectors, and Associated Equipment*, 517(154), 2004.

[11] O. Arcizet, T. Briant, A. Heidmann, and M. Pinard. Beating quantum limits in an optomechanical sensor by cavity detuning. *Physical Review A*, 73(033819), March 2006.

[12] O. Arcizet, P.-F. Cohadon, T. Briant, M. Pinard, and A. Heidmann. Radiation-pressure cooling and optomechanical instability of a micromirror. *Nature (London, United Kingdom)*, 444:71–74, November 2006.

[13] J. Arlt, K. Dholakiaa, L. Allena, and M. J. Padgetta. The production of multiringed laguerre-gaussian modes by computer - generated holograms. *Journal of Modern Optics*, 45(6):1231, 1998.

[14] R. Arnowitt., S. Deser, and C. W. Misner. *Gravitation: an introduction to current research, chapter 7, pp 227–265.* Wiley, 1962.

[15] C. Bini. *Lezioni di statistica per la fisica sperimentale.* Edizioni Nuova Cultura, 2011.

[16] F. Bondu, P. Hello, and J.-Y. Vinet. Thermal noise in mirrors of interferometric gravitational wave antennas. *Physical Letters A*, 246:227–236, May 1998.

[17] V. B. Braginsky and F. Y. Khalili. Quantum nondemolition measurements: the route from toys to tools. *Review of Modern Physics*, 68(1), January 1996.

[18] V. B. Braginsky and F. Y. Khalili. Low noise rigidity in quantum measurements. *Physical Letters A*, 257(5–6):241–246, July 1999.

[19] V. B. Braginsky and A. B. Manukin. Ponderomotive effects of electromagnetic radiation. *Zh. Teor. Exsp. Fiz.*, 52(987), 1967. (english version JETP 25, 653, (1967)).

[20] V.B. Braginsky, M.L. Gorodetsky, and F.Y. Khalili. Optical bars in gravitational wave antennas. *Physical Letters A*, 232(5):340–348, August 1997.

[21] V.B. Braginsky, S.E. Strigin, and S.P. Vyatchanin. Parametric oscillatory instability in Fabry-Pérot interferometer. *Physical Letters A*, 287(5–6):331–338, September 2001.

[22] V.B. Braginsky, S.E. Strigin, and S.P. Vyatchanin. Analysis of parametric oscillatory instability in power recycled ligo interferometer. *Physical Letters A*, 305(3–4):111–124, December 2002.

[23] V.B. Braginsky and Yu.I. Vorontsov. Quantum-mechanical limitations in macroscopic experiments and modern experimental technique. *Sov. Phys. Usp.*, 17:644, 1975.

[24] C. Brif. Notes on anelastic effects and thermal noise in suspensions of test masses in interferometric gravitational-wave detectors ligo-t990041-00-r, 1999. *LIGO technical note*, 1999.

[25] R. Brown. A brief account of microscopical observations made on the particles contained in the pollen of plants. *Philosophical Magazine*, 4:161 – 173, 1828.

[26] R. Brown. The miscellaneous botanical works of robert brown. *Esq., D.C.L., F.R.S.*, I:433 – 461, 1866.

[27] A. Buonanno and Y. Chen. Optical noise correlations and beating the standard quantum limit in advanced gravitational-wave detectors. *Class and Quantum Gravity*, 18(15):L95–L101, July 2001.

[28] A. Buonanno and Y. Chen. Quantum noise in second generation, signal-recycled laser interferometric gravitational-wave detectors. *Physical Review D*, 64(042006), July 2001.

[29] A. Buonanno and Y. Chen. Signal recycled laser-interferometer gravitational-wave detectors as optical springs. *Physical Review D*, 65(042001), January 2002.

[30] G. Cagnoli. Overview on thermal noise reduction research for future GW detectors, May 2014. `http://www.gravity.ircs.titech.ac.jp/GWADW2014/slide/Geppo_Cagnoli.pdf`.

[31] H. B. Callen and R. F. Green. On a theorem of irreversible thermodynamics. *Physical Review*, 86(5):702–710, June 1952.

[32] H. B. Callen and T. A. Welton. Irreversibility and generalized noise. *Physical Review*, 83(1):34–40, July 1951.

[33] T. Caniard, T. Briant, P.-F. Cohadon, M. Pinard, and A. Heidmann. Ultrasensitive optical measurement of thermal and quantum noises. *Optics and Spectroscopy*, 103(2):225–230, August 2007.

[34] C. M. Caves. Quantum-mechanical radiation-pressure fluctuations in an interferometer. *Physical Review Letters*, 45(2):75–79, July 1980.

[35] C. M. Caves. Quantum-mechanical noise in an interferometer. *Physical Review D*, 23(8):1693–1708, April 1981.

[36] P.-F. Cohadon, A. Heidmann, and M. Pinard. Cooling of a mirror by radiation pressure. *Physical Review Letters*, 83(16):3174, October 1999.

[37] The BICEP2 Collaboration. Bicep2 2014 i: Detection of b-mode polarization at degree angular scales. `http://arxiv.org/pdf/1403.3985.pdf`, March 2014.

[38] The Virgo Collaboration. Advanced virgo white paper. *VIRGO RELEASE*, VIR-NOT-DIR-1390-304, November 2005.

[39] The Virgo Collaboration. Advanced virgo technical design report. *VIRGO RELEASE*, VIR-0128A-12, April 2012.

[40] M. Colombini. *Thermal Noise Issue in the monolithic suspensions of the Virgo+ gravitational wave interferometer*. PhD thesis, Università di Roma, 2012.

[41] J. Connes, P. Connes, and J.-P. Maillard. *Atlas des Spectres dans le Proche Infrarouge de Venus, Mars, Jupiter, et Saturne*. Paris: Editions du CNRS, 1969.

[42] J. W. Cooley and J. W. Tukey. An algorithm for the machine calculation of complex fourier series. *Mathematics of Computation*, 19:297–301, 1965.

[43] T. Corbitt. *Quantum Noise and Radiation Pressure Effects in High Power Optical Interferometers*. PhD thesis, Massachusetts Institute of Technology, MIT, 2008.

[44] T. Corbitt, Y. Chen, F. Khalili, D. Ottaway, S. Vyatchanin, S. Whitcomb, and N. Mavalvala. Squeezed-state source using radiation-pressure-induced rigidity. *Physical Review A*, 73(023801), February 2006.

[45] T. Corbitt and N. Mavalvala. Quantum noise in gravitational-wave interferometers. *Journal of Optics B: Quantum Semiclassical Optics*, 6:S675–S683, January 2004.

[46] T. Corbitt, D. Ottaway, E. Innerhofer, J. Pelc, and N. Mavalvala. Measurement of radiation-pressure-induced optomechanical dynamics in a suspended Fabry-Pérot cavity. *Physical Review A*, 74(021802(R)), August 2006.

[47] T. Corbitt, C. Wipf, T. Bodiya, D. Ottaway, D. Sigg, N. Smith S. Whitcomb, and N. Mavalvala. Optical dilution and feedback cooling of a gram-scale oscillator to 6.9 mk. *Physical Review Letters*, 99(160801), October 2007.

[48] A. Corsi. *Gamma-Ray Burst afterglows: fireball physics and clues to the progenitor*. PhD thesis, Dipartimento di Fisica Università La Sapienza, Roma,, 2007.

[49] R. Cowen. How astronomers saw gravitational waves from the big bang. *Nature News*, March 2014. `http://www.nature.com/news/how-astronomers-saw-gravitational-waves-from-the-big-bang-1.14885`.

[50] A. Cumming, A. Heptonstall and. R Kumar, W. Cunningham, C. Torrie, M. Barton, K. A. Strain, J. Hough, and S. Rowan. Finite element modelling of the mechanical loss of silica suspension fibres for advanced gravitational wave detectors. *Classical and Quantum Gravity*, 26(21):215012, 2009.

[51] L. Cunningham, P.G. Murray, A. Cumming, E.J. Elliffe, G.D. Hammond, K. Haughian, J. Hough, M. Hendry, R. Jones, I.W. Martin, S. Reida, S. Rowan, J. Scott, K.A. Strain, K. Tokmakov, C. Torrie, and A.A. van Veggel. Re-evaluation of the mechanical loss factor of hydroxide-catalysis bonds and its significance for the next generation of gravitational wave detectors. *Physics Letters A*, 374:3993–3998, july 2010.

[52] P. DeBernardis. Lezioni di laboratorio specialistico astrofisica. Corso di Laurea Specialistica in Astronomia ed Astrofisica, Dipartimento di Fisica Università La Sapienza, Roma.

[53] P. DeBernardis. Tecniche sperimentali in astrofisica. Corso di Laurea Specialistica in Astronomia ed Astrofisica, Dipartimento di Fisica Università La Sapienza, Roma.

[54] S. DiPace. Studio del rumore termico degli specchi di virgo con sospensioni monolitiche. Master's thesis, Dipartimento di Fisica Università La Sapienza, Roma, 2011.

[55] EGO. European gravitational observatory. `http://www.ego-gw.it/public/virgo/virgo.aspx`.

[56] A. Einstein. Uber die von der molekularkinetischen theorie der warme geforderte bewegung von in ruhenden flussigkeiten suspendierten teilchen, on the movement of small particles suspended in a stationary liquid demanded by the molecular-kinetic theory of heat. *Annalen der Physik*, 322(8):549–560, May 1905.

[57] A Einstein. Die grundlage der allgemeinen relativitats theorie. *Annalen der Physik*, pages 769–822, March 1916.

[58] K. Eppley. *The numerical evolution of the collision of two black holes*. PhD thesis, Princeton University (Princeton, New Jersey), 1975.

[59] V. Ferrari. General relativity. Corso di Laurea in Fisica, Dipartimento di Fisica Università La Sapienza, Roma.

[60] R. Feynman, R. Leighton, and M. Sands. *The Feynman Lectures on Physics*, volume I. Masson, 1990.

[61] E. E. Flanagan and S. A. Hughes. Measuring gravitational waves from binary black hole coalescences. i. signal to noise for inspiral, merger, and ringdown. *Physical Review D*, 57(8):4535–4565, April 1998.

[62] R. L. Forward. Wideband laser-interferometer graviational-radiation experiment. *Physical Review D*, 17(2):379 – 390, January 1978.

[63] G. R. Fowles. *Introduction to Modern Optics*. Dover Publications, Inc. (New York), 1989.

[64] D. Friedrich, H. Kaufer, T. Westphal, K Yamamoto, A. Sawadsky, F. Ya. Khalili, S. L. Danilishin, S. Goßler, K. Danzmann, and R. Schnabel. Laser interferometry with translucent and absorbing mechanical oscillators. *New Journal of Physics*, 13(093017), September 2011.

[65] P. Fulda. *Precision Interferometry in a new shape: higher-order Laguerre-Gauss modes for gravitational wave*. PhD thesis, School of Physics and Astronomy, College of Engineering and Physical Sciences, University of Birmingham, June 2012.

[66] P. Fulda, K. Kokeyama, S. Chelkowski, and A. Freise. Experimental demonstration of higher-order laguerre-gauss mode interferometry. *Physical Review D*, 82(012002), July 2010.

[67] S. Gigan, H. R. Bo̎hm, M. Paternostro, F. Blaser, G. Langer, J. B. Hertzberg, K. C. Schwab, D. Baërle, M. Aspelmeyer, and A. Zeilinger. Self-cooling of a micromirror by radiation pressure. *Nature (London, United Kingdom)*, 444(2), November 2006.

[68] A. Gillespie and F. Raab. Thermally excited vibrations of the mirrors of laser interferometer gravitational-wave detectors. *Physical Review D*, 52:577, July 1995.

[69] G. I. González and P. R. Saulson. Brownian motion of a mass suspended by an elastic wire. *Journal Acoustical Society of America*, 96(1):207–212, July 1994.

[70] C. Gräf. *Optical Design and Numerical Modeling of the AEI 10 m Prototype sub-SQL Interferometer*. PhD thesis, Gottfried Wilhelm Leibniz Universität, 2013.

[71] M. Granata, C. Buy, R. Ward, and M. Barsuglia. Higher-order laguerre-gauss mode generation and interferometry for gravitational wave detectors. *Physical Review Letters*, 105(23):231102, November 2010.

[72] R. F. Green and H. B. Callen. On the theorem of irreversible thermodynamics ii. *Physical Review*, 88(6):1387–1391, December 1952.

[73] A. M. Gretarsson and G. M. Harry. Dissipation of mechanical energy in fused silica fibers. *Review of Scientific Instruments*, 70(10):4081–4087, October 1999.

[74] A. M. Gretarsson, G. M. Harry, S. D. Penn, P. R. Saulson, W. J. Startin, S. Rowan, G. Cagnoli, and J. Hough. Pendulum mode thermal noise in advanced interferometers: a comparison of fused silica fibers and ribbons in the presence of surface loss. *Physics Letters A*, 270(3-4):108–114, May 2000.

[75] D. G. Grier. A revolution in optical manipulation. *Nature*, 424:810–816, August 2003.

[76] D.-H. Gwo. Ultra precision and reliable bonding method, 2001. `http://ntrs.nasa.gov/archive/nasa/casi.ntrs.nasa.gov/20080004667.pdf`.

[77] Y. Hadjar, P.-F. Cohadon, C. G. Aminoff, M. Pinard, and A. Heidmann. High-sensitivity optical measurement of mechanical brownian motion. *Europhysics Letters*, 47(5):545–551, September 1999.

[78] S. G. Hahn and R. W. Lindquist. The two-body problem in geometrodynamics. *Annals of Physics*, 29(2):304 – 331, September 1964.

[79] G. M. Harry, T. Corbitt, M. Freytsis, D. Ottaway, N. Mavalvala, and S. Penn. Mechanical loss of laser-welded fused silica fibers. *Review of Scientific Instruments*, 77(023906), 2006.

[80] T. Haukaas. Euler bernoulli beams. University of British Columbia.

[81] D. Heiner. Silicon and sapphire as test masses for cryogenic detectors, May 2014.

[82] W. Heisenberg. Über den anschaulichen inhalt der quantentheoretischen kinematik und mechanik. *Zeitschrift für Physik*, 43(3–4):172–198, 1927.

[83] A. Heptonstall, I. Martin, A. Cumming, C. A. Cantley, G. Cagnoli, R. Jones, and D. Crooks. Production and characterisation of synthetic fused silica ribbons for advanced ligo suspensions. Technical report, Institute for Gravitational Research, University of Glasgow, 2005. LIGO Technical Note.

[84] IMPEX Hightech. Impex hightech website. `http://www.impex-hightech.de/`.

[85] S. Hild. Squeezing and qnd techniques. VESF Summer School, June 2012.

[86] Y. L. Huang and P. R. Saulson. Dissipation mechanisms in pendulums and their implications for gravitational wave interferometers. *Review Scientific Instruments*, 69:544, 1997.

[87] W. Kells and E. D'Ambrosio. Considerations on parametric instability in fabry-pérot interferometer. *Physical Letters A*, 299(4):326–330, July 2002.

[88] S. A. Kennedy, M. J. Szabo, H. Teslow, J. Z. Porterfield, and E. R. I. Abraham. Creation of laguerre-gaussian laser modes using diffractive optics. *Physical Review A*, 66:043801, October 2002.

[89] H. J. Kimble and Y. Levin et al. Conversion of conventional gravitational-wave interferometers into quantum nondemolition interferometers by modifying their input and/or output optics. *Physical Review D*, 65, December 2001.

[90] R. G. Knobel and A. N. Cleland. Nanometre-scale displacement sensing using a single electron transistor. *Nature (London, United Kingdom)*, 424(291–293), July 2003.

[91] S. Kobayashi and P. Mészáros. Gravitational radiation from gamma-ray burst progenitors. *The Astrophysical Journal*, 589(2):861–870, 2003.

[92] R. Kubo. Statistical-mechanical theory of irreversible processes. i. general theory and simple applications to magnetic and conduction problems. *Journal of the Physical Society of Japan*, 12(6):570–586, June 1957.

[93] R. Kubo. The fluctuation-dissipation theorem. *Reports on Progress in Physics*, 29(1 (Part I)):255–284, 1966.

[94] M. D. LaHaye, O. Buu, B. Camarota, and K. C. Schwab. Approaching the quantum limit of a nanomechanical resonator. *Science*, 304(5667):74–77, April 2004.

[95] L. D. Landau and E. M. Lifsits. *Fisica teorica. Vol. 2: Teoria dei campi.* Univ. Press, 2004.

[96] P. Langevin. Sur la théorie du mouvement brownien. *C. R. Acad. Sci. (Paris)*, 146:530–533, 1908.

[97] Y. Levin. Internal thermal noise in the ligo test masses: A direct approach. *Physical Review D*, 57(2):659–663, January 1998.

[98] Janis Libraries. Sapphire al2o3 transmission curve data sheet. `http://www.janis.com/Libraries/Window_Transmissions/Sapphire_Al2O3_TransmissionCurveDataSheet.sflb.ashx`.

[99] Y. T. Liu and K. S. Thorne. Thermoelastic noise in homogeneous thermal noise in finite sized gravitational-wave test masses. *Physical Review D*, 62(122002), November 2000.

[100] M Lorenzini and the Virgo Collaboration. The monolithic suspension for the virgo interferometer. *Classical and Quantum Gravity*, 27(8):084021, 2010.

[101] E. Majorana. Gravitational wave detectors and the control issues, dispense del corso di gravitazionegravitational. Corso di Laurea Specialistica in Astronomia ed Astrofisica, Dipartimento di Fisica Università La Sapienza, Roma, A.A. 2008/2009.

[102] F. Marquardt, J. P. Chen, A. A. Clerk, and S. M. Girvin. Quantum theory of cavity-assisted sideband cooling of mechanical motion. *Physical Review Letters*, 99(093902), August 2007.

[103] N. Matsumoto, T. Ando, T. Inoue, Y. Ohtake, N. Fukuchi, and T. Hara. Generation of high-quality higher-order laguerre-gauss beams using liquid-crystal-on-silicon spatial light modulators. *Journal of the Optical Society of America*, pages 1642–1651, July 2008.

[104] C. Mencuccini and V. Silvestrini. *FISICA II Elettromagnetismo-Ottica.* 1998.

[105] A. A. Michelson. XXXVIII. on the application of interference-methods to spectroscopic measurements. I. *Philosophical Magazine Series 5*, 31(191):338 – 346, 1891.

[106] A. A. Michelson. *On the application of interference methods to spectroscopic measurements.* Washington : Smithsonian Institution, 1892.

[107] A. A. Michelson and E. W. Morley. On the relative motion of the earth and the luminiferous ether. *American Journal of Science*, 34(203):333–345, 1887.

[108] C. W. Misner, K. S. Thorne, and J. A. Wheeler. *Gravitation.* W.H. Freeman and Company, San Francisco, 1973.

[109] T. Mori. Development of a high power optical cavity for optomechanical quantum nondemolition measurement. Master's thesis, Departement of Advanced Material Science, Graduate School of Frontier Science of the University of Tokyo, 2011.

[110] B. Mours, E. Tournefier, and J.-Y. Vinet. Thermal noise reduction in interferometric gravitational wave antennas: using high order tem. *Class and Quantum Gravity*, 23(20):5777–5784, September 2006.

[111] I. Nardecchia. Rumore termico delle sospensioni in advanced virgo. Master's thesis, Università Di Roma 1, 2012.

[112] I. Newton. *Philosophiae Naturalis Principia Mathematica*. J. Societatis Regiae ac Typis J. Streater, 1687.

[113] K. Numata, A. Kemery, and J. Camp. Thermal-noise limit in the frequency stabilization of lasers with rigid cavities. *Physical Review Letters*, 93(250602), December 2004.

[114] K. Numata, S. Otsuka, M. Ando, and K. Tsubono. Intrinsic loloss in various kinds of fused silica. *Classical and Quantum Gravity*, 19(7):1697 – 1702, March 2002.

[115] H. Nyquist. Thermal agitation of electric charge in conductors. *Physical Review*, 32:110 – 113, July 1928.

[116] H. C. Ohanian and R. Ruffini. *Gravitazione e Spazio-Tempo*. Zanichelli Editore S.p.A., 1997.

[117] A. Papoulis. *Probability, Random Variables and Stochastic Process*. McGraw-Hill International Edition, 1984.

[118] S. D. Penn, P. H. Sneddon, H. Armandula, J. C. Betzwieser, G. Cagnoli, J. Camp, D. R. M. Crooks, M. M. Fejer, A. M. Gretarsson, G. M. Harry, J. Hough, S. E. Kittelberger, M. J. Mortonson, R. Route, S. Rowan, and C. C. Vassiliou. Mechanical loss in tantala/silica dielectric mirror coatings. *Classical and Quantum Gravity*, 20(13):2917–2928, June 2003.

[119] N. Peschken. Electrostatic control of a suspended mirorr, stage report. École normale supérieure de Lyon, June 2011.

[120] T. Piran. Cylindrical general relativistic collapse. *Physical Review Letters*, 41(16):1085, October 1978.

[121] F. A. E. Pirani. On the physical significance of the riemann tensor. *Acta Physica Polonica*, 15:389–405, 1956.

[122] M. Punturo. The virgo sensitivity curve. *VIRGO NOTE*, VIR-NOT-PER-1390-51, October 2004.

[123] M. Punturo, M. Abernathy, F. Acernese, B. Allen, N. Andersson, K. Arun, F. Barone, B. Barr, M. Barsuglia, M. Beker, N. Beveridge, S. Birindelli, S. Bose, L. Bosi, S. Braccini, C. Bradaschia, T. Bulik, E. Calloni, G. Cella, E. Chassande Mottin, S. Chelkowski, A. Chincarini, J. Clark, E. Coccia, C. Colacino, J. Colas, A. Cumming, L. Cunningham, E. Cuoco, S. Danilishin, K. Danzmann, G. De Luca, R. De Salvo, T. Dent, R. Derosa, L. Di Fiore, A. Di Virgilio, M. Doets, V. Fafone, P. Falferi, R. Flaminio, J. Franc, F. Frasconi, A. Freise, P. Fulda, J. Gair, G. Gemme, A. Gennai, A. Giazotto, K. Glampedakis, M Granata, H. Grote, G. Guidi, G. Hammond, M. Hannam, J. Harms, D. Heinert, M. Hendry, I. Heng, E. Hennes, S. Hild, J. Hough, S. Husa, S. Huttner, G. Jones, F. Khalili, K. Kokeyama, K. Kokkotas, B. Krishnan, M. Lorenzini, H. Lück, E. Majorana, I. Mandel, V. Mandic, I. Martin, C. Michel, Y. Minenkov, N. Morgado, S. Mosca, B. Mours, H. Müller Ebhardt, P. Murray, R. Nawrodt, J. Nelson, R. Oshaughnessy, C. D. Ott, C. Palomba, A. Paoli, G. Parguez, A. Pasqualetti, R. Passaquieti, D. Passuello, L. Pinard, R. Poggiani, P. Popolizio, M. Prato P. Puppo, D. Rabeling, P. Rapagnani, J. Read, T. Regimbau, H. Rehbein, S. Reid, L. Rezzolla, F. Ricci, F. Richard, A. Rocchi, S. Rowan, A. Rüdiger, B. Sassolas, B. Sathyaprakash, R. Schnabel, C. Schwarz, P. Seidel, A. Sintes, K. Somiya, F. Speirits, K. Strain, S. Strigin, P. Sutton, S. Tarabrin, J. van den Brand, C. van Leewen, M. van Veggel and. C van den Broeck, A. Vecchio, J. Veitch, F. Vetrano, A. Vicere, S. Vyatchanin, B. Willke, G. Woan, P. Wolfango, and K. Yamamoto. The third generation of gravitational wave observatories and their science reach. *Classical and Quantum Gravity*, 27(8):084007, April 2010.

[124] P. Puppo. Virgo+ms sensitivity curve. *VIRGO NOTE*, VIR-0639D-09, December 2009.

[125] P. Puppo. Virgo+ms sensitivity curve. *VIRGO NOTE*, VIR-0639F-09, February 2012.

[126] P. Puppo. The thermal noise, dispense del corso di gravitazione sperimentale. Corso di Laurea Specialistica in Astronomia ed Astrofisica, Dipartimento di Fisica Università La Sapienza, Roma, A.A. 2008/2009.

[127] P. Puppo, M. Colombini, I. Nardecchia, E. Majorana, P. Rapagnani, and F. Ricci. Virgo+ thermal noise study. *VIRGO NOTE*, VIR-0074B-12, June 2012.

[128] S. Recchia. Design of the homodyne detector to measure the squeezing level of the light for advanced virgo. Master's thesis, Dipartimento di Fisica Università La Sapienza, Roma, 2013.

[129] F. Ricci. Gravitazione sperimentale. Corso di Gravitazione Sperimentale, Dipartimento di Fisica Università La Sapienza, Roma.

[130] F. Ricci. The search of gravitational waves. *LYCEN RI9517*, May 1995.

[131] H. Rubens and R. W. Wood. Focal isolation of long heat-waves. *Philosophical Magazine Series 6*, 21(122):249–261, 1911.

[132] B. Ryden. *Introduction to Cosmology.* Addison Wesley, 2003.

[133] P. R. Saulson. Thermal noise in mechanical experiments. *Physical Review D*, 42(8):2437–2445, October 1990.

[134] P.R. Saulson. *Fundamentals of interferometric gravitational wave detectors.* World Scientific Publishing, 1994.

[135] A. Schliesser, R. Rivière, G. Anetsberger, O. Arcizet, and T. J. Kippenberg. Resolved-sideband cooling of a micromechanical oscillator. *Nature Physics*, 4(415), April 2008.

[136] A. E. Seigman. *Lasers.* University Science Books, 1986.

[137] B. S. Sheard, M. B. Gray, C. M. Mow-Lowry, D. E. McClelland, and S. E. Whitcomb. Observation and characterization of an optical spring. *Physical Review A*, 69(051801(R)), May 2004.

[138] A. E. Siegman. Hermite-gaussian functions of complex argument as optical-beam eigenfunctions. *Journal of the Optical Society of America*, 63(9):1093–1094, September 1973.

[139] L. Smarr. *The Structure of General Relativity with a Numerical Example.* PhD thesis, University of Texas, Austin, 1975.

[140] L. Smarr. Spacetimes generated by computers: Black holes with gravitational radiation. *Annals of the New York Academy of Sciences*, 302:569, 1977.

[141] P.H. Sneddon, S. Bull, G. Cagnoli, D.R.M. Crooks, E.J. Elliffe, J.E. Faller, M.M. Fejer, J. Hough, and S. Rowan. The intrinsic mechanical loss factor of hydroxy-catalysis bonds for use in the mirror suspensions of gravitational wave detectors. *Classical and Quantum Gravity*, 20:5025–5037, 2003.

[142] J. D. Thompson, B. M. Zwickl, A. M. Jayich, F. Marquardt, S. M. Girvin, and J. G. E. Harris. Strong dispersive coupling of a high-finesse cavity to a micromechanical membrane. *Nature (London, United Kingdom)*, 452(6), March 2008.

[143] H. Vahlbruch. *Squeezed Light for Gravitational Wave Astronomy.* PhD thesis, Gottfried Wilhelm Leibniz Universität Hannover, 2008.

[144] J.-Y. Vinet. Reducing thermal effects in mirrors of advanced gravitational wave interferometric detectors. *Classical and Quantum Gravity*, 24(15):3897, July 2007.

[145] A. Di Virgilio. Measurement of the relative motion of two mirrors in presence of an optical spring. *Journal of Physics: Conference Series*, 122(012021), 2008. Presented at Amaldi7 conference, Sydney 2007.

[146] A. Di Virgilio, L. Barsotti, S. Braccini, C. Bradaschia, G. Cella, C. Corda, V. Dattilo, I. Ferrante, F. Fidecaro, I. Fiori, F. Frasconi, A. Gennai, A. Giazotto, P. La Penna, G. Losurdo, E. Majorana, M. Mantovani, A. Pasqualetti, D. Passuello, F. Piergiovanni, A. Porzio, P. Puppo, P. Rapagnani, F. Ricci, S. Solimeno, G. Vajente, and F. Vetrano. Experimental evidence for an optical spring. *Physical Review A*, 74(013813), July 2006.

[147] H. Vocca. *Studio del rumore termico in regime di stazionarietà e di non stazionarietà per l'interferometro Virgo.* PhD thesis, Università di Perugia, 2003.

[148] D. F. Walls and G. M. Milburn. *Quantum Optics.* 2008.

[149] J. Weber. Detection and generation of gravitational waves. *Physical Review, American Physical Society*, 117(1):306–313, January 1960.

[150] S. A. Webster, M. Oxborrow, S. Pugla, J. Millo, and P. Gill. Thermal noise limited optical cavity. *Physical Review A*, 77:033847, 2008.

[151] J. M. Weisberg, J. H. Taylor, and L. A. Fowler. Gravitational waves from an orbiting pulsar. *Scientific American*, 245:74–82, October 1981.

[152] R. Weiss. Electromagetically coupled broadband gravitational antenna. *Quarterly Progress Report, MIT Research Lab of Electronics Quarterly Progress Reports of the Research Laboratory for. Electronics*, 105:54–76, 1972.

[153] N. Wiener. Generalized harmonic analysis. *Acta Mathematica*, 55(1):117–258, December 1930.

[154] P. Willems. Dumbbell-shaped fibers for gravitational wave detectors. *Physics Letters A*, 300:162, 2002.

[155] P. Willems, V. Sannibale, J. Weel, and Valery Mitrofanov. Investigations of the dynamics and mechanical dissipation of a fused silica suspension. *Physics Letters A*, 297:37–48, May 2002.

[156] I. Wilson-Rae, N. Nooshi, W. Zwerger, and T. J. Kippenberg. Theory of ground state cooling of a mechanical oscillator using dynamical backaction. *Physical Review Letters*, 99(093901), August 2007.

[157] M. Xiao, L.-A. Wu, and H. J. Kimble. Precision measurement beyond the shot-noise limit. *Physical Review Letters*, 59(3):278–281, July 1987.

[158] K. Yamamoto. *Study of the thermal noise caused by inhomogeneously distributed loss.* PhD thesis, Department of Physics, Graduate school of Science, University of Tokyo, December 2000.

[159] C. Zener. Internal friction in solids. i. theory of internal friction in reeds. *Physical Review*, 52:230 – 235, August 1937.

[160] C. Zener. Internal friction in solids ii. general theory of thermoelastic internal friction. *Physical Review*, 53:90 – 99, January 1938.

[161] C. Zhao, L. Ju, J. Degallaix, S. Gras, and D. G. Blair. Parametric instabilities and their control in advanced interferometer gravitational-wave detectors. *Physical Review Letters*, 94(121102), April 2005.